



Integrated hydraulic modeling of groundwater flow and river-aquifer exchanges in the lower valley of Var River

Mingxuan Du

► To cite this version:

Mingxuan Du. Integrated hydraulic modeling of groundwater flow and river-aquifer exchanges in the lower valley of Var River. Other. Université Côte d'Azur, 2016. English. NNT : 2016AZUR4107 . tel-01484652

HAL Id: tel-01484652

<https://theses.hal.science/tel-01484652>

Submitted on 7 Mar 2017

HAL is a multi-disciplinary open access archive for the deposit and dissemination of scientific research documents, whether they are published or not. The documents may come from teaching and research institutions in France or abroad, or from public or private research centers.

L'archive ouverte pluridisciplinaire **HAL**, est destinée au dépôt et à la diffusion de documents scientifiques de niveau recherche, publiés ou non, émanant des établissements d'enseignement et de recherche français ou étrangers, des laboratoires publics ou privés.

UNIVERSITÉ NICE-SOPHIA ANTIPOLIS

ÉCOLE DOCTORALE STIC

SCIENCES ET TECHNOLOGIES DE L'INFORMATION ET DE LA COMMUNICATION

THÈSE

pour l'obtention du grade de

Docteur en Sciences

de l'Université Nice-Sophia Antipolis

Mention : Modélisation, eau et ville

présentée et soutenue par

Mingxuan DU

**Modélisation intégrée des écoulements souterrains et
des échanges nappe-rivière dans la basse vallée du Var**

**Integrated hydraulic modeling of groundwater flow
and river-aquifer exchanges in the lower valley of Var river**

Thèse dirigée par *Philippe GOURBESVILLE*
soutenue le 09/12/2016

Jury:

M. Reinhard HINKELMAN, Pr., Université technique de Berlin
M. Shie-Yui LIONG, Pr., Université nationale de Singapour
M. Olivier FOUCHÉ, M.C., Conservatoire National des Arts et Métiers
M. Philippe AUDRA, Pr., Université Nice-Sophia Antipolis
M. Olivier DELESTRE, M.C., Université Nice-Sophia Antipolis
M. Philippe GOURBESVILLE, Pr., Université Nice-Sophia Antipolis

Rapporteur
Rapporteur
Examineur
Président du jury
Co-Directeur
Directeur de Thèse

This dissertation is lovingly dedicated to my grandparents, Mrs. Xiulan Gong and Mr. Yongfeng Jing, who departed out of this world on 24 August and 3 October 2016.

Acknowledgement

When I look back at these last three years in this engineer school, Polytech Nice, I would like to list many people that helped me not only in my work, but also in my life, and show the deepest respect and acknowledgement to them at the beginning of this dissertation.

This study is achieved in the framework of AquaVar project, which is brought by the supervisor of my thesis, professor Philippe Gourbesville, the director of Polytech Nice and Innovative City Laboratory. He is a mentor to me from the very beginning of my work in the engineer school. I learned how to work as a researcher and as a professional engineer under his generous help, unselfish supports and kind tolerance. He contributed too much to the study and to the whole project, which makes me have the willingness to devote all that I have to this work.

I would like to thank professor Philippe Audra, for his precious help all along my work on this dissertation. I majored in coastal engineering for bachelor degree and in river surface water modeling for master (engineer) degree, thus my knowledge on hydrogeology is only on a basic level before I started this study. Thanks to his help, I started to gain my knowledge on groundwater modeling, which is one of the necessary professional competencies for this study. It is a pleasure to work under his supervision since he gives not only the guides to the research, but also precious suggestions and feedbacks on the presentations.

Dr. Olivier Delestre graciously contributed his time for this dissertation as an advisor and the first reader of this dissertation and all other papers that I've written. His valuable advices were always helpful for the research work. Five years ago, when I was a student in engineer school, he was my first professor on hydraulic modeling and numerical methods, from then I started to know this interesting subject. His meticulous approach has strongly affected me and I recognize him as a good example that is worthy of imitation.

I am very grateful to my colleagues of the AquaVar team at Innovative City Laboratory, Elodie Zattero and Qiang Ma, with whom I have excellent cooperation in the study. Their generous help has made many tough tasks easier for me. We worked as a team and overcame many obstacles during the last two years. It has been a great time to be a member of this team. I've spent a lot of time working with Elodie Zattero on field measurement and on the development of the coupling interface between her model and my model. I hereby thank her for all her help all the supports that she gave to me.

Dr. Olivier Fouché has made a huge contribution to the study as well as this dissertation. Despite the distance between Paris and Nice, he came to my office to offer his valuable suggestions for the study. I want to thank him for the time that he spent with us on a field measurements. I appreciate as well the opportunity that he gave me to present my study in IAH congress on September 2016.

Some foreigners found that the life in another country is tough due to the difference in culture. However, as a Chinese, I do not agree with this point of view because I've experienced a wonderful

time in France since I've received too much help from all my friends in France: Leslie Salvan, Morgan Abily, Lian Guey Ler, Arianna Calza, Jelena Batica and Vo Ngoc Duong. The story among us has made a great part of my unforgettable life in France. I would like to thank all of them for all the help through these years.

I want to thank my parents, professor Xiuguo Du and Mrs Cuiping Jing, who gave me countless supports in my whole life with their endless love, which encouraged me to get through the tough times. Not failing to live up to what my parents expect of me is one of the greatest force that drags me to the end of the study. Finally, my deepest love belongs to my dear wife, Mrs Yajing Zhang, thank you for your understanding and all that you've brought to this family.

Abstract

Hydraulic modeling with deterministic model is a common approach applied by researchers and engineers to study the groundwater flow and to provide information to decision makers. Nevertheless, groundwater flow modeling is a complicated process, especially in complex aquifers where the quantity and the quality of the measured data are not satisfying.

The unconfined alluvial aquifer is the main water resource in the lower valley of Var river, French Riviera, but it faces a threat of shortage and pollution. Despite numerous previous studies, the dynamics of the groundwater flow in the alluvial aquifer and the characteristics of the river-aquifer exchanges are still partially unknown. Therefore the local water management service requires a decision support system (DSS) based on numerical models to ensure a better groundwater management.

A hydraulic model is set up with FEFLOW software by considering precipitation, evapotranspiration, groundwater extraction and river-aquifer exchanges. The non-documented groundwater extraction for agricultural use and the transfer rates in the riverbed along the river have been calibrated.

The model is validated with a simulation of 1266 days. 6 points are chosen to evaluate the model efficiency. The Nash coefficient varies between 0.42 and 0.94; the mean absolute error varies between 0.13 and 0.37 m. Discussions are given regarding the actual evapotranspiration calculation, river-aquifer disconnection modeling and the reason of the inaccurate result on one site.

The model is applied to simulate the scenarios of flood and drought events. The simulations of pollution events in the unconfined aquifer show that the pollutant propagates faster in the upstream part than in the downstream part. Then a seawater intrusion study in the estuary of Var river reveals that the pumped volume in the municipal pumping stations may have a significant influence on the quality of water pumped in the airport. A first conception of the DSS tool is presented as the last example of model application.

In the last part of this study, a coupling interface is developed thanks to a Java which enables an automatic exchange of data between the groundwater flow model and the surface water flow model built with MIKE21FM. The simple test of functionality shows that the algorithm is correct. More tests should be done to validate the coupling interface.

Key words: groundwater flow, hydraulic modeling, river-aquifer exchanges, alluvial aquifer, FEFLOW, Lower valley of Var river, pollutant transport, seawater intrusion, decision support system.

Résumé

La modélisation hydraulique avec modèle déterministe est une méthode largement utilisée par des chercheurs et des ingénieurs pour étudier des écoulements souterrains et pour fournir des informations aux décideurs. Cependant, la modélisation est un processus complexe, notamment pour les aquifères où la quantité et la qualité des données ne sont pas satisfaisantes.

Étant une des sources principales de l'eau douce dans la basse vallée du Var, Côte d'Azur, France, la nappe libre de la vallée est menacée par la pénurie et la pollution. Malgré le grand nombre d'études effectuées dans cette zone, la dynamique des écoulements souterrains est toujours partiellement inconnue. Par conséquent, la métropole Nice Côte d'Azur (NCA) a besoin de développer un système d'aide à la décision (SAD) à base des modèles numériques afin d'assurer une gestion plus efficace de l'eau souterraine.

Un modèle numérique est développé avec FEFLOW en tenant compte des précipitations, de l'évapotranspiration, du pompage de l'eau souterraine, et des échanges nappe-rivière. Le volume d'eau pompé pour l'usage agricole et le taux d'échange du lit mineur du Var ont été calibrés.

La validation du modèle a été effectuée avec une simulation de 1 266 jours. 6 points ont été choisis pour évaluer la qualité du modèle. Le coefficient de Nash est de 0,42 à 0,94, et la valeur de l'erreur moyenne absolue est de 0,13 à 0,37 m. Les discussions ont porté sur le calcul de l'évapotranspiration, la méthode pour modéliser la déconnexion entre la rivière et la nappe, et la raison pour laquelle le résultat est moins satisfaisant sur un site.

Le modèle est utilisé pour simuler les scénarii des événements d'inondation et de sécheresse. Les simulations des scénarii de pollution montrent que la vitesse de propagation du polluant est plus grande en amont qu'en aval. L'étude de l'intrusion d'eau de mer confirme que le volume de pompage dans le champ captant municipal peut avoir une influence significative sur la qualité de l'eau pompée à l'aéroport. Une première conception du système d'aide à la décision est présentée comme le dernier exemple de l'application du modèle.

Une interface de couplage est développée en Java et sert à échanger les données entre le modèle souterrain et le modèle à surface libre élaboré avec MIKE21FM. L'essai de fonctionnement indique que l'algorithme est correct, mais d'autres tests sont nécessaires pour le valider.

Mots-clés : écoulements souterrains, modélisation souterraine, échanges nappe-rivière, nappe alluviale, FEFLOW, basse vallée du Var, transport de pollution, intrusion d'eau de mer, système d'aide à la décision.

Table of contents

Table of contents	5
List of abbreviations	8
List of symbols	9
Introduction	12
1. Study background.....	12
2. AquaVar project	13
3. Objectives of the research	15
4. Thesis structure	16
Chapter I. Var catchment and the lower Var valley	18
I.1 Var catchment	18
I.2 Lower Var valley	21
I.2.1 Geography and evolution of the valley	21
I.2.2 Geological context	26
I.2.3 Hydrological context.....	29
I.2.4 Hydrogeological context.....	38
I.3 Conclusion	50
Chapter II. Interpretation of the groundwater flow modeling	51
II.1 Hydrologic cycle of estuary area	51
II.2 Main issues regarding groundwater in lower Var river valley	53
II.2.1 Impact of erosion and deposition in the riverbed on the groundwater	53
II.2.2 Groundwater extraction	59
II.2.3 Extreme hydrological events	60
II.3 Hydraulic modeling approach.....	61
II.4 Interpretation of hydraulic modeling	62
II.4.1 Hydraulic modeling approach.....	62
II.4.2 Conceptual model of groundwater flow in lower Var river valley.....	64
II.5 Conclusion	70
Chapter III. Development of the numerical model of groundwater flow	71
III.1 Governing equations of groundwater flow.....	71
III.2 Model domain, topography and geological layers	75
III.2.1 Model domain	75
III.2.2 Mesh generation	78

III.2.3 Geological layers	80
III.2.4 Hydraulic parameters	84
III.3 Direct water recharge/loss	88
III.3.1 Estimation of <i>PET</i> and <i>AET</i>	88
III.3.2 Direct water recharge/loss	93
III.4 River-aquifer exchanges	95
III.5 Groundwater extraction	98
III.6 Model calibration	101
III.6.1 Grid convergence study	101
III.6.2 Sensitivity analysis	102
III.6.3 Results and discussions	106
III.7 Model validation	113
III.7.1 Presentation of the simulation	113
III.7.2 Simulation results and model evaluation	115
III.7.3 Discussions	123
III.7.4 Post-treatment of the results	130
III.8 Conclusion	135
III.8.1 Model setup	136
III.8.2 Model results and analysis	138
Chapter IV. Model application in groundwater management	139
IV.1 Scenario simulations of extreme hydrological events	140
IV.1.1 Methodology for scenario designing	141
IV.1.2 Inputs data for scenario simulations	152
IV.1.3 Scenario simulation results	153
IV.2 Scenario simulation of pollutant transport	157
IV.3 Scenario simulation of salt water intrusion	169
IV.3.1 Context of the seawater intrusion study in the lower Var river valley	169
IV.3.2 Setup of the seawater intrusion model of Var estuary	172
IV.3.3 Scenario design	176
IV.3.4 Seawater intrusion simulation results	178
IV.4 Conception of a management tool based on the numerical models	183
IV.4.1 Integrated monitoring system	183
IV.4.2 Data update in groundwater flow model	188
IV.5 Conclusion	189

Chapter V. Coupled groundwater and surface water model	192
V.1 A brief review of groundwater and surface water coupling	192
V.2 Conception of the coupling interface	195
V.3 Simulation test with the developed coupling interface	200
V.4 Conclusion.....	202
General conclusions and perspectives	203
M. Setup of the groundwater hydrodynamic model.....	204
2. Model application and DSS.....	206
3. Coupled model for groundwater and surface water flows	207
4. Improvements and perspectives	208
Bibliography.....	211
List of tables	222
List of figures	224
List of appendix.....	231
Appendix 1. International chronostratigraphic chart.....	232
Appendix 2. Geological layers in the lower valley	234
Appendix 3. Geological drilling test of confined aquifer in the estuarine area of Var river	236
Appendix 4. Measurement of groundwater level in the lower Var river valley.....	237
Appendix 5. Computational mesh types and characteristics	240
Appendix 6. Geographical survey methods	241
Appendix 7. Maximal values of daily average discharge measured at Napol éon III bridge used for Gumbel law calculation.....	243
Appendix 8. Monthly average discharge measured at Napol éon III bridge used for log- normal law calculation	244

List of abbreviations

AET	Actual evapotranspiration
BRGM	Bureau de Recherches Géologiques et Minières
CFL	Courant–Friedrichs–Lewy condition
CG06	Conseil Général Alpes-Maritimes (06)
COD	Chemical oxygen demand
DEM	Digital elevation model
DSS	Decision support system
EUR	Easily usable reserve of the water in the soil
GNSS	Global navigation satellite system
GPU	Graphical processing units
GUI	Graphical user interface
IDW	Inverse distance weighted
IFM	Interface manager
IGN	Institut national de l’information géographique et forestière
M.a	Million years (geology)
NCA	Nice Côte d’Azur
NGF	Nivellement général de la France
NSE	Nash-Sutcliffe efficiency coefficient
MAE	Mean absolute error
PDE	Partial differential equation
PET	Potential evapotranspiration
REA	Régie Eau d’Azur
TDS	Total dissolved solids

List of symbols

A	cross section area of the soil	[L]
B	thickness of the unconfined aquifer	[L]
c	runoff coefficient	[-]
C	concentration of the pollutant	[M/L ³]
d_{30}	diameter corresponding to 30% finer in the particle-size distribution of the soil	[L]
d_c	thickness of the clogging layer	[L]
D_d	molecular diffusion	[L ² /T]
D_m	tensor of mechanical dispersion	[L ² /T]
e	gravitational unit vector	[-]
H	water depth in the river	[L]
h_r	monthly potential evapotranspiration	[L]
H_j	theoretical duration of daytime in the month	[T]
I_g	monthly global radiation received by the soil	[M/T ³]
$I_g A$	theoretical global radiation	[M/T ³]
j_c	mass flux	[M/L ² /T]
K	hydraulic conductivity of the soil	[L/T]
K	tensor of hydraulic conductivity of the soil	[L/T]
K_a	hydraulic conductivity of the aquifer	[L/T]
K_c	hydraulic conductivity of the riverbed clogging layer	[L/T]
$K_r(s)$	relative hydraulic conductivity	[L/T]
ΔL	dimension of $x/y/z$ grid	[L]
n	Manning roughness coefficient	[T/L ^{1/3}]
n_T	total number of time steps of a numerical simulation	[-]
P	precipitation depth per unit area	[L]
q	flux of groundwater flow	[L/T]
Q	flow rate through the cross section in river or in aquifer	[L ³ /T]

q_{ag}	estimated pumping rate of water for agricultural use	[L/T]
q_{ex}	exchange flux, or exchange rate per unit area	[L/T]
Q_{in}	volume of water that enters the soil	[L ³]
Q_{ms}	specific mass supply per unit time per unit depth	[T ⁻¹]
Q_{out}	volume of water that leaves from the soil	[L ³]
q_r	flux of direct water recharge/loss	[L/T]
Q_R	increment of the groundwater storage	[L]
r	density ratio of the seawater	[-]
R	runoff height per unit area	[L]
Re	Reynolds number	[-]
S_{fx}	friction terms depending on the friction law	[-]
S_{fy}	friction terms depending on the friction law	[-]
$s(h)$	soil saturation	[-]
S_{ox}	terms of slope on x -axis	[-]
S_{oy}	terms of slope on y -axis	[-]
S_r	specific retention	[-]
S_s	specific storage	[L ⁻¹]
S_y	specific yield, also called drain/fillable porosity or effective porosity	[-]
t	time	[T]
T	return period of an event	[T]
T_M	monthly average air temperature	[F]
V_{soil}	total volume of the soil	[L ³]
V_{water}	volume of water stored in the soil	[L ³]
$z(x, y)$	topography	[L]
β_L	longitudinal dispersivity	[L]
β_T	transverse dispersivity	[L]
γ	fluid compressibility	[L ⁻¹]
Γ	coefficient of skeleton compressibility	[L ⁻¹]

δ_{tf}	time step of the groundwater flow model in FEFLOW	[T]
δ_{tm}	time step of the groundwater flow model in MIKE21FM	[T]
Δt	time step of the coupling interface	[T]
ε	porosity of the soil	[-]
μ	dynamic viscosity of the fluid	[M/L/T]
ρ	density of the fluid	[M/L ³]
ρ_f	density of the fresh water	[M/L ³]
ρ_s	density of the seawater	[M/L ³]
ϕ	transfer rate of the riverbed	[T ⁻¹]
ϕ_{in}	in-transfer rate	[T ⁻¹]
ϕ_{out}	out-transfer rate	[T ⁻¹]
ψ_g	groundwater level in the aquifer	[L]
ψ_s	water level in the river	[L]

Introduction

1. Study background

As an important natural resource, groundwater has become a main water source for domestic, agricultural and industrial uses. During the last century, human activities, especially urbanization and industrialization, have influenced intensively the consumption of groundwater. Many negative effects induced by over extraction, seawater intrusion and pollutant discharge or leakage have been always challenging the water management authorities.

The groundwater management emphasizes two major aspects: controlling the quality of the natural water resource and maintaining the quantity of water supply. Most urban agglomerations are built up along rivers or estuaries. The water supply relies on both surface water and groundwater. Understanding the exchange of water between the aquifer and its river is a key issue for the long-term water management regarding both aspects.

Hydraulic modeling is an effective way to study the groundwater. It provides not only the assessment of risks, but also reliable solutions for the decision makers. Two types of model are frequently used in the study of groundwater hydraulics: physical model and numerical model. Physical models reproduce a scaled geometry and physical flow in laboratory. They emphasize the similarity of the physics or the geometry between the models and the real cases. Numerical models, however, perform simulations of flow on computers. They emphasize the similarity of the mathematics between them such as the governing equations and hydraulic parameters, *etc.* For the study of groundwater, the physical modeling is much expensive and time consuming compared with the numerical modeling due to the complexity of porous media. Therefore the latter is more widely used as the computer science and the pioneering works in hydroinformatics have been rapidly developed since the 1970s [Verruijt, 1970; McDonald and Harbaugh, 1984; Diersch and Kolditz, 1998].

The reliability of a numerical model is only a question of employing appropriate governing equations, numerical methods, and boundary conditions. For different cases, the aims of modeling are not the same, so the models need to be built are also different. Hence, the need for a reliable numerical model always exists so that they can undertake daily management or reactions to special events.

The conception of the integrated modeling is commonly used in the field of computer science. The integrated modeling means to unify several modules. Even though each of them can stand alone usefully, they are even more useful when put together, in order to achieve complex functions according to the needs [Geofrion, 1988]. As for water resource management, the model system often involves modules on several subjects such as hydraulics, hydrology, meteorology and ecology [Roelvink, 2005]. This diversity can be reflected in all the process of modeling, from the very beginning of the construction of model system, which is data collection, to the end of the model application, which is always analysis of the model results. The researchers and engineers should carefully consider the aim and the needs of the research project in order to correctly choose the modules that should be taken into account in the modeling system.

Unlike surface water flow, groundwater flow exists in the porous media or karst aquifer. It means that the hydraulics of groundwater is a result of the fluid dynamics interacting with soil or rock, so the groundwater flow modeling process is fraught with uncertainties. For example, the interpolation of measured data, lack of measurement of physical parameters, estimation of numerical factors may all cause uncertainties. The difficulty of groundwater modeling lies in using an appropriate method to minimize the uncertainty in order to make the model correct, or at least, the most rational.

This research project includes the scientific study of an integrated groundwater hydraulic model and its possible application in the field of water management. On one hand, it explains the methodology for the design of a hydraulic model regarding several problematic issues, on the other hand, the model must be able to describe and reproduce the groundwater hydraulics in the aquifer as well as the river-aquifer exchanges in the studied area.

2. AquaVar project

The unconfined aquifer of the lower Var valley has become the main fresh water resource of the state (département) of Alpes-Maritimes. It provides the water supply for industrial, agricultural and domestic use to the Nice Côte d'Azur conurbation and also to many communities located between Antibes city and Menton city, which form a total population of 600 000. The local water management authority, Régie Eau d'Azur (REA), has started a research project called AquaVar, whose objective is to optimize the freshwater resource management by producing an integrated water management tool. The project has been initiated since 2014 and it is planned to last for 4 years.

This project emphasizes the understanding of the water cycle in the Var catchment and the quantification of the river-aquifer exchanges in the lower valley of Var river, which cover different temporal and spatial scales of the water management. The results of the research are expected to be able to provide the arguments to support the decision-making regarding the daily operations, reactions to accidental events and influence of future developments. Once completed, this project will lead to economic, social and ecological profits thanks to the optimized water management plan.

The final aim of the project is to develop a deterministic modeling system which is able to simulate the water cycle at the catchment scale and to simulate the river-aquifer exchange at the sub-catchment scale. Four functions must be fulfilled in order to meet the needs of the local water management authority:

- the modeling system will be used to predict the impact of future construction projects on river and groundwater hydraulics, as well as the river morphology evolution induced by sediment transportation;
- it will be also used in long term scenario simulation to analyze the response of the catchment to climate change;
- the modeling system should be able to predict the impact of extreme meteorological events such as drought and flood at sub-catchment scale;
- it should contain a pollutant transport module in order to simulate the seawater intrusion and accidental chemical pollutant leakage into the river or into the unconfined aquifer.

Considering the project needs, the modeling system is thus designed, which contains 3 individual models and a coupling interface:

- a hydrological model will be set up to simulate the rainfall-runoff process of the whole catchment by considering precipitation, snow melting, infiltration and evapotranspiration;
- a river hydraulic model will be set up to simulate the surface flow in the lower Var river which considers the river-aquifer exchanges;
- a groundwater flow model will be set up to simulate the unconfined aquifer in lower Var river valley by taking into account evapotranspiration, infiltration, river-aquifer exchanges and groundwater extraction;

- a coupling interface will be developed to couple the hydrodynamic module of the river hydraulic model and the groundwater flow model, in order to perform accurate simulations of the river-aquifer exchanges in the aim of revealing the interaction between the surface and subsurface flow in the lower valley of Var river.

Once developed, these components will be combined together to form the core of an information system that can be operated by the local water management authority to support the water management. The information system provides not only the real time monitoring data, but also the predicted hydrological and hydraulic simulation results calculated by the validated models that are explained above.

3. Objectives of the research

Previous studies have been carried out to study the hydraulics of the unconfined aquifer in the lower valley of Var river [Guglielmi, 1993; Guglielmi and Reynaud, 1997; Emily et al. 2010; Potot, 2011; Potot et al., 2012]. The methodology applied is based on stationary hydrogeological [Guglielmi, 1993; Guglielmi and Reynaud, 1997; Emily et al. 2010] or hydrochemical [Potot, 2011; Potot et al., 2012] measurements. Therefore, these studies are not able to provide results on the hydrodynamics in transient mode. Providing that the contour map of groundwater levels are generated from stationary measurements, it can only give qualitative conclusion of river-aquifer exchanges at the seasonal scale, the hydrodynamics of the aquifer still remains partially unknown, or at least unquantified due to the limitation of the methodology. This has left a research gap that needs to be filled. Hence, a research on the hydrodynamics of the unconfined aquifer is strongly needed, because it represents more accurately the realistic state of the aquifer.

Considering this research gap and the limitations of the previous studies, the study purpose of this research work is therefore given:

- The data need to be collected and analyzed to improve the understanding of the surface water and groundwater hydraulics. The conclusion of the data analysis will help the setup of the conceptual model and the numerical model of groundwater flow.
- A conceptual model will be set up by considering the main processes in the water cycle in lower Var river valley, including precipitation, evapotranspiration, river-aquifer exchange, groundwater abstraction, *etc.*

- A numerical model will be set up with FEFLOW software based on the conceptual model. This numerical model needs to contain two modules: hydrodynamics of the groundwater flow and pollution transport in unconfined aquifer. The model should be able to perform simulations of steady and transient states. Regarding the hydrodynamic module, it will provide the evolution of groundwater table versus time and the river-aquifer exchange flux in different river sections. The pollutant transport module will provide a map of concentration distribution and the evolution of concentration versus time at selected points.
- Once the model is validated, some scenarios such as floods and droughts need to be simulated in order to know the response of the groundwater flow under the extreme hydrological conditions. Pollutant scenarios such as accidental pollutant injection and seawater intrusion will also be simulated. This study will characterize the vulnerability of the groundwater reserve in the unconfined aquifer in the lower Var river valley.
- The river-aquifer exchanges are complicated processes which depend on the transient state of the water level in the river and the groundwater level in the aquifer. It would be more appropriate to simulate this exchange with a coupled surface-groundwater flow model. Therefore a coupling interface will be built to couple the FEFLOW [Diersch, 2014] and Mike21FM [DHI, 2011] software.

4. Thesis structure

According to the study aim, this thesis is divided into five consecutive chapters and each chapter unfolds a specific subject explained above. The first chapter introduces the Var catchment and the lower Var river valley on several aspects. The next three chapters form the second part of the thesis, which focuses on the procedure to develop the hydraulic model of the groundwater flow as well as its application examples. The fifth chapter presents the coupling scheme of surface-groundwater flow model and a first test on the Var river case study. The last chapter presents the premier conception of an information system based on the modeling system, as it could be used by the water management service in the decision making process.

These chapters exactly follow the order of the cognitive process of comprehension to the natural world. The introduction of the study area shows the problematic issues and related characteristics with the collected data. From these data the conceptual models can thus be built, because the latter are the

simplified interpretation of the complex natural world. The numerical model is built to accomplish this interpretation by using mathematical equations and numerical schemes. It helps people to have a better understanding of the reality, therefore it can predict the future by simulating the scenarios, which are designed to anticipate the possible events. After a series of simulations, the advantages and limitations will show up, this makes the room to improve the existing model. In this case, the coupled model is the improvement of the river-aquifer exchange simulation. The conception of the development of the information system emphasizes always the application of the numerical models in the decision making process.

Chapter I. Var catchment and the lower Var valley

I.1 Var catchment

The Var catchment is located in southeastern France, which is also known as the famous vacation resort, the French Riviera. The catchment, which covers most of the department of Alpes-Maritimes and a small part of the department of Alpes-de-Haute-Provence, has a total area of 2 800 km². The catchment is characterized by a conspicuous variation of altitude from 0 m at the Mediterranean sea, to 3132 m at the mountain peaks of Mont G das (Figure I.1).

The ridge lines divide the whole catchment into 5 sub-catchments, which are drained respectively by 5 rivers. The Var river, which is the longest river in the catchment, begins at the spring in the village of Estenc, in the south of the mountain pass of Cayolle. The river flows through a distance of 114 km and finally runs into the Mediterranean sea between Nice and Saint-Laurent-du-Var (Figure I.2). The elevation varies from 1790 m to 0 m, which forms a steep average streamline slope of 1.57%.

The Var river receives water mainly from 5 large tributaries named respectively the Cians (25 km), the Tin e (75 km), the V subie (48 km), the Coulomp (20 km) and the Est ron (66,7 km). They are all typical mountain streams with “V”-shaped transverse profiles in the valley which are formed by the natural trenching effect (Figure I.1). As the main stream, the Var river shows two transverse profile shape features along its 114 km’s path. In the upstream part, the average width of Var river is 50 m in the riverbed and 300 m in the valley. Its average slope is 1.83%, which makes it a typical mountain stream. After the confluence with V subie, the river flows into its lower valley, the slope drops to 0.5% and the averaged width of the river becomes 278 m while the mean width of the flood plain is as large as 1.1 km.

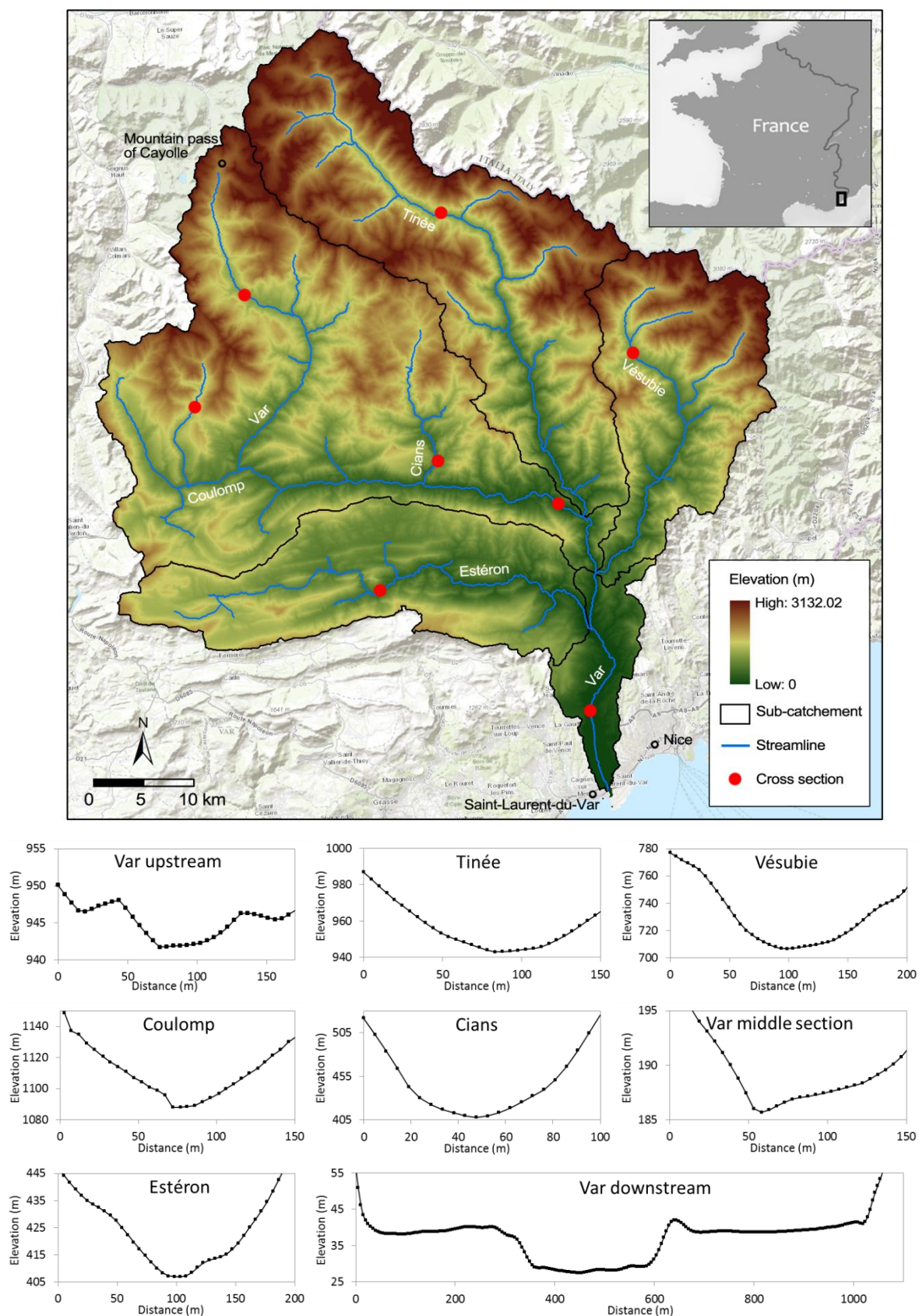


Figure I.1. Illustration of physiography of Var catchment and cross sections (Author's design. Source: 5 m DEM from M éropole Nice Côte d'Azur, noted as NCA in the text below).

The GIS analysis with the 75 m resolution DEM (Digital elevation model) shows the geographical information and land-use of all the sub-catchments (Table I.1 and Table I.2). It can be seen that all sub-catchments are characterized by steep slopes. The two largest sub-catchments, Est éron and Upper Var, are the steepest among them. The lower Var river drains water from all the sub-catchments and conveys it in the 22 km-long valley. The average slope in the downstream part (22.34%) is milder than the upstream sub-catchments, but this value still represents a steep slope. Moreover, the narrow stream width in the lower valley limits the ability of drainage. Considering the extension area and the steep slope (Table I.1), it is very likely to produce flash floods once an intensive rainfall pours in the mountainous area.

Table I.1. Summary table of geographical information of the 5 sub-catchments. (Source: 75 m DEM provided by NCA)

	Est éron	Upper Var	Tin é	V ésubie	Lower Var
Area (km ²)	755.45	1091.43	403.14	459.43	162.97
Average slope of land (%)	38.50	37.58	32.08	25.72	22.34

Table I.2. Summary table of land use information of the 5 sub-catchments. (Source: 75 m DEM provided by NCA)

	Est éron	Upper Var	Tin é	V ésubie	Lower Var	Var catchment
Artificial area (%)	0.24	0.22	0.60	0.42	1.04	0.36
Agricultural area (%)	0.77	3.34	3.29	7.60	24.02	4.51
Forest & natural area (%)	98.94	96.29	95.93	91.95	72.59	94.90
Wetlands (%)	0.00	0.15	0.16	0.02	0.00	0.08
Water bodies (%)	0.05	0.00	0.02	0.00	2.35	0.15

The GIS analysis shown in Table I.2 indicates that the distribution of the land uses on the 4 upstream sub-catchments are similar, while the lower Var river valley shows an obvious contrast. The forest is the predominant land cover in the whole Var catchment, while the lower Var sub-catchment has the lowest forest cover percentage due to the development of human activities. Many large municipalities such as Nice, Saint-Laurent-du-Var and Carros are located in the lower Var river valley (Figure I.2), thus the artificial area including urban zone and industrial zone in the lower valley is bigger than the other sub-catchments. In the lower Var river valley, a considerable proportion of the flood plain is used as agricultural land for diverse crops such as lettuce, fruits and garden plants.

I.2 Lower Var valley

I.2.1 Geography and evolution of the valley

The lower valley of Var river is the last section of the Var catchment. It connects the mountainous sub-catchments in the upstream part to the Mediterranean sea (Figure I.2). Starting from the weir No.16, the total length of the lower valley is 22 km, through which the elevation of the riverbed decreases from 119 m to -2 m. The valley is surrounded by the mountains on both sides, whose elevation reaches 1000 m on the right bank and 800 m on the left bank. In the upstream part, some small valleys lie perpendicularly and connect the main channel, while in the downstream part, many small valleys are parallel to the Var valley.

The width of the valley varies depending on the section. The alluvial sediments brought by the Estéron broaden the Var river valley at the confluence. The width remains around 900 m until the river reaches the narrowest section in the middle part of the valley, where the width is merely 600 m. After the narrowing, the valley regains its width progressively until it forms a small estuarine delta, where an airport has been built since the middle of the 20th century. The construction of the airport has blocked the sediment transport driven by the alongshore current from the river mouth to the beach of Nice [Dumasdelage, 2016]. In general, the lower valley of Var river is a typical Mediterranean river valley, which is characterized by a steep slope, a narrow flood plain made of alluvial sediments and incompletely developed meanders due to the constraint of the mountains aside.

The alluvial delta divides the coast into two bays which are called, according to their symmetrical shape, the Baie des Anges. The Var river is prolonged by a steep submarine canyon that was formed in subaerial condition during the Messinian age of the Miocene epoch [Clauzon, 1978]. The desiccation of Mediterranean sea due to the dry climate as well as the closure of the Strait of Gibraltar made the coastal rivers incise into the continental margin and form deep canyons. This event is referred to as Messinian Salinity Crisis [Gargani, 2004; Anthony et al., 2010]. As the reopening of the Strait of Gibraltar occurred at 5.33 million years ago, the sea regained its water level and the canyons were drowned under water and partially refilled by sediments, while they are still an extension of the river valley on the land. The bathymetry of the continental shelf in this area has a high slope. The map on Figure I.2 indicates that the average slope of the near shore bottom varies from 10% to 30%. The submarine canyon of the Var river valley has a slope of 16%.

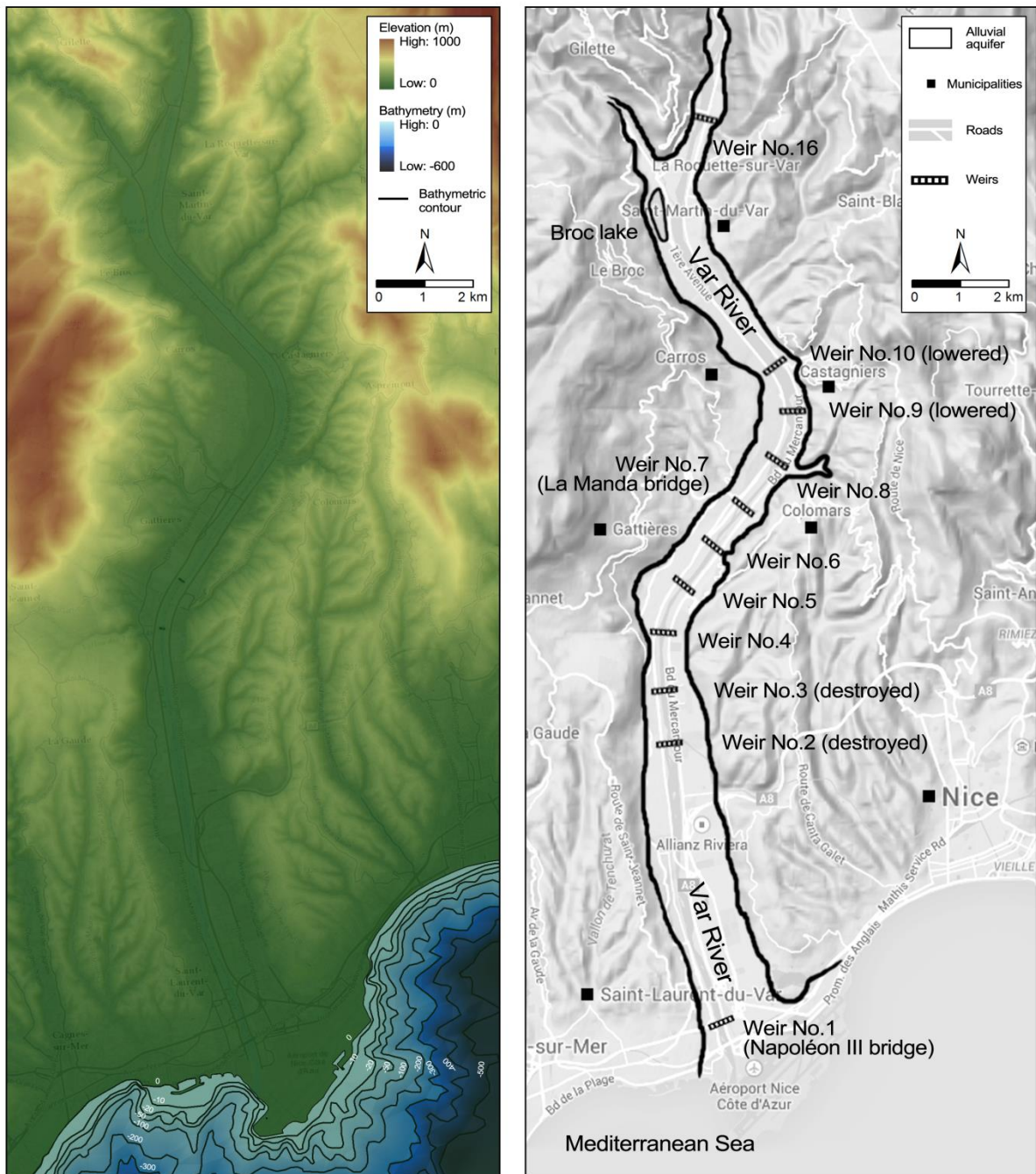


Figure I.2. Elevation (left) and map (right) of the lower valley of Var river (Author's design. Source: 75 m DEM from NCA, bathymetry contour from National Institution of Geography and Forestry, noted as IGN in the text below, Guglielmi [1993], ESRI world map).

Since the beginning of the 19th century, human activities have changed the landscape of Var river valley. Several municipalities have been developed in the coastal area, the need of land has become a rigid demand as long as the growth of population (Figure I.3). Since the 1980s, Nice has become the fifth largest city in France thanks to the prosperity of the tourism in the French Riviera. 300 000 people live in the Nice city and another 100 000 people live in the nearby towns including Saint-Laurent-du-Var, Carros, Saint-Martin-du-Var, *etc.*

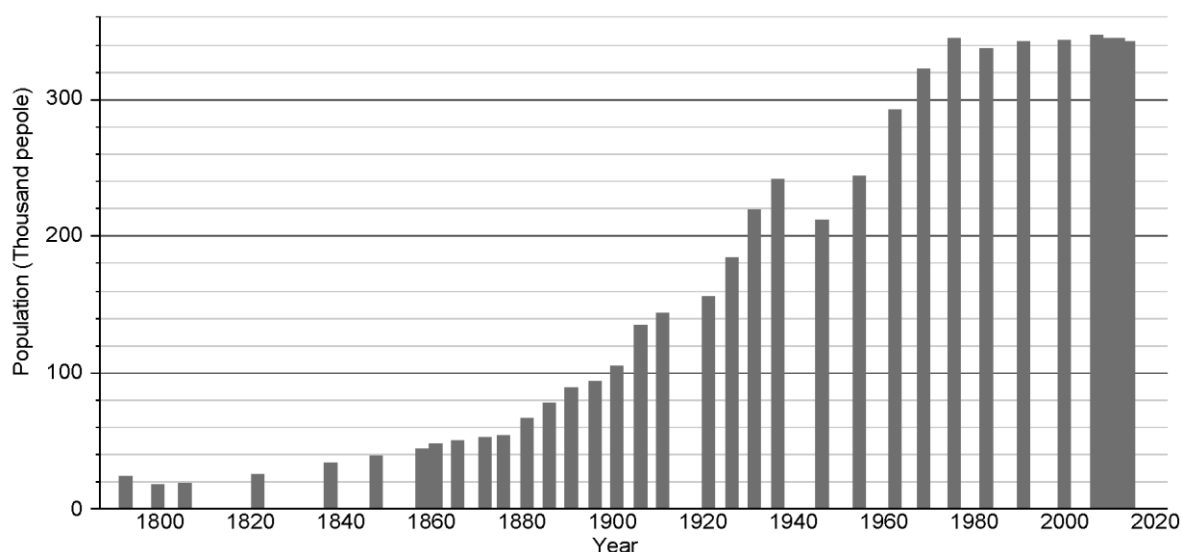


Figure I.3. The demographic evolution of Nice city since the 19th century (Source: Data base of the National Institute of Statistics and Economic Studies of France - INSEE).

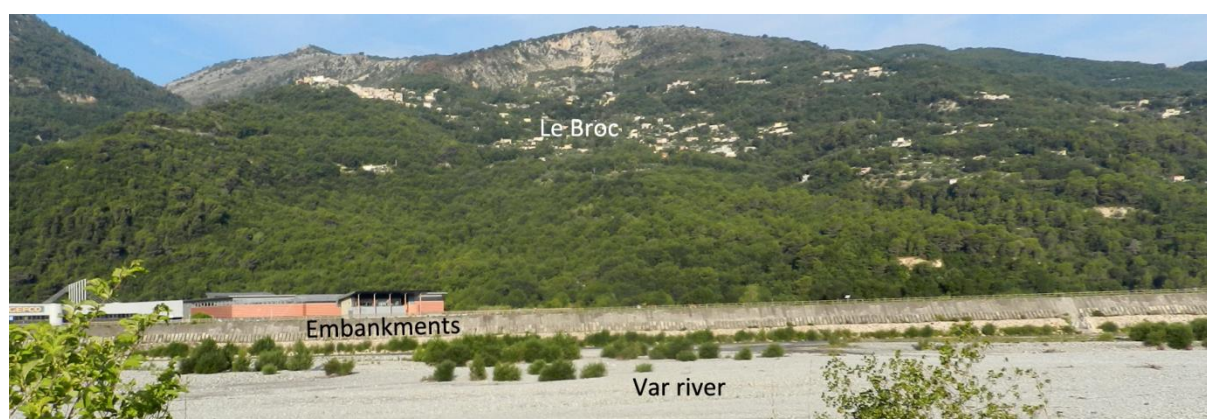


Figure I.4. Embankments built with rubbles and concrete blocks along the lower Var river (photo taken by author on July 2014).

The urbanization of this area has induced increasing need for constructing land so that land has been reclaimed from the river flood plain. The morphology of the river has been reshaped and the riverbed is strictly narrowed by artificial embankments with rubbles and concrete blocks (Figure I.4). This led

to an increase of the water velocity, thus erosions happened gradually and were observed in many places along the river.

Before 1984, the sand and gravels in the alluvial sediment of Var river were widely used as a material source of the concrete industry. Because of the strong connection between the Var river and its aquifer, as the revelation of riverbed erosion, groundwater depletion has also been reported [Souriguère, 2003]. In 1967, the most severe shortage of groundwater happened in the valley, the groundwater table was decreased by 8 m below its static level. In order to slow down the erosion process on the riverbed so as to maintain the groundwater level, weirs were built on the riverbed since 1971 to reserve the sediment so as to maintain the groundwater level. Meanwhile the industrial companies have developed a new site located in Le Broc village (Figure I.2) to extract the gravels. However, the mining has resulted in a hollow on the ground so that groundwater exfiltration occurred until an artificial lake was formed (Figure I.2 and Figure I.5). Finally a ministerial decree has been approved in 1984 to forbid the extraction of sediment either in the valley or in the riverbed. By the end of 1986, 11 weirs were finally constructed in different sections of the river, while two of them are destroyed in the flood of 1994 (Figure I.2) [Souriguère, 2003].



Figure I.5. Evolution of the Estéron-Var confluence and the formation of Le Broc lake (Source: IGN and www.valleeduvar.fr).

The construction on the flood plain never stopped since the beginning of the industrialization in the lower Var valley on 1960s. In the middle 1970s, the municipality of Carros started to build an industrial zone on the right bank of the flood plain of Var, between the confluence and La Manda bridge (Figure I.2). 200 hectares of flood plain have been reclaimed and turned into high imperviousness land. Soon afterwards, another 50 hectares of flood plain have been used to build the industrial zone of Saint-Laurent-du-Var on the right bank of the flood plain. In the middle section of the valley, the flood plain is developed for agricultural activities on both bank sides, but mixed with industrial areas. The estuary of the valley is highly urbanized (Figure I.6). The administrative center of the department of Alpes-Maritimes (06), the National Interest Market of Nice (Marché d'Intérêt National) and the airport have been built next to the left bank of the river, and a vast commercial center named Cap3000 is located on the right bank of the river mouth.



Figure I.6. Highly urbanized zone in the estuarine area of Var river (Author's design. Source: www.geoportail.gouv.fr).

Figure I.7 shows the land use map of the Var river valley, which is published by the European Environment Agency. In a general view, the main land uses in the valley are industrial units in the upstream area, agricultural land in the middle part and urban zone in the downstream area,

The construction of the road within the riverbed has narrowed once again the width of the river. For example, on the right bank of the river, the road 202bis passes under the deck of La Manda bridge, while on the left bank of the river, another road has been built which passes under the arch of Napoléon III bridge (Figure I.2). Nowadays, the width of riverbed varies from 150 to 280 m, which means that the stream line of Var river is strictly limited between the embankments.

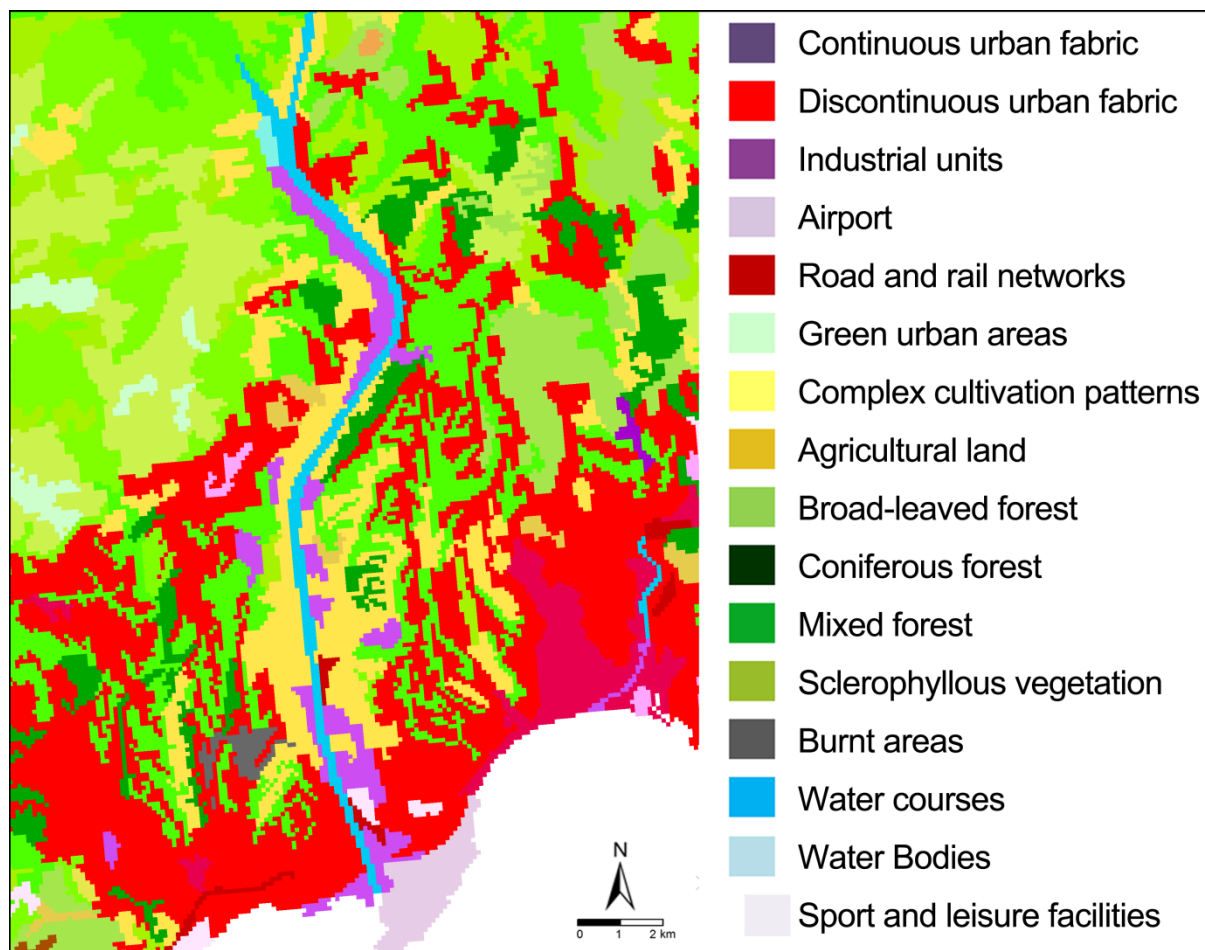


Figure I.7. Land use map of the lower valley of Var river (Source: Data base of European Environment Agency, data of 2006, resolution of 100 m).

I.2.2 Geological context

Guglielmi [1993] has studied the geology in the lower Var river valley. Another recent research on the bedrock of the alluvium carried out by Emily et al. [2010] has completed the knowledge of the geological environment of the lower valley of Var river. The lower valley of Var river is a transition zone between the subalpine area in Nice and the extended part of the Provencal geology structures. In the eastern area, the subalpine geology consists mainly of the limestone formed during Jurassic (201.3-145 M.a) and Cretaceous (145-66 M.a) periods, fractured by NW-SE faults. The Provencal geology

structures in the west of the area are characterized by the folded and faulted Jurassic limestone lying on the Triassic (252.17-201.3 M.a) clayed marl.

The formation of the geological layers in the valley is a result of the tectonic activities during Pliocene (5.33-2.58 M.a) and Quaternary (2.58-0 M.a). As explained in the Section I.2.1, the submarine canyon was created during the Messinian crisis event (5.96-5.33 M.a) in the late Miocene (23.03-5.33 M.a), after which the marine invasion occurred along the canyon and even reached the northern border of the lower Var river valley that is seen today. The strong eustatic movement has led to the deposition of the marine marls and, at the last step, a deposition of a huge quantity of gravels that afterwards forms afterwards a thick layer of conglomerate. The thickness of the Marl at some place is over 150 m, while a thickness of the conglomerate more than 400 m is observed. The geological eras and epochs mentioned in this paragraph are shown in the chronostratigraphic chart in Appendix 1.

During the Quaternary, the alternating transitions from glacial to interglacial periods have formed the layered terraces [Dubar et al., 1992]. The depositions happened in the post-glacial period and the Holocene, along with an eustatic sea level rise. It is the very period when the sediments of Var river are brought and deposited by a graded order, the sedimentation of the gravels, sands, silts occurred from the upstream to the downstream section in accordance with their diameters. A decline of the sea level rise has resulted a progradations of the coarse sediments, which are transported to the estuary of the Var river [Dubar, 2003].

Figure I.6 and Figure I.7 are the geological plan and cross section view of the studied area, based on a series of drilling results and field survey carried out by previous studies and by Emily et al. [2010]. The direct contact between the alluvial materials and the Pliocene bedrock layer is observed in both upstream section and estuarine zone. At the cross section No.5 (Figure I.9), the Jurassic limestone is folded and takes direct contact with the alluvium. At the section No.6 (Figure I.9), the faults occurred underneath the alluvium so that it contacts the Eocene marl. Due to the lack of the observed data for certain depths, the bedrock at some areas is not able to be identified.

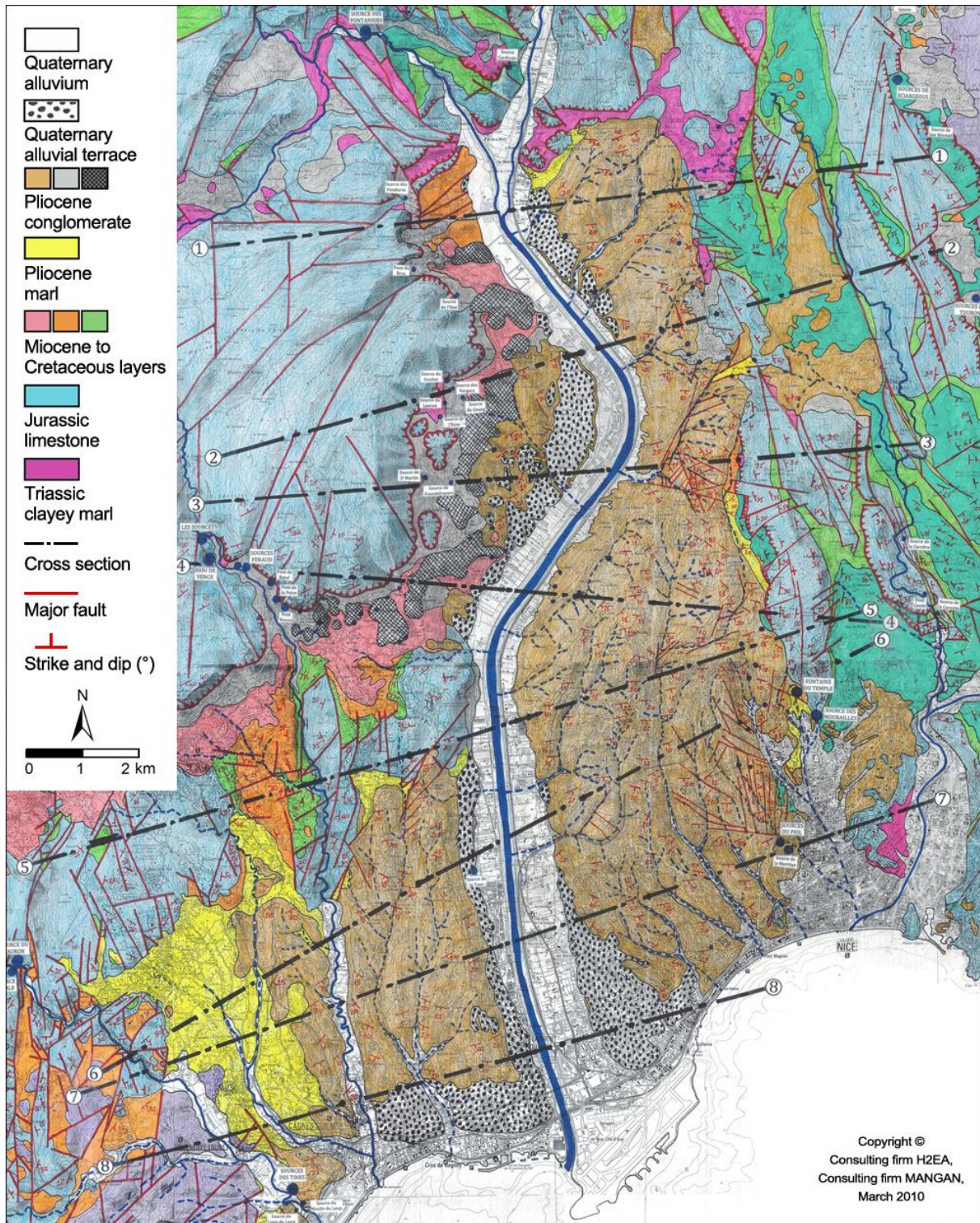


Figure I.8. Geological map of lower valley of Var river (Source: Emily et al. [2010]).

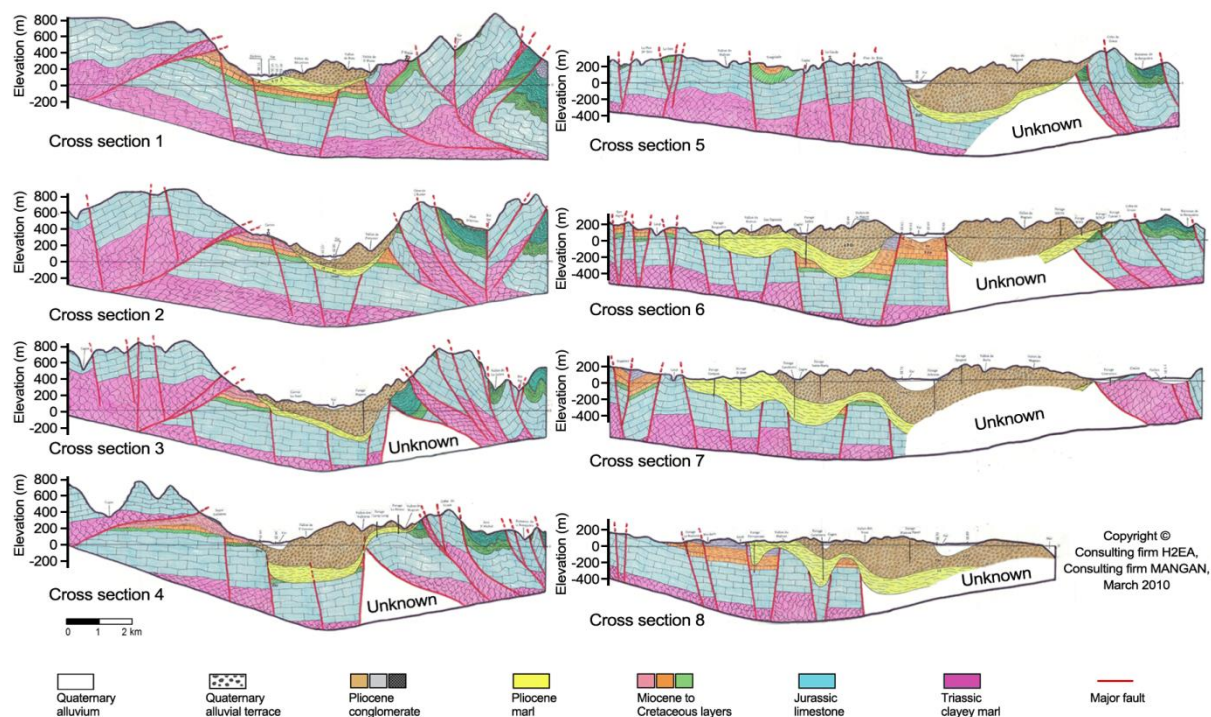


Figure I.9. Cross sections of the profiles displayed in Figure I.8, the legend is the same as the one used in geological map (Source: Emily et al. [2010])

I.2.3 Hydrological context

I.2.3.1 Precipitation and evapotranspiration

In Var catchment, the precipitation is recorded by the national meteorology service Météo-France (www.meteofrance.com). There are 78 stations (Figure I.10) distributed in the whole catchment and in adjacent mountains, with an altitude from 2 m to 2035 m, to ensure a complete knowledge at different elevations. The available data of recorded precipitations at certain stations are dating up to 1928. In the lower valley of Var river, 14 stations are used to monitor the precipitation. The installation of the devices has a low density in the mountainous area of the catchment, because the agglomeration of the population is in the downstream area. The altitude of these stations varies from 691 m (Levens station) to 2 m (Airport station) to ensure a complete measurement of the meteorology in the lower Var river valley (Figure I.10).

In order to know the influence of the altitude on the rainfall, the monthly precipitation depths recorded in 2014 at three stations are compared in Figure I.11. Through the comparison, it can be seen that the difference of monthly precipitations among three stations is less than 50 mm. In the spring of 2014, Carros station observed the highest precipitation depth, in summer time, it is the Levens station that often measures the heaviest rainfall and Airport station measures the highest precipitation in winter. It

means that there is no evident correlation between the precipitation depth and the altitude. At least this non-correlation can be confirmed between the coastal area where the altitude equals to 2 m, and the mountainous area where the altitude is 691 m.

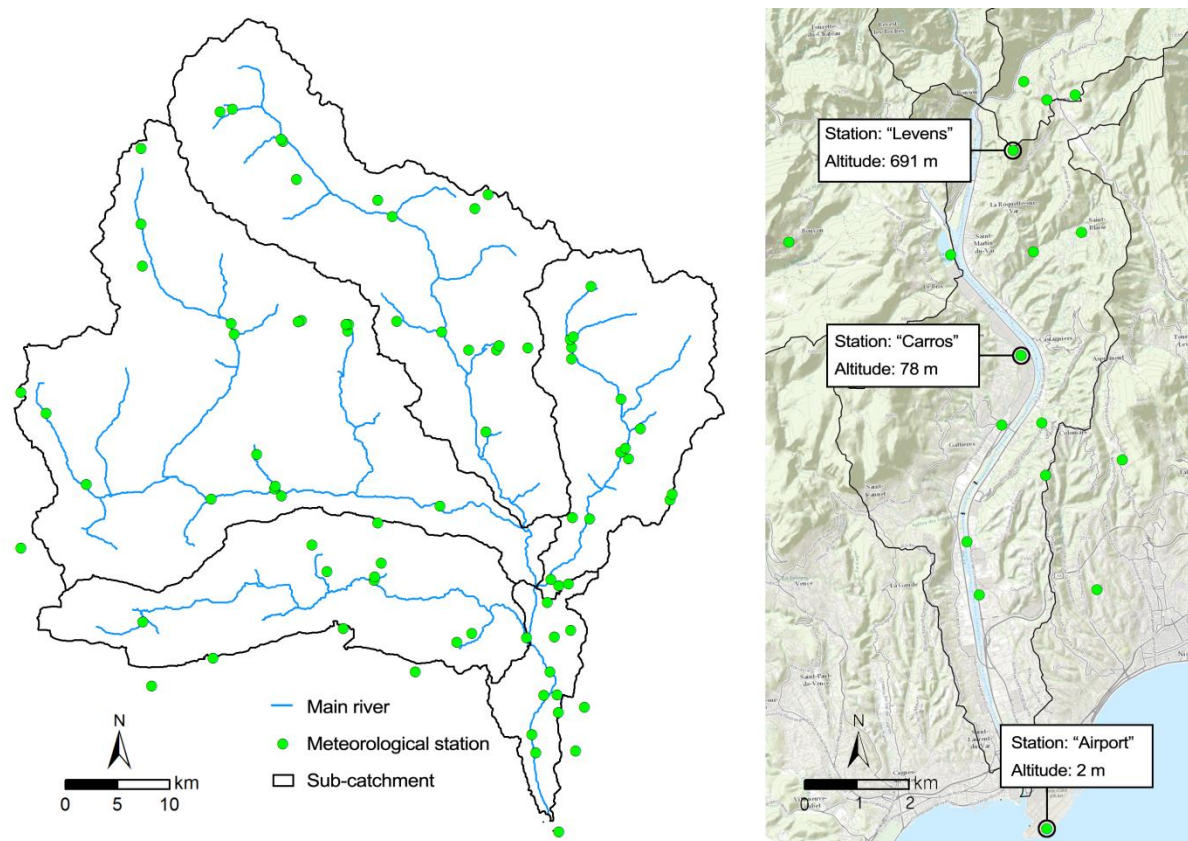


Figure I.10. Location of the precipitation monitoring points in the Var catchment and the lower Var river valley (Source: M \acute{a} \acute{o} -France).

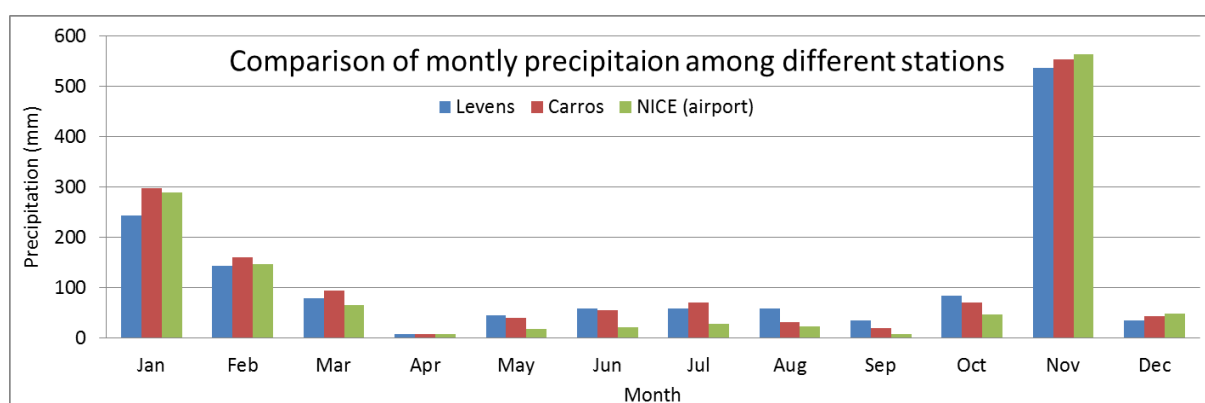


Figure I.11. Comparison of the monthly precipitation in 2014 among Levens, Carros and Airport stations (Source: M \acute{a} \acute{o} -France).

Considering the non-correlation, the data measured at the meteorological station of the airport is used to represent the rainfall features of the valley, because it has the longest recorded time series. Figure

I.12 shows the evolution of the precipitation in daily, monthly and annual time scale, recorded at the airport. For the annual and monthly data, the average value of cumulative precipitation is also calculated and shown in the figure. While for the daily data, the average value is meaningless, because there are too many nil values in the time series.

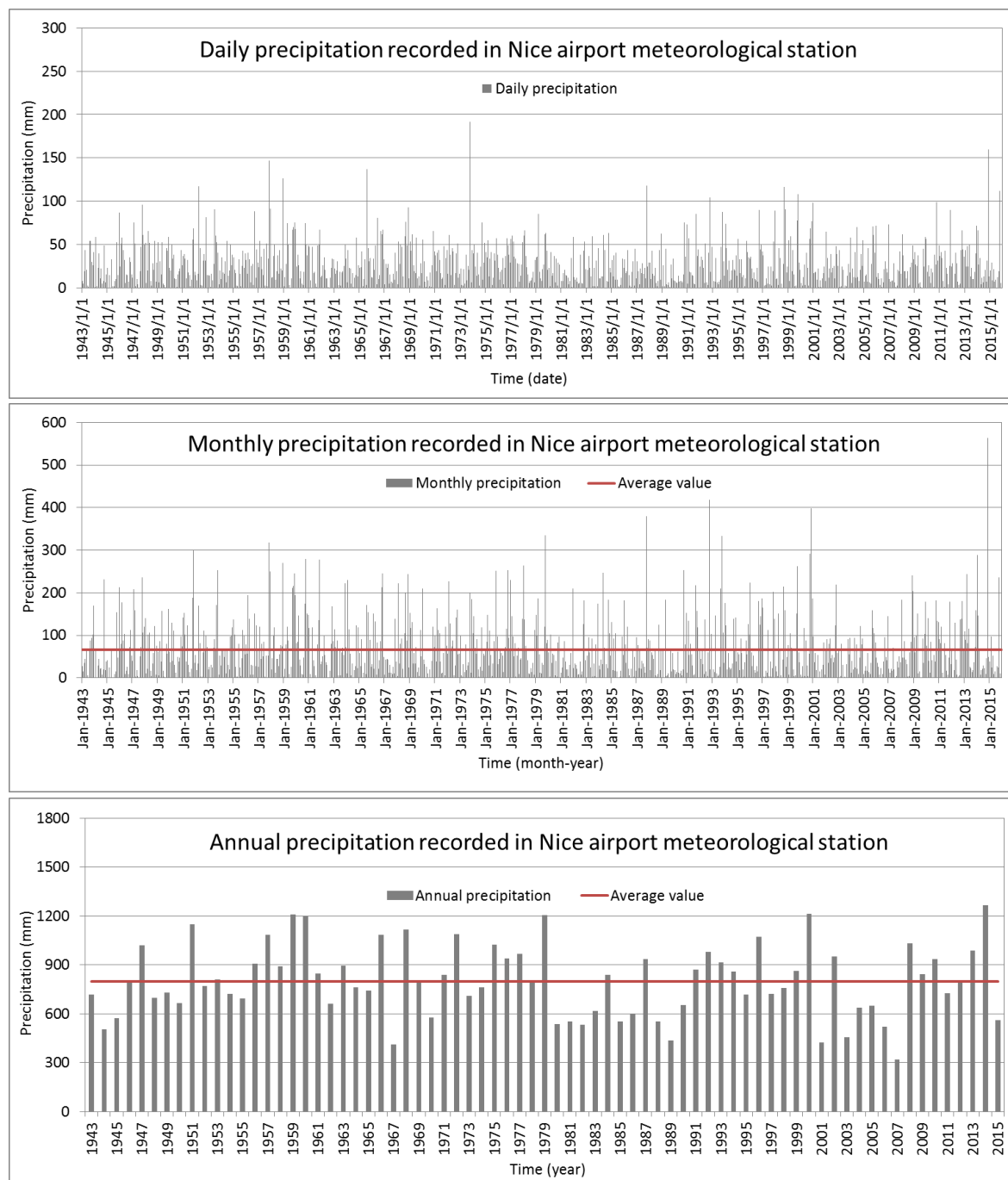


Figure I.12. Precipitations in different time scale (daily, monthly and annual scale) recorded in the meteorological station of Nice airport (Source: Météo-France).

Among the measurements that last for 73 years, only 10 days are observed with a heavy rainfall which is greater than 100 mm in 24 hours. In most cases, the daily rainfall is less than 50 mm, the statistic calculation of daily rainfall shows that 97.6% of the rainy days have a precipitation less than 50 mm, and even a precipitation greater than 20 mm has only a frequency of occurrence of 14.3%. It means that the heavy rainfall event such as storm or torrential downpour has a small probability in the lower Var river valley. However, once occurs, such heavy daily rainfall would lead to severe urban flooding. Through the temporal distribution of extreme daily rainfall, no clear tendency can be observed. To put it in another way, there is no obvious evidence showing that the extreme intense precipitation is more frequent.

The average value of monthly rainfall in the lower Var river valley equals to 66.5 mm. However, under the Mediterranean climate, the precipitation is unequally distributed according to the season (Figure I.13). The summer is characterized by an inadequate rainfall, while the autumn and winter are the main rainy seasons. The driest months are June, July and August, when the lowest monthly rainfall decreases to less than 1/3 of the average value. The rainy season, in contrast, brings almost twice as much as the average value. It can be observed on Figure I.12 that the extreme monthly rainfall becomes increasingly frequent and the extreme value also increases. If the time series is divided into two periods from the mid time point, which is the year 1979, an obvious trend can be seen by comparing the two periods. In the first half, monthly precipitations higher than 200 mm are observed quite often, however, only one event of 300 mm rainfall is observed. While during the last four decades, the monthly precipitations that are higher than 200 mm are less frequently observed comparing to the first decades, but the extreme value is much higher. 6 extreme monthly rainfall events happened from 1979 to 2015, and the highest precipitation reaches 563.2 mm in November 2014. This indicates that the precipitation has a trend of becoming more unstable, thus the extreme events are more frequent than before. The high monthly precipitation is not a direct reason to urban flooding, but it can increase the soil saturation thus a fluvial flooding is more likely to happen. There is no other proof to substantiate that this contrast is due to the climate change, but it is very possible that this tendency continues and may be a potential trigger of fluvial flooding in the lower Var river valley.

The annual precipitation can be used to define rainy and dry periods in a larger time scale. The average annual precipitation is 797.9 mm, which is a dividing line between rainy years and dry years. Four concave parts can be recognized as dry periods from the time series: 1943-1950, 1962-1970, 1980-1990 and 2001-2007, and rainy periods are therefore observed alternately among them. It forms a rainy-dry cycle and the length is around 20 years. It is possible that a rainy year happens in the middle of a dry period and vice versa, but such single exceptions are easy to be seen and they can hardly break the cycle. Two severe droughts happened respectively in 1967 and 2015 in the valley and, seen from the cycle, they all happened in a dry year of a dry period. It can be also read on annual precipitation time series that the continuous dry years are more likely to occur in recent decades. The minimum value of annual precipitation is 317.8 mm observed in 2007, which followed a consecutive drought since 2003. This unequal distribution of water in time resembles exactly the patterns of monthly rainfall distribution discussed in the previous paragraph, because they both mean a frequent occurrence of extreme meteorological events.

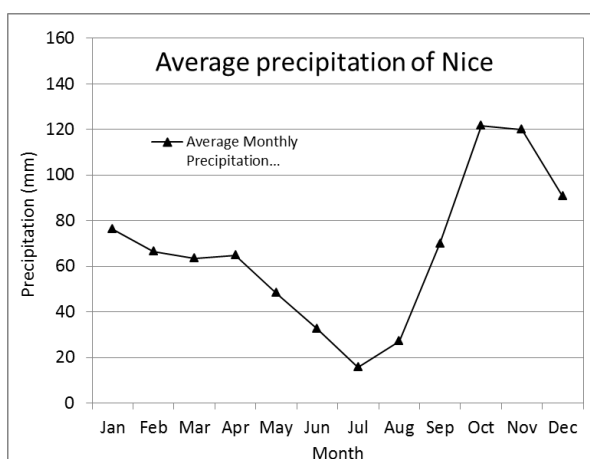


Figure I.13. Average monthly precipitation recorded at Nice airport station from 1943 to 2015 (Source: Météo-France).

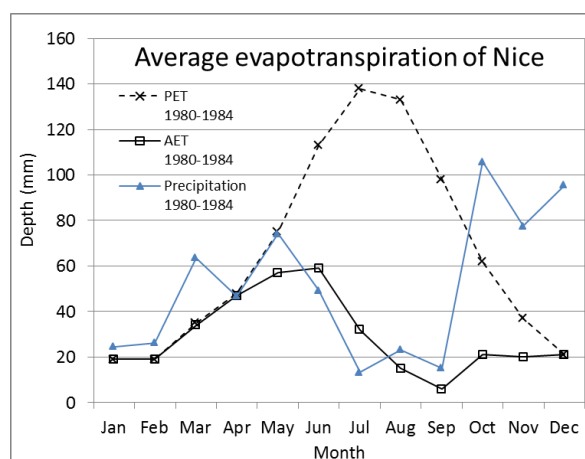


Figure I.14. Average potential and actual evapotranspiration at Nice from 1980 to 1984 (Source: Carrega [1988], Météo-France).

The evapotranspiration, including actual evapotranspiration (*AET*) and potential evapotranspiration (*PET*), can hardly be measured in a study on a sub-catchment scale, only estimation by using different formulas is an applicable method. Many studies are carried out on the estimation of evapotranspiration in the Mediterranean area in the south of France [Chaouche et al., 2010; Garrigues et al., 2015; Carrega 1988; Delaroziere-Bouillin, 1971]. Among them, Carrega [1988] has used Thornthwaite formula (Eq. 26 and Eq. 27, see Section II.3.1.2) to calculate the average monthly *PET* and *AET* in 4

french cities in the Mediterranean area from 1980 to 1984. Figure I.14 shows the result of Nice. The *PET* reaches its peak value in July because the *PET* is strongly related to the temperature and the duration of sunlight, while the *AET* decreases in summer until it drops to its lowest level in September due to the limit of precipitation and water storage in the soil. In total, the annual *PET* is estimated to be 798 mm and the annual *AET* is 350 mm. However, this calculation is based on the measured data from 1980 to 1984, which is totally in a dry period so that it may not reflect the real *PET* and *AET* level in Nice.

Delaroziere-Bouillin [1971] has used Thornthwaite formula and Turc formula (Eq. 23, Eq. 24, Eq. 25, Eq. 28 and Eq. 29, see Section III.3.1.1 and III.3.1.3) to calculate the average annual *PET* and *AET* of 55 french cities by using the data measured from 1958 to 1967. The Turc formula gives a higher estimation (*PET*=1025 mm and *AET*=588 mm) than Thornthwaite formula (*PET*=783 mm and *AET*=498 mm). These results are more reliable than those given by Carrega [1988], because this period contains both rainy and dry years. Nevertheless, the comparison between the two methods indicates that the estimation of evapotranspiration varies largely according to the applied formula. As an important factor of groundwater modeling, the calculation of *PET* and *AET* will be discussed in Chapter II and Chapter III.

I.2.3.2 Surface water flow in Var river and its tributaries

The surface water is a direct reflection of the rainfall and also to the snow melting, in consequence, all the steams in Var catchment have the same hydrological characteristics. A high discharge occurs in spring due to the melting of the snow in the Alps. Then a dry period appears in the summer because of inadequate rainfall in the whole catchment. Winter is the flood season when both the fluvial flooding and urban flooding are very likely to happen due to the frequent and heavy rainfall.

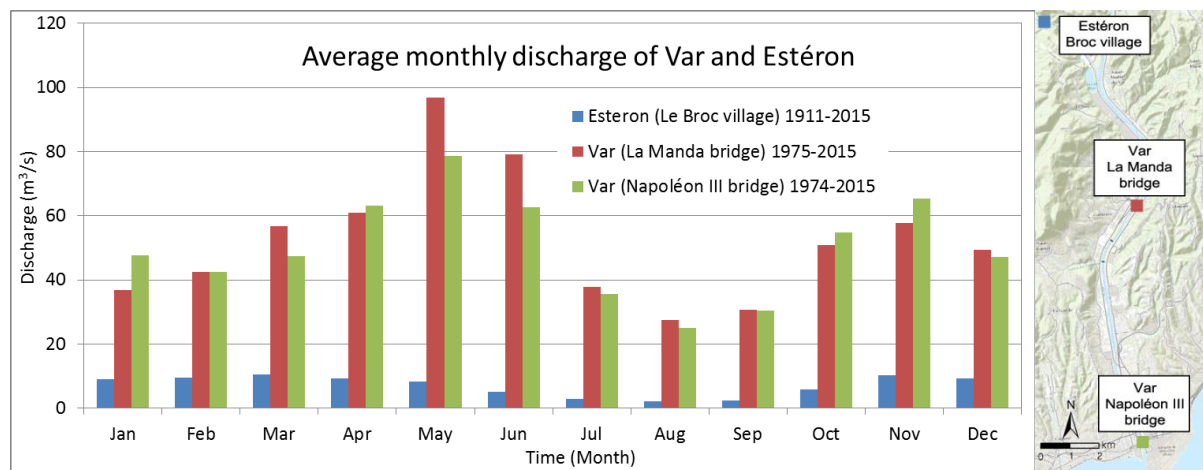


Figure I.15. Average monthly discharge of lower Var river and Estéron river, measured at three stations (Source: Eaufrance).

In the lower valley, three river monitoring stations are set along the valley, one is located on the Estéron river (Broc village) and the other two are respectively installed in the middle section (La Manda bridge) and the mouth of the Var river (Napoléon III bridge). Figure I.15 shows the location of these monitoring stations as well as the average monthly discharge since the beginning of the monitoring. At the northern boundary of lower valley, the Estéron river joins the Var river and contributes to an average annual discharge of $7 \text{ m}^3/\text{s}$, which is a statistical result obtained from a record that lasts for 104 years. This value is in the same order of magnitude as the other main tributaries such as Vésubie ($7.9 \text{ m}^3/\text{s}$) and Tinnée ($6.7 \text{ m}^3/\text{s}$).

Through the comparison between the discharge recorded at La Manda bridge and Napoléon III bridge, it can be seen that, during spring and summer, the discharge of upstream part is higher than the downstream part. This is due to the evaporation and the exchange between the river and its aquifer. Knowing that the water body surface is not large and the air temperature is not extremely high, it seems that the evaporation could not be the predominant cause of such loss. Even though the small canals that drain rainfall water from the steep ravine in the mountain join the Var river by highway culvert, the amount of water contributed by these canals is not significant because the precipitation during this period, especially in summer, is too low. Such a huge loss of water between the two stations is more likely to be caused by the river-aquifer exchanges, mainly the river infiltration towards the aquifer. The infiltration rate is calculated in next chapters.

During autumn and winter, however, the discharge recorded at Napoléon III bridge is higher than that at La Manda bridge. The increment of discharge can be caused by both the river-aquifer exchanges and the drained storm water in the downstream area. On one hand, the aquifer receives rainfall water and feeds the river in some sections, on the other hand, the steep sub-catchment along the valley contributes a significant amount of water during the rainy season in winter.

The annual average discharge recorded at La Manda bridge and at Napoléon III bridge are $52.3 \text{ m}^3/\text{s}$ and $50.2 \text{ m}^3/\text{s}$ respectively. It indicates that the river-aquifer system of the river section between the two stations forms a quasi-equilibrium state of the water budget in a hydrological year.

The monthly discharge measured at Napoléon III bridge is shown in Figure I.16. A period with high base flow and frequent extreme peak discharge can be found from 1991 to 2000, which is the very rainy period that can be identified from Figure I.12. The most severe flood event was recorded in November 1994, which brought an instantaneous peak discharge of $3760 \text{ m}^3/\text{s}$ (www.vigicrues.gouv.fr). An immense damage of 187 million Euros was caused by this flood with a hundred year return period. The second severe flood occurred in November 2011, which has an instantaneous peak discharge of $1290 \text{ m}^3/\text{s}$ (www.vigicrues.gouv.fr). Like the flood of 1994, it happened also in the middle of another rainy period from 2008 to 2014 (Figure I.12).

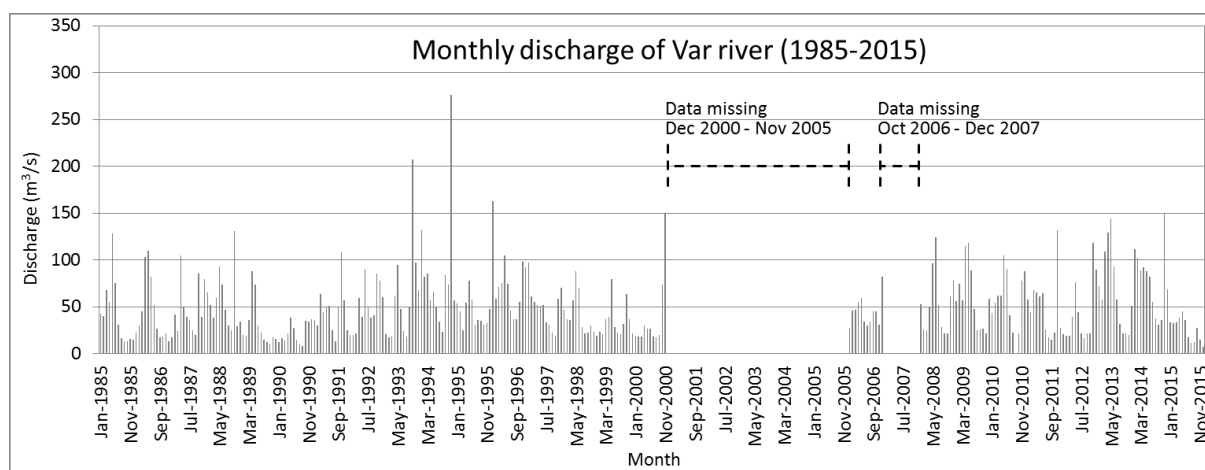


Figure I.16. Monthly discharge measured at Napoléon III station from 1985 to 2015 (Source: Eaufrance).

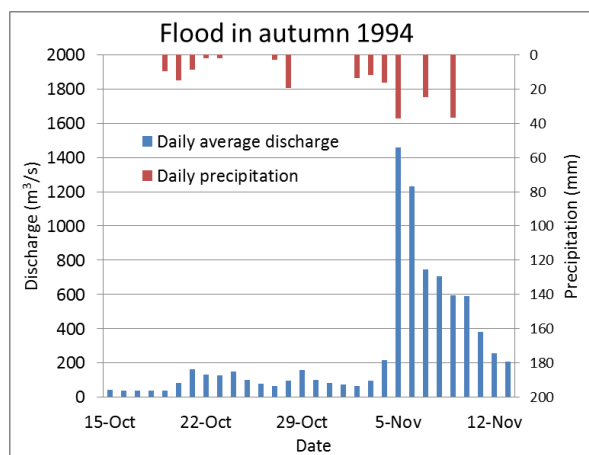


Figure I.17. Flood in Var, recorded in 1994
(Source: Eaufrance, M é t o -France).

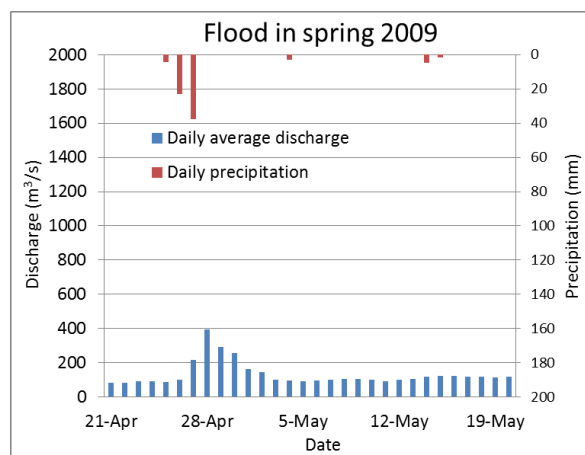


Figure I.18. Freshet in Var, recorded in 2009
(Source: Eaufrance, M é t o -France).

Generally speaking, there are two possible flood seasons: the freshet period in spring and the flood period in winter. However, the formation and the characteristics of these two kinds of flood are different. The flood in winter is usually formed after continuous rainfall events that lead to soil saturation. In this case, even a medium rainfall would produce a flood. Figure I.17 shows the daily cumulated rainfall and daily average discharge of the flood event in November 1994. After a few rainy days in late October, a precipitation of 40 mm/day was already enough to generate the 100-year flood. For this kind of flood, the base flow before the peak flow is not high, around 30 m³/s, while the latter could be considerably higher than the former.


On the contrary, a spring thaw in the Alps can also produce a flood, commonly called freshet. In the Var river, it usually happens from April to early June, depending on the air temperature in the high altitude mountainous area. Because of the snow melting, the base flow in the Var river can be as high as 100 m³/s, while the peak flow is not remarkably high thanks to the unsaturated soil. Figure I.18 shows a typical freshet that happened in the lower Var river. The base flow before the event was nearly 90 m³/s (www.vigicrues.gouv.fr), then a precipitation of the same level as the one which generated the flood in 1994 induced a small flood with a daily average discharge of 400 m³/s.

I.2.3.3 Surface water quality

No massive pollution event has ever been observed in the Var river. The regional water agency of Rhone-Mediterranean and Corsica (RMC) has investigated the surface water quality in the lower Var river valley on 2001 [Sourigu ère, 2006]. The water quality is evaluated regarding the concentration of nitrate (NO₃⁻), total nitrogen (N) and total phosphorus (P), and the detection of micro-organism (MO),

micro-pollutant (MP) and effect of proliferation of vegetation (EPV). Five grades are used to describe the water quality level: very good, good, medium, poor and very poor. Table I.3 is a list of the evaluation results based on four observation points along the river. It indicates that the water quality is generally good, especially regarding the test of nitrate, total nitrogen and total phosphorus. However, the micro-organisms are detected all along the river due to the existence of certain aquatic species.

Table I.3. Surface water quality evaluation in the lower Var river (Source: Water agency of RMC)

Index	Location				
	1.	2.	3.	4.	
Nitrate (NO ₃ ⁻)	Very good	Very good	Very good	Very good	
Total nitrogen (N)	Very good	Good	Very good	Good	
Total phosphorus (P)	Good	Good	Very good	Good	
Micro-organism (MO)	Medium	Poor	Medium	Poor	
Micro-pollutant (MP)	No record	No record	No record	Medium	
Effect of proliferation of vegetation (EPV)	Very good	Very good	Very good	Good	

I.2.4 Hydrogeological context

I.2.4.1 Aquifers in lower Var river valley

The lower Var river valley has an abundant groundwater reserve in the aquifers formed in Holocene alluvium layer and Pliocene conglomerate layer. The groundwater provides the source of drinking water for a total number of 600,000 people in the valley and adjacent areas. Besides, the groundwater is also the source of water for agricultural and industrial activities in the lower valley. The annual pumping volume is around 50 million m³ for all kinds of water consumption.

The aquifer that is most consumed is the shallow aquifer in the alluvium. The alluvium consists of the younger deposits brought from the upper sub-catchment. This alluvium fills the V-shape paleochannel formed in ancient geological era. The deepest depth of the alluvium is over 100m under the ground surface. Guglielmi [1993] has investigated the geological layers in the lower valley and 22 profiles are used to demonstrate the alluvium as well as the conglomerate layers (Appendix 2).

In the upstream area, the sediments have a high hydraulic conductivity. Moreover, no lens of clay and silt is observed, so the aquifer is totally unconfined and has a strong exchange with the surface water body such as Var river and Le Broc lake by a direct connection with them. The depth of the

groundwater level varies from 4 m to 8 m under the surface of the ground. In the upstream part, the alluvium shows a good hydraulic conductivity between 10^{-3} to 10^{-2} m/s. The highest value observed at the industrial zone of Carros is 0.041 m/s Guglielmi [1993].

The river section from weir No.10 to weir No.2 (Figure I.2) is a section where both the surface water and groundwater are strongly influenced by the sedimentation and erosion caused by these infrastructure of the weirs. The depth of the groundwater level varies from 10 to 16 m under the terrain surface. The aquifer is confirmed to be disconnected with the river. The hydraulic conductivity is in the order of magnitude of 10^{-3} m/s, given by the hydrogeological test conducted by consulting services or companies such as Geological Research Mining Bureau of France (BRGM), Ant éa Group, Veolia, Fondasol during the last 30 years.

Lens of silt and clay are observed in the alluvium at the estuarine area, therefore a confined aquifer is formed beneath this aquitard, while an unconfined aquifer always exists above [Emily et al. 2010]. Figure I.19 has been made based on 56 drillings on the study area (Appendix 3). It has been proved that the lens begins at the inland area that is 3 km away from the seashore, and it becomes thicker towards the sea. To the north of the profile C-C, the lens has only a depth of several meters while it becomes as thick as 50 to 80 m at the profile B-B. In this area, the volume of the unconfined aquifer is no longer enough for the water consumption, thus boreholes are created to explore the confined aquifer in this area. The hydraulic conductivity measured in this area is one order of magnitude lower than that of the middle section of the valley, between 10^{-4} to 10^{-3} m/s.

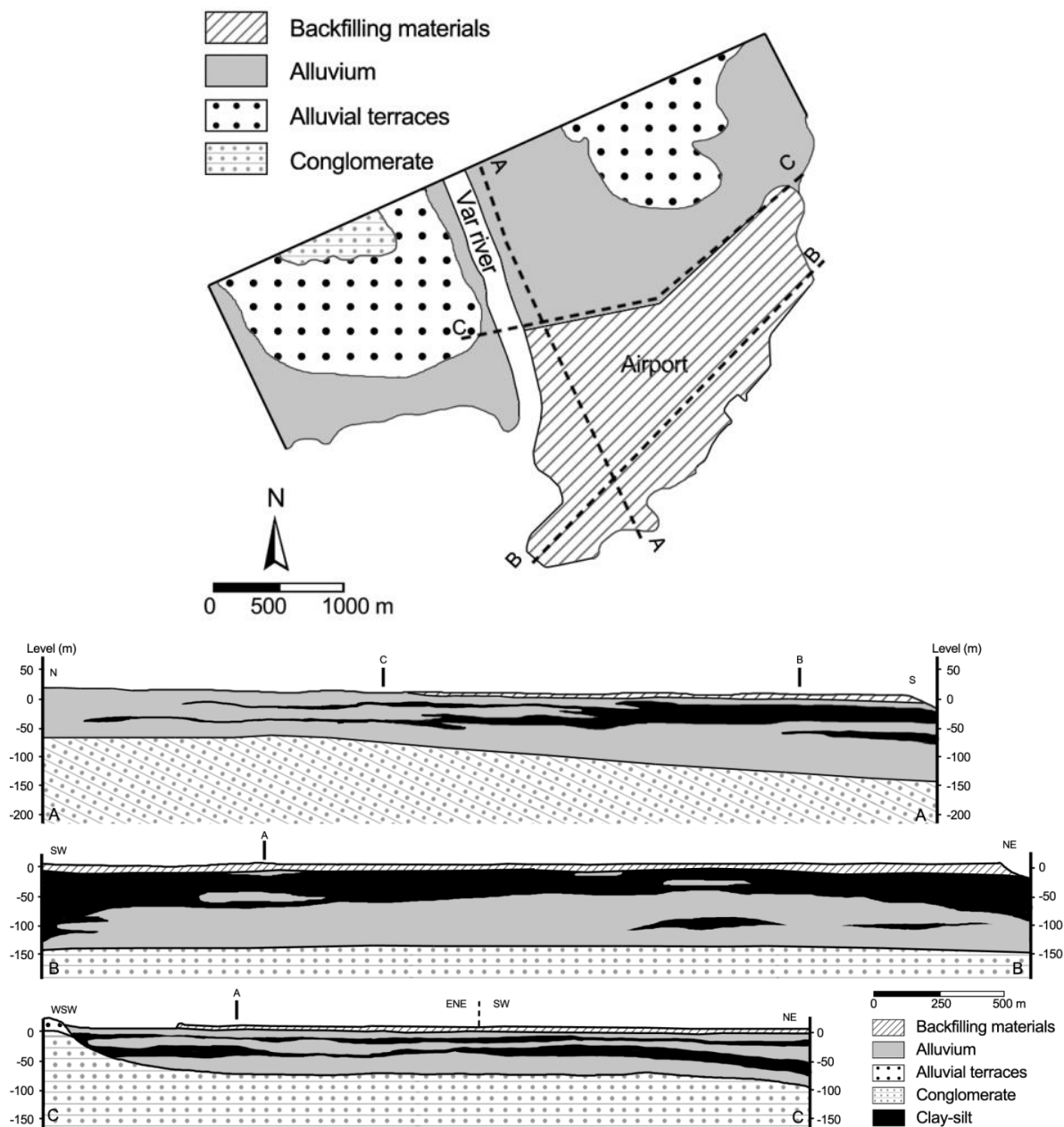


Figure I.19. Geological profiles at the estuarine area of the lower Var river valley (Author's design. Source: Emily et al. [2010]).

The second aquifer exists in the conglomerates layer formed during the Pliocene era, under the quaternary deposits of the lower valley. This aquifer is mainly porous, but in some eastern area the aquifer exists in fissured rock. Thanks to the great thickness of the conglomerate, the aquifer is estimated to have an immense reservoir of groundwater. Guglielmi [1993] has calculated that the hydraulic conductivity of the porous media of the conglomerate equals to 2.6×10^{-6} m/s. In general, the aquifer in the conglomerate is connected with that in the alluvium, so it is also unconfined in the upstream and confined at the estuarine area due to the lens of silt and clay.

Under the conglomerate, a layer of marl which is impermeable separates the Pliocene conglomerate and the Jurassic limestone, which forms a karst aquifer in the fissured rock. Because of the lack of marl, the limestone has a direct contact with the conglomerate and the alluvium at the right bank side in the south of the middle section (cross section 5 shown in Figure I.8 and Figure I.9).

I.2.4.2 Description of groundwater extraction

The extraction of groundwater is authorized for three activities, including the production of drinking water for the local inhabitants, consumption for the industrial activities, and irrigation of agricultural crops. The pumping stations for drinking water production are operated by Veolia company and the municipality of Nice Côte d'Azur. The pumping volume is well planned and documented. The boreholes are also created by the industrial companies in the lower Var river valley. The pumping volume is also recorded by the regional water agency (Agence de l'eau RMC). For the agricultural water consumption, the pumping volume is not documented at all, and it becomes a challenge for the groundwater management. Figure I.20 shows the location of the boreholes where the groundwater is mainly pumped in the lower Var river valley.

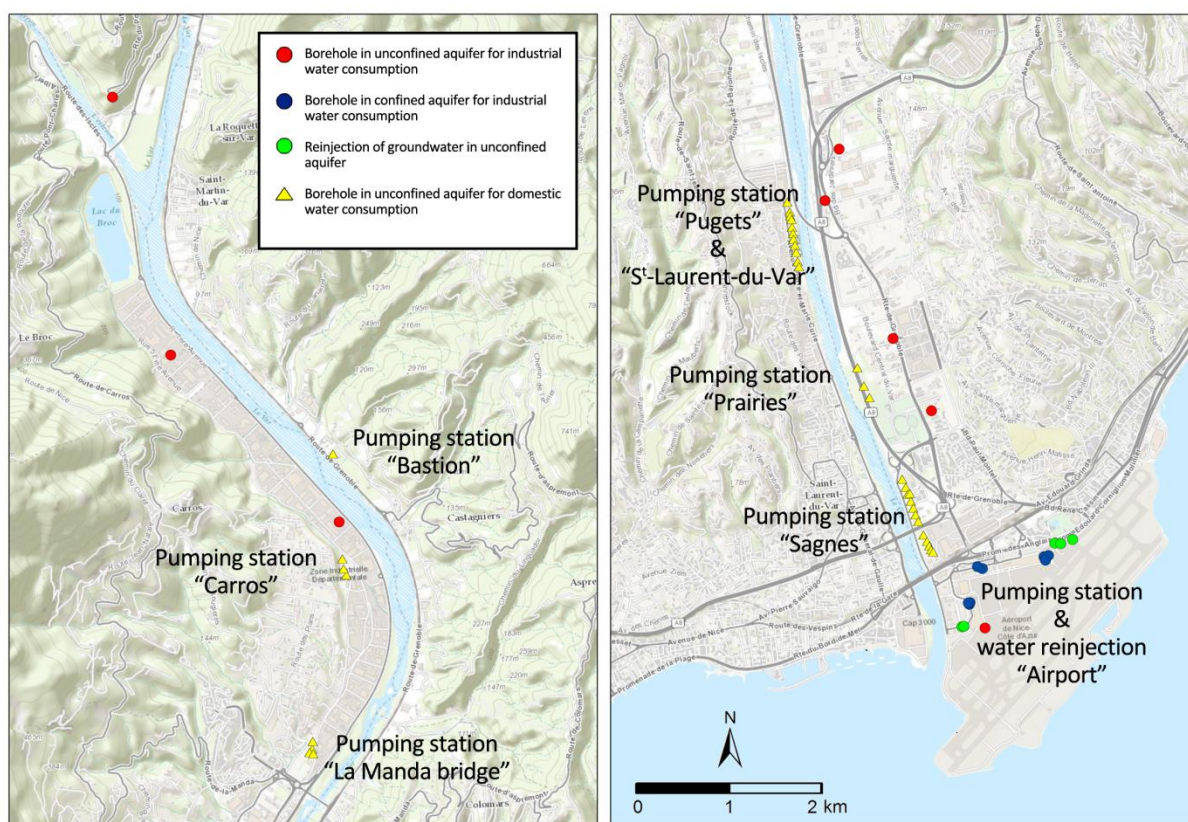


Figure I.20. Location of the water pumping stations and main groundwater consuming companies in the lower Var river valley (Source: Veolia company, municipality of Nice Côte d'Azur, Nice Airport).

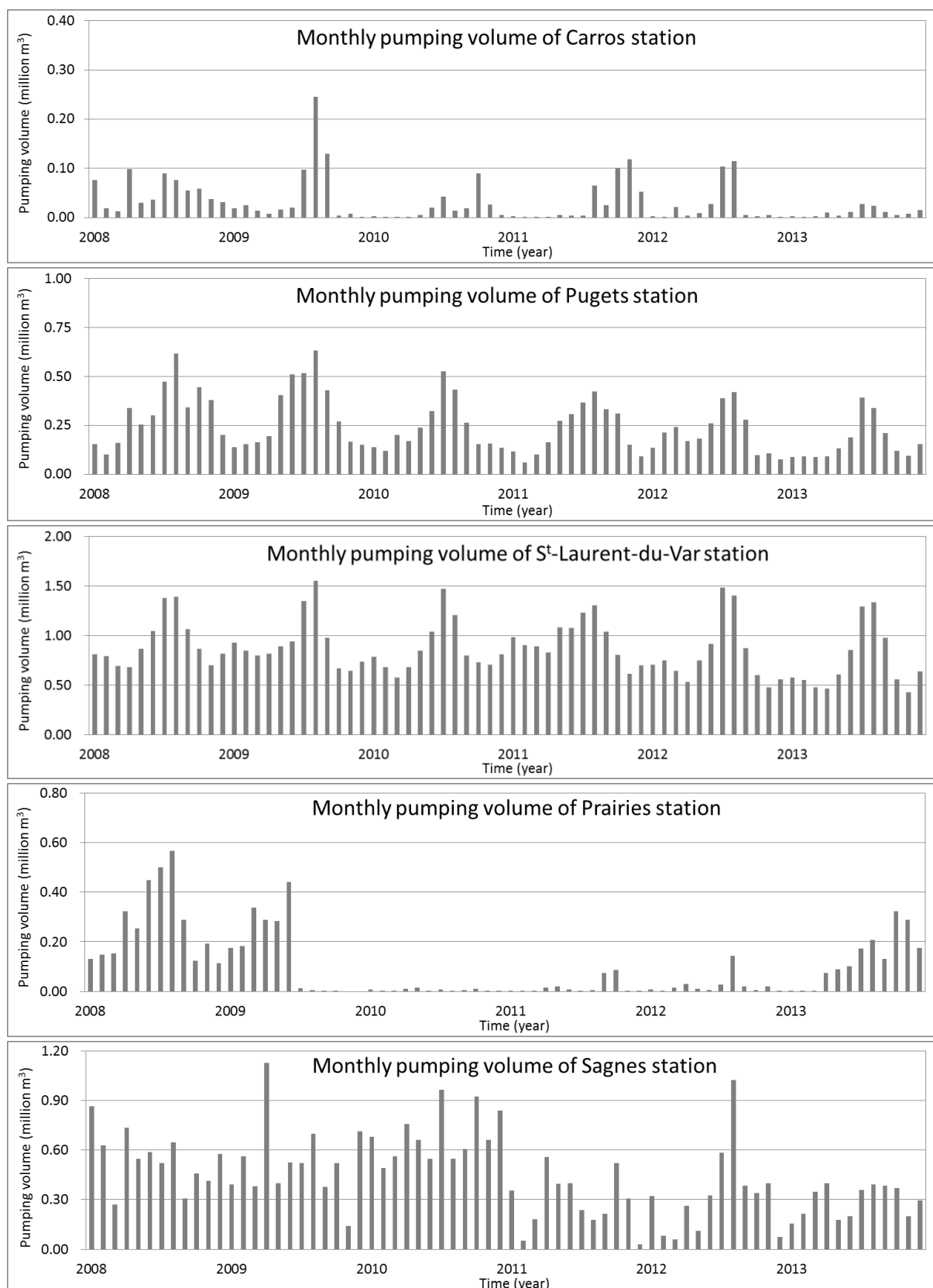


Figure I.21. Monthly pumping volumes of the municipal drinking water stations in the lower Var river valley (Source: Veolia company and municipality of Nice Côte d'Azur).

Regarding the drinking water production, there is a bigger demand of water in the downstream part where the population is dense, so more boreholes are created in the downstream part than in the upstream part. Accordingly, the volume extracted in the downstream part is much greater than the one in the upstream part. Figure I.21 shows the monthly water pumping volume in some main stations. In the station of Carros, Prairies and Sagnes, the pumping volume decreased abruptly from the year 2013, 2010 and 2011, respectively. It can be inferred that the drinking water production varies not only according to the season, but also to the water management plan, and the latter is impacting more the groundwater extraction than all other factors.

In the upstream area, the Carros station pumps the least groundwater among the three stations. It pumps an average volume of 0.07 million m³ water per month, which forms an annual pumping volume of 0.84 million m³ per year. The Bastion station has an average monthly pumping volume of 0.13 million m³, which represents an annual production of 1.56 million m³ of drinking water. The La Manda station produces 1.8 million m³ in average per year, but the annual pumping volume varies depending on the water management plan. In 1997 and 1999, the annual pumping volume was around 1 million m³ while it increased to 3.5 million m³ in the year 2000.

In the downstream area, the Pugets and S^t-Laurent-du-Var station has the greatest pumping volume. Equipped with 11 boreholes distributed along the river with a distance of 1 km, the joint station produces 1.14 million m³ of water per month, an annual volume of 13.68 million m³. This amount of water is the main drinking water source of the city of S^t-Laurent-du-Var. On the left bank of the river, the stations of Prairies and Sagnes are used as the alternate source of drinking water for Nice city. On average, only 6.48 million m³ of water are pumped each year in these two stations, which is the supplement of the main drinking water supply brought by the canal from V ésubie valley. As an alternate source, the temporal distribution of the pumping volume is quite irregular. In the Pugets and S^t-Laurent-du-Var station, the pumping volume is very regular depending on the season: a great amount of water is needed during the summer, while less water is demanded in winter.

Compared to the drinking water, the pumping volume of water for industrial use is much less. Even though many small industries, such as auto repair shops or repositories, are authorized to pump groundwater by their own need, their consumed volume is absolutely negligible compared to the other water consuming activities such as building material manufacturing or cooling system for the

machines. Table I.4 shows the main water consuming industries in the lower Var river valley. The Allianz Riviera stadium was brought into service in 2013 after two years of construction, before 2011 there was no such water consumption. The printing house of Nice-Matin newspaper once pumped the groundwater from unconfined aquifer as the cooling water for the printing machines, but it was stopped after a reform of their cooling system. The boreholes are abolished after 2013 and after then the cooling water is supplied by the municipal drinking water pipelines. The Airport of Nice consumes a great amount of water for the air conditioning system and other daily operational activities. Despite of the huge quantity of water pumping from the confined aquifer, most of it is reinjected into the unconfined aquifer after having used by the air conditioning system. The real water consumption is around 0.7 million m³ per year.

Table I.4. Annual groundwater pumping volume for industrial water use in the lower Var river valley (Source: Water agency RMC, Nice Airport).

Companies	From unconfined aquifer (m ³)	From confined aquifer (m ³)	Reinjection (m ³)
La Mesta Chimie Fine	63 254	-	-
Elis Riviera	97 382	-	-
Initial BTB	49 457	-	-
Allianz Riviera Stadium	497 496 (After 2013)	-	-
M éridionale de Granulats	925 859	-	-
Azur éenne de Granulats	604 805	-	-
Nice-Matin	1 199 061 (Before 2013)	-	-
Nice Airport	419 634	1 542 200	1 291 294

I.2.4.3 Analysis of data from monitoring piezometers

The monitoring of the groundwater level in daily time step in the lower Var river valley started from the 1960s. A few piezometers created at several points of interest are equipped with sensors that can record the groundwater level. Three decades later, a network of groundwater level monitoring is accomplished and it covers from the very beginning of the valley to the river mouth [Chery and Cattani, 2003; Chery et al., 2008]. There are 21 piezometers in the alluvium that are monitored, and 5 piezometers in the conglomerate aquifer are monitored. Figure I.22 shows the location of the piezometers with monitoring sensors and Table I.5 shows their altitude and depth.

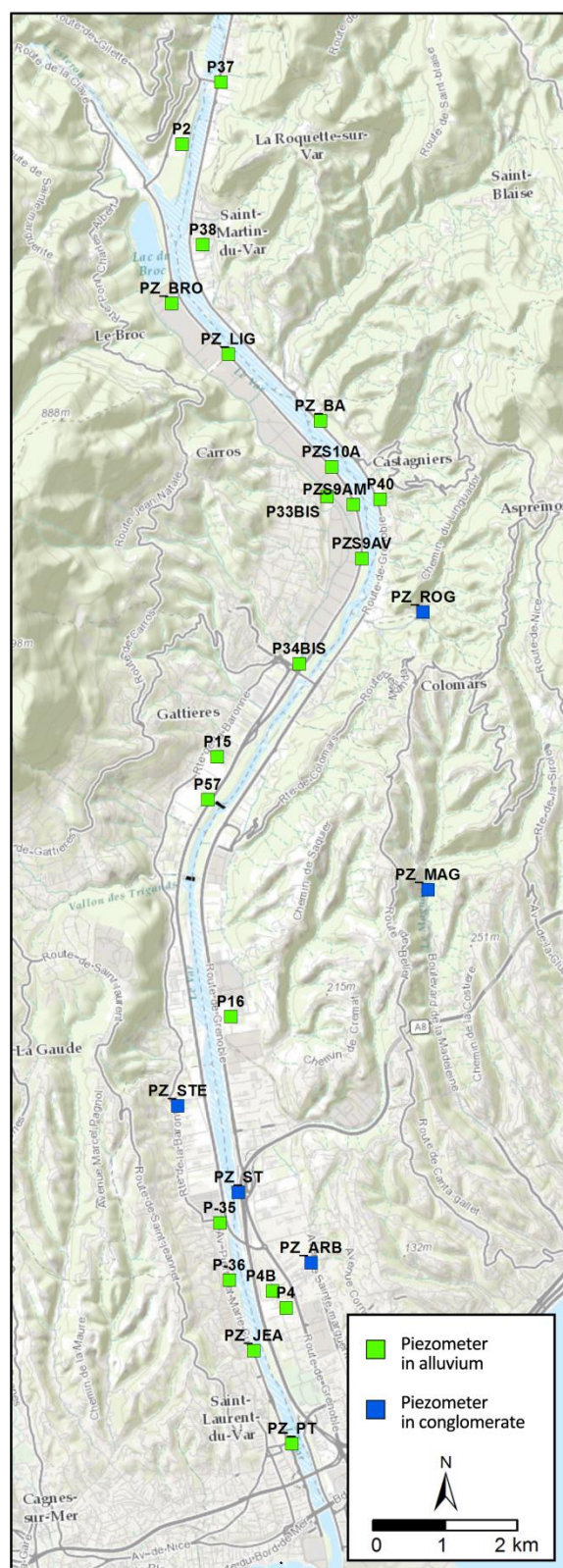


Table I.5. Altitude and borehole depth of the piezometers in the lower Var river valley (Source: Eaufrance).

Piezometer	Altitude (m)	Depth (m)
P37	120	20
P2	116	29
PZ_LIG	115	10
PZ_BRO	114	18
P38	104	20
PZ_BA	88	12
PZS10A	79	10
P33BIS	76	18
P40	75	20
PZS9AM	75	10
PZS9AV	70	12
PZ_ROG	134	390
P34BIS	65	13
P15	58	20
P57	52	59
PZ_MAG	140	490
P16	35	20
PZ_STE	31	500
P-35	23	12
P-36	21	11
PZ_ARB	20	354
PZ_ST	20	447
P4B	17	15
PZ_JEA	17	30
P4	16	10
PZ_PT	12	70

Figure I.22. Location of the piezometers in the lower Var river valley (Source: Eaufrance).

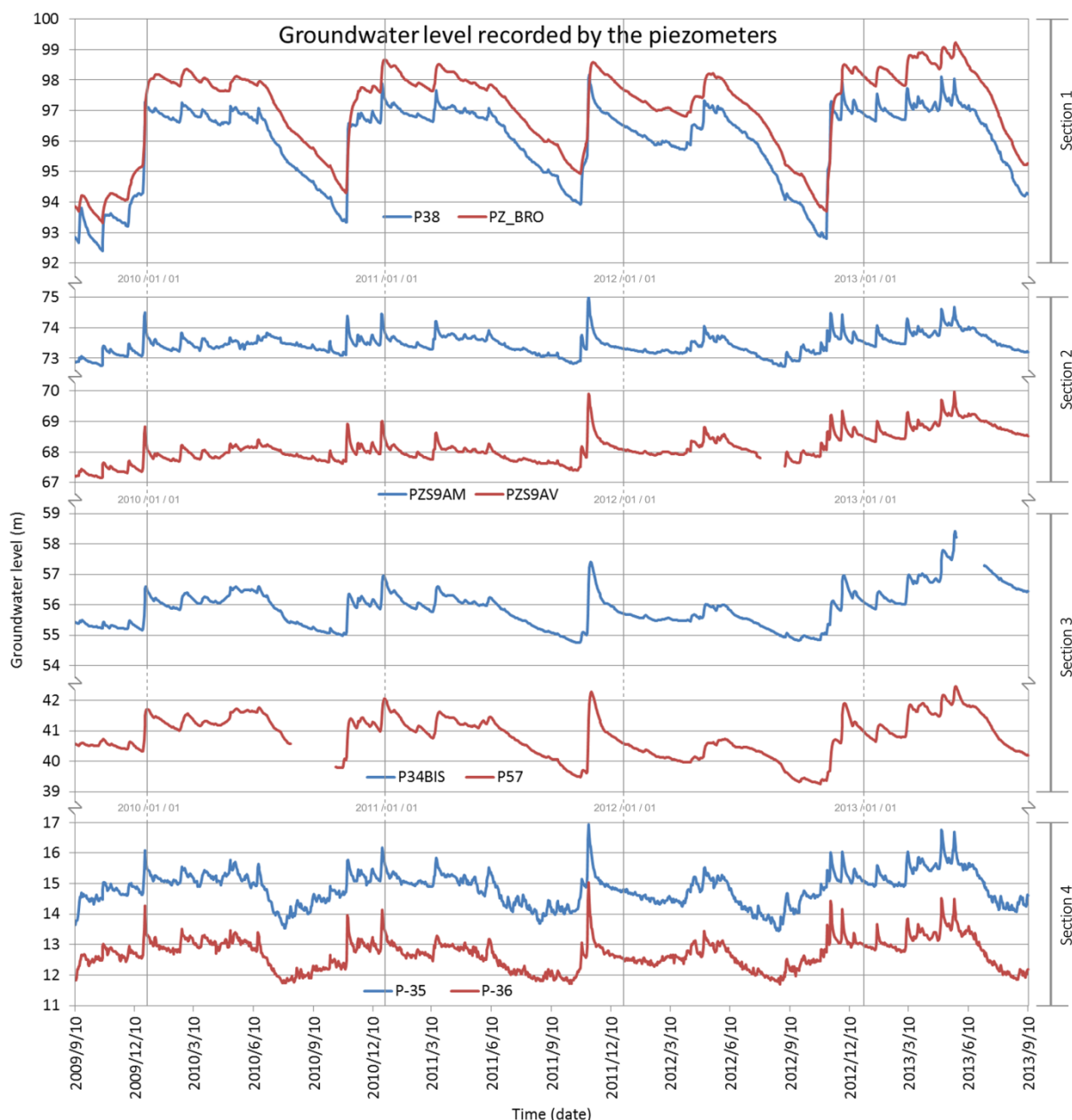


Figure I.23. Representative groundwater level recorded by piezometers along the Var river (Source: Eaufrance).

The monitoring points are not uniformly distributed along the valley (Figure I.22). Apparently, more piezometers are monitored in the upstream area, where a lot of constructions are made in the industrial zone of Carros. Besides, since there are two pumping stations, the piezometers are also used to monitor the influence of the groundwater pumping on the unconfined aquifer. There are also many monitoring points in the downstream area for the same reason. In the middle section between the weir No.2 to No.8, only four piezometers are monitored with sensor.

The behavior of the aquifer can be seen from the time series of the groundwater level. Figure I.23, 8 piezometers and the groundwater level recorded from 2009 to 2013 (4 years) are chosen to show the characteristics of the aquifer in each section of the valley. In general, the time series show that the groundwater level is strongly influenced by the season. The rainy season and dry season can be easily distinguished in all sections. Secondly, the groundwater level is also influenced by the water level in the Var river. The peak values occurring on each time series are caused by the river flood on November 2011.

In section 1, the groundwater is mainly influenced by the season. The fluctuation of the groundwater level in this section is as big as 4 m. The shape of the time series is not similar to the other time series. This might be because of the high hydraulic conductivity in this section. Section 2 is characterized by a small fluctuation whose amplitude is less than 2.4 m. Section 3 is the section with the weirs, where the variation of the groundwater level is less sharp. Even though the groundwater level is 10 to 16 m lower than the ground surface, the groundwater level is still synchronized with the surface water level, like the other piezometers. Section 4 is an active area where the river-aquifer exchanges are more intense than other river sections because the amplitude of the groundwater level is more than 3 m. Due to the impact of the pumping stations, the measured groundwater level varies a lot and the fluctuation is very pointy.

In order to have a global view of the groundwater level, extra measurements are needed so as to make a groundwater level contour map. A measurement campaign was conducted from July 27th to 31st 2015. The supplement measurement has to fulfill the monitoring gaps such as the left bank side at S^t-Martin-du-Var, the left bank side of the middle section from weir No.3 to weir No.8, and the section from piezometer P16 to P35. The depth of groundwater surface was measured by a portable sensor with a resolution of 1 cm. The coordinates and altitude of the piezometer was measured by a GNSS (Global navigation satellite system) device with a resolution of 1 mm.

According to the database of Eaufrance, nearly 500 boreholes and drillings have been created (Appendix 4). Nevertheless, a huge part of them are not available to be measured due to three main reasons:

- The drilling was not created for the purpose of water so that the drilled depth was not enough to reach the aquifer.

- The borehole was used before, but it is abandoned nowadays since there is no more water.
- The borehole is still used for water extraction, while there is no access for the portable sensor.
- The boreholes are created by the individual farmers and they denied to cooperate and refused to show the borehole in their yard.

Finally 53 points are chosen to conduct the measurement and the measured data is interpolated by using the Kriging method. The contour map of July 2015 is shown and compared with the map of March 1994 (dry period) and October 1999 (rainy period) in Figure I.24.

In general, the direction of the groundwater flow is parallel to the river channel. The hydraulic gradient is higher in the middle section than in the upstream or downstream part. Compared to the contour map of previous years, an obvious groundwater level depletion is observed around Le Broc lake and in the northern area of the lake. The groundwater level is decreased at least by 3 m compared to the dry period of the year 1999, and 6 m compared to the rainy period of the year 1994. In the area near the weirs No.10 and No.9, the groundwater level is 75 m in 2015 and this value is 2 meters higher than the previous years. For the section of weirs as well as the rest downstream part, no significant change has been observed regarding the groundwater level and the hydraulic gradient, which means that the groundwater table in this area is stable over the recent 20 years.

Through the contour map and the comparison, it can be inferred that the construction of the weirs has influenced the groundwater level and led to the groundwater depletion. This subject is discussed in the next chapter. Since the lowering of the weirs No.10 and No.9 in 2009, the problem of groundwater depletion in this area has been improved.

The groundwater level contour map is a common method used in hydrogeological study. However, there are several inconveniences when using this method. First of all, the quality of the contour map depends on the density of measuring points. If the number of points is insufficient or the spatial distribution is not representative, the contour map is thus not able to represent correctly the groundwater level in the study area. Secondly, in the area where there are river-aquifer exchanges, the contour map could not be able to represent the groundwater level if there is no measurement of the water level in the river. Even though the water level in the river is measured, it is hard to choose the location of measured points because the connection/disconnection relation between the river and the aquifer is difficult to define without further field surveys.

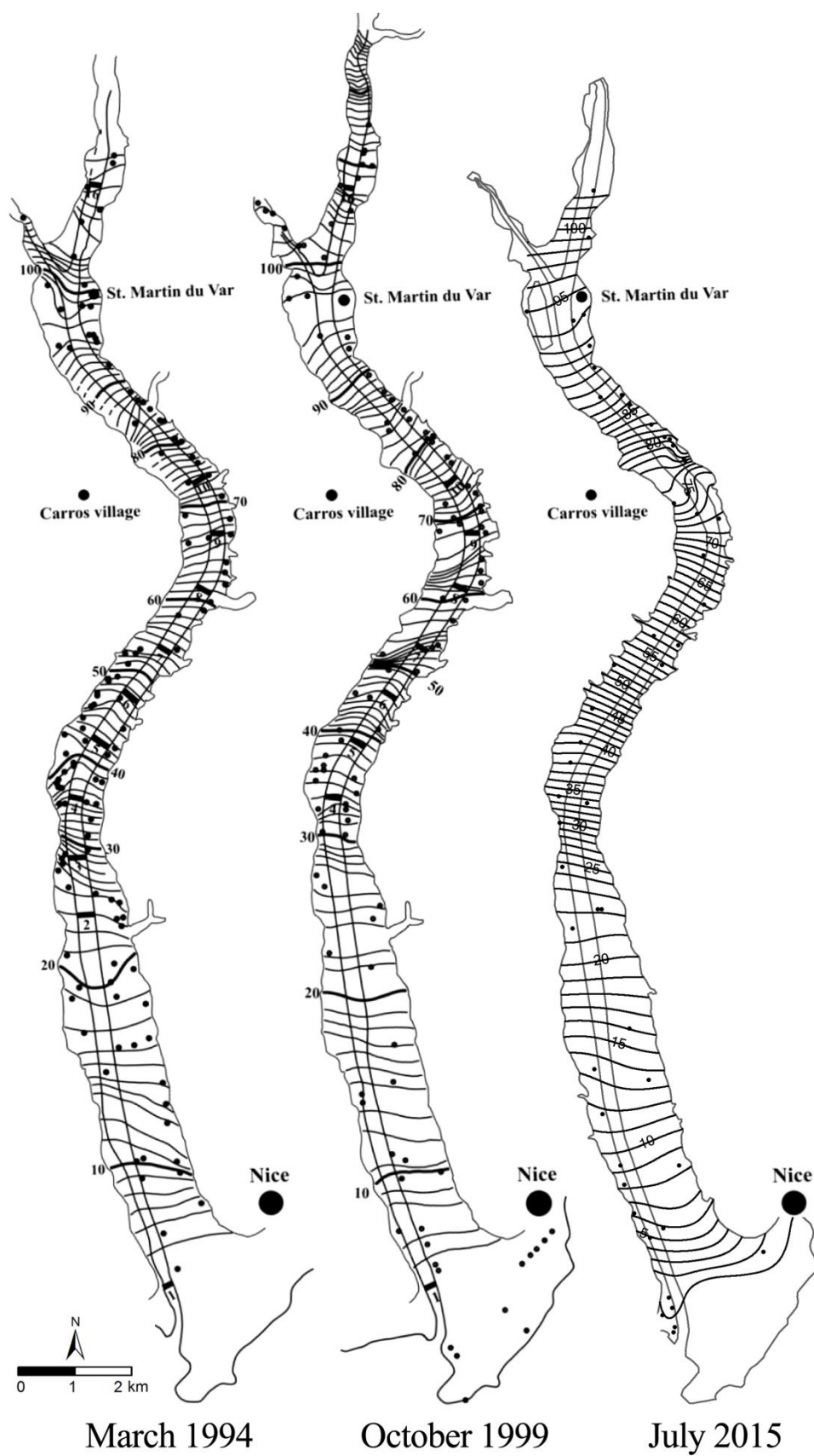


Figure I.24. Groundwater level contour map in the lower Var river valley. The map of 1994 and 1999 are made by Guglielmi Y. and Hocaht M. [Potot 2011], the map of 2015 is made by Du M. and Zavattero E.

I.3 Conclusion

A maximum of data are collected to help the understanding of all aspects regarding the geography, hydrology, geology and hydrogeology in the lower Valley. Based on these data, a first description of the lower Var river valley can be given.

The lower Var river valley is an area with diverse land use and complex geological layers. After having been developed since the 19th century, the river and the flood plain are no longer kept in their natural state. The mixture of industrial, agricultural and urban area has induced a problematic issue to the groundwater management.

Regarding the hydrology, the lower Var river valley has a typical Mediterranean climate, thus the need of groundwater is extremely high in summer. During the rainy season in winter, the valley is under the risk of river flood, which could be a source of groundwater contamination. These two characteristics are the most basic issues that could challenge the groundwater management.

As for the hydrogeological features, three aquifers exist in the lower Var river valley, including the one in the alluvium and, the one in the conglomerate and the karst aquifer in the limestone. The alluvial aquifer is unconfined in the upstream part of the lower valley, but a confined aquifer is observed in the downstream part due to the clay and silt lenses at the estuarine area. Among the three aquifers, the first one is the most exploited by the inhabitants for industrial, agricultural and domestic water use. It is the studied aquifer in this research work. The aquifer in the alluvium is thus complex because of its interaction with the other aquifers, and various influencing factors such as precipitation, evapotranspiration, river-aquifer exchanges, groundwater extraction, *etc.*

The groundwater level recorded by the piezometers along the river indicates that the behavior of the aquifer is different according to the river sections. Either connected or disconnected to the river, the aquifer is always impacted by the water level in the river. The quality of the contour map of groundwater level in July 2015 is limited by the number of measuring points. However, through the comparison with previous studies, the upstream part of the valley is facing to the problem of groundwater depletion. But it has been proved that the lowering of the weirs has a positive effect on the groundwater restoration.

Chapter II. Interpretation of the groundwater flow modeling

II.1 Hydrologic cycle of estuary area

The hydrologic cycle of water is a global definition which includes a series of phenomena of the transformation, movement and renewal of water [Chahine, 1992; Roads, 1994; Rodda, 1995; Fouché, 2013]. In reality, the water movement is very complex, thus it is divided into separated paths and studied by different specific disciplines such as hydrology, meteorology, oceanography, glaciology, limnology, *etc.* Hydraulic modeling is therefore an interdisciplinary subject that is applied by water resources development and water resources management. It only focuses on one or several paths in the whole hydrologic water cycle depending on the study aim. The complex water movement can be schematized as Figure II.1.

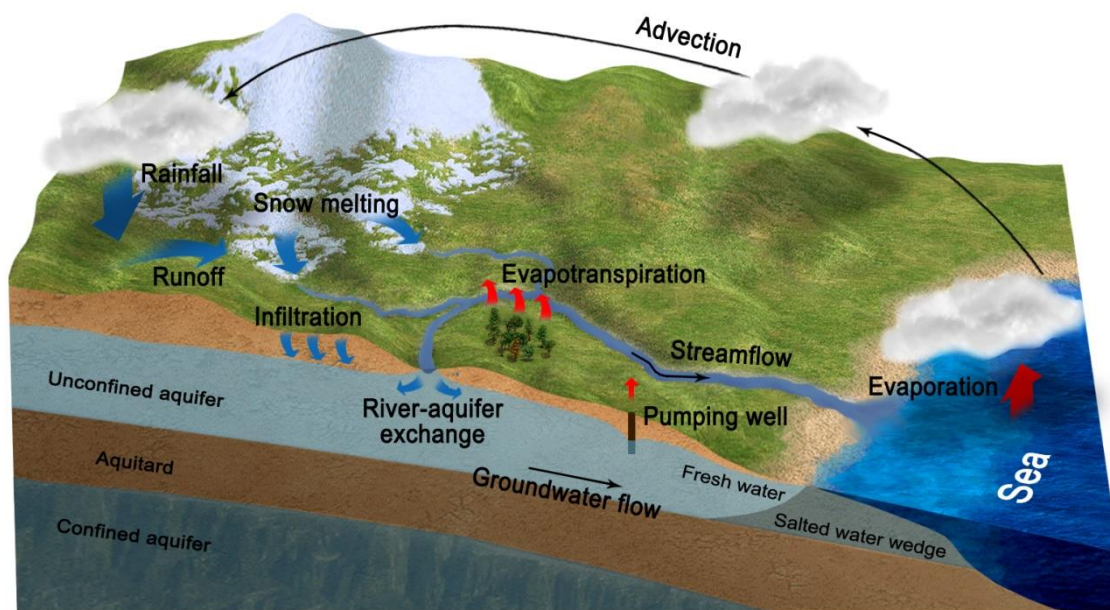


Figure II.1. Illustration of a general example of the water cycle in estuarine area (Author's design).

In this cycle, the water in the oceans receives the heat from the sun, then a part of it evaporates into the air. Along with the water from evapotranspiration, it is condensed into the clouds by the cool air in the atmosphere. Clouds are moved towards the inland by the air current. The water in the cloud then falls on the ground in the form of precipitation, either snow or rainfall. Due to the gravity, the rainfall on the ground flows as surface runoff, while the snow only contributes to the surface runoff when the

temperature is high enough to melt the snow. A part of surface runoff is drained by the rivers and moves as streamflow towards the lakes, reservoirs and oceans. The other part infiltrates into the ground and replenishes the aquifers underground.

The groundwater stores a huge amount of fresh water and it moves slowly towards an outlet, which could be a spring, a surface water body such as rivers and lakes, or to the oceans. The aquifers can be divided into two types, the unconfined aquifer and the confined aquifer. The unconfined aquifer is in the permeable layer such as sand and gravels, or even in the less permeable layer such as sandy silt or sandy clay. The confined aquifer is overlain by an impermeable layer, which is recognized as aquitard. By definition, the confined aquifer is under pressure, which means the piezometric head is above the level of the aquifer.

The unconfined aquifer has the most active exchange with the atmosphere [Zektser, 1993]. More precisely, the unconfined aquifer locates under an unsaturated zone, where the water amount varies but the porous media is not saturated. The top slice of the unconfined aquifer is called water table, beneath which the pores are totally saturated (Figure II.2). Usually, without indicating the saturation, the term “groundwater” refers to the aquifers under the water table, either unconfined or confined. The unsaturated zone receives the infiltration from rainfall and transmits water into the air by evapotranspiration through the plants and the soil surface. Meanwhile, the unconfined aquifer is recharged by the water from the unsaturated zone.

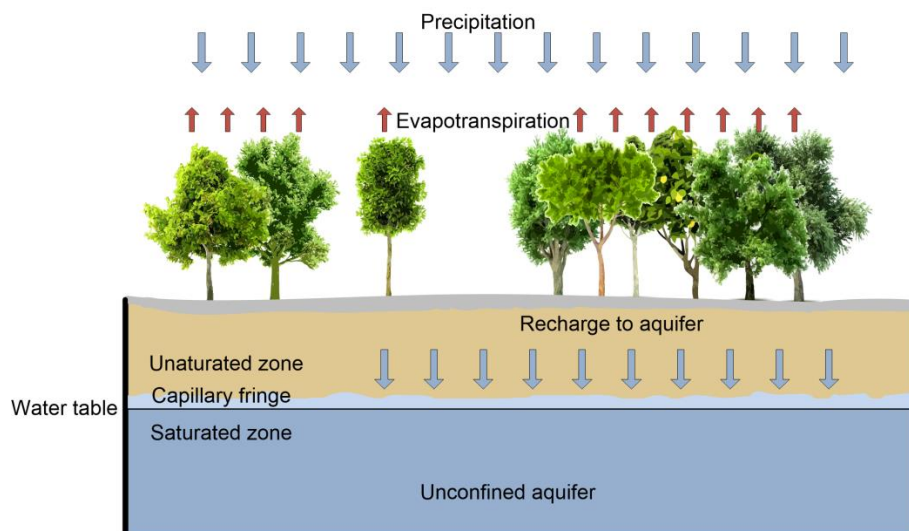


Figure II.2. Illustration of a typical profile of an unconfined aquifer (Author's design).

The water in the unconfined aquifer may have an exchange with the surface water, usually named as river-aquifer exchanges. The exchange may happen in both directions. This exchange influences the discharge in the river and also the groundwater table of the aquifer. At populated place, the water in aquifers may be extracted by humans and used as a water source. In the coastal area, where the fresh groundwater encounters the salty groundwater, a salt water wedge occurs due to the density driven flow from the sea to the land.

The hydrological and hydraulic modeling is used to understand and describe the water cycle. They are usually simplified and conceptual representation of specific parts of the hydrologic cycle, according to the aim and the scale of the study [Bloschl, 2006]. The hydrological models, as is implied by the name, are developed to understand the water distribution in large catchment scale such as surface runoff or evapotranspiration. The hydraulic models focus only on the mechanical properties of the conveyance of water such as streamflow or groundwater flow. Sometimes the hydrological models are coupled with hydraulic models to describe a complicated process of water cycle.

II.2 Main issues regarding groundwater in lower Var river valley

II.2.1 Impact of erosion and deposition in the riverbed on the groundwater

Because of the urbanization of the lower Var river valley, the flood plain has been reclaimed to meet the need of the urban development. The river embankments that have been constructed since the early 20th century have limited the width of the riverbed, thus the water velocity during the peak flow increases comparing to the state without embankments. As a consequence, erosion has occurred during each flood peak and the level of riverbed has decreased. Accordingly, the groundwater level also decreased due to the connection between the river and the aquifer. In order to stabilize the unbalanced sediment transport and to maintain the groundwater level, engineers have built 11 weirs since 1970s along the river (Figure I.2).

The weir No.1 is located on the upstream side of the Napoléon III bridge. Its main function is to prevent the seawater encroachment in the river under low-flow condition. The weir No.16 has been built on the downstream side of the Charles Albert bridge in order to protect its foundation of pillars which lies on the sediments of Var river (Figure II.3). The other weirs, from weir No.2 to weir No.10 are constructed in the meandering section of the river so as to stabilize the strong flow as well as the sediment transport.



Figure II.3. The weir No.1 (left, photo taken by author on July 2014) and the weir No.16 (right, photo taken by Mossot on October 2011).

IGN has published the aerial photograph of Var river taken from the 1950s. These photos show an obvious evolution of the riverbed since the construction of the weirs (Figure II.4). Before the construction of the weirs, the river morphology was in its natural state, which shows many parallel branches with small meanderings. From 1974 to 1983, it can be seen that the river channeling was still ongoing and, at the end of ten years, the sediment deposition with dense vegetation already occurred on the river side within the section of weirs. The flood of 1994 has destroyed the weir No.2 and No.3 [Souriguère, 2003], however, the sediment deposition has not been changed at all by such a strong peak flow ($Q=3760 \text{ m}^3/\text{s}$). After the demolition, the river section between weir No.2 and weir No.4 regained immediately its natural state on 1995 with small meandering and parallel branches. But the sediment erosion became predominant effect after losing the control of weir No.2 and weir No.3, the consequence is that the sediment erosion has induced a difference in elevation of about 8 meters, which endangered the stability of the foundation of weir No.4 on its downstream side. Therefore a second weir has been built next to the weir No.4 to prevent it from collapsing.

The impact of the sedimentation on the groundwater level is that the fine sediments and the vegetation have formed a clogging layer that is less impermeable. It blocks the river aquifer exchange, especially the seepage from the river to the aquifer. Furthermore, the major land use on the flood plain of the section is the agricultural land, thus a huge volume of groundwater is pumped for irrigation every summer. Without an efficient recharge from river seepage, the groundwater table withdrawal is inevitable.

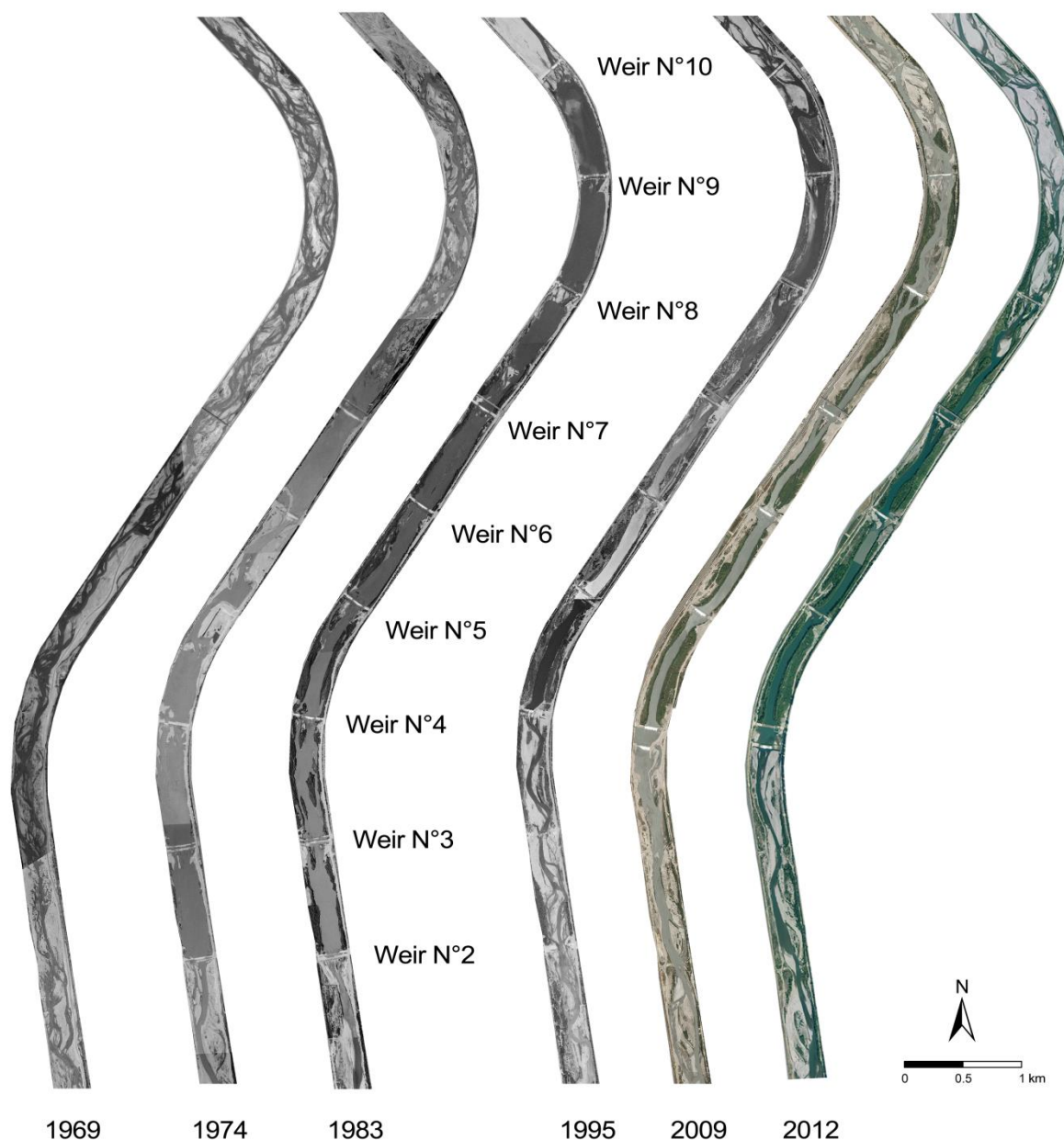


Figure II.4. Evolution of the riverbed of the lower Var river from 1969 to 2009 (Source: IGN).

Figure II.5 shows a long term measurement of the groundwater table near the weir No.2, it proves clearly the impact of the construction of the weir on the groundwater. Since the construction of weir No.2 on the riverbed, the fine sediment started to accumulate on the riverbed. The seepage from the river has been declined gradually so the groundwater level dropped as it was less recharged by the surface water. During the flood event of 1994, the piezometer was out of order for almost one year. After the restoration of the device, two flood events were observed on 2000 and 2002 (Figure II.5). Each peak was followed by a severe withdrawal. The most reasonable explanation is that, without the

control of weir, erosion happened and the riverbed level decreased, which led also to the decrease of the groundwater table. Nowadays, the water exchange in this section has reached an equilibrium therefore the groundwater level is stabilized between 24 and 26 m.

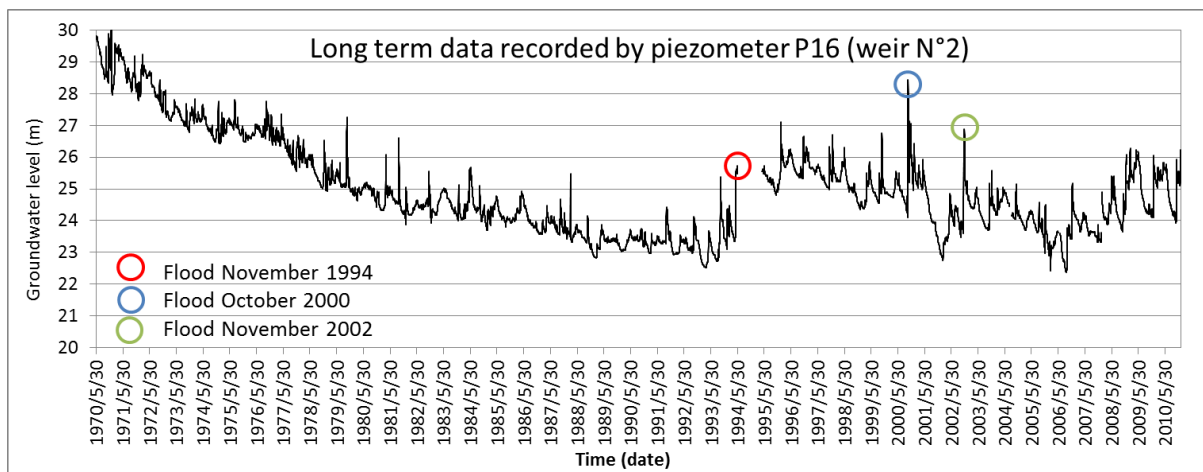


Figure II.5. Evolution of the groundwater level from 1970 to 2010 at weir No.2, recorded by the piezometer P16 (Source: Eaufrance).

The departmental council of Alpes-Maritimes has realized the negative effect of the weirs, therefore a restore plan to lower the crest level of each weir is ongoing in the lower Var river valley, in order to weaken the current “stair” morphology toward a “Mediterranean sedimentary facies”, and to recreate an equilibrium between the erosion and deposition on the riverbed [Souriguère, 2003; Souriguère, 2006].

Weir No.10 and No.9 have been lowered, a conspicuous positive result is already proved by many observations. In Figure II.4, the photo of 2012 shows that the river section between the lowered weir No.10 and No.9 has been reverted to the natural state. Thanks to this change, even the section between the weir No.8 and No.7 also started the restoration.

A field survey of the sediment distribution on the riverbed was carried out during the dry season of 2014 to guarantee a maximum exposure of the sediment. Based on 153 photos taken during the field visit, a map is made to demonstrate the composition of the sediment on the riverbed (Figure II.6). The sediments are classified into 6 types according to the proportion and the diameter of the coarse sediment. Thanks to the lower crest, the river regains its dynamic between weir No.10 and No.9 so that the coarse sediment has been already delivered to the downstream section until weir No.8. The downstream side of weir No.4 is still covered by coarse sediment which indicates that the erosion

process keeps happening there. The river morphology on the section from weir No.8 to weir No.4 remains unchanged.

In summary, the sediment transport is the most problematic issue which influences not only the surface hydraulics, but also the groundwater flow in the lower Var river valley. Regarding the water resource management in the lower Var river valley, a feasible way to study the influence of the sediment transport on the groundwater flow in the future is to set up a hydraulic model which enables to simulate the sediment transport under different scenarios, then the results are used by the groundwater flow modeling as a constant input data for the scenario simulation. The current results show that reducing the crest level of the weirs can help the river to regain its Mediterranean sedimentary facies, and to prevent the groundwater level from decreasing. However, more studies should be made to know the effect on the groundwater exploitation and on the safety issue of the foundation of La Manda bridge and Charles Albert bridge.

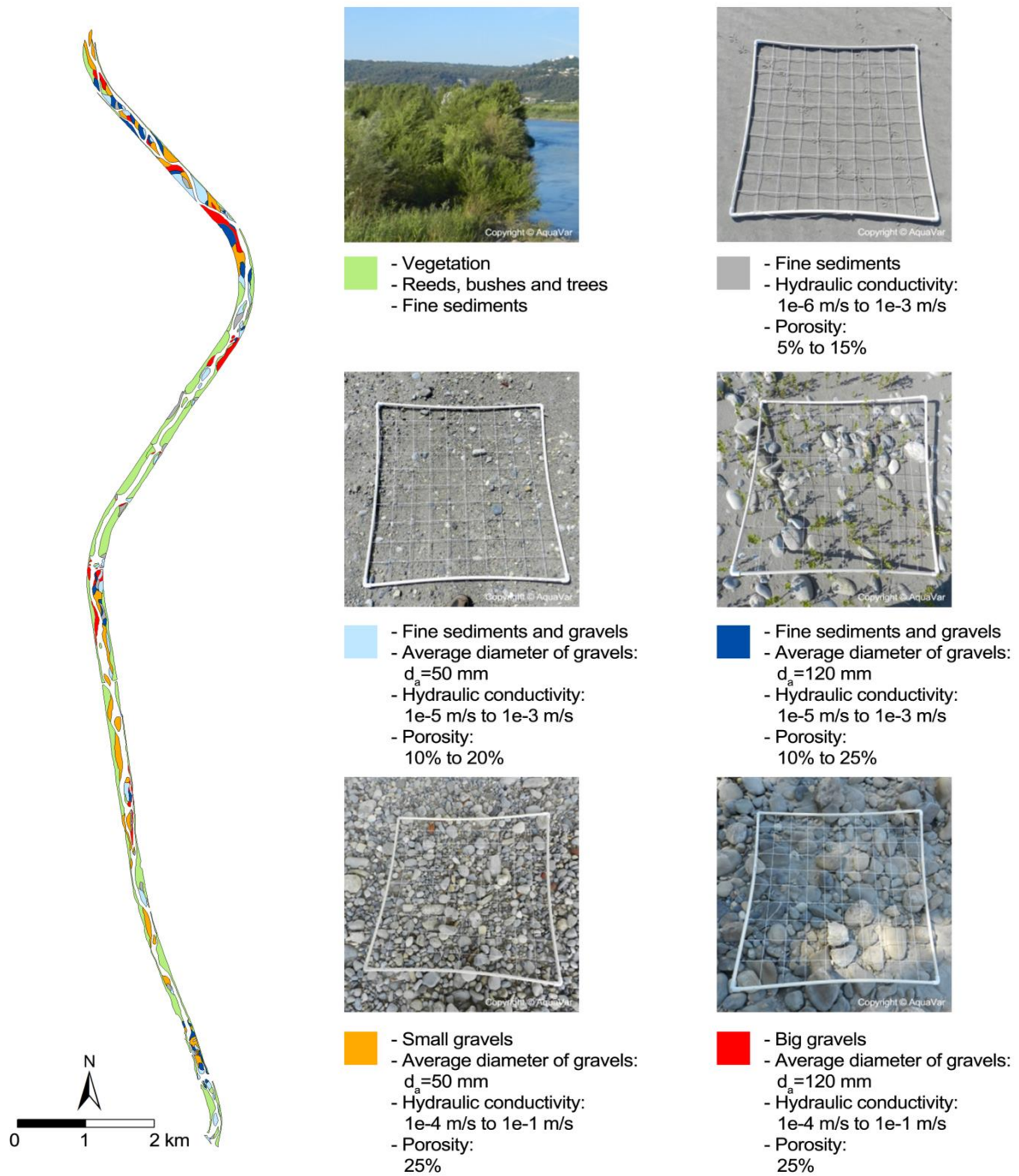


Figure II.6. Sediments distribution on the riverbed of lower Var river, measured by author on July 2014.

II.2.2 Groundwater extraction

Water pumped from the aquifer is used for drinking water production, industrial consumption and agricultural irrigation. The first two kinds of use are documented by the local water management authority and the regional water agency. However, among important consumers of the groundwater, the volume of groundwater consumed on agricultural activities is not recorded.

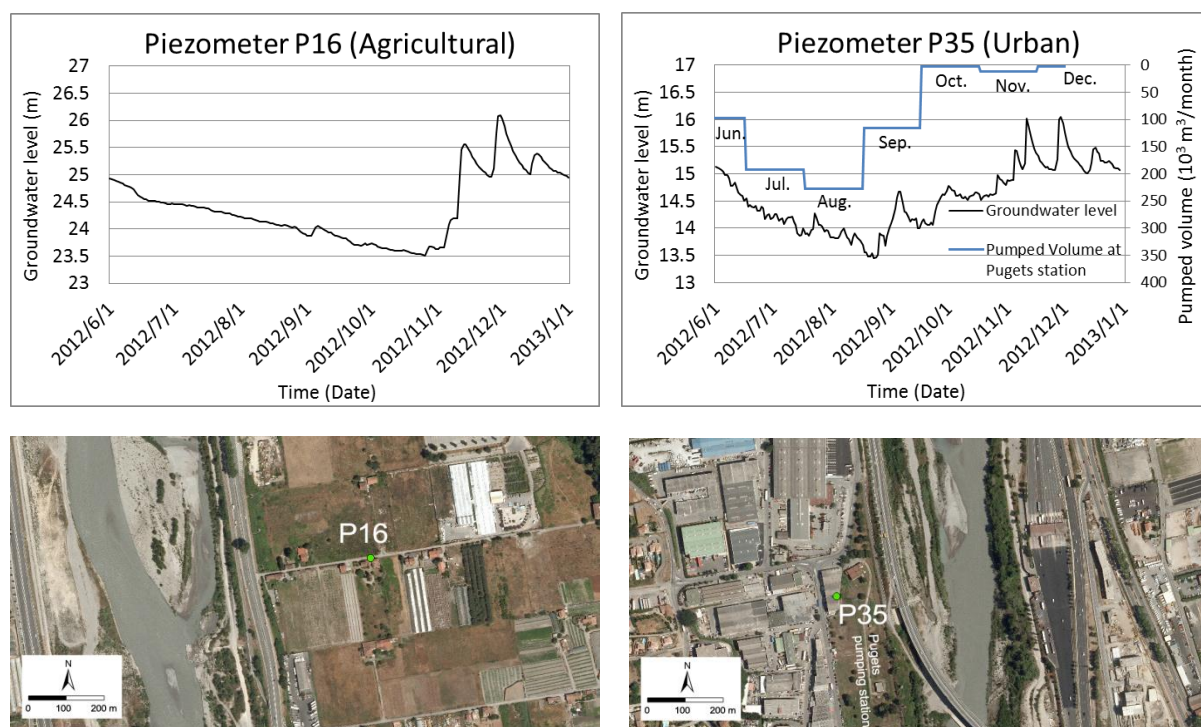


Figure II.7. Comparison of the groundwater level pattern during summer between agricultural land (P16) and urban area (P35) (Source: Eaufrance, Veolia).

Figure II.7 compares the groundwater level measured by two piezometers P16 and P35 (Figure I.22) during the summer on 2012. The piezometer P16 is located in the middle of a 25-hectare farm land, while the piezometer P35 is located in the Pugets pumping station, surrounded by an industrial zone. The hydraulic conductivity of these two places are in the same order of magnitude, from 10^{-4} m/s to 10^{-3} m/s, the effective porosity in these two areas are also similar (around 0.05), the groundwater table depths are respectively 9 to 11 m at P16 and 8 to 10 m at P35, which are also quite similar. Therefore these two areas have the same hydrogeological properties and the same level of river-aquifer exchanges.

Through the measurement of P35, an obvious correlation between the pumping volume and the groundwater level can be observed: during the months of July and August 2012, the huge pumping

volume has caused a decrease of 1 m; then a growth of groundwater level appeared, owing to the reduced pumping volume on September and October. It proves that the pumping volume affects directly the groundwater level and, after September 2012, the groundwater level in this area should have raised if there was no huge pumping volume. However, the measurement at P16 shows a continuous reduction of groundwater level after September. The difference of the groundwater level pattern implies that the farmers have made a great pumped volume of water from the aquifer.

The groundwater pumped by the individuals, including farmers and other small industries such as garages and garden centers, is neither documented nor well planned. The consumed volume depends only on the weather condition. When a dry season appears, the farmers pump much more water to keep the crops alive, thus a drought is likely to happen. Without doubt, this challenges the water resource management. A quantitative data is needed to anticipate the pessimistic scenario in order to elaborate the water pumping plan in municipal pumping stations.

II.2.3 Extreme hydrological events

The water-related extreme hydrological events mainly refer to floods and droughts, which may cause severe economic damages in both developed and developing areas [Kundzewicz et al., 1993; Kundzewicz and Matczak, 2015]. The groundwater is vulnerable for both flood and drought. During the flood event, the exchange between the surface water and the groundwater is increased due to the big inundated area and raised water level, thus the groundwater faces the threat of pollution. During the drought event, the groundwater shortage occurred because of the insufficient rainfall and low river seepage.

Diverse approaches have been used to resolve the issues involved with flood and drought control planning and management in the decision making process [Johnson, 1990]. From the management level, the consequence of flood and drought in surface water is usually simulated by deterministic models [Garrote, 2007; Martin-Carrasco, 2007]. These results could be used as input data to simulate the influence of the extreme hydrological events on the groundwater.

The lower Var river valley has experienced both: the severe drought in 1967 [Souriguère, 2003; Nicod, 1974] is one of the direct inducements of the construction of the weirs; the flood in 1994 [Guinot and Gourbesville, 2003] has caused a damage of 187 million euros and lead to the fortification of the existed river bank and the construction of higher levees in the downstream area of the Var river

(Figure II.8). One of the main issues brought by such extreme hydrological events is their impact on the groundwater. The results of simulations play an important role in the decision making process. For example, during the flood event, the groundwater is easily polluted by the flood water, therefore the groundwater pumping stations should be shut down before the overland flow occurs. For the drought event, the simulations results of scenarios can provide arguments to carry out water pumping plan when facing groundwater scarcities.

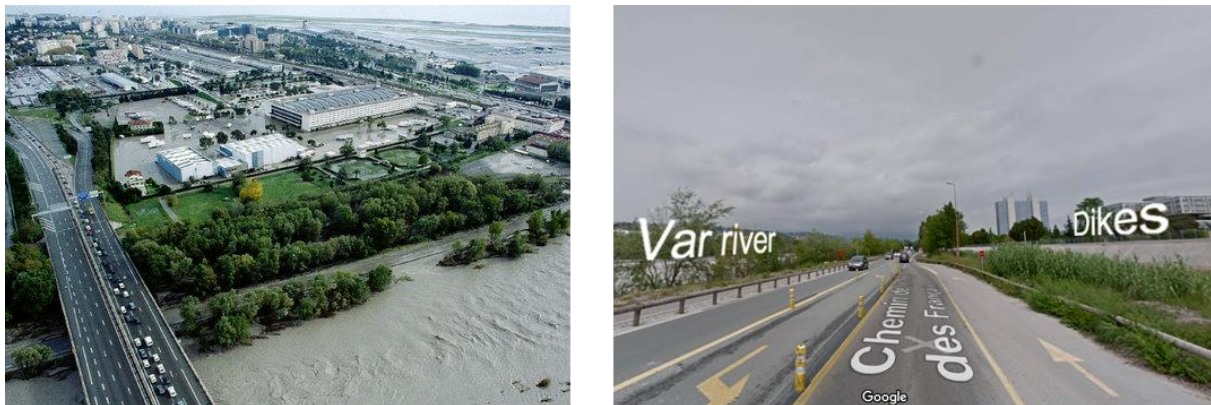


Figure II.8. Flood of 1994 in the lower valley of Var river and the levees located on the left bank in the downstream part (Source: Nice-Matin, Google Street).

II.3 Hydraulic modeling approach

Conceptual model is the basic and essential step of hydraulic modeling [Anderson and Woessner, 1992; Cunge, 1995]. It helps the engineers and researchers to interpret the reality based on measured data and conclusion of field surveying [Bredehoeft, 2005]. The conceptual step is necessary in order to set up a numerical model afterwards, by using proper data and suitable computing codes [Teresita Betancur, 2012].

During this step, hypotheses are often made to explain the phenomena and/or to complete the gap between the mathematical formulation and the reality of the physical processes. This is very common especially in hydrogeology study. The study of the underground world is less accurate due to the difficulties in measurement. Even though nowadays sampling is no longer costly thanks to the new tools and methods, the hydrogeological study is still not comparable to the study on surface hydraulics regarding accuracy and uncertainty. Many hypotheses are made unavoidably to understand the physical processes and only a few of them can be verified quantitatively with measured data [Voss,

2005; Wagener et al. 2007]. As a result, these hypotheses are a source of uncertainty in the whole modeling system and it may significantly impact every step of the development of numerical model.

Due to the complexity of the porous media, a fully distributed quantitative description of the aquifer is not possible. Borehole can be created only at the site of interest. The geophysical investigation on these limited sites provides the essential information. These measured data and the hypotheses may strengthen the comprehension of the study area so that important process of groundwater flow can be represented by a simplified conceptual model, then turned into a numerical model.

Regarding the lack of data, a sensitivity analysis of certain unmeasured parameters is commonly used to know the input-output relation. These parameters can be thus calibrated before the validation of the numerical model. Once validated, the numerical model justifies the correctness of the conceptual model as well as the hypotheses. Furthermore, simulations of scenarios can be carried out by the numerical model in order to provide useful information for groundwater management in the decision making procedure.

II.4 Interpretation of hydraulic modeling

II.4.1 Hydraulic modeling approach

Groundwater flow modeling includes a series of steps that involves many disciplines such as mathematics, computer science, hydraulics and hydrogeology. Fitts [2002] has identified the 3 steps to develop a modeling system, which are:

- (1) collect and review all the data about the material physical properties,
- (2) develop a conceptual system to represent the real flow system (it must capture the key features of the reality),
- (3) simulate the conceptual system with a computer code and proper input data.

Collection and validation of measured data are usually a time consuming step, yet extremely important for the formation of the conceptual model and numerical model. In order to have a comprehensive view of the area, the data in various subjects are quite often needed, such as meteorological, geological, hydrological, hydraulic, even social and economic data.

Conceptual model should be made regarding the study purpose and study domain. Simplifications of the modeling or hypotheses are often needed. Obviously, at this stage, the professional experience

plays an important role. A good model conception can minimize the workload of the steps given in Figure II.9.

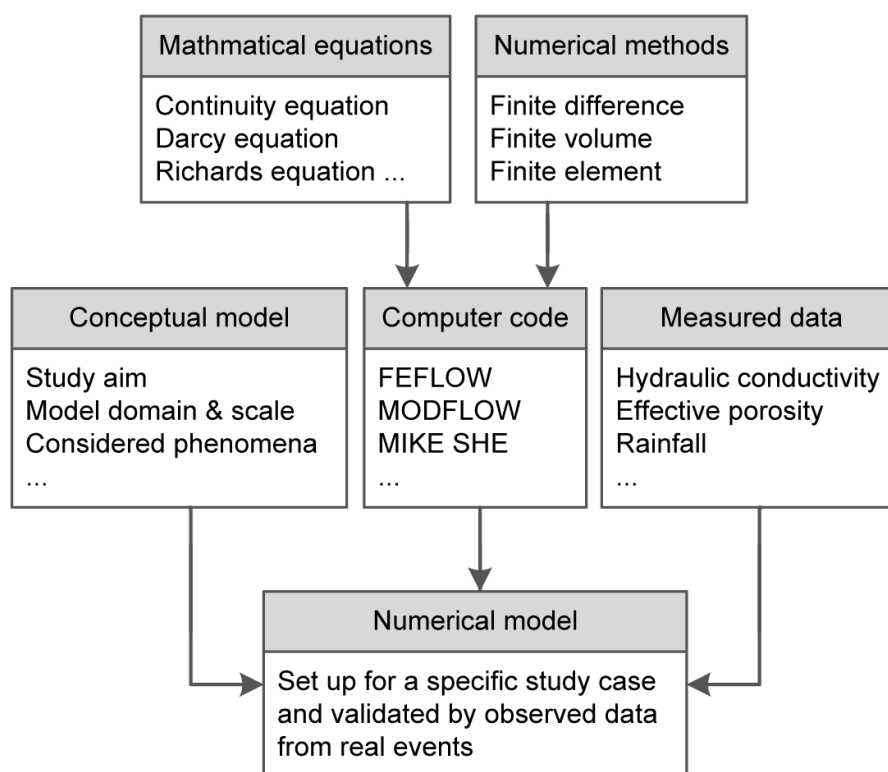


Figure II.9. Work flow of groundwater modeling. This diagram also explains the general hydraulic modeling approach, in this case, the equations and computer code should be replaced by their related substitutions.

Figure II.9 illustrates the basic work flow of modeling, for instance, groundwater flow modeling is used as an example. Classical hydraulic equations have been widely used for a long time (*e.g.* shallow water equation for free surface flow, Darcy's equation, *etc.*). These partial derivative equations (PDEs) are discretized and solved using certain numerical methods (mainly finite differences, finite elements and finite volumes methods). The implementation of such calculating engine constitutes the core of the computer programs that can be either open source codes or commercial codes.

With all these three elements, a numerical model is therefore developed for a specific case study. Measured data can be used as material parameters (*e.g.* hydraulic conductivity K , specific storage S_s , specific yield S_y), source/sink terms (*e.g.* water pumping volume) or boundary conditions (*e.g.* hydraulic head of groundwater) in the model. Some unmeasured data or those which have large uncertainty need to be calibrated. The numerical model must be validated through one or several

validation cases which include various events, so as to make sure the model is able to provide good results under all circumstances.

II.4.2 Conceptual model of groundwater flow in lower Var river valley

In general, the water that is exploitable is in the unconfined aquifer. Hence the modeling system focuses only on the saturated zone of the unconfined aquifer. The impact of confined aquifer and karst are either neglected or modeled by other models. Regarding the lateral delimitation of the area that determines the study domain of the model, the hydrogeological catchment is delimited by geological faults and impermeable layers. In Mediterranean coastal area, the unconfined aquifer is commonly connected to the sea, so the downstream boundary extends to the sea level.

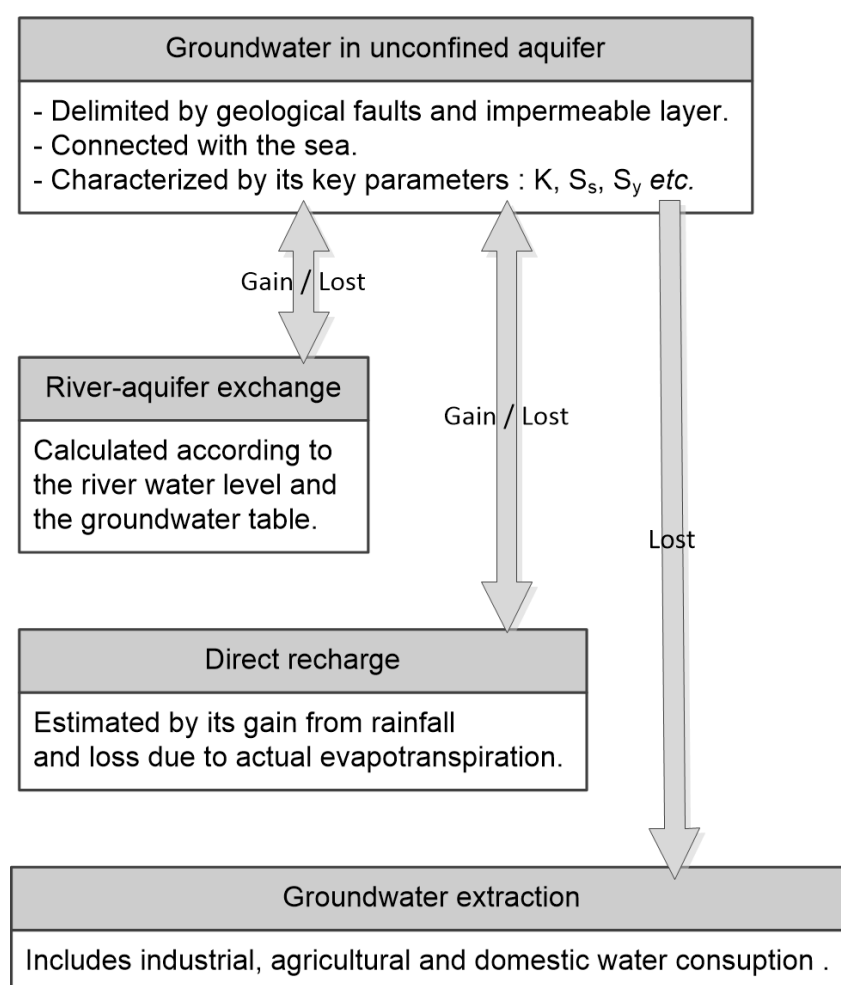


Figure II.10. Conceptual model developed for unconfined aquifer in the lower Var river valley.

Figure II.10 summarizes the conceptual model. In the groundwater flow model, it is unnecessary to consider all the processes included in the recycle shown in Figure II.1. Some factors are negligible owing to their slight influence on the groundwater flow (evaporation on the sea, advection), and some

factors are not considered since they are studied in other models (snow melting, runoff). Finally only river-aquifer exchanges, direct recharge/loss caused by rainfall/evapotranspiration, and groundwater extraction are the source/sink terms that are considered as the most influencing factors and have a direct impact on the groundwater flow. The first two terms can either feed or drain the aquifer depending on the dry or rainy season, while the last one always leads to a withdrawal of groundwater.

II.4.2.1 Porous media

The studied scope includes the hydrogeological catchment which is delimited by the faults and impermeable layers. The considered layers are: alluvium, alluvial terraces, conglomerates, marls, impermeable layers from Miocene to Cretaceous, and limestone. Because the marls and the impermeable layers from Miocene to Cretaceous do not cover the whole area, the layer of limestone has a direct contact with the alluvium at the section where weir No.4 is located.

The porous media of the unconfined aquifer in the lower Var river valley consists of the alluvium and the conglomerates. It is characterized by their key hydrogeological parameters including the hydraulic conductivity K , specific storage S_s , specific yield S_y , etc.

II.4.2.2 River-aquifer exchanges

The river-aquifer exchanges are calculated according to the difference between the water level in the river ψ_s and the hydraulic head of the groundwater ψ_g . The direction of the exchange depends on the relative position of the two levels. River-aquifer exchanges occur basically in three ways [Winter et al., 1988]. As shown in Figure II.11, in the situation that connection exists between the river and the aquifer, river can either be fed by its aquifer when adjacent hydraulic head is higher (Figure II.11-1), or it can also feed its aquifer when the water level is higher (Figure II.11-2). The third situation, shown in Figure II.11-3, is that river is disconnected to the aquifer, when an unsaturated zone occurs underneath the riverbed [Marti, 2005, Winter et al., 1988]. This is because a clogging layer, which is a part of the riverbed has a lower hydraulic conductivity than the underlying aquifer, meanwhile the velocity of the groundwater flow is too high to catch enough recharge from the infiltration [Brunner et al., 2009a, Brownbill et al., 2011]. A criterion has been given by Brunner et al. [2009a,b] as the following inequality:

$$\frac{K_c}{K_a} \leq \frac{d_c}{H + d_c}, \quad \text{Eq. 1}$$

where K_c is the hydraulic conductivity of the riverbed clogging layer (m/s), K_a is the hydraulic conductivity of the aquifer (m/s), d_c is the thickness of the clogging layer (m), and H is the water depth in the river (m).

Apparently, a river is very likely to be disconnected to the aquifer at the section where vegetation is presented in the riverbed, because the vegetation suggests fine sediment deposition. Furthermore, the leaves and roots help the formation of the clogging layer.

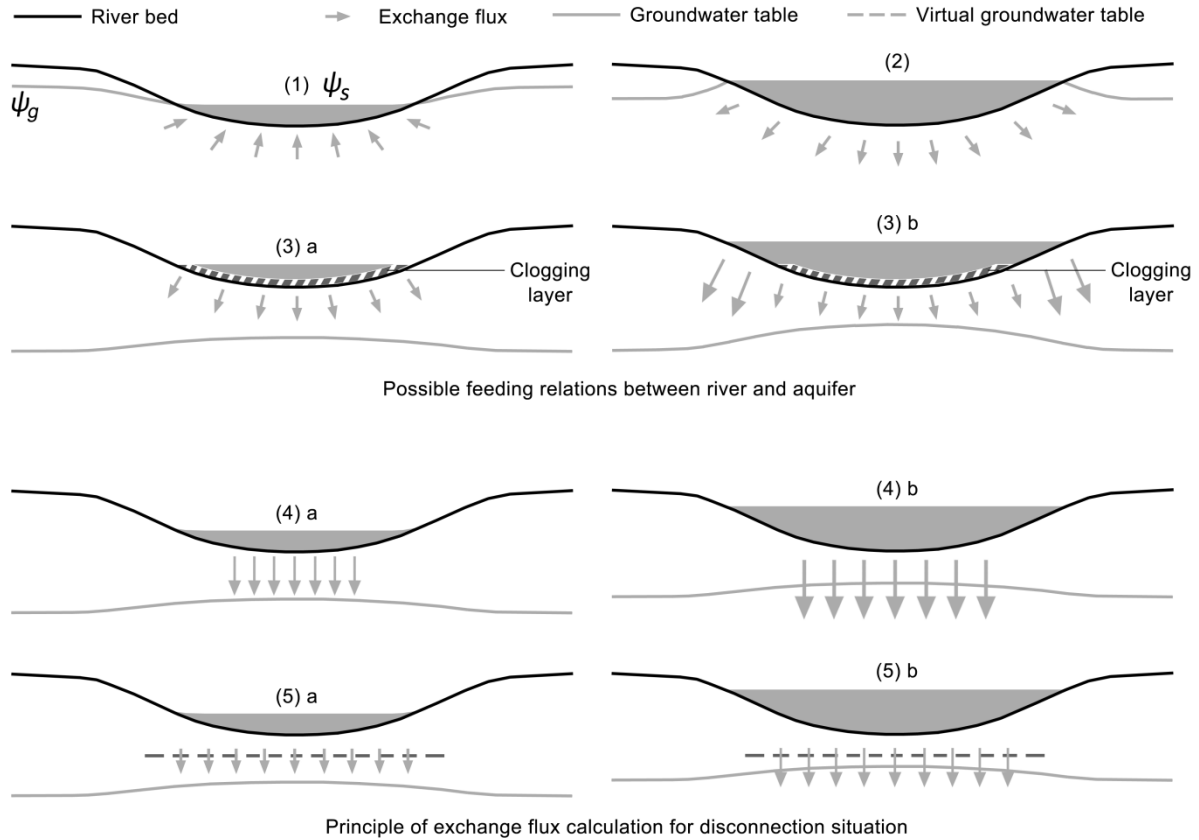


Figure II.11. Illustration of all possible feeding relations between river and its un-confined aquifer: (1), (2) and (3). The overestimated exchange flux for disconnection situation calculated with general equation (4). The exchange flux calculation with modified equation for disconnection situation (5) (Author's design).

Regarding the calculation of exchange rate, Diersch and Kolditz [1998] have used a transfer boundary expressed by a simple equation to quantify the exchange rate q_{ex} per unit area:

$$q_{ex} = \phi \cdot (\psi_s - \psi_g), \quad \text{Eq. 2}$$

where, q_{ex} is the exchange rate per unit area (m/s), ϕ is the transfer rate (1/s), ψ_s and ψ_g are respectively the water level in the river and the groundwater level in the aquifer (m). Two ϕ may be used (ϕ_{in} and ϕ_{out}) for different interchange directions, like presented in Figure II.11-1 and Figure

II.11-2. In the first case, $\psi_s - \psi_g < 0$, then ϕ_{out} should be used to calculate the q_{ex} . In the second case, $\psi_s - \psi_g > 0$, then ϕ_{in} should be used to calculate the q_{ex} . Normally, the out-transfer rate ϕ_{out} is higher than the in-transfer rate ϕ_{in} , because the exfiltration has an unblocking effect.

The limitation of this equation is that it is only valid for connection case, which means the saturated zone. The application of this equation in numerical model to simulate a disconnection case on a river section will overestimate the q_{ex} (Figure II.11-4). Richards equation [Richards, 1931] can simulate the variably saturated flow, by assuming that the hydraulic conductivity K is a function of the volumetric water content in porous media. However, changing the governing equation to Richards equation in order to simulate the unsaturated zone would tremendously increase the computing time and the risk of the non-convergence of the simulation [Short et al., 1995; Tocci et al. 1997]. After all, according to the criterion (Eq. 1), the disconnection exists only at some river sections during certain period.

To avoid this problem, a virtual groundwater level can be used to define a minimum groundwater level ψ_{min} (Eq. 3). This level is set somewhere under the riverbed [Diersch and Kolditz, 1998]. As a consequence, once the real groundwater level drops below it, ψ_{min} will replace the ψ_g so that the q_{ex} is limited. Nevertheless, the q_{ex} still varies with the rise and fall of the water level in the river (Figure II.11-5) :

$$q_{ex} = \begin{cases} \phi_{in} \cdot (\psi_s - \psi_g), & \text{if } \psi_g \geq \psi_{min} \\ \phi_{in} \cdot (\psi_s - \psi_{min}), & \text{else} \end{cases} \quad \text{Eq. 3}$$

II.4.2.3 Direct water recharge/loss

This term refers to the gains of water from rainfall and the loss due to the actual evapotranspiration. The direct recharge/loss is merely considered on the top layer of the ground, where the exchange between the aquifer and the atmosphere is direct. In the real case, the recharge of the groundwater is only a part of infiltrated water from rainfall. The rest of it stays in the unsaturated zone and it can go back to the atmosphere by evapotranspiration. In order to simplify the calculation in this model, the infiltration is considered to be equal to the water recharge in the groundwater.

When there is no rainfall, the actual evapotranspiration equals to the loss. Otherwise, precipitation forms not only the runoff, but also the infiltration so that aquifer gets recharged (Figure II.12). For a given period, the water balance of a given area has the simple expression as below:

$$Q_R = P - R - AET, \quad \text{Eq. 4}$$

where, the Q_R (mm) is increment of the groundwater storage due to the rainfall and AET (mm). Q_R contributes to the water quantity in the aquifer, P is precipitation depth per unit area (mm), R is runoff height per unit area (mm) and AET is actual evapotranspiration per unit area (mm). The precipitation data is usually well recorded by the meteorological stations, while the AET can be only estimated by using certain formulas such as Turc formula, Thornthwaite formula, *etc.* R is roughly estimated by using a dimensionless runoff coefficient c , which represents the total runoff R over total precipitation P [Savenije, 1996; McNamara et al., 1998].

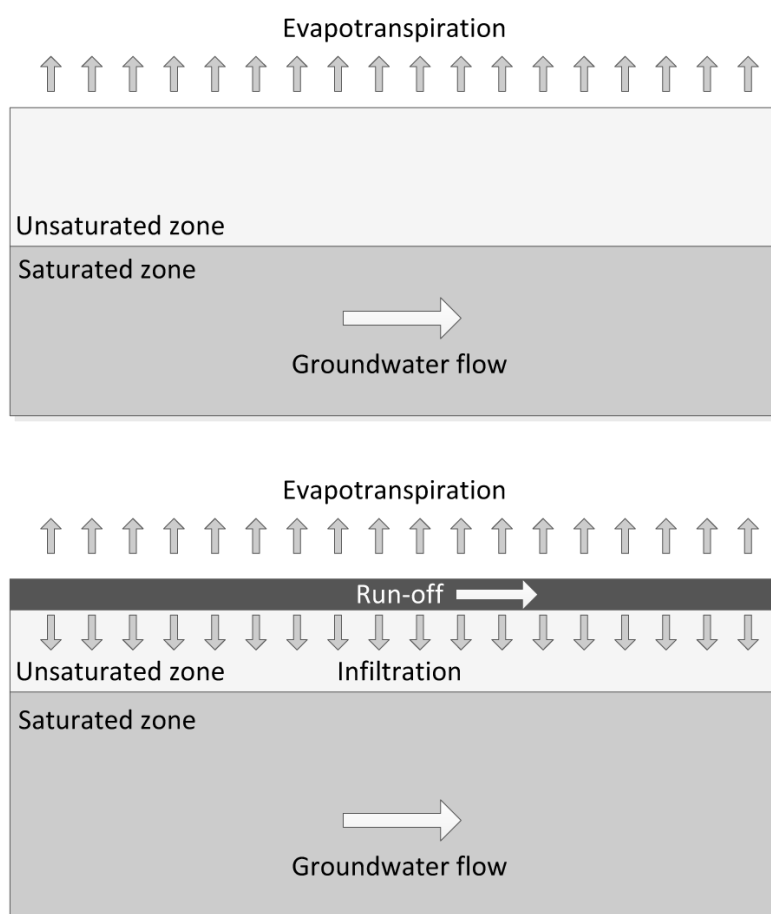


Figure II.12. Illustration of the direct water recharge/loss in the unconfined aquifer (Author's design).

II.4.2.4 Groundwater extraction

Groundwater is exploited for three main utilities: drinking water supply, industrial production and agricultural irrigation. In the conceptual model, the industrial water use is assumed to be constant over time because the production scale is stable, while the two other kinds of water consumption show a seasonal distribution. More water is consumed in summer than winter. This feature is especially typical on the agriculture land, because rainfall is abundant in winter and spring.

Drinking water supply relies on the large pumping stations that may contain several wells even up to 10 wells near major cities. The factories that extract groundwater from unconfined aquifer usually have one or two wells for the whole site. The water pumping rate is often well documented. The location of the well and pumping rate on agricultural land, however, remains unknown due to the difficulties of field investigation and reluctance of users to communicate pumped volumes. To that end, only estimated values can be used as no accurate data can be provided.

Inverse simulation approach [Murray-Smith, 2000] is a practical way to estimate the volume of water extracted from the groundwater for agricultural use. Often used for dynamic simulation models, this method allows the determination of the time history of “inputs” needed to achieve a specified time history for a selected set of “outputs”. In the case study of Var river, the agricultural water use is the unknown input. It should be estimated and then used as an input data in the numerical model. If the simulated groundwater level matches well the measured data, it means that the estimated input of pumped water of agricultural use is correctly estimated.

The first estimation method is given based on the evolution of the groundwater table of the farmland. For the area of farmland between weir No.4 and weir No.7 (Figure I.2), during a period when the precipitation is low, the groundwater table is too deep to be reached by the root of the crops, thus the precipitation can be totally turned into evapotranspiration and no percolation of water will contribute to the saturated zone. Besides, the hydraulic conductivity K is in the same order of magnitude in this area, therefore the hydraulic gradient of the groundwater table in this section can be treated as a spatially uniform value. As a consequence, the inflow and outflow within a given time of this given porous media section are the same. The only factor that may cause the decline of the groundwater table is the groundwater extraction. By making such assumptions, the pumping rate can be estimated as:

$$q_{ag} = -\frac{\partial \psi_g}{\partial t}, \quad \text{Eq. 5}$$

where, q_{ag} is the estimated pumping rate of water for agricultural use (m/s), ψ_g is the groundwater level (m), and t the time (s). Negative value is used here because the groundwater level keeps dropping when the water is pumped.

The second possible method to estimate the pumped water volume for agricultural use is to investigate the water consumption of the crops. Assuming that the farmers afford the full demand of water of all

their crops, the pumping rate can be thus expressed by a function of the species of crops, area of the farmland of each species and the water consumption of each species.

The first method of estimation is less accurate than the second one because the hypothesis of uniform K is a condition that can be hardly achieved. While the second method is difficult to operate since it concerns too much knowledge on botany. Also, the existing species of crops are too various to be investigated. Therefore the first method of estimation is the most reliable one considering that it is established based on the conservation of mass in the groundwater.

II.5 Conclusion

The hydrologic cycle has complicated processes which involve various disciplines. Hydrological and hydraulic models are used to understand the processes. However, hydrological and hydraulic modeling is only a conceptual approach which focuses on certain part of the hydrologic cycle depending on the aim of the study.

The main issues of the lower valley of Var river are presented in this chapter, including the impact of the erosion and sedimentation on the riverbed, the groundwater extraction and the threat of the extreme hydrological events. A hydraulic model of saturated of groundwater flow needs to be built to provide solutions regarding these issues. Thus, the model must consider the basic physical parameters such as hydraulic conductivity K , specific storage S_s , *etc.*, in order to describe the hydrogeological characteristics of the aquifer. Besides, several terms also need to be considered such as direct water recharge/loss, river-aquifer exchanges and groundwater extraction.

The conceptual model presented in this chapter forms a basic framework of the numerical model. By using proper computer code and measured data, a numerical model can be set up to describe the groundwater flow in the studied area.

Chapter III. Development of the numerical model of groundwater flow

III.1 Governing equations of groundwater flow

The governing equations for the saturated flow are the fluid continuity equation [Verruijt, 1970] and the Darcy equation [Verruijt, 1970]. The fluid continuity equation, also recognized as the equation of the conservation of mass, is established based on the transient, saturated groundwater flow that goes through a small cube of porous medium in unconfined aquifer (Figure III.1). Two assumptions are made in order to simplify the condition:

- the medium is porous, incompressible and non-deformable. In the following explanation, the word “soil” is used as an example,
- the fluid is of constant density. In the following explanation, the word “water” is used as an example.

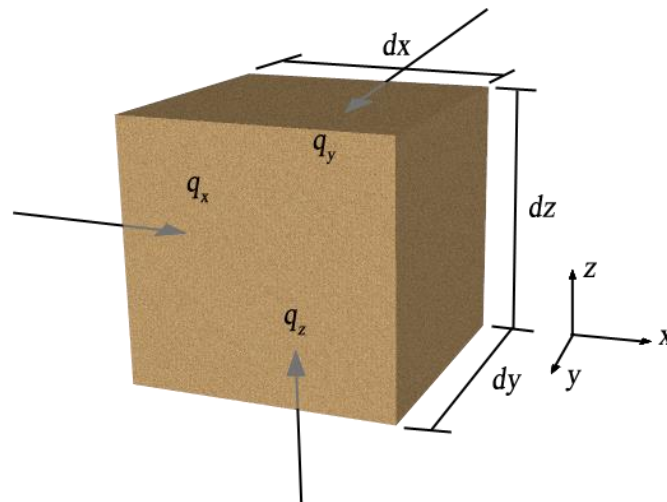


Figure III.1. Illustration of the derivation of the fluid continuity equation of the transient, saturated groundwater flow (Author's design).

In this case, the variation of the mass of water stored in the soil only depends on the flux that enters in and leaves from the soil. By considering the three dimensions of the cube, the volume of water that goes in the soil per unit time through the three directions is:

$$Q_{in} = q_x \cdot dydz + q_y \cdot dxdz + q_z \cdot dxdy, \quad \text{Eq. 6}$$

and the volume of water that goes out from the soil per unit time through the three directions is:

$$Q_{out} = \left[q_x \cdot dydz + \left(\frac{\partial q_x}{\partial x} dx \right) \cdot dydz \right] + \left[q_y \cdot dx dz + \left(\frac{\partial q_y}{\partial y} dy \right) \cdot dx dz \right] + \left[q_z \cdot dx dy + \left(\frac{\partial q_z}{\partial z} dz \right) \cdot dx dy \right], \quad \text{Eq. 7}$$

where, Q_{in} (respectively Q_{out}) is the volume of water that enters the soil (respectively leaves from the soil) per unit time (m^3/s), q_x (respectively q_y and q_z) is the flux of water in x -direction (respectively in y - and z -direction) that goes through the surface of the soil cube (m/s), dx (respectively dy and dz) is the length in x direction (respectively in y - and z -direction) of the soil cube.

Considering the situation that the water volume that leaves from the soil is bigger than that enters, in other word, the water is being drained from the medium. Without external source or sink term, the difference from the entering and leaving terms within unit time is expressed by the following relation:

$$\Delta Q = Q_{out} - Q_{in} = -\frac{\partial V_{water}}{\partial t}, \quad \text{Eq. 8}$$

where V_{water} is the volume of water stored in the soil (m^3). The ratio is negative because the soil is gaining water in this case.

The specific storage S_s of the medium is hereby brought. In a saturated flow, it is the volume of water that an unit volume of aquifer releases from storage under an unit decline in hydraulic head by the expansion of water. So Eq. 8 can be written as:

$$\frac{\partial V_{water}}{\partial t} = S_s \cdot V_{soil} \cdot \frac{\partial \psi_g}{\partial t} = S_s \cdot \frac{\partial \psi_g}{\partial t} \cdot dx dy dz, \quad \text{Eq. 9}$$

where, S_s is specific storage (m^{-1}), V_{soil} is the total volume of soil considered (m^3), ψ_g is the hydraulic head of the groundwater (m), for unconfined aquifer, its value equals to the groundwater level. In this equation, the right hand side becomes positive because the S_s indicates a loss of water in the soil.

By combining the equations from Eq. 6 to Eq. 9, the following expression can be obtained:

$$S_s \cdot \frac{\partial \psi_g}{\partial t} + \left(\frac{\partial q_x}{\partial x} + \frac{\partial q_y}{\partial y} + \frac{\partial q_z}{\partial z} \right) = 0, \quad \text{Eq. 10}$$

or a vector form can be used:

$$S_s \cdot \frac{\partial \psi_g}{\partial t} + \nabla \mathbf{q} = 0, \quad \text{Eq. 11}$$

where \mathbf{q} is the vector notion of the flux of groundwater flow (m/s).

This flux is calculated by Darcy equation, also called Darcy's law. It describes the movement of the groundwater flow in saturated area (Figure III.2). The Darcy equation is physically based and used to calculate the flux of groundwater flow through a given section according to the hydraulic gradient.

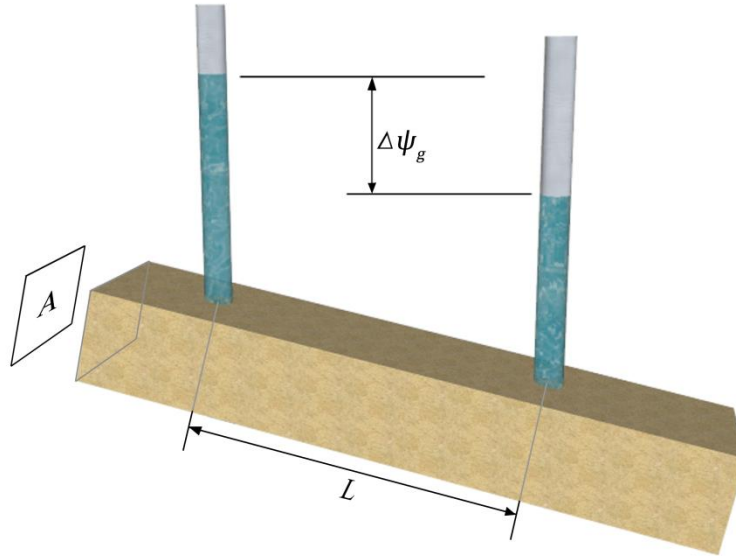


Figure III.2. Illustration of Darcy equation of the saturated groundwater flow (Author's design.).

For a given piece of soil with a length of L and a cross section of A , Darcy equation is written in the form below:

$$Q = K \cdot A \cdot i = -K \cdot A \frac{\Delta\psi_g}{L}, \quad \text{Eq. 12}$$

where, Q is groundwater flow rate through the cross section (m^3/s), K is hydraulic conductivity of the soil (m/s), A is cross section of the soil (m^2), i is hydraulic gradient (m/m), which is the ratio between the hydraulic drop $\Delta\psi_g$ and L the distance between two considered points in the soil. Considering only the velocity of the groundwater flow, the Darcy equation can be simplified:

$$q = K \cdot i = -K \frac{\Delta\psi_g}{L} \quad \text{Eq. 13}$$

where, q is velocity of groundwater flow (m/s).

Darcy equation is applicable to the groundwater flow that has a Reynolds number less than 10. The definition of the Reynolds number of groundwater flow is given as:

$$Re = \rho \cdot v \cdot \frac{d_{30}}{\mu}, \quad \text{Eq. 14}$$

where, Re is the Reynolds number (dimensionless), ρ is density of the fluid (kg/m^3), which is approximately 1000 kg/m^3 for water, d_{30} is the diameter corresponding to the 30% finer in the

particle-size distribution of the soil (m), μ is the dynamic viscosity of the fluid (kg/m/s or Pa·s), for water of 20 °C, this value is estimated to be 10^{-3} kg/m/s. Normally, most of the groundwater flow in the natural porous media satisfies this condition.

In FEFLOW software developed by DHI WASY, these two equations are generalized to adapt to the variable saturation and solved with finite element method [Diersch and Kolditz, 1998; Diersch, 2005]. The porosity and external mass supply are introduced into the continuity equation. In Darcy equation, the hydraulic conductivity becomes a function of the saturation. Therefore the Eq. 11 and Eq. 13 become:

$$S_s \cdot s(h) \frac{\partial h}{\partial t} + \varepsilon \frac{\partial s(h)}{\partial t} + \nabla \mathbf{q} = Q_{ms} \quad \text{Eq. 15}$$

$$\mathbf{q} = -K_r(s) \mathbf{K} (\nabla \psi_g + \chi \mathbf{e}), \quad \text{Eq. 16}$$

where, $\psi_g = h + z$ is the hydraulic head (m), z is the elevation of the reference datum (m), h is the pressure head of water from the reference datum (m), $s(h)$ is the medium saturation, which is a function of h , ($s = 1$ if medium is saturated), \mathbf{q} is the Darcy flux vector (m/s), Q_{ms} is the specific mass supply per unit time per unit depth (s^{-1}), $S_s = \varepsilon \gamma + (1 - \varepsilon) \Gamma$ is the specific storage due to fluid and medium compressibility (m^{-1}), ε is the porosity, which varies between 0.001 (granite) and 0.55 (soil) [Heath; 1983], γ is fluid compressibility (m^{-1}), Γ is the coefficient of skeleton compressibility (m^{-1}), $K_r(s)$ is the relative hydraulic conductivity, ($0 < K_r < 1$, $K_r = 1$ if saturated at $s = 1$), \mathbf{K} is the hydraulic conductivity tensor for the saturated medium, χ is the buoyancy coefficient including fluid density effects, \mathbf{e} the gravitational unit vector. Assuming $s=1$, only \mathbf{K} and S_s are the needed parameters in this equation.

For a saturated flow in the unconfined aquifer, the saturation term $s(h)$ becomes 1 and the specific storage S_s is extended to a dimensionless term storativity S , given by

$$S = S_s B + S_y, \quad \text{Eq. 17}$$

where, B is the thickness of the unconfined aquifer (m), S_y is specific yield (dimensionless), also called drain/fillable porosity or effective porosity, which is defined as the volume of water released from storage by an unconfined aquifer per unit surface area of aquifer per unit decline of the water table. It is a part of the total porosity ε [Bear, 1979],

$$\varepsilon = S_y + S_r, \quad \text{Eq. 18}$$

where S_r is specific retention (dimensionless), it refers to the amount of water retained by capillary forces during gravity drainage of an unconfined aquifer.

Considering the terms of vertical depth B and the drain/fillable porosity S_y , the full continuity equation for saturated flow in unconfined aquifer can be written as [Diersch, 2014]:

$$(S_s B + S_y) \cdot \frac{\partial h}{\partial t} + \nabla(Bq) = B\varepsilon Q + P, \quad \text{Eq. 19}$$

where P is the accretion of the mass added into the system per unit area per unit time (m/s).

III.2 Model domain, topography and geological layers

III.2.1 Model domain

Previous studies of the Var river [Guglielmi, 1993; Emily et al., 2010; Potot, 2011] have proved the existence of the exchange of water between the alluvial aquifer and the conglomerate aquifer. Because of the lack of quantified data, it is impossible to take the exchange of water as a boundary condition or an external source/sink term. The only reasonable way to consider this term in dynamic way is to enlarge the model domain, thus the exchange between the alluvial aquifer and conglomerate aquifer is calculated according to the hydraulic gradient and the hydraulic conductivities of the layers in the numerical model. The limit of the model has to be the delimitation of the hydrogeological catchment so as to simplify the boundary conditions of the numerical model.

Commonly, the concept of catchment refers to the hydrological catchment, or hydrological basin, which is an extent or an area of land where all surface water from rain, melting snow, or ice converges to a single point at a lower elevation, usually the exit of the basin, where the waters join another body of water, such as a river, lake, reservoir, estuary, wetland, sea, or ocean. The hydrological catchment is the basic unit to study the rainfall-runoff process. Once the exit of the catchment is given, the area of the catchment can be defined by the delimitation of the ridge lines based on the direction of the runoff. However, in the study of groundwater flow, the exchange between the surface water body and the groundwater needs to be taken into account. In this case, the hydrological catchment is no longer an appropriate unit because it does not consider the geological layers that contain the groundwater flow.

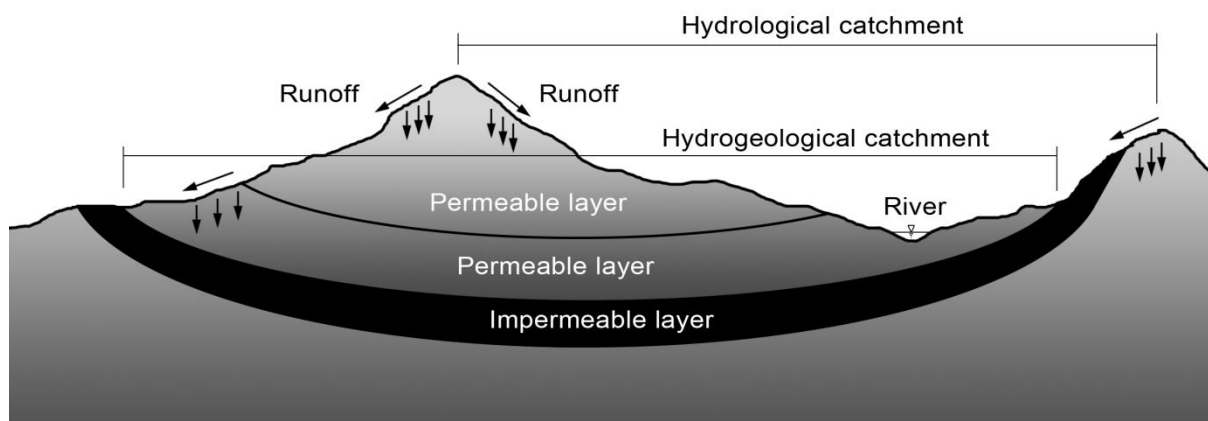


Figure III.3. Illustration of the definition of hydrological catchment and hydrogeological catchment (Author's design).

In this study, the hydrogeological catchment is used as the boundary of the numerical model. The hydrogeological catchment is delimited by the end of the impermeable layer or geological faults. The unconfined groundwater in the hydrogeological catchment is possible to have an exchange with the surface water body. Figure III.3 demonstrates the difference between the hydrological and hydrogeological catchment. For a surface hydrological study, the runoffs divided by the ridge line have two directions. The water flows out of the hydrological catchment will not join the river in the target catchment. For a hydrogeological study, even the infiltration happens in the adjacent hydrological catchment, as long as the permeable layers are still in the same hydrogeological catchment, the water always contributes to the same aquifer and may have an exchange with the river in the targeted hydrological catchment. The groundwater modeling in the lower Var river valley involves not only the alluvial aquifer, but also the conglomerate aquifer that has a strong exchange of water with it. Therefore, the model domain is delimited by the hydrogeological catchment in this area.

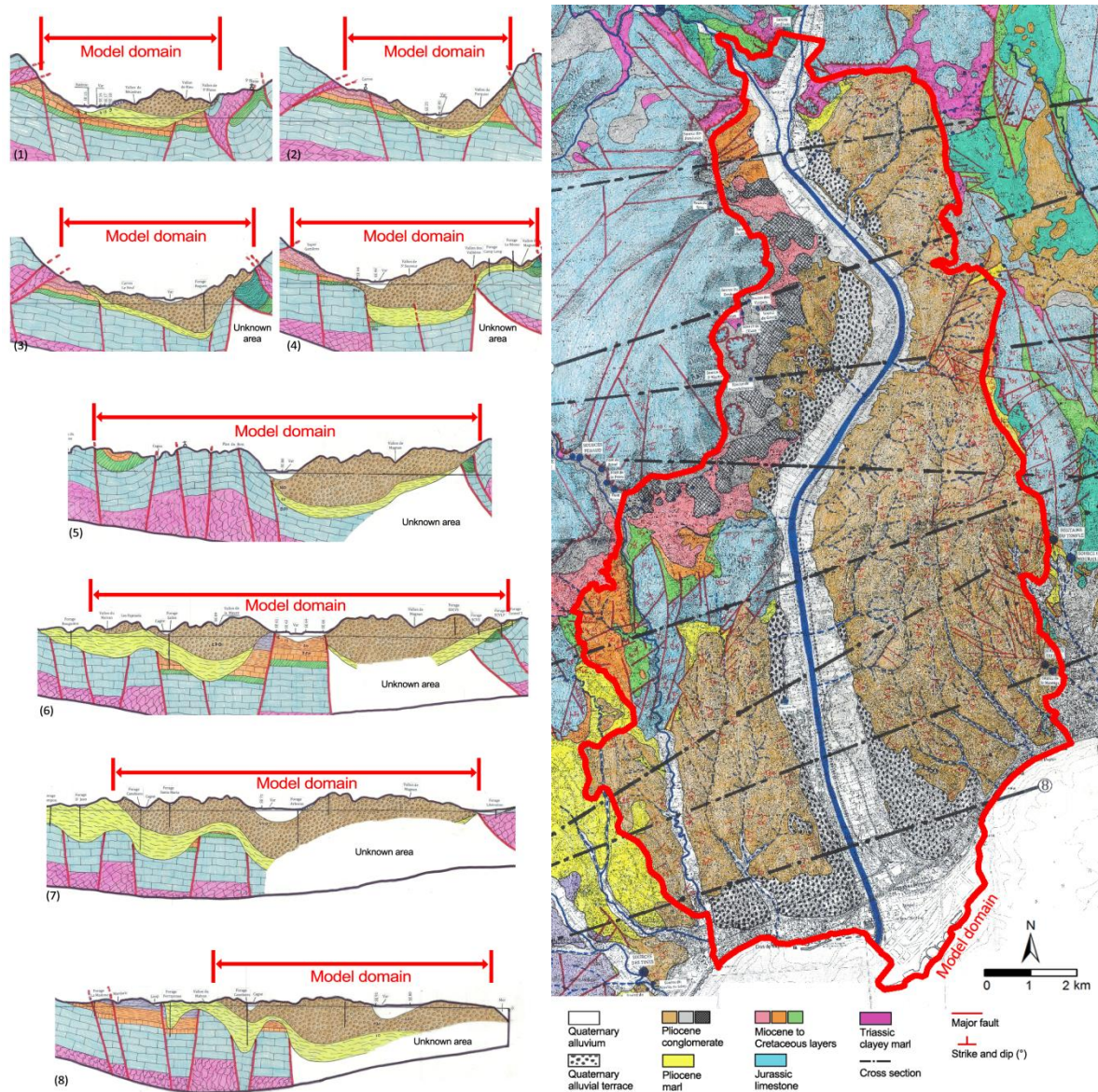


Figure III.4. Model domain delimitation: hydrogeological catchment boundary on the cross sections (left) and the model domain (right) (Source: Emily et al. [2010]).

The model domain is delimited by the border of the conglomerate identified on 8 cross sections and on the map made by Emily et al. [2010] (Figure III.4). The model covers an area of 146.4 km² and the depth of the model varies from 100 m to 600 m. The east and the west boundaries are the limit of the conglomerate layer (*e.g.* cross sections 6, 7 and 8) or the major faults that separate the direction of groundwater flow (*e.g.* cross sections 1, 2, 3 and 4). As a consequence, no boundary condition is assigned on the east and west boundary of the model. In the area near cross section 5, the alluvial aquifer has a direct contact with fractured limestone bedrock. The groundwater flow in fractured limestone is difficult to be modeled because of Darcy equation is no longer validated due to the high

flow velocity in the karst. Nevertheless, the limestone has to be modeled as porous medium, because the FEFLOW software does not have the function adapted for the groundwater flow in karst environment.

For the northern boundary, the model starts from weir No.16 (Figure I.2) on Var river, and the place where the Estéron river valley broadens before the river joins the Var river (Figure III.4). The groundwater level measured by the piezometer P37 (Figure I.22) is assigned as hydraulic head boundary condition in the Var river valley. In Estéron river valley, no measured data is available due to the lack of piezometer. Hence, a hypothesis is made to estimate the hydraulic head boundary condition. It is assumed that the depth of the groundwater table in the Estéron river valley equals to that in the Var river valley, because the hydraulic characteristics such as the riverbed slope and the type of sediment at these two places are similar. The hydraulic head data can be thus estimated by using the difference of the ground elevation between the two places and the measured hydraulic head at P37. At the southern boundary, the alluvial aquifer has been proved to be connected to the sea. Therefore the sea level is used as the downstream boundary condition of the unconfined aquifer.

Cross section 5 (Figure III.4) shows a local connection between the limestone and the alluvium, which makes the layer of limestone necessary in the model of unconfined aquifer. Vertically, the model has to contain the recent alluvium, alluvial terraces, conglomerate, marls, layers from Miocene to Cretaceous and limestone. The layers from Miocene to Cretaceous are mainly composed by the limestone and marls. They are grouped as one layer in the numerical model due to its small presented area and slight influence on the groundwater flow in the unconfined aquifer in alluvium and conglomerate.

III.2.2 Mesh generation

The unstructured mesh is used in order to describe the area with different grid sizes (see Appendix 5). Generally speaking, the shape of the triangles may noticeably impact the calculation time and the quality of the result [Bern and Eppstein, 1992]. A triangular mesh formed with elements with small interior angles consumes longer calculation time than a mesh formed with equilateral triangles. Furthermore, the large aspect ratios caused by the small interior angle in triangles may give large interpolation error. When generating the mesh of the model, a correction is carried out to ensure a

good mesh quality (Figure III.5). The principle of the improvement of the mesh quality emphasizes on the diminution of the elements with small interior angle and the removal of the unnecessary elements.

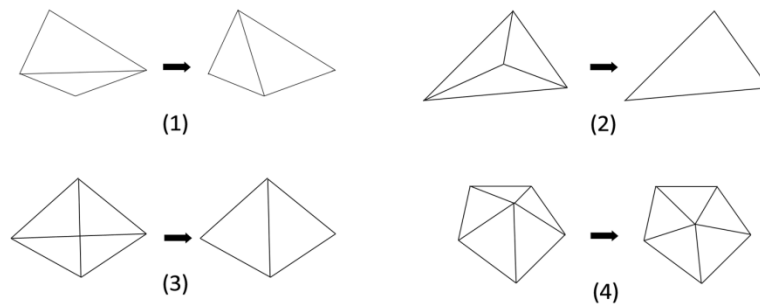


Figure III.5. Improvement of the mesh of the model, the cells on the right side are the improved ones.

The grid size in the model is related to two predominant factors: the importance of studied area and the computing cost. For an important area, more detailed model input (topography, water level in the river, *etc.*) and output (hydraulic head, Darcy flux, *etc.*) are needed, thus the grid size is small in order to conduct an accurate calculation and to obtain a high resolution result. For a less important area, the grid size can be bigger than for other area so as to reduce the total number of cells and, consequently, the simulation time would be saved to a certain extent. In general, three sizes of meshes are generated in this numerical model (Figure III.6) :

- The surface water bodies such as river and lake have a strong exchange of water with the aquifer. The surface water bodies are given as a boundary condition of the numerical model, which implies that a steep hydraulic gradient could exist in these areas. Besides, the riverbed is an important area where a detailed output is also required. A grid size of 25 m is therefore assigned to the riverbed of Var river and the lake of Le Broc.
- The water extraction leads to a high hydraulic gradient within a certain area. Pumping stations equipped with more than one borehole are very common in this 22 km valley. In the numerical model, a grid size of 25 m is used in order to perform an accurate calculation.
- The flood plain, which is also an important area of the study, is described by a grid size of 50 m. It is larger than the grid size of the riverbed because the hydraulic gradient is normally milder and usually no boundary conditions are assigned on the flood plain except for the boreholes.
- Coarse grids of 100 m are applied on the rest of the area of the model, where the major land use is forest. Yet the grid size cannot be too coarse because the complex geological layers need to be represented correctly.

With the 4 types of grid size and the criterion of the improvement of the mesh quality, the mesh of the numerical model is hereby generated and shown in Figure III.6. By using FEFLOW software, 6 layers (7 slices) are generated by a total number of 198954 nodes and 336138 2D cells. Through the interior angle analysis of the mesh of the model, it can be seen that the interior angles vary between 60° to 90° ; and few elements with an interior angle of more than 90° is observed, which means that the transition between the 3 grid sizes is smooth enough, especially on the flood plain.

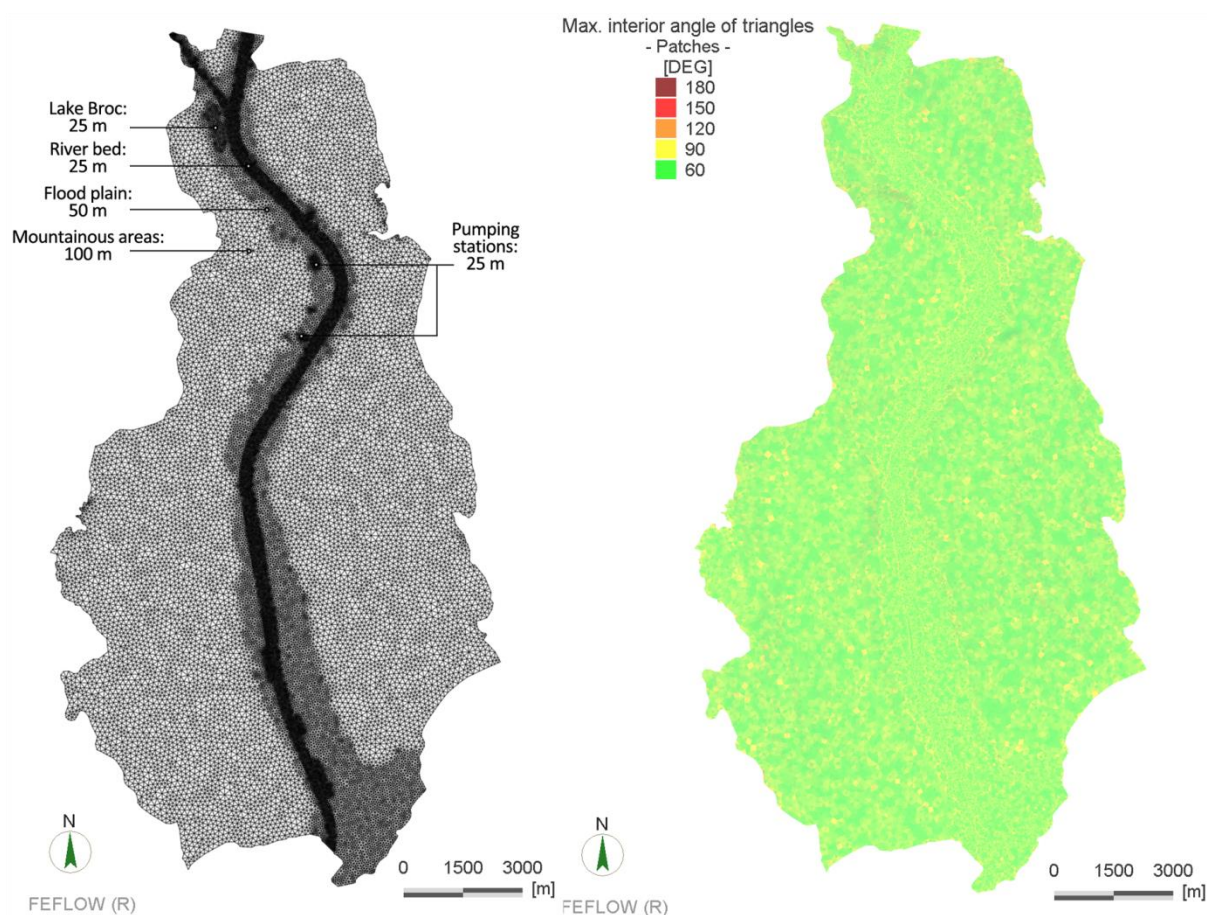


Figure III.6. Different grid sizes of the mesh of the model and the interior angle of the grids.

III.2.3 Geological layers

The representation of the discontinuity of the geological layers in numerical models is a challenge for model setup. In the modeled domain, discontinuity is observed in each layer (Figure III.4). For instance, the lost stratum of conglomerate and marls layers in cross sections 5 and 6 must be considered because they are able to influence the exchange of water between the alluvial aquifer and its bedrock.

The representation of the discontinuity due to the geological faults in the layers is explained with Figure III.7. The lost stratum is represented by a thin layer whose thickness can be ignored compared to the thickness of other major layers. Then the hydraulic conductivity of the adjacent major layer is assigned to this layer with small thickness.

The first example is a reverse fault with the partial continuity, it is the case of the cross section 2 (reverse fault in limestone layer) and the cross section 6 (partial continuity of limestone and marls from Miocene to Cretaceous). On the left side of the fault, three layers, noted as K_1 , K_2 and K_3 overlays in the order in which they are formed. On the right side of the fault, the layers rise to the surface and the most recent layer K_1 is eroded. It forms a discontinuity of the layer K_1 and a partial continuity in the layers K_2 and K_3 . In the numerical model, the bottom slice of K_1 is raised on the right side of the fault. However, since this slice does not exist in the reality, the thickness of the first layer has to be a small value in order to approach to the real case. Moreover, the hydraulic conductivity of this thin layer should be the same as K_2 . The bottom slice of the K_2 layer is also raised up at the right side of the fault.

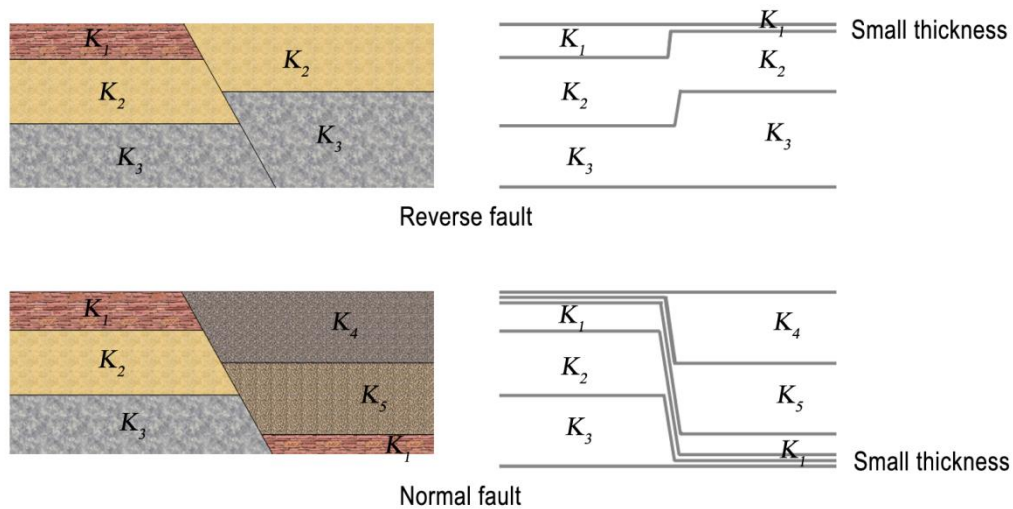


Figure III.7. Representation of discontinuity of geological layers in reality (on the left) and in the numerical model (on the right).

The second example demonstrates a case of the discontinuity of the layers with lost stratum of K_4 and K_5 on the left side of the normal fault. For the eroded part of K_4 and K_5 on the left side, layers with small thickness are used and hydraulic conductivity of the K_1 is assigned to the two layers. In the same way, the bottom slices of K_2 and K_3 on the right side of the fault are also set beneath the layer K_1 .

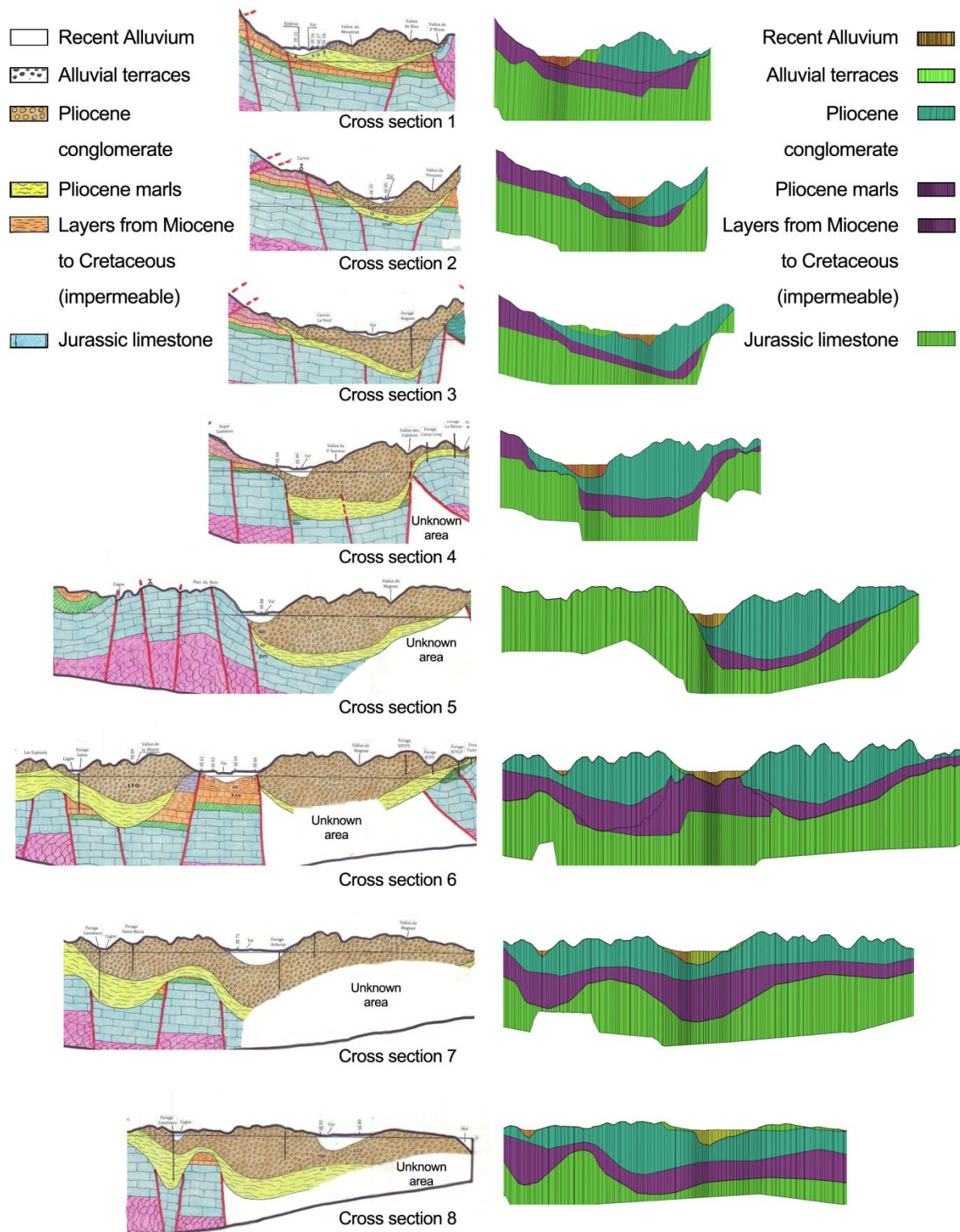


Figure III.8. Creation of the geological layer information on each cross section (Source: Emily et al., [2010] and Guglielmi [1993]).

There are only two sources of data that can be used to build the geological layers in the numerical model. The geological map provided by Emily et al. [2010] (Figure III.4) has a holistic view of the geological layers in the lower valley and its extended areas. Nevertheless, due to the limitation of the number of geological drilling tests, this hand-made map is not accurate enough to set up a numerical model, especially for the layer of alluvium, where the unconfined aquifer exists. Therefore the map drew by Guglielmi [1993] (Appendix 2) is consulted to ensure a more accurate description of the layer of alluvium. This map focuses on the geological layers under the flood plain, especially the geophysical characteristics of the alluvium layer. A total number of 117 points along the valley have been chosen to carry out the electric survey in the alluvium. The geological layers in the numerical model, therefore, are built by a combination of the two maps.

The top slice is built with the DEM data of 5 m resolution measured in 2009, provided by IGN. The other slices are digitalized by using geographical software ArcGIS. Figure III.8 shows a comparison between the original map and the digitalized cross sections. In general, the geological layers are correctly represented on each cross section. Then the 8 cross sections are interpolated with FEFLOW software by using IDW (inverse distance weighted) method to generate the 3D geological layers (Figure III.9).

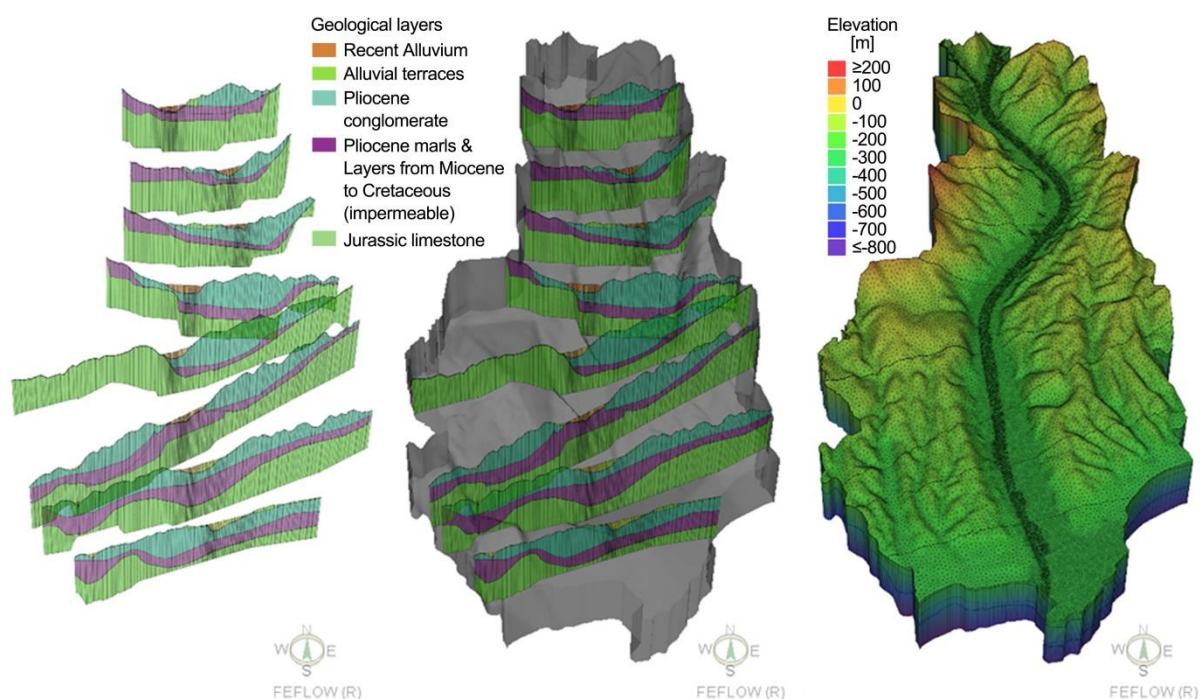


Figure III.9. Interpolation of the cross sections so as to set up the 3D model that consists of 6 layers.

Theoretically, 8 cross sections created based on two maps along a 22 km is not an input data that is accurate enough for a numerical model. Moreover, the cross sections are also digitalized from two hand-made maps with low resolution. Many hypotheses and personal understandings have been added in order to create the map based on limited geological drilling test results. It means that the data that has been used to set up the geological layers in this model is also a source of uncertainty.

III.2.4 Hydraulic parameters

III.2.4.1 Specific storage S_s and specific yield S_y

According to the governing equations of FEFLOW (Eq. 16 and Eq. 19), the parameters that may have an influence on the groundwater flow are the hydraulic conductivity K , the specific storage S_s and specific yield S_y . For an unconfined aquifer, S_s is usually too small to have a significant impact compared to S_y , because the compressibility of the water and the skeleton sediment of the aquifer are too small. The compressibility Y of certain material measured by Domenico and Mifflin [1965] is listed in Table III.1. The compressibility of water at 25 °C equals to $4.6 \times 10^{-10} \text{ Pa}^{-1}$, given by Fine Rana and Millero [1973]. Therefore the specific storage S_s of materials of unconfined aquifer such as sand and gravel in the natural environment has an order of magnitude of 1×10^{-3} to $5 \times 10^{-5} \text{ m}^{-1}$. Table III.2 lists the range of S_s of certain materials measured by Domenico and Mifflin [1965].

Table III.1. Representative values of vertical drained compressibility of various geologic materials (Source: Domenico and Mifflin [1965]).

Material	Compressibility Y (Pa^{-1})
Plastic clay	$2 \times 10^{-6} - 2.6 \times 10^{-7}$
Stiff clay	$2.6 \times 10^{-7} - 1.3 \times 10^{-7}$
Medium-hard clay	$1.3 \times 10^{-7} - 6.9 \times 10^{-8}$
Loose sand	$1 \times 10^{-7} - 5.2 \times 10^{-8}$
Dense sand	$2 \times 10^{-8} - 1.3 \times 10^{-8}$
Dense, sandy gravel	$1 \times 10^{-8} - 5.2 \times 10^{-9}$
Rock, fissured	$6.9 \times 10^{-10} - 3.3 \times 10^{-10}$
Rock, sound	$< 3.3 \times 10^{-10}$

Table III.2. Representative values of specific storage S_s of various geologic materials (Source: Domenico and Mifflin [1965]).

Material	Specific storage S_s (m^{-1})
Plastic clay	$2.6 \times 10^{-3} - 2 \times 10^{-2}$
Stiff clay	$1.3 \times 10^{-3} - 2.5 \times 10^{-3}$
Medium-hard clay	$9.2 \times 10^{-4} - 1.3 \times 10^{-3}$
Loose sand	$4.9 \times 10^{-4} - 1 \times 10^{-3}$
Dense sand	$1.3 \times 10^{-4} - 2 \times 10^{-4}$
Dense, sandy gravel	$4.9 \times 10^{-5} - 1 \times 10^{-4}$
Rock, fissured	$3.3 \times 10^{-6} - 6.9 \times 10^{-5}$
Rock, sound	$< 3.3 \times 10^{-6}$

Heath [1983] reports the values (in percent by volume) of porosity, specific yield and specific retention of various materials in Table III.3. Apparently, in the lower Var river valley, the alluvium that consists of sand and gravels has a small specific storage value with the order of magnitude between 10^{-4} and $10^{-5} m^{-1}$. Compared to the specific yield S_y , the specific storage S_s is too small to have a big influence on the storativity $S = S_s B + S_y$, where the thickness B is usually between 10 m to 100 m. But for some areas where the alluvium has a more complicated composition such as mixed sediment of clay, silt, sand and gravel, the value of $S_s B$ is in the same order of magnitude as the value of S_y .

Table III.3. Representative values of porosity ε , specific yield S_y and specific retention S_r of various geologic materials (Source: Heath [1983]).

Material	Porosity ε	Specific yield S_y	Specific retention S_r
Clay	0.5	0.02	0.48
Sand	0.25	0.22	0.3
Gravel	0.2	0.19	0.01
Limestone	0.2	0.18	0.02
Sandstone (unconsolidated)	0.11	0.06	0.05
Basalt (young)	0.11	0.08	0.03
Granite	0.001	0.0009	0.0001

The representative values given in Table III.3 summarize the range of the possible values of S_s and S_y for the general case. For the case study of the lower Var river valley, however, more precise values are needed. Potot [2011] has estimated that the porosity in the unconfined aquifer of the lower Var river

valley varies between 0.1 to 0.3. The field measurement in the pumping station of Carros (see Figure I.20) reveals that the porosity of the aquifer is between 0.04 and 0.12. Garnier et al. [1981] have measured the porosity of the soil in the pumping station of Pugets (see Figure I.20), which is 0.05 in this area. Knowing that for the main composition of alluvium in the lower valley is sand and gravel, the porosity ϵ equals approximately the specific yield S_y . The reasonable range of the value of S_y used to build the numerical model is from 0.04 to 0.3. A calibration is needed to elaborate the spatial distribution of S_y in the layer of alluvium. Regarding the alluvial terraces, the S_y value and its spatial distribution are assumed to be the same as the alluvium because of their similar geophysical characteristics. The S_y of the bedrock layers is set to be 0.1. For the value of S_s of the bedrock layers, an uniform value of 10^{-4} m^{-1} is used in the entire domain due to its negligible influence compare to S_y .

III.2.4.2 Hydraulic conductivity K

The hydraulic conductivity of the alluvium is an important variable to describe the hydrogeological feature of the aquifer. Many studies and field measurements have been carried out in the lower Var river valley [Emily et al. 2010; Mangan, 2000, 2005, 2011, 2012; Garnier et al., 1981; Garnier, 1987; Gulgielmi, 1993, Gulgielmi and Reynaud, 1997; Kassem, 1997]. In the numerical model, 54 measured values have been interpolated by using the inverse distance weighted method [Shepard, 1968] to describe the spatial distribution of the hydraulic conductivity in the alluvium layer. As for the layer of conglomerate, only one measurement has been made in the east area of the model, where the conglomerate reaches its maximum thickness. The measured hydraulic conductivity of conglomerates is $K = 2.6 \times 10^{-6} \text{ m/s}$ [Emily et al., 2010]. Empirical values from previous study are applied [Domenico and Schwartz, 1990; Heath, 1983] for the other layers. The values are shown in Table III.4.

Table III.4. Hydraulic conductivity values used in the numerical model.

Geological layers	Hydraulic conductivity K (m/s)
Quaternary Alluvium	Interpolated values of measured data
Quaternary Alluvial terraces	1×10^{-4}
Pliocene conglomerate	2.6×10^{-6}
Pliocene marl	1×10^{-9}
Layers from Miocene to Cretaceous	1×10^{-9}
Jurassic limestone	1×10^{-5}

Through the field survey, it has been observed that the sediment in the alluvium is vertically stratified (Figure III.10). This property has also been proved by Guglielmi [1993] and Emily et al. [2010]. The numerical model has to be able to represent this phenomenon in order to be realistic. In Darcy's equation (Eq. 16), the hydraulic conductivity is a tensor with all his components:

$$\mathbf{K} = \begin{bmatrix} K_{xx} & K_{xy} & K_{xz} \\ K_{yx} & K_{yy} & K_{yz} \\ K_{zx} & K_{zy} & K_{zz} \end{bmatrix}. \quad \text{Eq. 20}$$

When the local coordinate system is aligned with the global coordinate system, which is the very case in the numerical model set up by FEFLOW in this study, it becomes:

$$\mathbf{K} = \begin{bmatrix} K_{xx} & 0 & 0 \\ 0 & K_{yy} & 0 \\ 0 & 0 & K_{zz} \end{bmatrix}. \quad \text{Eq. 21}$$

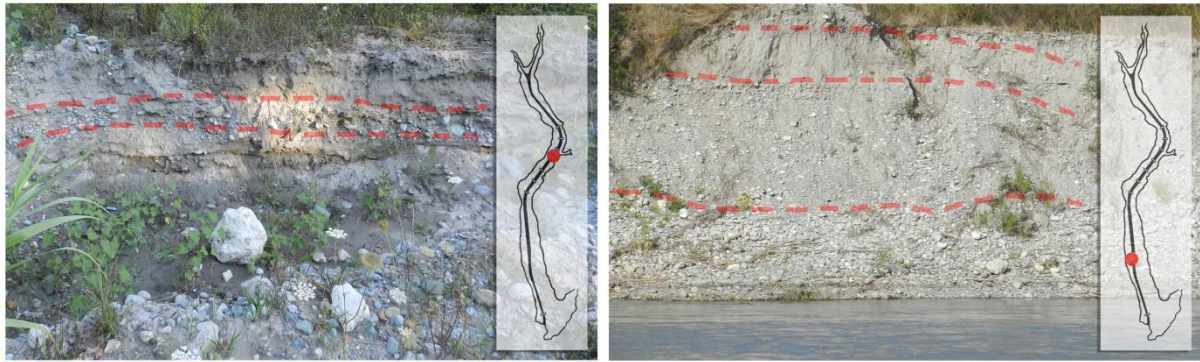


Figure III.10. Stratified sediments of the porous media in the alluvium of lower Var river valley (Photo taken by author on July 2014)

To reproduce the anisotropy of the alluvium, an anisotropy ratio is applied. Todd [1980] has reported this ratio ranging between 0.1 and 0.5 for alluvium and possibly as low as 0.01 when clay layers are present. From this point of view, the measured data of the alluvium is only assigned to the K_{xx} and the K_{yy} , while the z component K_{zz} is set to be less than for the other two directions by one order of magnitude:

$$K_{zz} = 0.1 K_{xx} = 0.1 K_{yy}. \quad \text{Eq. 22}$$

The other layers are treated as an isotropic porous media. Even though this hypothesis is less realistic for karst in the limestone layer, the unconfined groundwater simulation will not be influenced, because the impact of karst water on unconfined aquifer can be neglected due to the small contact zone between them (Figure III.8).

Figure III.11 illustrates the spatial distribution of the hydraulic conductivity value K_{xx} , K_{yy} and K_{zz} in the alluvium layer and in other bedrock layers. The location of points of measurement (Figure III.11) reveals that more studies have been carried out in the downstream area, especially the area near to the river mouth. In the alluvium, the hydraulic conductivity varies from 0.04 m/s to 0.00001 m/s. The value is higher in the upstream part of the valley than in the downstream part.

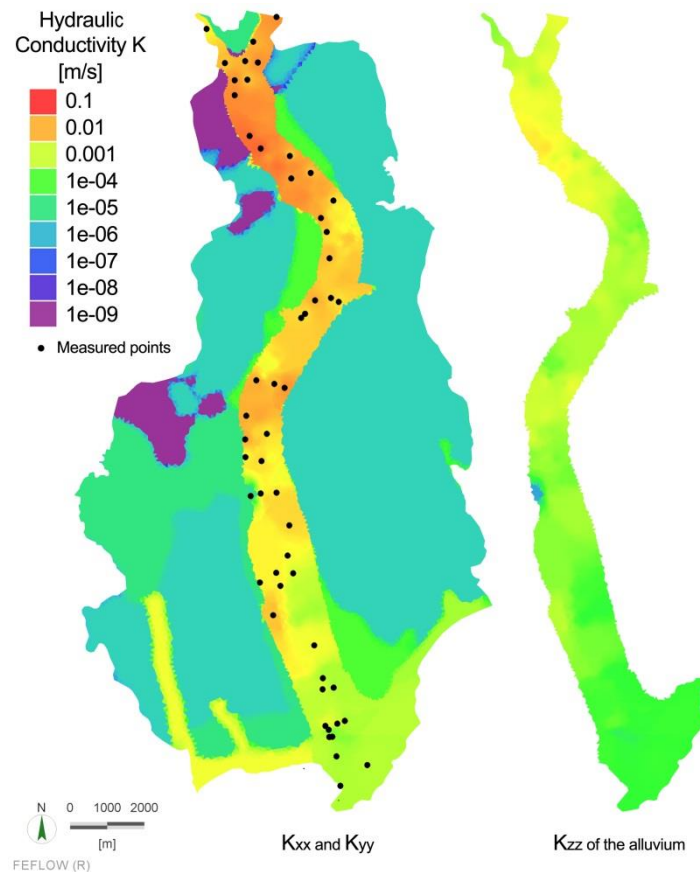


Figure III.11. Representation of hydraulic conductivity anisotropy in the numerical model.

III.3 Direct water recharge/loss

III.3.1 Estimation of PET and AET

Different formulas have been given depending on data availability [Laborde, 2010; Thornthwaite and Mather, 1957; Black, 2007]. For most meteorological stations, temperature, precipitation and solar insolation hours are the data which are currently provided. A method to estimate the AET with these data can be formulated from the Thornthwaite water balance algorithm (Figure III.12).

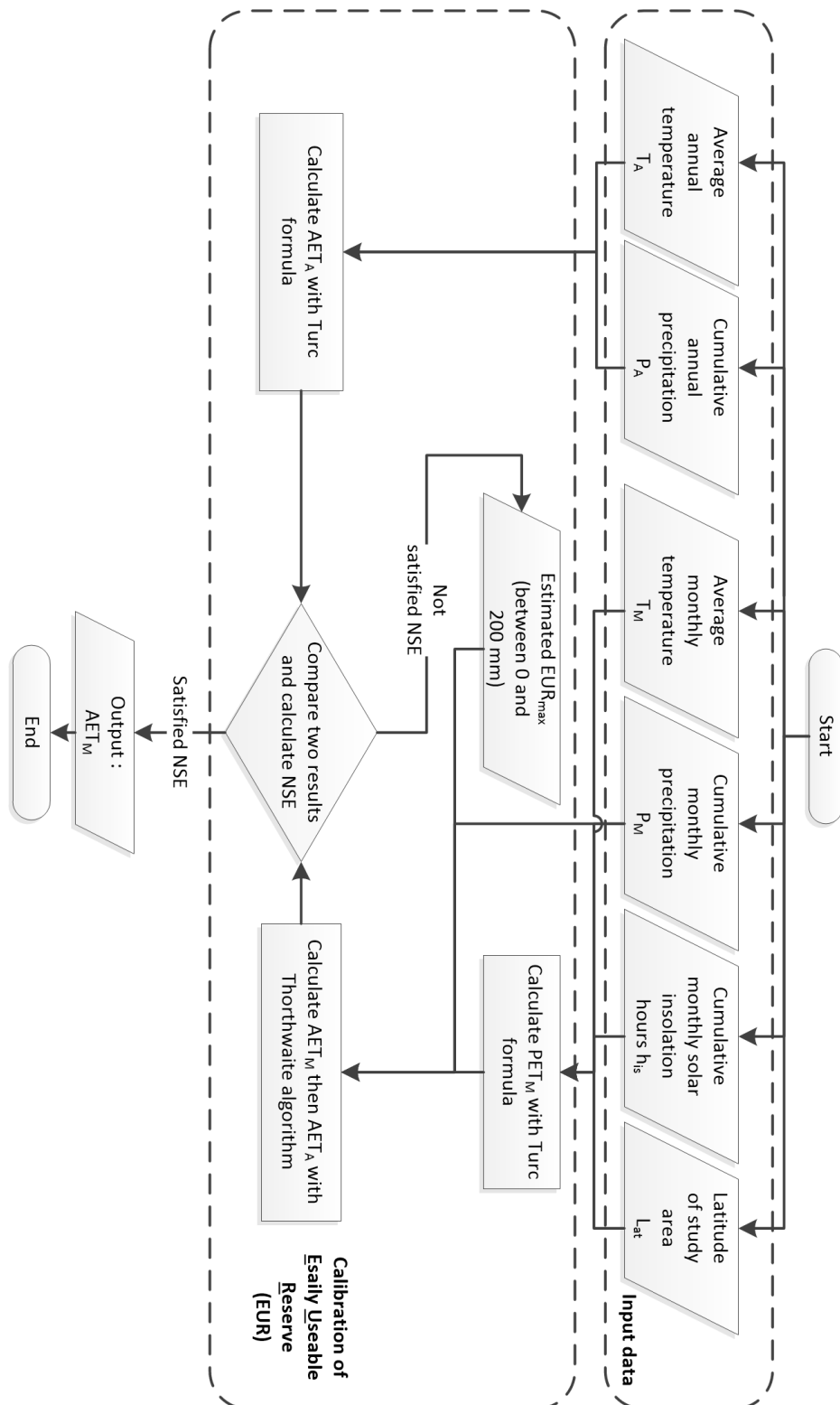


Figure III.12. Data flow diagram for AET calculation. The variables with subscripts “M” denote the monthly value and “A” means the annual value.

To start, monthly *PET* (potential evapotranspiration) is calculated by Turc formula (Eq. 23) with monthly data of temperature, precipitation, solar insolation hours and latitude of the studied area. Then the monthly *AET* can be calculated by Thornthwaite water balance algorithm, where the initial empirical parameter *EUR* (Easily Useable Reserve of water in the soil) is set to be 0. Since this parameter is unknown, it has to be calibrated by trial and error method. The calibration refers to the comparison between the annual *AET* (the sum of monthly *AET*) calculated by Thornthwaite algorithm (Eq. 26 and Eq. 27) and the one that is calculated by Turc formula (Eq. 28 and Eq. 29). Finally, the monthly *AET* calculated with the calibrated *EUR* is given as an output.

This calibration must take the annual *AET* calculated by Turc formula as a reference value. Even though it is merely an estimated value of the order of magnitude of annual *AET* with empirical equation using temperature and precipitation, this method has been proved to be more adaptable to the Mediterranean climate in southern France [Delaroziere-Bouillin, 1971]. Therefore this calibration ensures the order of magnitude of annual *AET* calculated by the Thornthwaite algorithm.

III.3.1.1 Monthly *PET* calculation

The Turc formula to calculate the monthly *PET* is given below:

$$PET_M = 0.4 \frac{T_M}{T_M + 15} (I_g + 50) k_h, \quad \text{Eq. 23}$$

where, PET_M is the monthly potential evapotranspiration (mm), T_M is the monthly average air temperature (°C), k_h is a coefficient that equals to 1 if the relative humidity h_r is higher than 50 % (which is generally the case in Mediterranean climate), otherwise $k_h = 1 + (50 - h_r)/70$, I_g is monthly global radiation received by the soil (cal/cm²/day), if the I_g is not measured, it can be estimated with solar insolation hours h_{is} is:

$$I_g = I_g A \left(0.18 + 0.62 \frac{h_{is}}{H_j} \right), \quad \text{Eq. 24}$$

where, $I_g A$ is the theoretical global radiation (cal/cm²/day), h_{is} is the measured duration of daytime in the month (hour), H_j is the theoretical duration of daytime in the month (hour).

The following formulas are given to calculate the $I_g A$ and H_j of each month in one year, by using the latitude of the study area L_{at} and the number of the month i ($i=1$ for January and 12 for December):

$$\begin{cases} H_j = 362.7 + 0.201 L_{at} + (4.085 L_{at} - 80.99) \cos(30.01 \cdot i - 188.9) \\ I_g A = 1035 - 9.078 L_{at} + (7.050 L_{at} + 49.90) \cos(29.92 \cdot i - 182.5) \end{cases} \quad \text{Eq. 25}$$

III.3.1.2 Monthly *AET* calculation

The Thornthwaite water balance algorithm is developed based on the basis of water balance (Eq. 4), it introduces the conception of Easily Useable Reserve of water in the soil (EUR), which represents the water stored between the aquifer and the ground surface that can be easily used for evapotranspiration. The capacity of *EUR* varies from 0 to 200 mm and depends on the soil type of the study area [Laborde, 2010].

One hypothesis is made to apply this formula: the satisfaction of the demand from *PET* is prior to the recharge of the EUR, which also must be refilled before forming the runoff. Therefore the Thornthwaite water balance algorithm on monthly scale is established as followed. The monthly *AET* is evaluated following the expression:

$$AET_M^i = \begin{cases} PET_M^i, & \text{if } P_M^i > PET_M^i; \\ P_M^i + \min(EUR^{i-1}, PET_M^i - P_M^i), & \text{else} \end{cases} \quad \text{Eq. 26}$$

then the *EUR*^{*i*} is calculated as followed:

$$EUR_M^i = \begin{cases} \min(EUR_{max}, EUR_M^{i-1} + P_M^i - PET_M^i), & \text{if } P_M^i > PET_M^i; \\ \min(0, EUR_M^{i-1} + P_M^i - PET_M^i), & \text{else} \end{cases} \quad \text{Eq. 27}$$

III.3.1.3 Annual *AET* calculation

The annual actual evapotranspiration can be estimated by Turc formula:

$$AET_A = \frac{P_A}{\sqrt{0.9 + \frac{P_A^2}{L^2}}}, \quad \text{Eq. 28}$$

with

$$L = 300 + 25T_A + 0.05T_A^3, \quad \text{Eq. 29}$$

where, *AET*_{*A*} is the annual actual evapotranspiration (mm), *P*_{*A*} is the annual cumulative precipitation (mm), *T*_{*A*} is the annual average temperature (°C).

III.3.1.4 Calibration of *EUR*_{max}

The *EUR* is calibrated with the data measured from 2000 to 2013 at Nice airport meteorological station. A series calculation of *AET*_{*M*} and their sum of the year *AET*_{*A*} have been performed by using different values of *EUR*_{max}. After comparing the *AET*_{*A*} calculated by the Thornthwaite algorithm (Eq. 26 and Eq. 27) and by the Turc formula (Eq. 28 and Eq. 29), the best *EUR*_{max} can be found. The tested *EUR*_{max} value varies from 0 to 200 mm.

As explained in Figure III.12, the criterion of the calibration is the Nash-Sutcliffe Efficiency (NSE) coefficient. It is used to evaluate the quality of the predictive time-related result of a model [Nash and Sutcliffe., 1970]. It is defined as:

$$NSE = 1 - \frac{\sum_{t=1}^{n_T} (X_o^t - X_m^t)^2}{\sum_{t=1}^{n_T} (X_o^t - \bar{X}_o)^2}, \quad \text{Eq. 30}$$

where, \bar{X}_o is the mean of observed values, X_m^t is the result value predicted by the model at t moment, X_o^t is the observed value at t moment and n_T the total number of the time steps of the numerical simulation.

NSE can be only used to evaluate the time dependent model and it is very sensitive to the peak values in a data series. NSE ranges from $-\infty$ to 1. A NSE that equals to 1 corresponds to a perfect match of model results to the observed data. A NSE that equals to 0 indicates that the model predictions are as accurate as the mean of the observed data, whereas a negative NSE implies that the observed mean is a better predictor than the model. Essentially, the closer the model efficiency is to 1, the more accurate the model is.

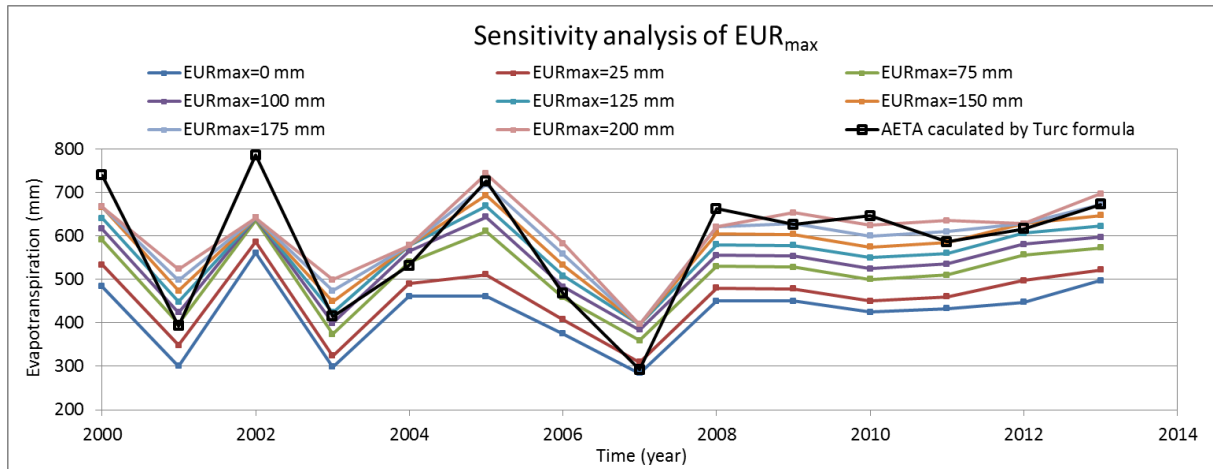


Figure III.13. Sensitivity analysis of the EUR_{max} .

Through the result of the sensitivity analysis (Figure III.13), it can be concluded that the AET_A calculated by two methods have the same tendency. The variance of the AET_A due to the EUR_{max} is around 200 mm. In the year 2002, the AET_A estimated by the Turc formula is much higher than that calculated by the Thornthwaite algorithm, because the Turc formula does not take the reserve of water in the soil into account when calculating the AET . Therefore it may overestimate the value because in reality the AET during the summer is low due to the lack of precipitation. Since the Turc formula is

established on the annual scale, it cannot consider particularly the effect of a dry season or a wet season.

The EUR_{max} that suits the best simulated result is found to be 153 mm in the lower Var river valley, which corresponds to a NSE coefficient 0.773. Figure III.14 shows the comparison of the AET_A calculated by the two methods after calibration. The values calculated by the Thornthwaite algorithm always have a low fluctuation. This is a buffering effect when the EUR is considered in the calculation and the time step becomes one month instead of a whole year. After the year of 2008, the actual evapotranspiration calculated by the two methods are very close.

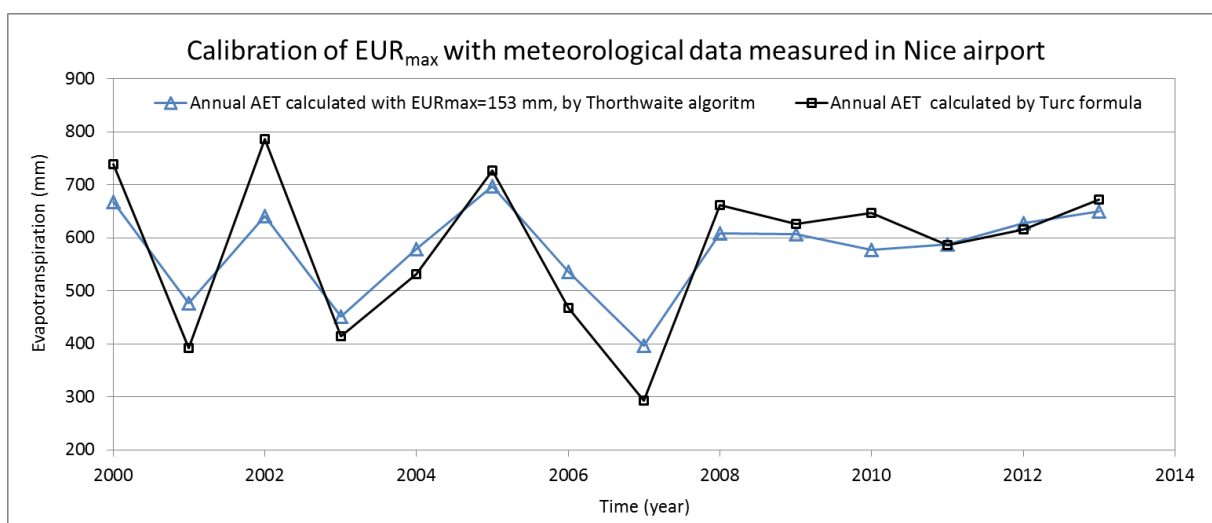


Figure III.14. Results of the calibrated EUR_{max} and comparison of the AET_A calculated by the two methods.

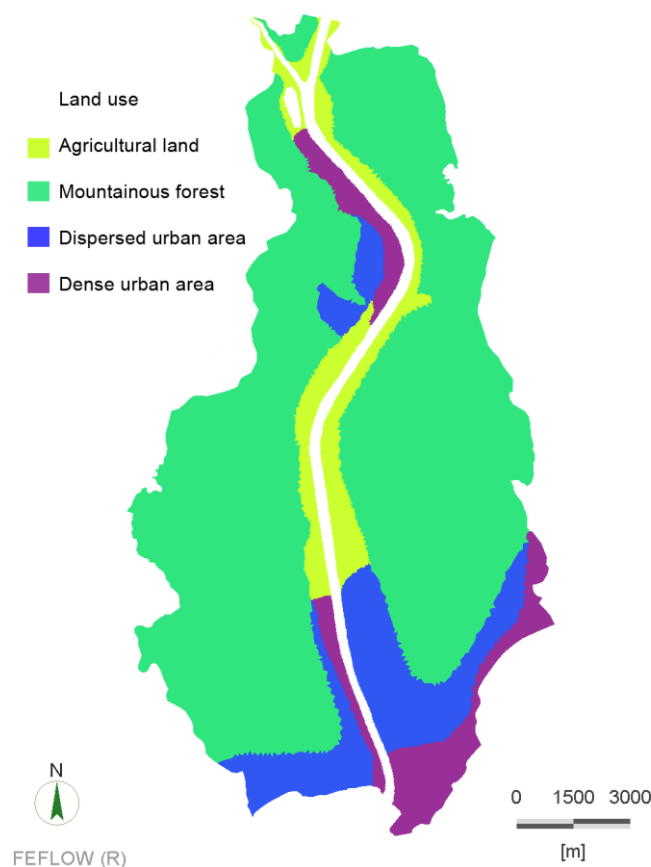
III.3.2 Direct water recharge/loss

The infiltration from precipitation is calculated with a simple assumption that the precipitation has only two destinations: forming runoff or contributing to the infiltration. In hydrology studies, a common way to estimate the runoff is assuming that the runoff is directly proportional to the total precipitation. The ratio between the runoff and the precipitation is defined as the runoff coefficient c [Savenije, 1996], which depends on the land use of the studied area. Despite that this method does not consider the change of the amount of infiltrated water caused by the variation of the soil saturation during continuous rainfall events, this method, however, is still widely used thanks to its simplicity and reliability.

Table III.5. Land use description and estimated runoff coefficient in the lower Var river valley.

Land use	Runoff coefficient c
Industrial & dense urban area	0.9
Dispersed urban area	0.8
Mountainous forest	0.7
Agricultural land	0.6

Table III.5 shows the 4 common land use types in the lower Var river valley and the corresponding runoff coefficients. Figure III.15 is the land use map of the studied area. On the map, the riverbed and Le Broc lake is not included because there are boundary conditions assigned on these areas. Compared to the flux generated by the river-aquifer exchanges, the exchange flux caused by the direct water recharge/loss is too small to be considered.

**Figure III.15. Land use map in the lower Var river valley.**

The direct water recharge/loss describes the sum of the water which enters in and goes out from the model. Assuming that all the infiltrated water goes to the saturated flow, and the AET is also from the saturated flow, the direct water recharge flux q_r can be given by the following formula:

$$q_r = (1 - c) \cdot P_D - AET_D , \quad \text{Eq. 31}$$

where, q_r is the flux of direct water recharge/loss (mm/day), c is the runoff coefficient (dimensionless), P_D is the daily cumulative precipitation measured by the meteorological stations (mm/day), AET_D is the daily lost due to the actual evapotranspiration (mm/day). An equitable distribution of the monthly actual evapotranspiration AET_M is used to obtain its value. The sign of q_r determines the recharge or the loss of the water in the model.

III.4 River-aquifer exchanges

The river-aquifer exchanges are assigned as a transfer boundary condition of the numerical model [Diersch, 2014]. Eq. 2 and Eq. 3 show the application of the transfer boundary to quantify the river-aquifer exchange flux. In this model, the input data ψ_s , which represents the water level in the river, is the output of a river hydraulic model built with MIKE11 software [Havnø 1995]. This model solves the 1D Saint-Venant equation with finite difference method. Figure III.16 shows an illustration of the 1D shallow water equation.

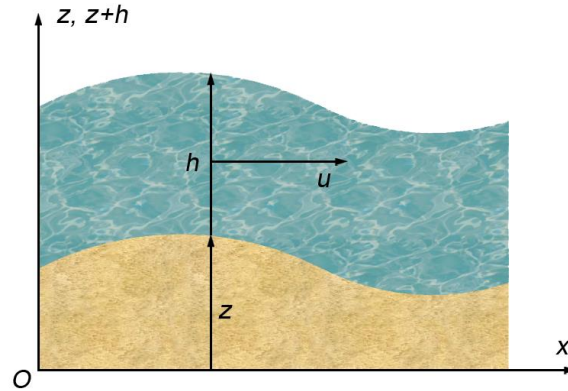


Figure III.16. Illustration of 1D shallow water equation.

The simplified equation in the case of no Coriolis or viscous forces is written as below [DHI, 2009; Delestre, 2010 ; Delestre et al. 2014]:

$$\left\{ \begin{array}{l} \frac{\partial A}{\partial t} + \frac{\partial Q}{\partial x} = P - I \\ \frac{\partial Q}{\partial t} + \frac{\partial (Q^2/A)}{\partial x} + gA \frac{\partial h}{\partial x} = gA(S_0 - S_f) \end{array} \right. , \quad \text{Eq. 32}$$

with the slope term

$$S_0 = -\frac{\partial z(x)}{\partial x}, \quad \text{Eq. 33}$$

and the Manning's friction term due to the roughness of the riverbed:

$$S_f = n^2 \frac{Q|Q|}{A^2 R^{\frac{4}{3}}}, \quad \text{Eq. 34}$$

where, g is the gravitational constant (m/s^2). A is the wetted section (m^2). Q is the orthogonal projection of flow rate aligned with x -axis (m) through the section A , therefore $Q = Au$, with u the velocity of the flow (m/s). h is the water depth (m). $P(t, x)$ is the precipitation rate per unit width (m^2/s). $I(t, x)$ is the infiltration rate of water per unit width (m^2/s). S_f is the friction term depending on the friction law (dimensionless). S_0 is the term of slope on x -axis (dimensionless). $z(x)$ is the topography (m). n is the Manning friction coefficient ($\text{s/m}^{1/3}$). The values of Manning roughness coefficient are tabulated depending on the kind of ground considered [Chow, 1959].

Several assumptions are made to apply the equation. First of all, the horizontal length scale is much greater than the vertical length scale, also called “shallow water assumption”. For this reason, this system of partial differential equations is called shallow water system. Secondly, the direction of the water velocity is always perpendicular to the cross section, and the velocity is uniform on the cross section. The vertical velocity is assumed to be very small to be neglected. The first equation of this system (Eq. 32) is the conservation of the mass, and the second equation is the conservation of momentum.

A river hydraulic model of the lower Var river has been set up with MIKE11 software. It starts from the downstream side of weir No.16 (Figure I.2) which is defined as the beginning of the lower Var river, and ends at the river mouth where the Var river flows into the Mediterranean sea. The bathymetry is obtained from the DEM data measured in 2009, which is the same topographical data used to set up the groundwater flow. The distance between two cross sections is around 500 m and the maximum grid size Δx is 100 m. The cross section interval is reduced to 50 m for a better description of the topography where the slope has a marked change.

The upstream boundary condition is the daily discharge measured at the La Manda bridge station (Figure I.15). For this reason, the branch of the Esteron is not included in this model. The downstream

boundary condition is the mean sea level which is approximately 0.3 m. The model has been validated in a previous study by using the flood event of 1994 [Ormella Mancha et al., 2013].

The water level simulated by this model is assigned in the groundwater flow model as a transfer boundary. However, since MIKE11 is not coupled with FEFLOW, the river-aquifer exchanges are not calculated in a fully dynamic mode. In this model, 30 points along the river are chosen to be the controls points, where the time series result calculated by MIKE11 is exported and assigned in FEFLOW (Figure III.17). Between the adjacent control points, the transfer boundaries are interpolated with IDW method. The control points are not equally distributed along the 22 km river. For the river section where the slope is mild, less control points are set in order to reduce the pre-processing time. For the section where the weirs are (were) built, more control points are set due to the rapid change of the channel slope. In this river section, control points are set on the upstream side and downstream side of the weir to represent the sharp drop of the surface elevation of the water. In the downstream area, more control points are used because there are three important pumping stations, therefore the boundary condition needs to be more precise.

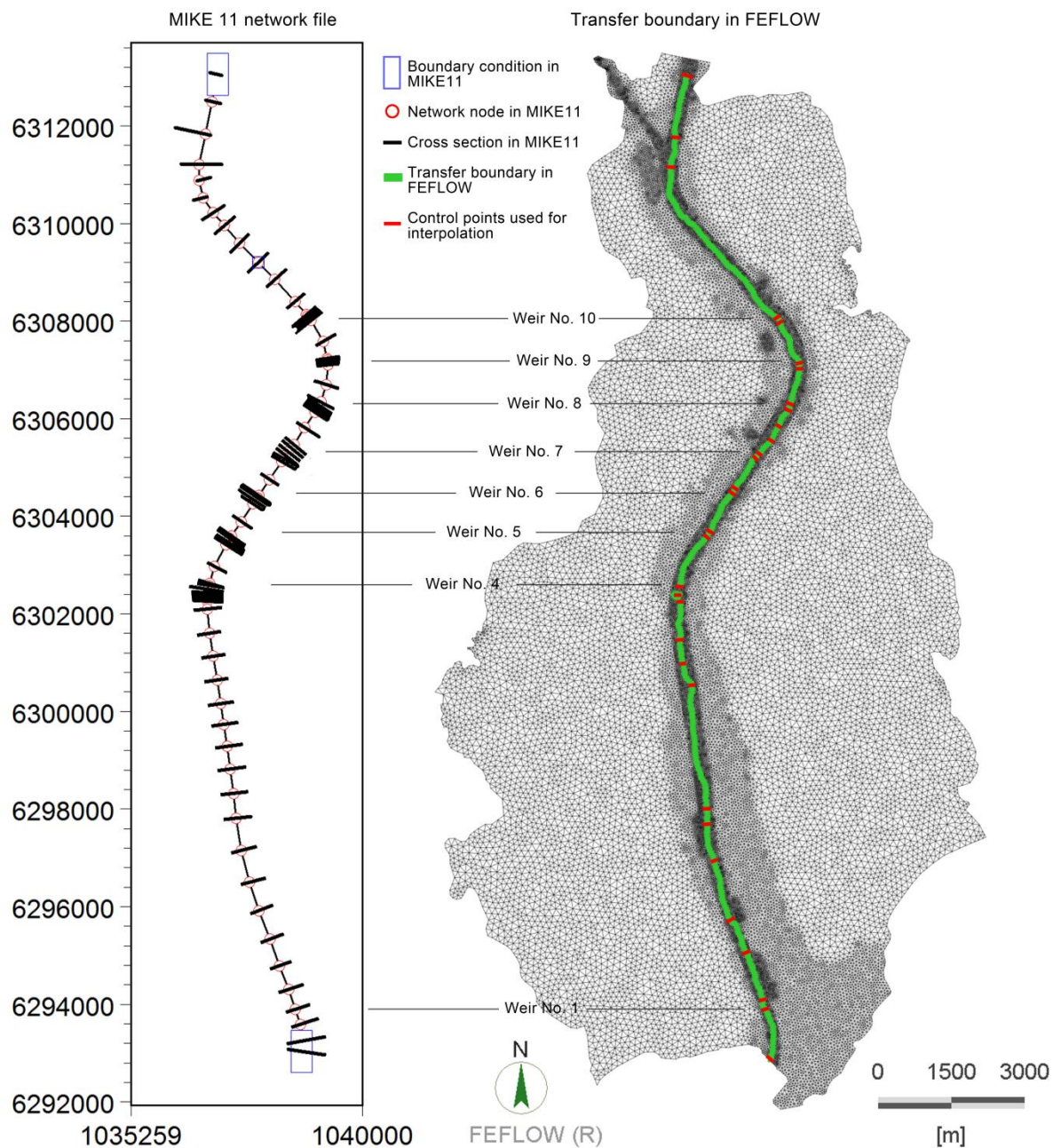


Figure III.17. River hydraulic model built by MIKE11 (left) and the transfer boundary condition assigned in groundwater flow model (right).

III.5 Groundwater extraction

In the numerical model, the groundwater extraction is modeled by a well boundary condition, which is a discharge assigned on a node of the top slice of the model. As introduced in the previous sections (I.2.4 Hydrogeological context), there are three types of water consumption: domestic use, industrial use, and agricultural use. The domestic water use is supplied by municipal pumping stations (Figure I.20). The recorded pumping volume shown in Figure I.21 is used to calculate the daily pumping

volume in a single well, then the values are assigned to the model. The major water consuming industries and their pumping volumes are listed in Table I.4. These pumping volumes in the companies, except for airport, are converted to daily values in a single well. The wells and their pumping values are assigned in the top slice (Figure III.19).

Regarding the water extraction in the airport, thanks to the well documented pumping volumes and the detail locations of each well, the wells are represented according to their real location. The boreholes created in the shallow unconfined aquifer are assigned on the nodes on the top slice of the model, whereas the boreholes created in the confined aquifer are assigned on the bottom slice of the first layer. Even though the numerical model focuses on the groundwater flow in unconfined aquifer, the water pumped from the confined aquifer in the airport must be modeled because a large quantity of it is reinjected into the unconfined aquifer. Hence, taking the pumped volume from confined aquifer ensures a conservation of the mass in the model. Otherwise the reinjected water is created out of nothing.

One of the main land uses in the lower valley of Var river is agricultural land and almost 1/3 of the valley is of concern (Figure III.15). Private pumping wells in the unconfined aquifer are authorized for irrigation in this area, while the abstracted volumes are not properly documented. To estimate groundwater abstraction for agricultural use, inverse simulation approach [Murray-Smith, 2000] is used in this study. It is assumed that in summer, when the precipitation is quasi absent, the water table evolution is totally determined by the pumping activities. Thus, the decreasing rate of the piezometric level on farmland caused by water abstraction for irrigation can be expressed by Eq. 5. In the summer of 2012, the lower valley has suffered from a drought. No precipitation is observed from September 6th to 22nd, 2012, while the need of the groundwater for irrigation is still strong. The piezometers P34BIS, P15, P57 and P16 are located on the farmland, where the pumped groundwater is mainly used for irrigation. Thus, the groundwater level measured by these piezometers during this period is used to estimate the groundwater consumption for agricultural use (Figure III.18). With this representative example, the non-documented groundwater extraction on the farmland in the studied area is estimated: $q_{ag}=0.015$ m/s only for summer time (August, September and October). In the numerical model, the wells on the farmland are set on an area of 20 ha. Figure III.19 shows the spatial distribution of the pumping wells and water reinjection points.

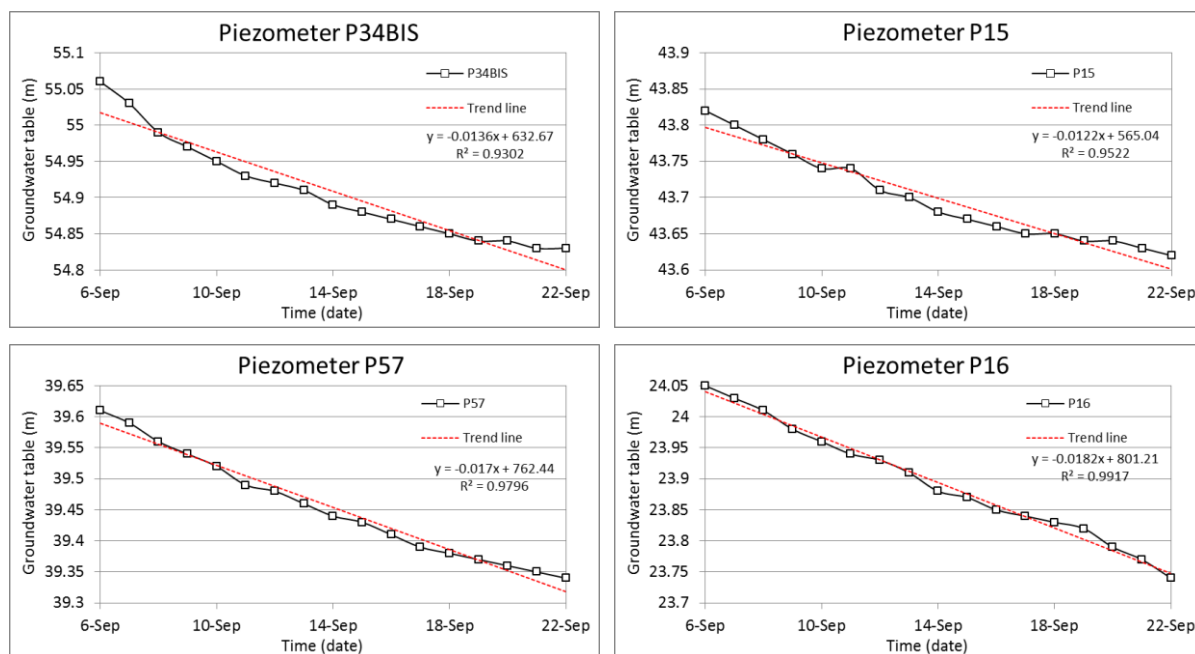


Figure III.18. Groundwater level measured by the piezometer in the farmland in lower Var river valley from September 6th to 22nd for different piezometers (Source: Eaufrance).

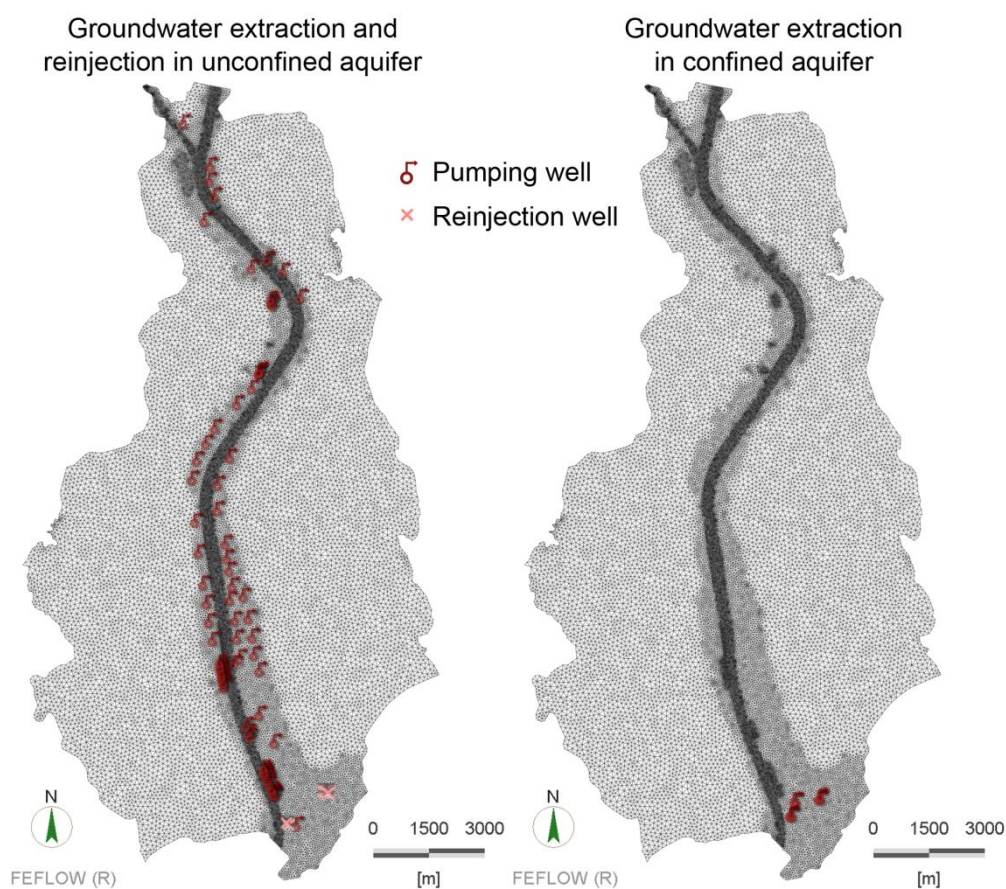


Figure III.19. Illustration of the groundwater pumping wells and water reinjection points in the lower Var river valley.

III.6 Model calibration

III.6.1 Grid convergence study

For a numerical simulation, small grid size would lead to accurate results but would also increase the computing cost. In order to optimize the ratio of the precision to the computing time, the grid convergence is studied to find a biggest grid size that insures the model precision. The grid convergence of the numerical model is studied by performing simulations with different cell sizes. A small area in the middle section of the lower valley is chosen to perform the simulations with 4 different cell sizes: 100 m, 50 m, 25 m and 10 m, and two points are set to compare the simulation results (Figure III.20). Point 1 is located on the upstream area of the weir No.4, where the river feeds the aquifer. Point 2 is located on the downstream side of the weir, where the aquifer feeds the river. Therefore the simulations results cover the two possible river-aquifer exchange directions.

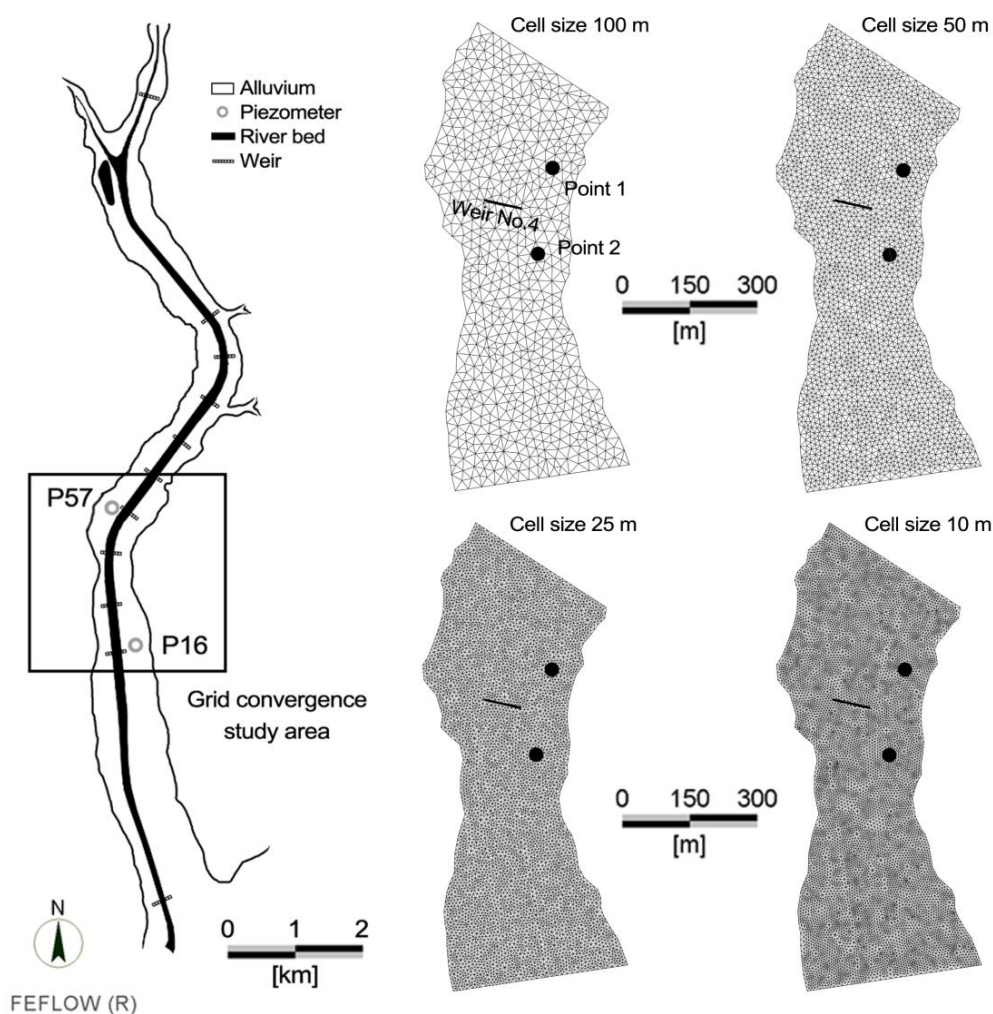


Figure III.20. Location of the area for grid convergence study and the 4 different cell sizes.

The simulations are performed from 1st Nov. to 30th Nov. 2014, with a time step of 15 minutes. For these 4 simulations, the upstream boundary condition (north) is the groundwater level measured by piezometer P57 and the downstream boundary condition (south) is the groundwater level measured by piezometer P16. The initial condition of the simulations is the interpolated groundwater level between the northern and the southern boundaries. Thus the only variable of these 4 simulations is the cell size. The results of the simulations at the two points of interest are shown in Figure III.21. It can be seen that, with the same input data, the groundwater levels simulated with different cell sizes show almost no difference. Therefore the model is able to provide a grid-independent result when the cell size is less than 100 m (100 m included).

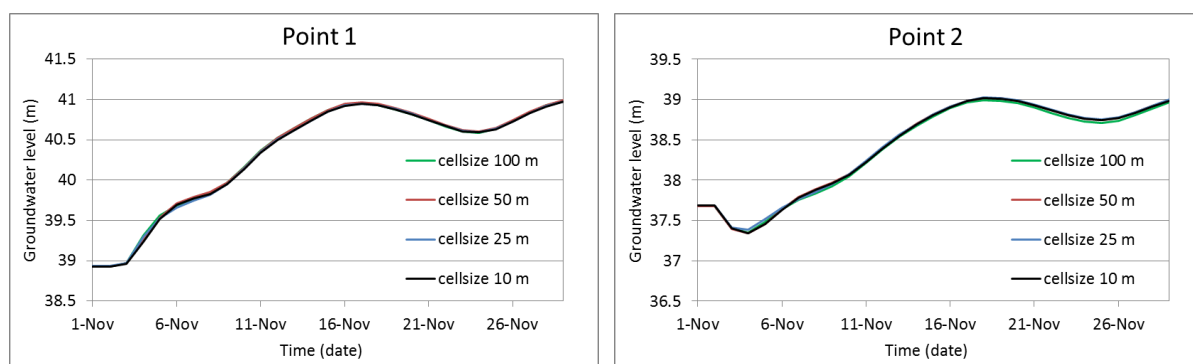


Figure III.21. Comparison of the simulation results for grid convergence study at two points of interest.

III.6.2 Sensitivity analysis

The specific yield S_y is an important geophysical parameter for an unconfined aquifer. It determines how much water that the soil can absorb/release in/from the pore space of the soil when there is a change of the groundwater level. Few measurements of specific yield have been carried out in the alluvium of the studied area. Even though a rough range of its value is given by Table III.3, a calibration of this parameter is still necessary to make input data more accurate in order to set up the model.

Because of the intense river-aquifer exchanges and the high hydraulic conductivity of the alluvium, the groundwater table is strongly related to the water level in Var river. The transfer rate ϕ used to calculate the exchange rate depends on the sediments of the river bottom. No measurement has been done regarding this parameter. Hence, a calibration of in/out-transfer rate is also needed to complete the input data.

A sensitivity analysis is performed before the calibration so as to gain a better understanding of the groundwater flow that is modeled. In general, a sensitivity analysis is a study of how the uncertainty in the output of a model can be apportioned to different sources of uncertainty in its inputs [Saltelli, 2002]. It is widely used in the process of numerical model setup [Bahremand and De Smedt, 2008; Tavakoli et al., 2013] for various purposes including:

- increased understanding of the relationships between input and output variables in a system or model;
- identification of model inputs causing significant uncertainties in the output and their influence on the interval of the variation of output values;
- simplification of the calibration stage by focusing on the sensitive parameters and on reasonable interval of variation.

In this study, the sensitivity analysis focuses on the investigation of the variation interval of the outputs caused by the change of inputs. The conclusion of the sensitivity analysis helps to increase the understanding of the model. Hence, less time would be spent on the calibration stage. Table III.6 summarizes the variation interval of the target parameters and the other fixed parameters used by the simulations of sensitivity analysis.

Table III.6. Summary of the parameters included in the sensitivity analysis.

Parameter	Variation interval	Other parameters
Specific yield S_y	From 0.05 to 0.2	Measured K , $S_s=0.0001 \text{ m}^{-1}$, $\phi_{in}=10^{-4} \text{ s}^{-1}$ and $\phi_{out}=10^{-5} \text{ s}^{-1}$
In-transfer rate ϕ_{in}	From 1×10^{-6} to $1 \times 10^{-4} \text{ s}^{-1}$	Measured K , $S_s=0.0001 \text{ m}^{-1}$, calibrated S_y and $\phi_{out}=10^{-4} \text{ s}^{-1}$
In-transfer rate ϕ_{out}	From 1×10^{-5} to $1 \times 10^{-3} \text{ s}^{-1}$	Measured K , $S_s=0.0001 \text{ m}^{-1}$, calibrated S_y and $\phi_{in}=10^{-5} \text{ s}^{-1}$

The specific yield S_y , the in-transfer rate ϕ_{in} and out-transfer rate ϕ_{out} are studied independently. Figure III.22 shows the location of the piezometers used in the sensitivity analysis. Five piezometers are chosen to study the influence of the S_y , while three are used to study the transfer rates. This is caused by the difference of the degree of knowledge between the parameters. The spatial distribution of the S_y in the layer of alluvium is almost totally unknown, therefore more piezometers are needed to present an equally distribution along the valley. The transfer rates, however, are related to the

sediment on the riverbed. A previous study has already given a related qualitative description of the spatial distribution of the sediment on riverbed (Figure II.6), thus only three piezometers are used in the study of the transfer rate.

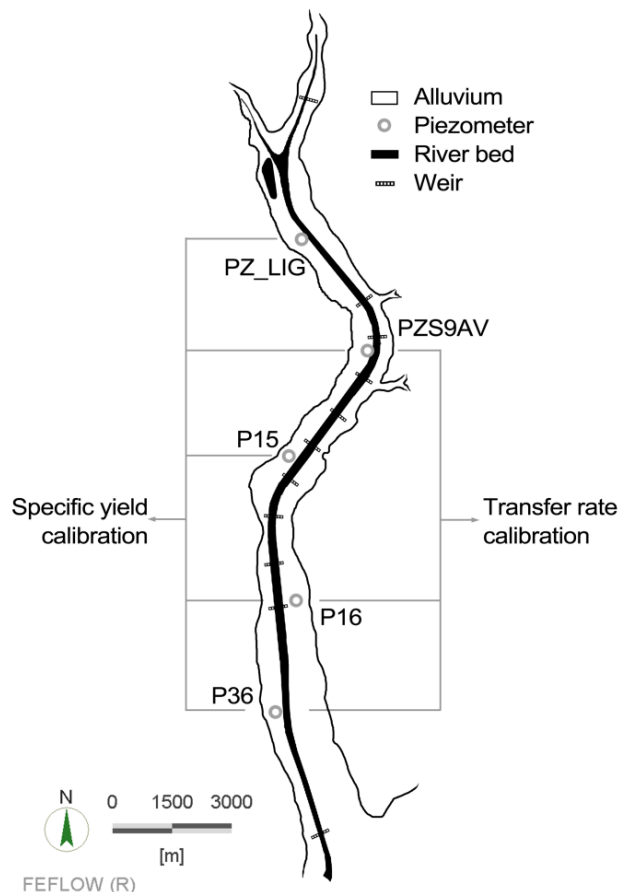


Figure III.22. Location of the piezometers used in the calibration.

Regarding the calibration of the specific yield, each piezometer represents a characteristic of the alluvium. The PZ_LIG and PZS9AV represent the alluvium of high perviousness of water. P15 stands for the media with a clogging layer where the groundwater level is disconnected from the river. P16 is located in a region where the hydraulic conductivity of the alluvium decreases. P36 represents the alluvium with lens of clay and silt, which is the typical characteristic of the alluvium in the downstream area. As for the calibration of the transfer rate, only three piezometers are included. PZS9AV represents the section of the weirs where the riverbed is covered by the fine sediment. P16 stands for the section with destroyed weir, thus the fine sediment is eroded and coarse sediments are found on the riverbed. The riverbed near P36 is covered with fine sediment and vegetation.

A series of simulations are performed with different values for tested parameters. The simulations start from May 10th, 2012 to February 26th, 2013, which is 293 days long, containing a dry period in the summer and a rainy period in winter. The daily discharge (Figure III.23, left) in the Var river measured at La Manda bridge is used in the surface hydraulic model to calculate the water level in the river and then used as the transfer boundary in the groundwater flow model. The groundwater level measured at P37 (Figure III.23, right) is the upstream boundary condition of the model, while the downstream boundary condition is the mean sea level, which equals to 0.3 m.

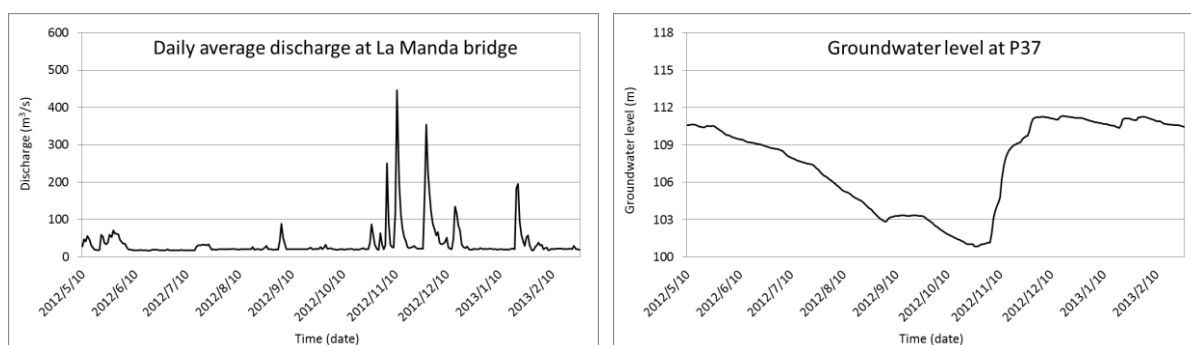


Figure III.23. Daily discharge in the river (left) and upstream boundary condition (right) for the simulations of sensitivity analysis (Source: Eaufrance).

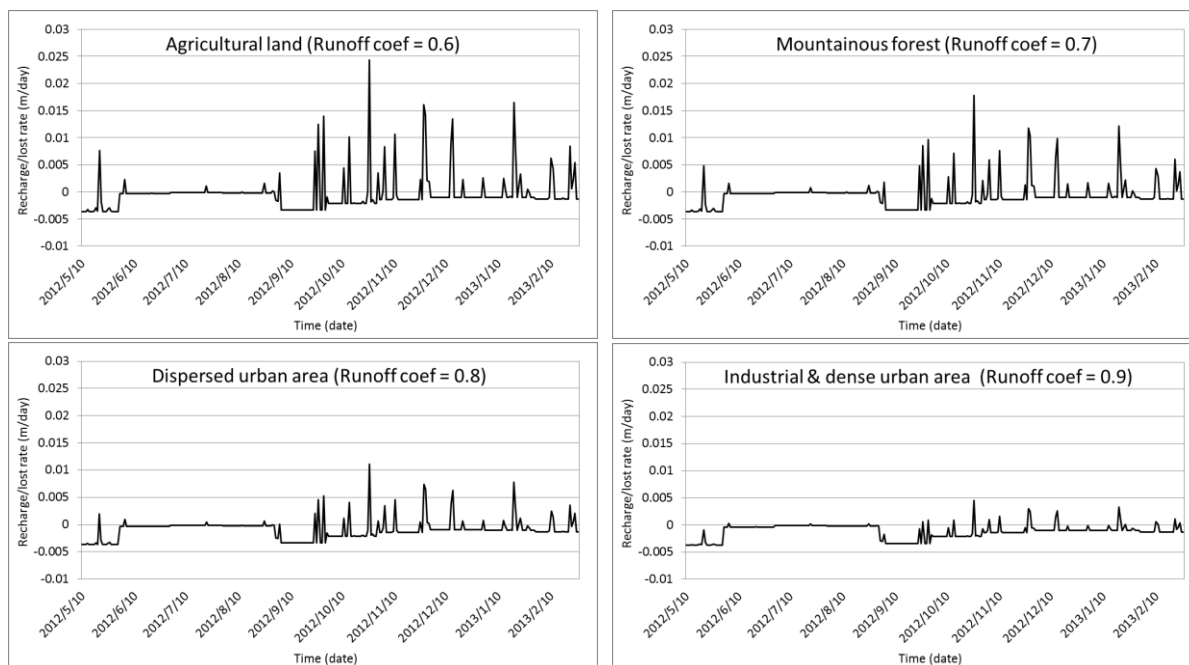


Figure III.24. Direct water recharge/loss in the model for the simulations of sensitivity analysis.

Figure III.24 shows the direct water recharge/loss on the top layer of the model caused by rainfall and actual evapotranspiration. The groundwater extraction and reinjection for domestic and industrial

water use are assigned with the measured value (Figure I.21 and Table I.4), while the estimated value of the agricultural water consumption is assigned as explained in the section: III.5 Groundwater extraction. Regarding the initial condition of these simulations, the groundwater level that is measured on May 10th, 2012 by all the piezometers in the alluvium is used to generate an interpolated map, which is the initial condition of the simulations. Variable time step is used for the simulation, the minimum time step is 0.01 day and the maximum is 1 day.

III.6.3 Results and discussions

The simulation results of the sensitivity analysis of the specific yield S_y are shown in Figure III.25 and Table III.7. The specific yield influences groundwater level when there is a fluctuation, especially for the peak phase and the recession phase after the swelling. Through the comparison of the groundwater level simulated with different S_y values, it can be seen that a lower S_y value corresponds to a bigger amplitude of the peak, and a faster recession process. A higher S_y leads to a smaller amplitude and a smoother evolution of the groundwater level. According to the definition of the specific yield, compared to a low porosity ratio, high porosity ratio in the soil means that the water level increases by a smaller increment when absorbing the same quantity of water, or decreases slower when releasing the same quantity of water. This characteristic is confirmed by the tests.

Table III.7 has given the average variation and maximum variation of the simulated groundwater level, which are criteria to identify the sensitivity of the model to the targeted parameters. In this model, the upstream area is the least sensitive to the variation of S_y , because the simulated result is more impacted by the boundary condition assigned on Le Broc lake. In the section of the weirs, the groundwater level is more sensitive to S_y , because the maximum variation of groundwater level at P15 is 1.10 m. Thanks to the result of sensitivity analysis, S_y is calibrated to match the amplitude of measured groundwater level (Figure III.28). The calibrated S_y is then used as an input for the sensitivity analysis of transfer rate.

Through the simulation results with different transfer rates (Figure III.26 and Table III.8 for ϕ_{in} , Figure III.27 and Table III.9 for ϕ_{out}), the predominant water exchange direction along the river can be detected by comparing the reaction of simulated groundwater level. For piezometers PZS9AV and P16, groundwater level is sensitive to both ϕ_{in} and ϕ_{out} values, it infers that groundwater table reacts sharply to both infiltration and exfiltration. The infiltration influences more when the groundwater

level is low, while the exfiltration has more impacts after the peaks. This indicates that the two directions of exchange exist, but they happen during different seasons. The downstream section near the point P36 is more likely to respond to infiltration, especially during the dry season when the groundwater level is low. The maximum variation of groundwater level simulated with different ϕ_{in} values is 3.16 m. The value of ϕ_{out} does not influence too much on the results since the maximum variation of groundwater level is merely 0.63 m, which means that in this section the water level in the river is always higher than the groundwater level. Among the three parameters studied in the sensitivity analysis, the transfer rates ϕ_{in} and ϕ_{out} are identified as the most influential parameters for the groundwater flow in the lower Var river valley.

Based on the result of the sensitivity analysis and the measured data, the value range of each parameter is well defined regarding different river sections. This limitation of value range helps to save a lot of time on model calibration. Actually, only a minor adjustment is needed to calibrate the targeted parameters. The results of calibration are shown in Figure III.28.

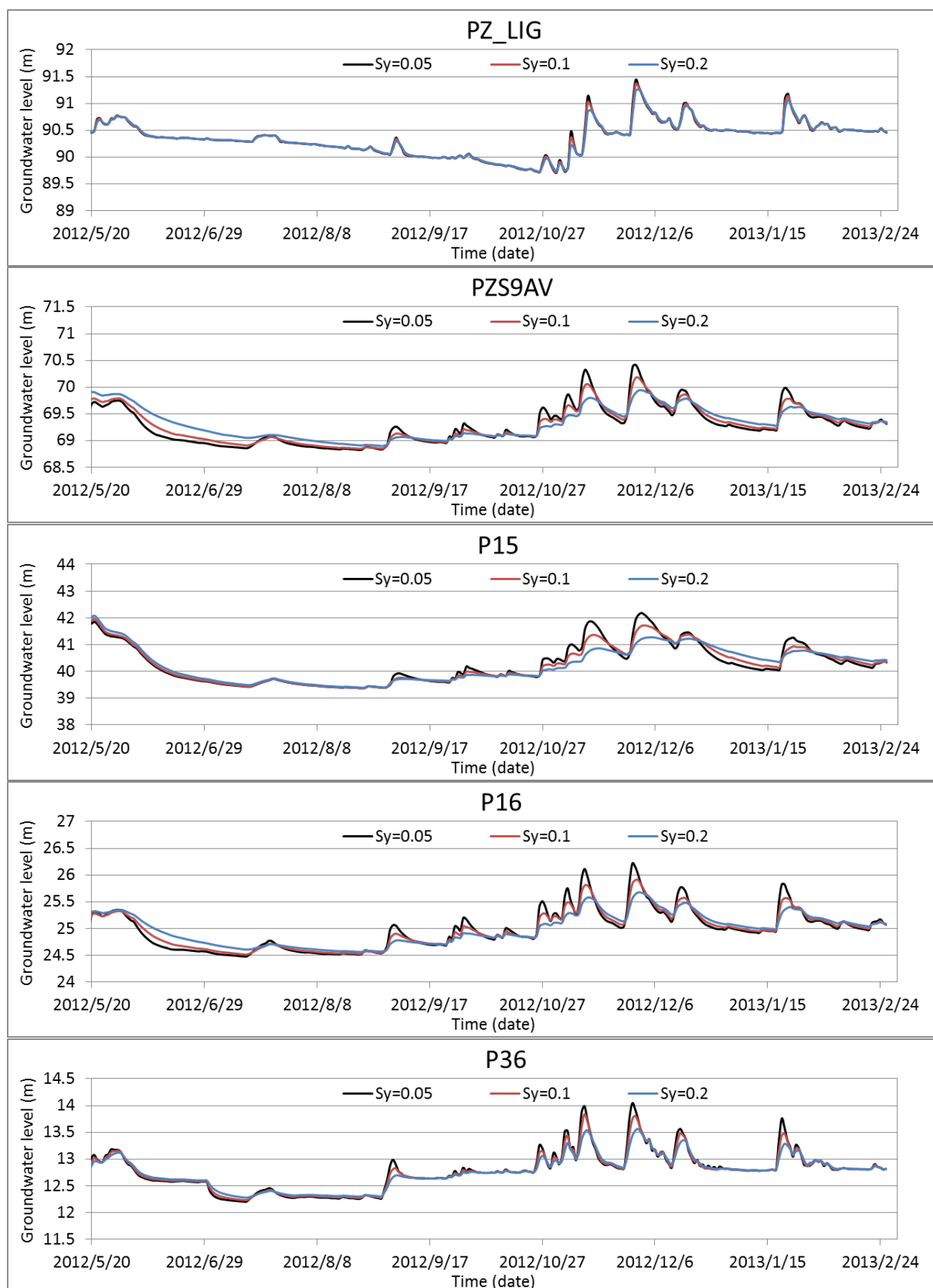


Figure III.25. Sensitivity analysis of the specific yield S_y at different locations.

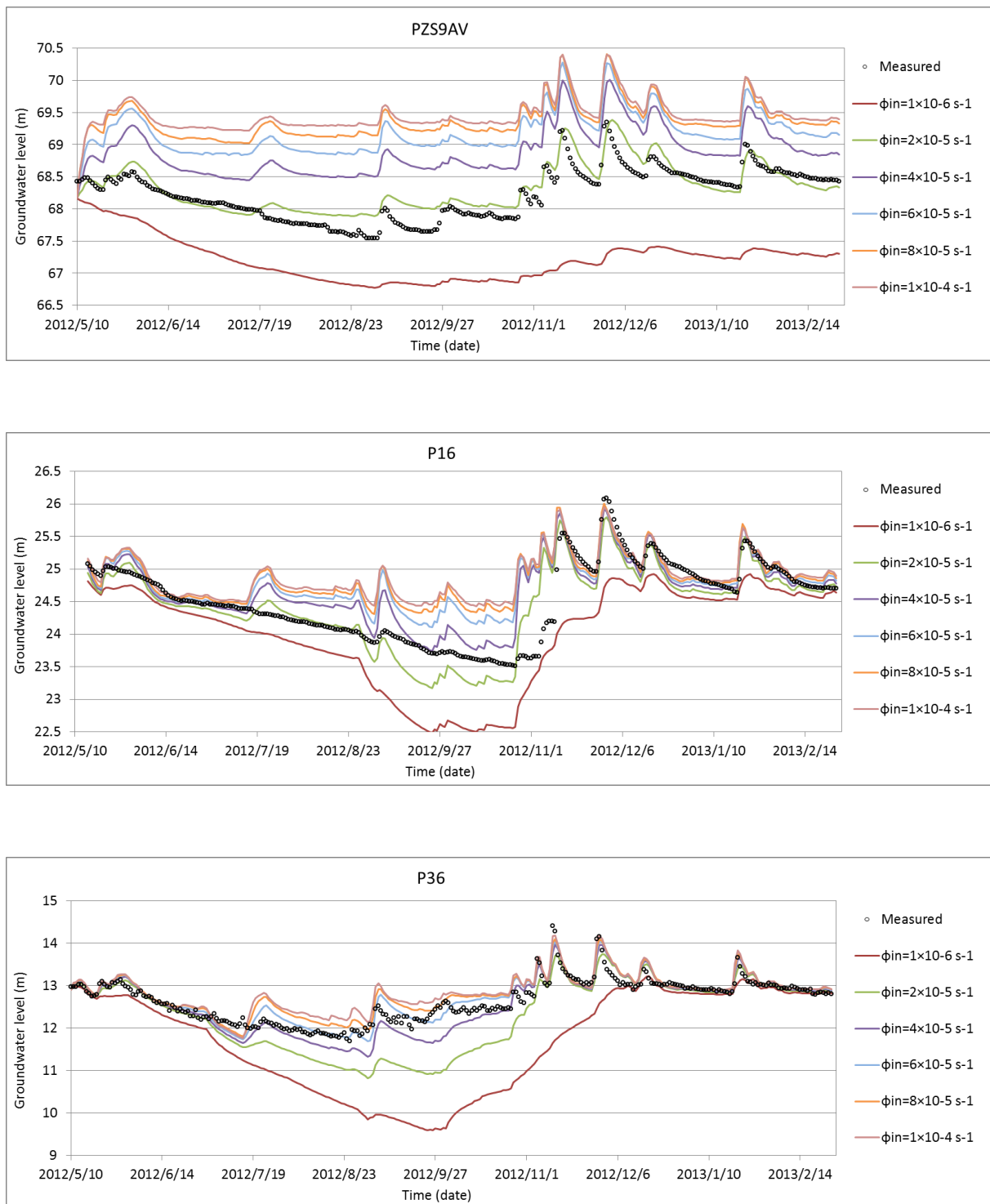


Figure III.26. Sensitivity analysis of the in-transfer rate ϕ_{in} at different locations.

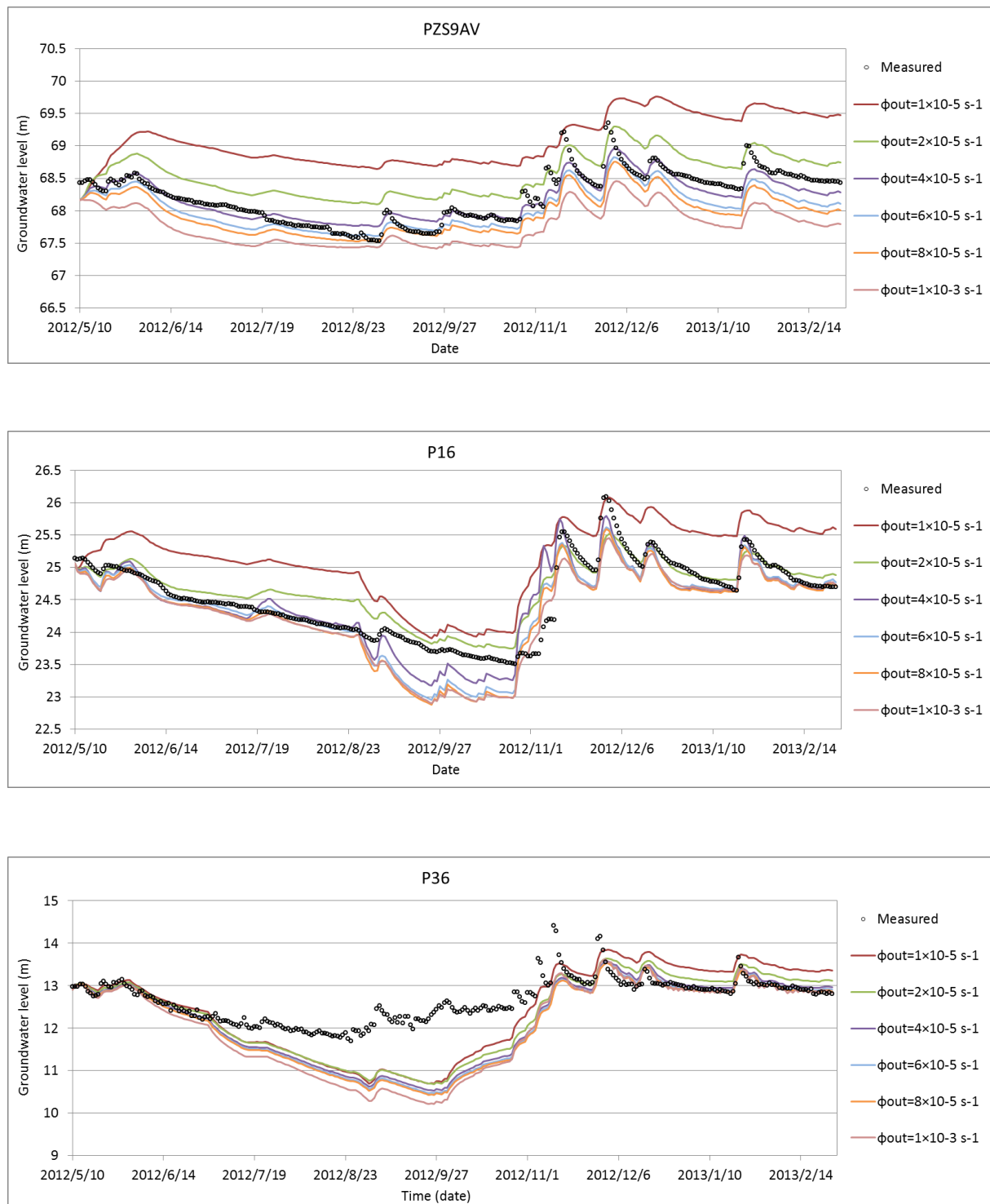

 Figure III.27. Sensitivity analysis of the out-transfer rate ϕ_{out} at different locations.

Table III.7. Result of sensitivity analysis of specific yield S_y .

Tested parameter: Specific yield (Drain/fillable porosity) S_y					
Variation interval: From 0.05 to 0.2					
Location	PZ_LIG	PZS9AV	P15	P16	P36
Average variation of the simulated groundwater level (m)	0.02	0.14	0.19	0.12	0.06
Maximum variation of the simulated groundwater level (m)	0.65	0.81	1.10	0.88	0.61

Table III.8. Result of sensitivity analysis of the in-transfer rate ϕ_{in} .

Tested parameter: In-transfer rate ϕ_{in}			
Variation interval (s^{-1}): From 1×10^{-6} to $1 \times 10^{-4} s^{-1}$			
Location	PZS9AV	P16	P36
Average variation of the simulated groundwater level (m)	2.24	0.87	1.15
Maximum variation of the simulated groundwater level (m)	3.26	2.23	3.16

Table III.9. Result of sensitivity analysis of the out-transfer rate ϕ_{out} .

Tested parameter: Out-transfer rate ϕ_{out}			
Variation interval (s^{-1}): From 1×10^{-5} to $1 \times 10^{-3} s^{-1}$			
Location	PZS9AV	P16	P36
Average variation of the simulated groundwater level (m)	1.32	0.84	0.39
Maximum variation of the simulated groundwater level (m)	1.69	1.04	0.63

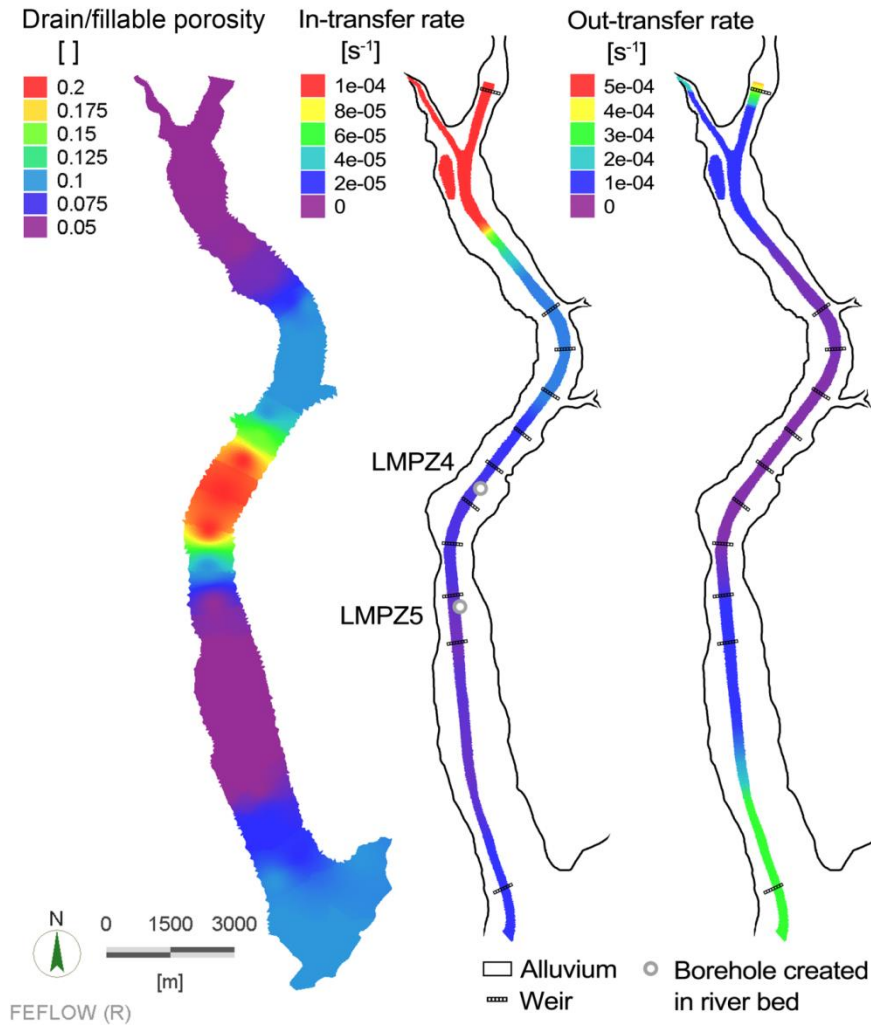


Figure III.28. Calibrated values of specific yield S_y and in/out-transfer rate ϕ_{in} , ϕ_{out} .

Two boreholes with a depth of 20 m have been created within the riverbed (Figure III.28). The grading curves of the sediments are then analyzed and the results are shown in Figure III.29. It shows that the sediments at LMPZ5 are better graded than that at LMPZ4 for each vertical section. Furthermore, regarding the grain size distribution, the mean particle diameter d_{50} and the effective particle diameter d_{10} of the sediments at LMPZ5 are smaller than those at LMPZ4. Right after the creation of the boreholes, a measurement on November 2015 has indicated that the groundwater table is observed below the bottom of the riverbed, which means that the infiltration is happening at these two locations. In the numerical model, for the infiltration situation, it can be read that $\phi_{in}=2 \times 10^{-5} \text{ s}^{-1}$ at LMPZ4 and $\phi_{in}=0.9 \times 10^{-5} \text{ s}^{-1}$ at LMPZ5. The calibration result is thus qualitatively coherent with the grading curve analysis.

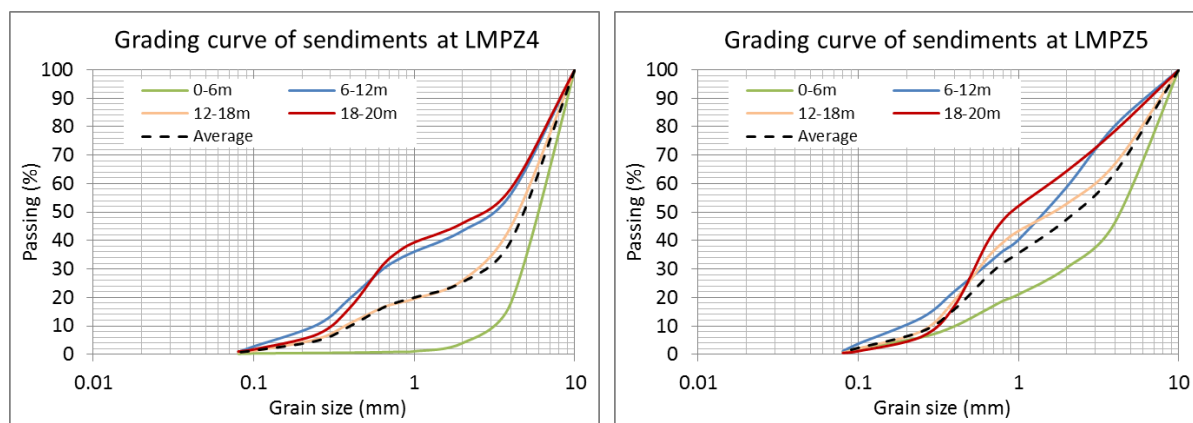


Figure III.29. Grading curves of the sediments in boreholes LMPZ4 and LMPZ5.

III.7 Model validation

III.7.1 Presentation of the simulation

A simulation from September 10th, 2009 to February 26th 2013 (1266 days) has been performed as a model validation. An extreme flood event on November 2011 and a severe drought event in spring and summer of 2012 are included in this period. Therefore this period is representative for the hydrological environment in the lower Var river valley. Moreover, the topography that is used to set up this model is from the year of 2009, therefore it is more reasonable to include this year in the simulation. There are totally 21 piezometers in the alluvium of lower Var river valley, 6 of them are chosen to represent different sections along the valley (Figure III.30) thanks to their fully record of digital data during the simulation period.

For the model validation, the daily discharge (Figure III.31) in the Var river measured at La Manda bridge is used in the surface hydraulic model to calculate the water level in the river and then used as the transfer boundary in the groundwater flow model. The groundwater level measured at P37 (Figure III.31) is the upstream boundary condition of the model, while the downstream boundary condition is the mean sea level, which equals to 0.3 m. Like the simulations performed for the sensitivity analysis, the initial condition is a groundwater level map generated by interpolating the measured values on September 10th, 2009. A variable time step from 0.001 day to 1 day is used in order to strike a balance between the calculation time and the numerical stability of the simulation.

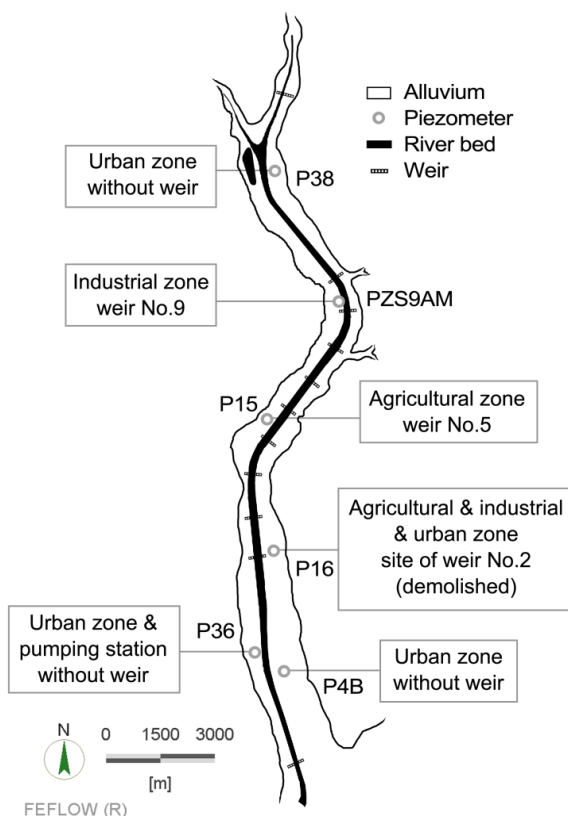


Figure III.30. Location of the piezometers used in the validation of the model and the represented characteristics of the domain.

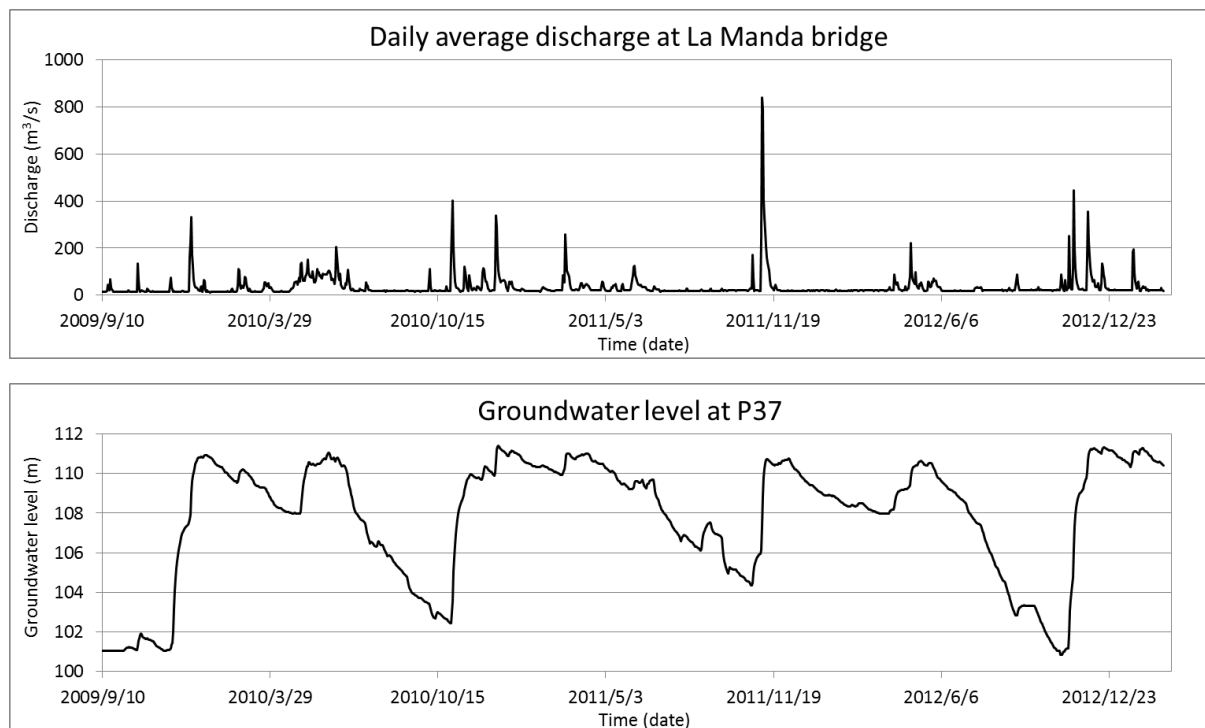


Figure III.31. Daily discharge in the river and upstream boundary condition for the simulations of model validation (Source: Eaufrance).

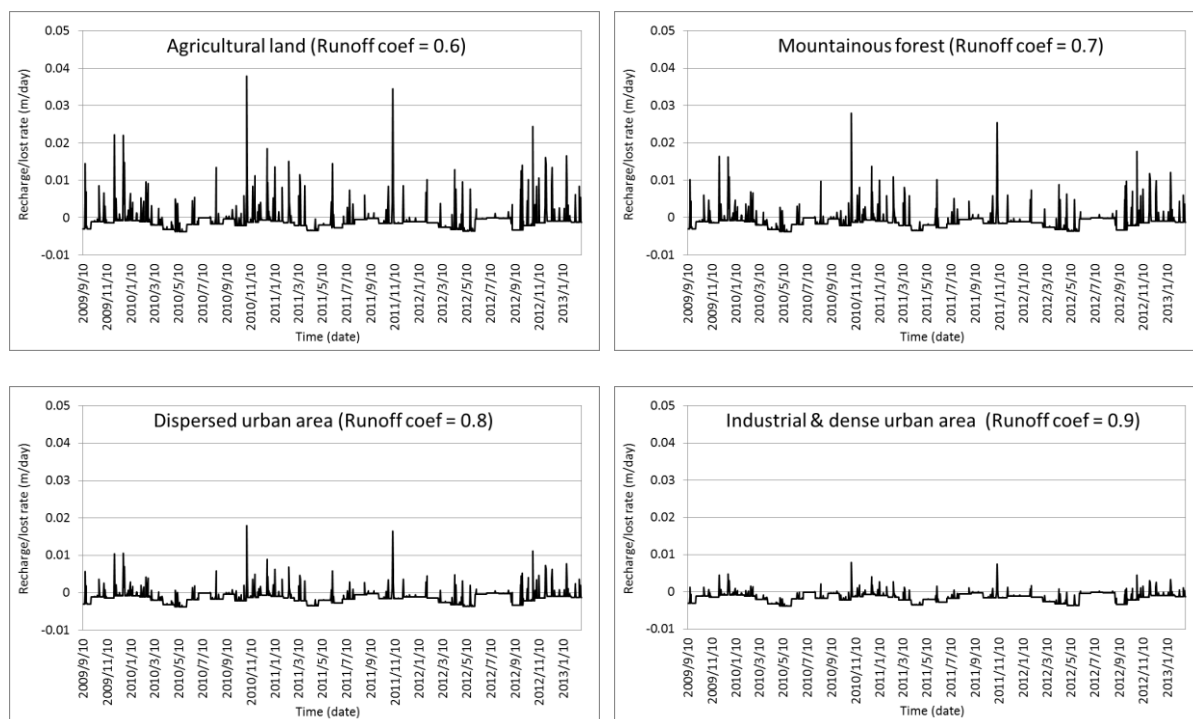


Figure III.32. Direct water recharge/loss for the model validation for different land use.

The direct water recharge/loss caused by precipitation/evapotranspiration are calculated and shown in Figure III.32. For the different areas located on Figure III.30, the positive values indicate the precipitation, while the negative values represent the actual evapotranspiration. It can be seen that the highest actual evapotranspiration in the studied area appears in May and October, when the temperature is high enough to stimulate a high potential evapotranspiration and the precipitation is also adequate to support it. The aquifer is usually recharged during winter when the rainfall is more frequent.

According to the runoff coefficient estimated for each type of land use, the water recharge is the highest on the agricultural land. For a common rainfall event, the farm land receives a recharging flux of less than 10 mm/day. But for extreme events such as the rainfall of November 2010 and November 2011, the aquifer under the farmland is recharged by a flux that is higher than 30 mm/day in the model.

III.7.2 Simulation results and model evaluation

The comparison between the simulated and measured time series of groundwater level at each chosen piezometer is shown in Figure III.33 and Figure III.34. Linear regression, *NSE* coefficient (Eq. 30) and mean absolute error (*MAE*) are the two indexes used to evaluate the model validation, which are respectively shown in Figure III.35.

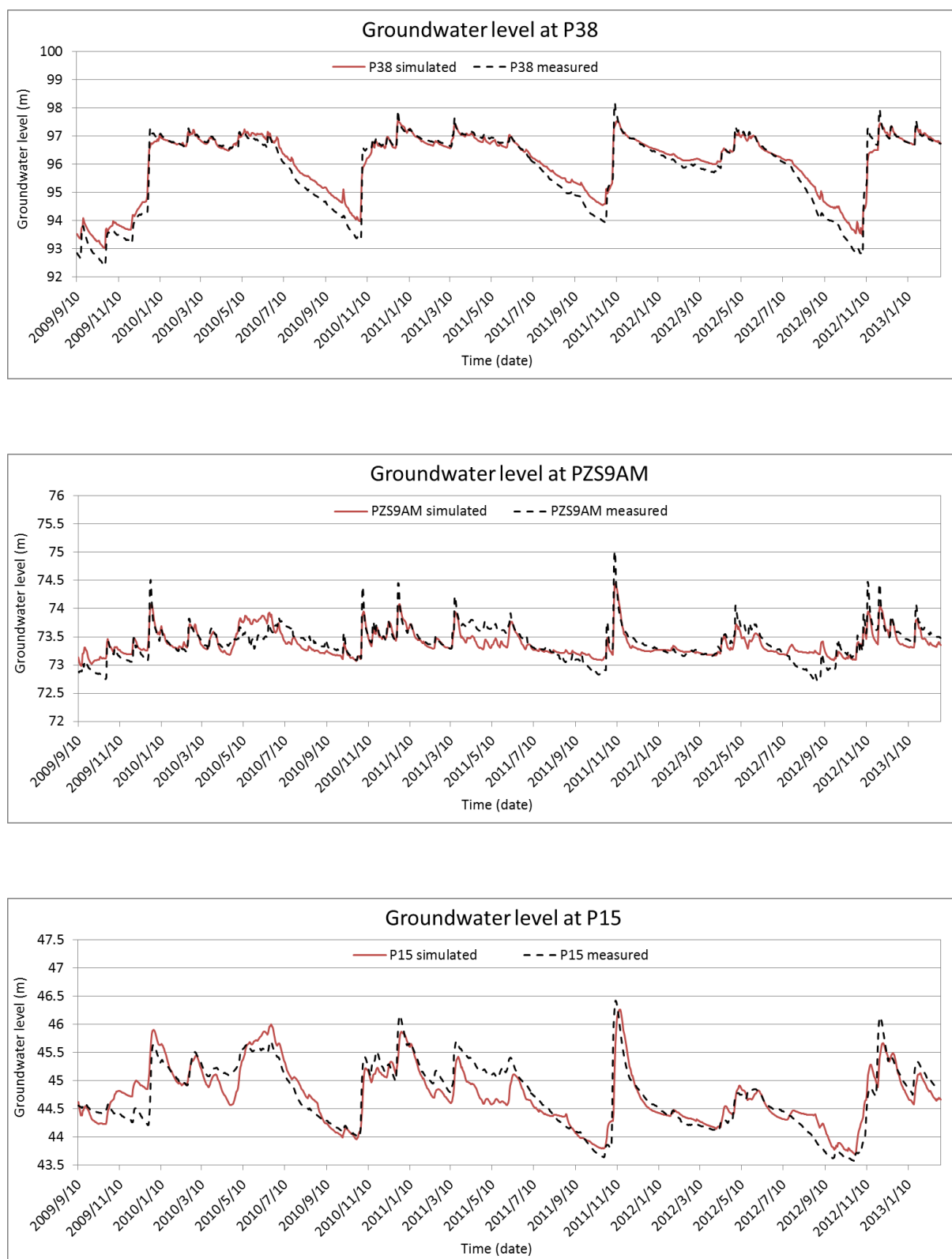


Figure III.33. Simulation results of the model validation at the upstream piezometers of the study area.

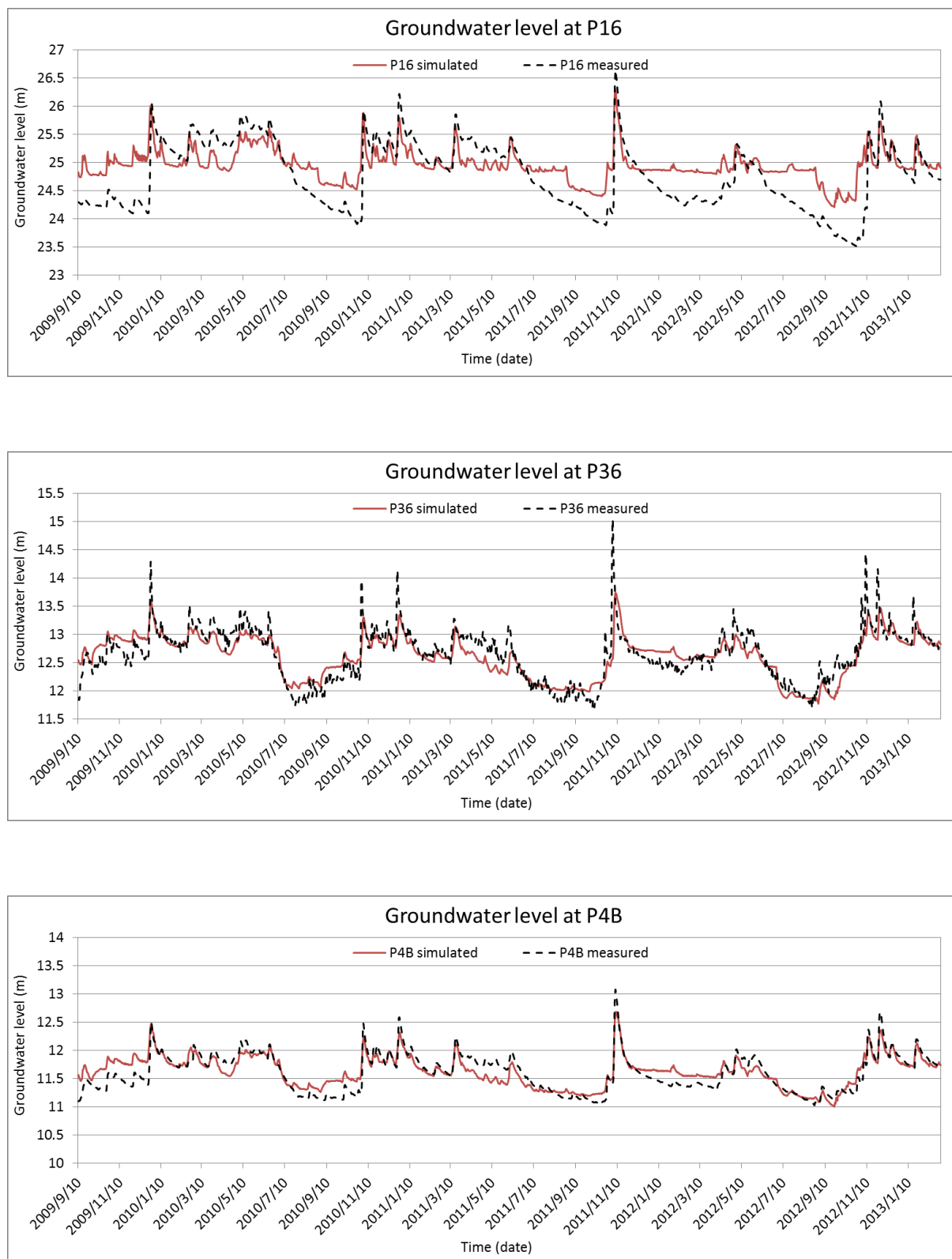


Figure III.34. Simulation results of the model validation at the downstream piezometers of the study area.

In general, the model is able to represent the trend of the groundwater table evolution. The seasonal fluctuations, which are typical in the Mediterranean area, are well simulated. At the beginning of the simulation, the effect of the initial condition lasts for almost three months until the first peak arrives in the aquifer of the lower Var river valley on November 2009. It means that it takes less than 2 months of simulated time to perform the model warming up.

At the piezometer P38 which stands for the upstream urban area, the groundwater level is well simulated. On one hand, the chosen location is near to the upstream boundary and to Le Broc lake, where the hydraulic head is assigned. Therefore the simulated groundwater level is strongly impacted by the boundary conditions. As long as the measured data are used as boundary conditions, the simulated values at this location are therefore also close to the measured values. On the other hand, the geological study shows that the hydraulic conductivity is more homogeneous than other areas. No clay or silt lenses are detected in this area. It is close to the hypothesis of the numerical model, thus the model is likely to give good simulation results. The groundwater level in this area is characterized by a large fluctuation according to the season, which is caused by the high hydraulic conductivity. Since the groundwater flow has a large velocity, the recharge of groundwater in the summer is not as high as the aquifer needs to maintain its level. The results show that the model can perfectly reproduce this feature by using a high hydraulic conductivity value.

The piezometer PZS9AV represents an area where the industrial activity is the predominant land use. The piezometer is next to the river bank. Therefore the groundwater level is strongly influenced by the water level in the river. A mild fluctuation of groundwater level (1.5 m for normal cases and 2 m for extreme case) is observed. The numerical model is able to reproduce this characteristic by considering the transfer boundary. However, the peak and trough levels with large fluctuations are not well simulated, the numerical model is likely to underestimate the peak and overestimate the trough values. Apart from that, the simulated result is more accurate for the period with small peaks and troughs, for example, from March to October 2010.

In the section where the weirs are constructed in the riverbed, the predominant land use is the farmland. The result shows that the groundwater level at P15 is well simulated by considering a virtual level to model the disconnection between the river and the aquifer (Eq. 3). The model shows a good performance at the peak and trough. The groundwater level during the summers of 2010, 2011 and

2012 is close to the measured data, which means that the groundwater extraction for agricultural use is correctly estimated. However, two obvious withdrawals of simulated groundwater level are observed on April and May 2010 and at the same period on 2011, which are very different from the measured data. This error is studied and explained in the next section.

The simulation result is less satisfying at piezometer P16. Through the measured data, the groundwater level during the summer has a notable withdrawal, while it is not reproduced by the model. After the demolition of weir No.2, the riverbed has regained its natural morphology and fine sediments are eroded away (Figure II.4). Even though the aquifer is still disconnected to the river, the exchange between the river and aquifer exists. It is the reason why each peak of groundwater level corresponds to a peak of discharge in the river. Knowing that only the model gives good results of the rainy season, the river-aquifer exchanges are thus correctly modeled. More discussions about the error during dry season are given in the following section.

P36 stands for the downstream urban area, where a pumping station affects strongly the groundwater level so that the measured groundwater level has always a high frequency fluctuation. The simulated result cannot show such a fluctuation because the input of this model is calculated from monthly pumped volume. Thanks to the accurate recorded pumped volume, the groundwater level of summer is well simulated. The only fault seen from the result is that the peak values are always underestimated, and the difference value varies in accordance with the amplitude of the peak. For the extreme event of November 2011, the difference value is more than 1 m. For the other small peaks, the difference value is around 0.5 m.

The piezometer P4B represents the downstream urban area without pumping station nearby. The model is able to simulate not only the peak values during winter, but also the trough values during summer. The general fluctuation of the measured groundwater level is less than 1.5 m for most of the time. It shows that a dynamic exchange between the river and the aquifer is in this area. The model has correctly calculated this exchange and reproduced it with a small error. A little underestimation is observed for each peak value but it is totally acceptable.

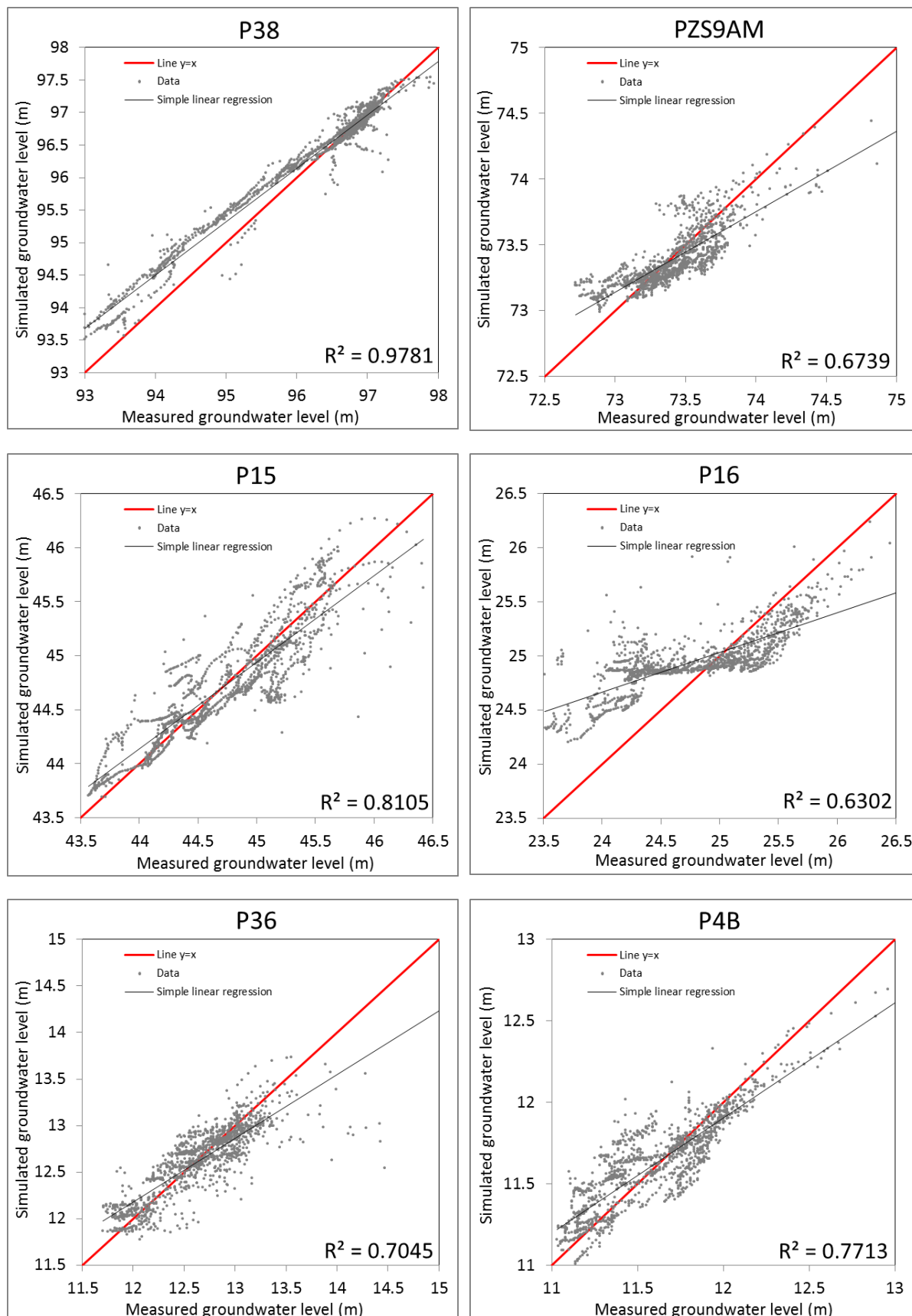


Figure III.35. Linear regression of measured and simulated groundwater level at different piezometers.

Figure III.35 is the linear regression of the simulated and the measured groundwater level. In general, the simulated results have a positive correlation with the measured data. The results are less satisfying only at piezometer P16, especially for the lower water level situation. The results of piezometers which are located next to the river banks such as PZM9AM, P36 and P4B indicate that the model underestimate the peak groundwater levels in the areas next to the river. For the other three points which are located remotely from the river banks, the underestimation of the peak values is less notable. This underestimation is caused by the transfer boundary in the groundwater flow model. In this model, the transfer boundary is the water level simulated by a river hydraulic model. The upstream boundary condition of the latter one is the measured daily average discharge at La Manda bridge, which is certainly lower than the instantaneous discharge. For example, the daily average discharge measured at La Manda bridge on November 5th, 2011 is 841 m³/s, while the maximum instantaneous discharge equals to 1220 m³/s at 11 o'clock. The maximum recorded groundwater level is 75.02 m at 24 o'clock of November 5th. The reaction of the groundwater level is much slower than the reaction of the water level in the river. Once the groundwater level reaches its maximum value, it takes more time for the groundwater to drop to its static level than the river water level. Therefore the recorded value of groundwater level is very close to the maximum value, but the daily average discharge is much less than the maximum discharge. Hence the transfer boundary calculated with the daily average discharge is underestimated. The results can be improved by changing the daily average discharge to the instantaneous discharge if the latter one is available.

The Nash Sutcliffe Efficiency (*NSE*) coefficient is calculated to evaluate the model performance (Figure III.36). In this figure, the *NSE* is calculated not only for the whole simulated period, but also for individual years from 2010 to 2013. The *NSE* confirms again the conclusion that is obtained from the linear regression, that the model gives better results at piezometers P38, P15, P36 and P4B (Figure III.30), where the *NSE* is higher than 0.75. The model gives less satisfying results at piezometers PZS9AM and P16, where the *NSE* is less than 0.7.

Nevertheless, the *NSE* may not give a complete evaluation of the performance. For example, the coefficients calculated on separated years show that the *NSE* is very sensitive to peak values. When there is no high peak value in the time series, the coefficient is usually small. The *NSE* of 2010 at piezometer PZS9AM equals to 0.35, but the comparison between the simulated and measured values

on Figure III.33 indicates that the model actually performs well for this period. Another example is the evaluation at piezometer P38. The positive correlation between the simulated and measured values leads to a high *NSE* coefficient. But the comparison of the time series shows a difference of 0.5 m for the low groundwater level situation. Considering the limitation of the *NSE*, the mean absolute error (*MAE*) is introduced as an additional index to add more arguments in order to evaluate the model.

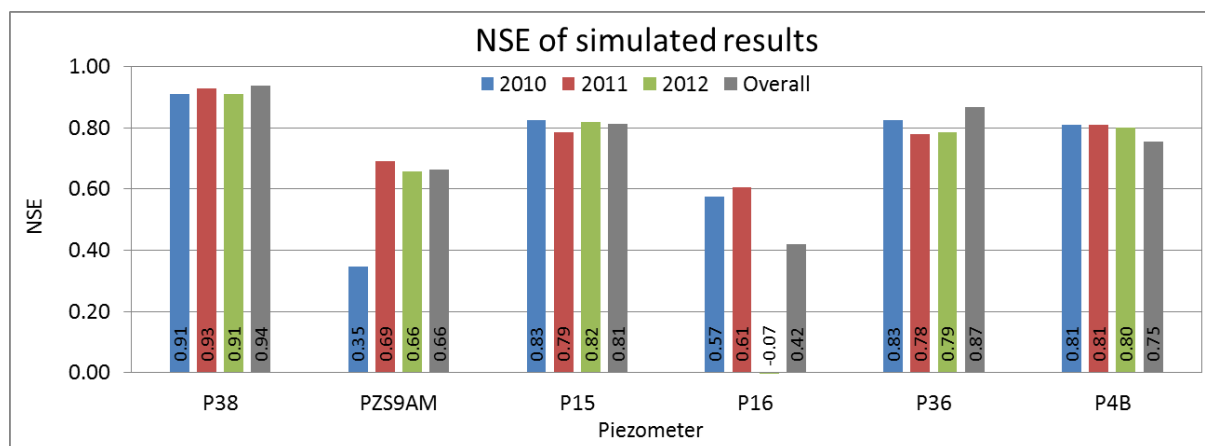


Figure III.36. NSE coefficient of the simulation results of model validation at different piezometers.

Through the comparison of the *MAE* (Figure III.37), it can be seen that the simulated peak value at piezometer P38 is not as satisfying as the *NSE* shows. The overall *MAE* through three years at P38 is the highest among the other piezometers except for P16. This error cannot be seen if the *NSE* is the single index of evaluation due to the high fluctuation of the groundwater level in this area. Besides, the result at PZS9AV has only a *MAE* of 13 cm compared to the measured data, which means that the model has a good performance at these places.

Most of the *MAE* (separated and overall) values are less than 20 cm. This is a very satisfying result for a model valley that measures 22 km. The *NSE* and *MAE* consistently show that the model gives less satisfying result at P16, which is representative for the river section with demolished weir and a complicated land use that is mixed with industrial, agricultural and urban area. Through the time series result, it is seen that the simulated groundwater level has an obvious error for the dry season. The overall *NSE* is the lowest one among the 6 chosen points (0.42) and the overall *MAE* is the highest (37 cm). During the year of 2012, the dry season appeared in spring and in summer, thus the lower groundwater level duration is extremely long. The *NSE* of year 2012 is a negative value, the corresponding *MAE* is also the highest, which reaches 46 cm.

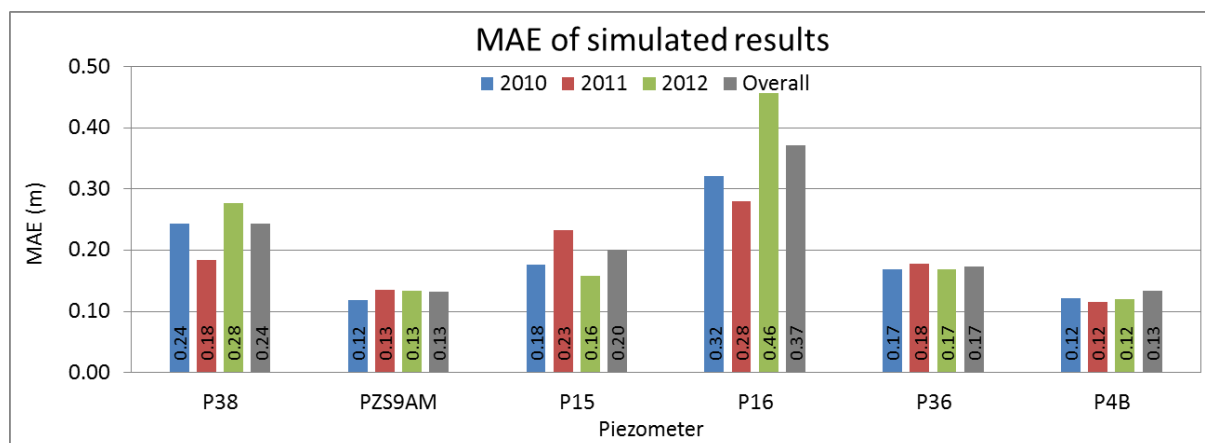


Figure III.37. Mean absolute error (MAE) of the simulation results of model validation.

III.7.3 Discussions

III.7.3.1 Lack of unsaturated layer

An underestimation of the simulated groundwater level at P15 is observed during the spring (April and May) of 2010 and 2011. This error can be explained by the difference between the real process of evapotranspiration and the conceptual process applied in the numerical model. As explained in the previous section (Figure III.32), this period is recognized as a high evapotranspiration season according to the Thornthwaite algorithm. In the numerical model, the value of calculated *AET* is directly taken from the aquifer because the unsaturated layer is not modeled. But in the reality, the groundwater level in this area is far below the ground surface (about 13 m or even deeper) so that the aquifer is too low to afford this exchange with the atmosphere. In another word, the only source of *AET* in reality is the *EUR* formed by residual water in the surface soil layer after the rainfall (Figure III.38). Hence, the loss of water from the aquifer is overestimated in the numerical model. This error is especially notable for a dry spring after a rainy winter, when the *EUR* is involved to afford the high *AET* demand. According to the algorithm, the *EUR* reaches its maximum value after a rainy winter, then for a dry spring, the *EUR* in the soil affords the *AET* due to the lack of precipitation. Finally this high *AET* is deducted directly from the aquifer in the numerical model. But in reality, the whole process happens in the surface layer of the soil and the aquifer is not involved at all.

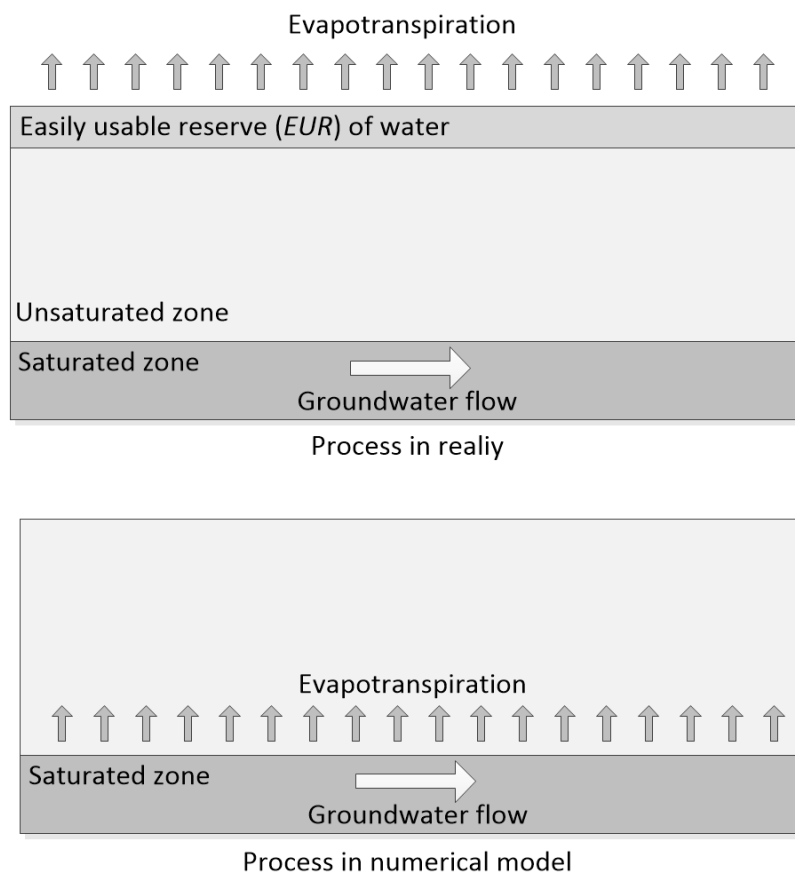


Figure III.38. Difference between the real process of evapotranspiration and the conceptual process applied in the numerical model (Author's design).

In conclusion, this error is more likely to happen when the two following conditions are detected: a) a dry spring after a rainy winter; b) in the area where the groundwater level is too low. This explains why the error is obvious at piezometer P16, where the groundwater level has depth more than 12 m, but less detectable at piezometers P36 and P4B, where the groundwater level has depth less than 7.5 m and 6.6 m, respectively. It can also explain why this error is not observed during the spring of 2012. The precipitation during the winter of 2012 is too little to refill the EUR in the soil ($P_{Jan} + P_{Feb} + P_{Mar} = 85.3$ mm), while the years of 2010 and 2011 have a more rainy winter ($P_{Jan} + P_{Feb} + P_{Mar} = 255.6$ mm for 2010 and $P_{Jan} + P_{Feb} + P_{Mar} = 291.7$ mm for 2011).

Another simulation is performed with the AET calculated with $EUR_{max} = 0$ mm (Figure III.39). According to the explanation, the underestimation of simulated groundwater level is due to the high AET which is deducted directly from the aquifer in the numerical model. With the new EUR_{max} , the AET decreases thus the underestimation of the groundwater level in spring disappears. However, this new EUR_{max} leads to an overestimation of the groundwater level in the urban area (P36) during

winter season (January and February) of 2011, because the AET is underestimated. The comparison also shows that the influence of different AET values on the simulated groundwater level is not significant. At least, the results simulated with AET that is calculated with different EUR_{max} have the same tendency with the measured data.

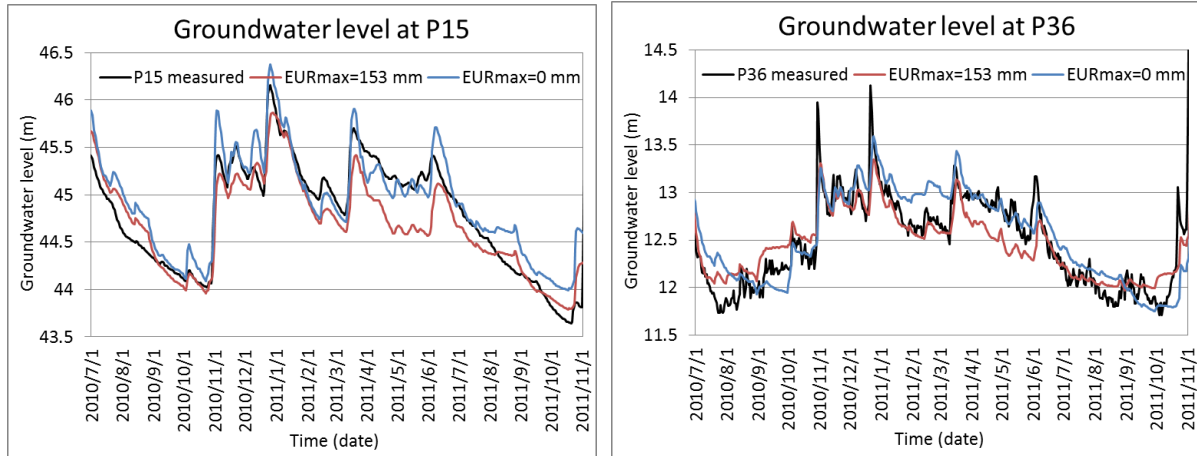


Figure III.39. Comparison of the simulation results with different EUR_{max} value.

III.7.3.2 Two approaches to model the river-aquifer disconnection

In the groundwater flow model, the disconnection between the river and the aquifer is modeled by a virtual level ψ_{min} (Eq. 3). Since the unsaturated layer is not considered in the model, the principle to model the disconnection is to limit the flux of river-aquifer exchanges. The virtual level ψ_{min} helps to reduce the flux by replacing the real groundwater level ψ_g which is lower. With the calibrated transfer rate ϕ , the flux of exchange can therefore be modeled by this method.

The method to model the disconnection is not unique. In this section, another method is used to perform a simulation so as to compare with the virtual level method. The “maximum flux” method introduces a threshold value of the flux of exchange q_{max} , the calculation of the transfer boundary becomes:

$$q_{ex} = \begin{cases} \phi_{in} \cdot (\psi_s - \psi_g), & \text{if } \phi_{in} \cdot (\psi_s - \psi_g) \leq q_{max} \\ q_{max}, & \text{else} \end{cases} \quad \text{Eq. 35}$$

This method can also limit the flux of exchange, but the disadvantage of this method is quite clear: when the calculated flux exceeds the threshold q_{max} , the flux cannot vary in proportion to the water level in the river (Figure III.40).

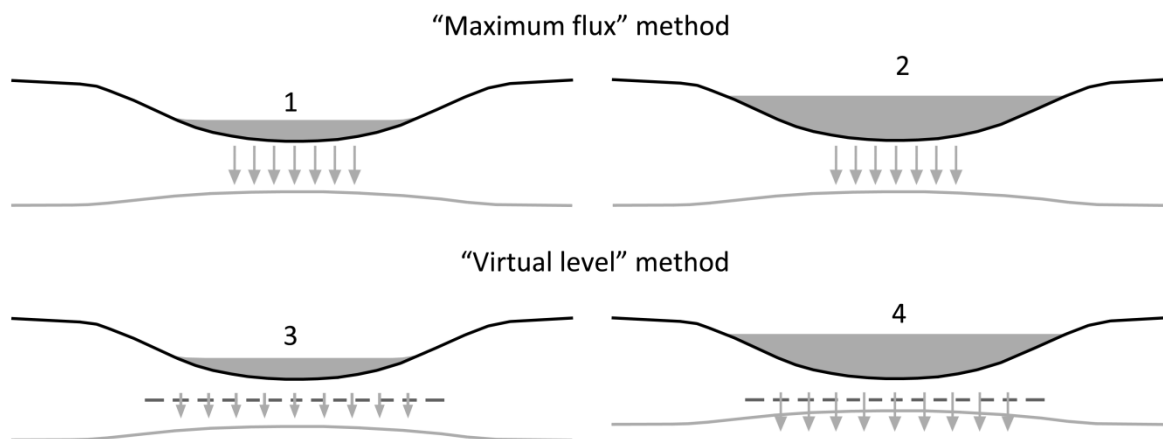


Figure III.40. Principle of two methods to model the disconnection between the river and the aquifer (Author's design).

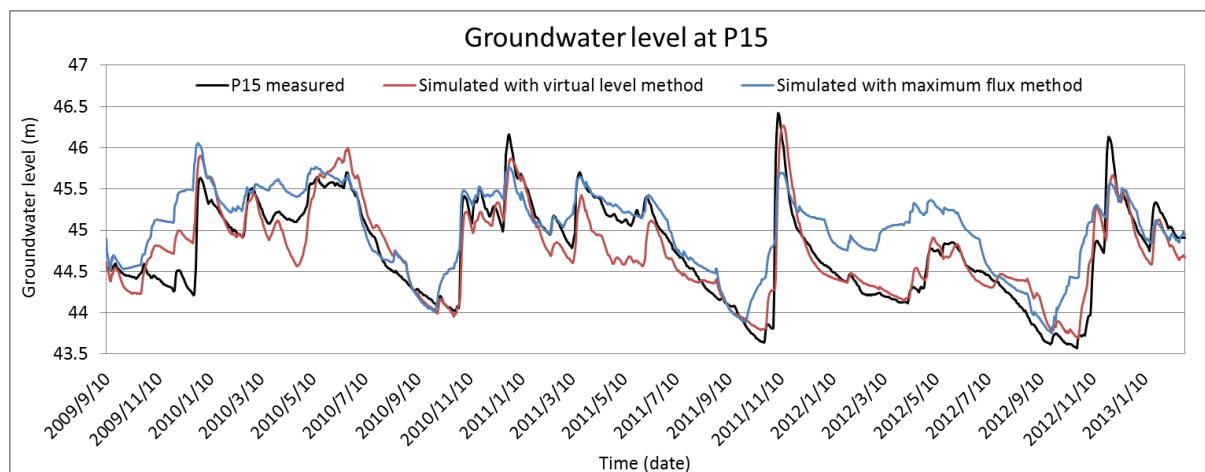


Figure III.41. Comparison of the results simulated with two methods that model the disconnection.

A simulation is performed with the same input data except for the disconnection modeling method. Figure III.41 shows the comparison of the simulated groundwater level at P15, where the disconnection between the river and the aquifer is observed. Through the comparison, the main defect of this method is the insufficient simulated flux when there is an extreme peak of the groundwater level. The flood peak on November 2011 has provoked a raise of water level in the river, which has also brought a peak of groundwater level through the river-aquifer exchanges. In the numerical model with the maximum flux method, the limit of the q_{max} leads to an underestimated flux, therefore the peak is not modeled correctly. By contrast, the virtual level method can simulate the peak because the flux, even though limited by the calculation with ψ_{min} , is still in proportion to the surface water level. The application of the maximum flux makes it difficult to find a value of q_{max} to fit both the rainy season and the dry season. The q_{max} may either 126optimization126 the peak value, or overestimate

the trough value of the flux, especially for the case when the fluctuation is huge, like the period from November 2011 to September 2012 shown in Figure III.41. Above all, the comparison proves that the maximum flux is not well adapted to model the river-aquifer disconnection due to the presence of clogging layer.

III.7.3.3 Analysis of the output quality

The model evaluation tells that the groundwater flow model gives a less satisfying simulated result at piezometer P16. The time series shows that the peak value is well simulated, which means that the river-aquifer exchange is correctly calculated with a calibrated transfer rate ϕ_{in} in the case of infiltration. Since the groundwater table has a depth of 12 m, the feeding direction from aquifer to river is not likely to happen in this area. Besides, the specific yield, which mainly determines the amplitude of the peak, is also calibrated after the sensitivity analysis. The left influential factors in the numerical simulation of groundwater flow are: hydraulic conductivity, groundwater extraction, geological layers and direct water recharge/loss. Hence, the low quality of the simulated result at piezometer P16 is caused by the inaccuracy of these inputs.

Among the four inputs, the geological layers and the hydraulic conductivity have a big uncertainty. The geological layers of the model are built with two digitalized maps which are made based on geological drilling tests. A lot of hypotheses have been added when the maps have been made. Therefore it has become a big source of inaccuracy of the model.

The hydraulic conductivity of the alluvium used in the model comes from measured values, but the values of field measurement could be not representative depending on the complexity of the alluvium. Moreover, the measuring points are irregularly distributed in the valley (Figure III.11). For the area without measurement, only interpolated values of hydraulic conductivity are used, which is also a source of inaccuracy.

In this model, the undocumented groundwater extraction should also be responsible for the inaccuracy model. In the current model, the undocumented groundwater extraction for agricultural use is estimated with measured groundwater level, accompanied with many hypotheses. The report of the local water agency only gives the consumption of groundwater pumped by big industries. However, it is also possible that the sum of the groundwater consumed by the small industries becomes a great quantity which should be no longer ignored.

To direct recharge/loss is a model input that is calculated with precipitation, runoff coefficient and *AET*. The precipitation is a measured value and *AET* is a variable that is calculated with measured values by using a validated algorithm. They are used to the whole model so it should not be responsible for a local error. The runoff coefficient, which is a factor directly multiplied by the precipitation, is an empirical parameter that depends on the land use. The runoff coefficient is therefore a source of inaccuracy.

The geological study shows that no lens is detected in the alluvium in this area, and the hydraulic conductivity varies between 0.003 to 0.005 m/s [Guglielmi, 1993]. Thus neither the inaccuracy of the geological layer data nor the interpolation of the hydraulic conductivity should be a cause of bad output of the model. The error is observed particularly during the dry season, when the precipitation is too few to give a significant impact on the groundwater level, so the runoff coefficient seems not to be the cause of such a notable error. All things considered, it is reasonable to assume that the error shown in the simulated result is mainly caused by the wrong estimation of the non-recorded groundwater extraction in this area.

Figure III.42 is a land use map of the area where the piezometer P16 is located. It can be seen that this area has a complex land use distribution containing industrial, agricultural and urban zone. In the model, this area is totally considered as farmland, but it is possible that the industries consume more groundwater than the farmland, or the farmland itself also consumes more than what is estimated.

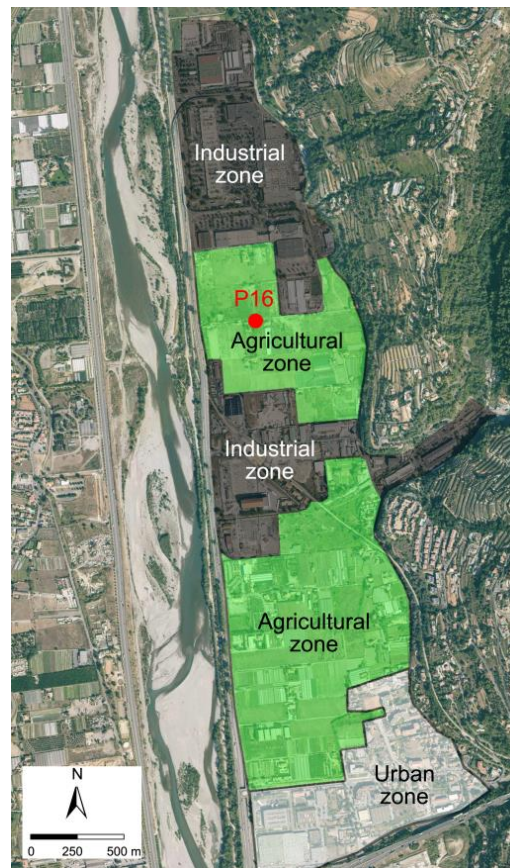


Figure III.42. Complicated land use in the area of piezometer P16 (Author's design. Source: www.geoportail.gouv.fr).

III.7.4 Post-treatment of the results

III.7.4.1 Contour map of groundwater level

The simulated results of two hydrological conditions are exported and compared. September 1st, 2012 is chosen to represent the dry period, and December 15th, 2012 for the rainy period during winter.

Figure III.43 shows the contour map of groundwater level. The groundwater level has a higher gradient in the section near the weir No.9 and the weir No.4. In the downstream section where the groundwater level drops from 25 m to 0 m, the hydraulic gradient is much milder than the upstream area. For the whole valley, the groundwater level in summer is lower than that in winter, but this difference is more notable at some places such as the confluence of Esteron and Var and the upper section, where the difference is more than 4 m, and the municipal pumping stations in the downstream section, where the water level in the summer is much lower due to the high demand of water.

III.7.4.2 Darcy flux

Figure III.44 illustrates the simulated Darcy flux in the alluvial aquifer, the bullets indicate the flow direction and the color shows the magnitude. For both dry period and rainy period, the valley has a higher groundwater flux near Le Broc lake, where the value is around 0.001 m/s on the right bank of the river. The flux decreases to 10^{-4} m/s in the section of the weirs. The flux is around 10^{-5} m/s in the downstream section where the municipal pumping stations are located, and it keeps decreasing till 10^{-6} m/s in the aquifer of the airport.

Generally, the direction of the flux is primarily parallel to the streamline of the river. But it is slightly diverted because of the river-aquifer exchanges. During the dry period, it can be seen that the water flows back to the aquifer from sea. It means that under certain circumstances, for instance, dry period with a high pumping rate at the airport, seawater intrusion may happen. During the rainy period, the groundwater flow in the unconfined aquifer is towards the sea, thus the seawater intrusion is less likely to occur.

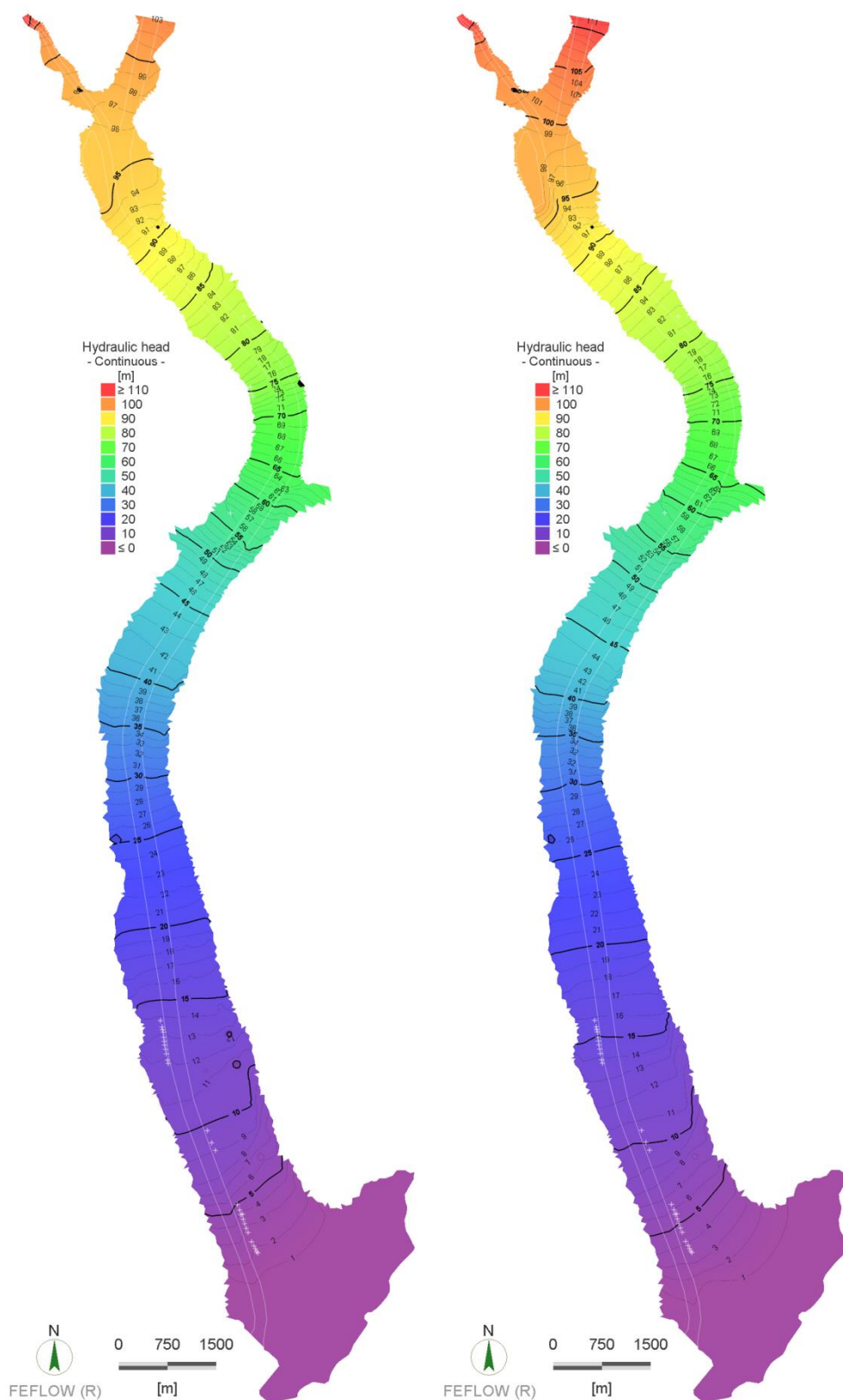


Figure III.43. Contour map of groundwater level during the dry period (left) and rainy period (right).

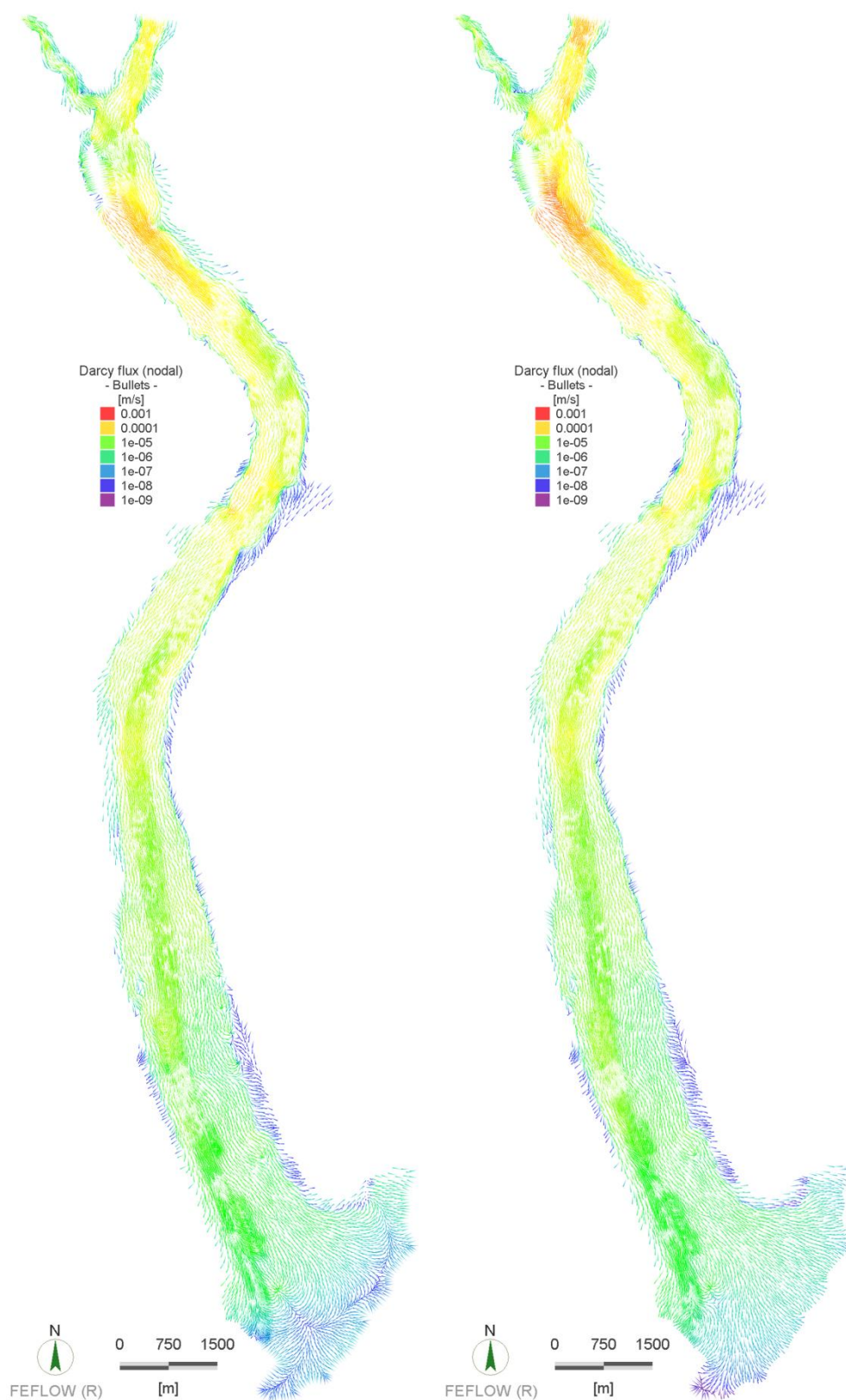


Figure III.44. Nodal Darcy flux of groundwater flow during the dry period (left) and rainy period (right).

III.7.4.3 River-aquifer exchanges

Figure III.45 shows the simulated results of river-aquifer exchanges. On the left figure which indicates qualitatively the feeding direction, 4 sections are identified as river-aquifer feeding direction and 3 sections are found between them where aquifer-river feeding direction appears. The comparison between the result of dry period and rainy period indicates that, when groundwater level rises during the winter, the river section where the aquifer feeds the river is longer. On the right side of the figure, some sections are chosen to show the contrast of exchange flow rate in detail. The unit used in the post-processing is m^3/day , which is the product of the flux of exchange, calculated with Eq. 3, times the area of the computational grid on the riverbed that it represents, which is around 300 m^2 . It shows that the river has a stronger exchange in the upstream area than in the downstream area. Near Le Broc lake, the aquifer feeds the river with a flow rate more than $15000 \text{ m}^3/\text{d}$, equivalent to 0.58 mm/s . Since the groundwater level is always beneath the water level in the river at the section of weirs, the direction of the exchange flux is always towards the aquifer. Despite of the disconnection, there is $2000 \text{ m}^3/\text{d}$ of water going into the aquifer during dry season, which equals to a flux of 0.07 mm/s . In the downstream area, the exchange flux has two directions, but the magnitudes for both directions are not more than $500 \text{ m}^3/\text{d}$, which is 0.02 mm/s .

Figure III.46 shows a longitudinal profile of the riverbed as well as the groundwater table, which corresponds also to the slope of the riverbed. It is apparent that the weirs have a negative effect on the groundwater resource conservation. The groundwater table withdrawal is more severe in the weir sections. The restoration appears near the lowered weirs (weir No.10 and No.9) and the destroyed weirs (No.3 and No.2), because the river-aquifer exchanges become stronger since the natural river profile has been regained.

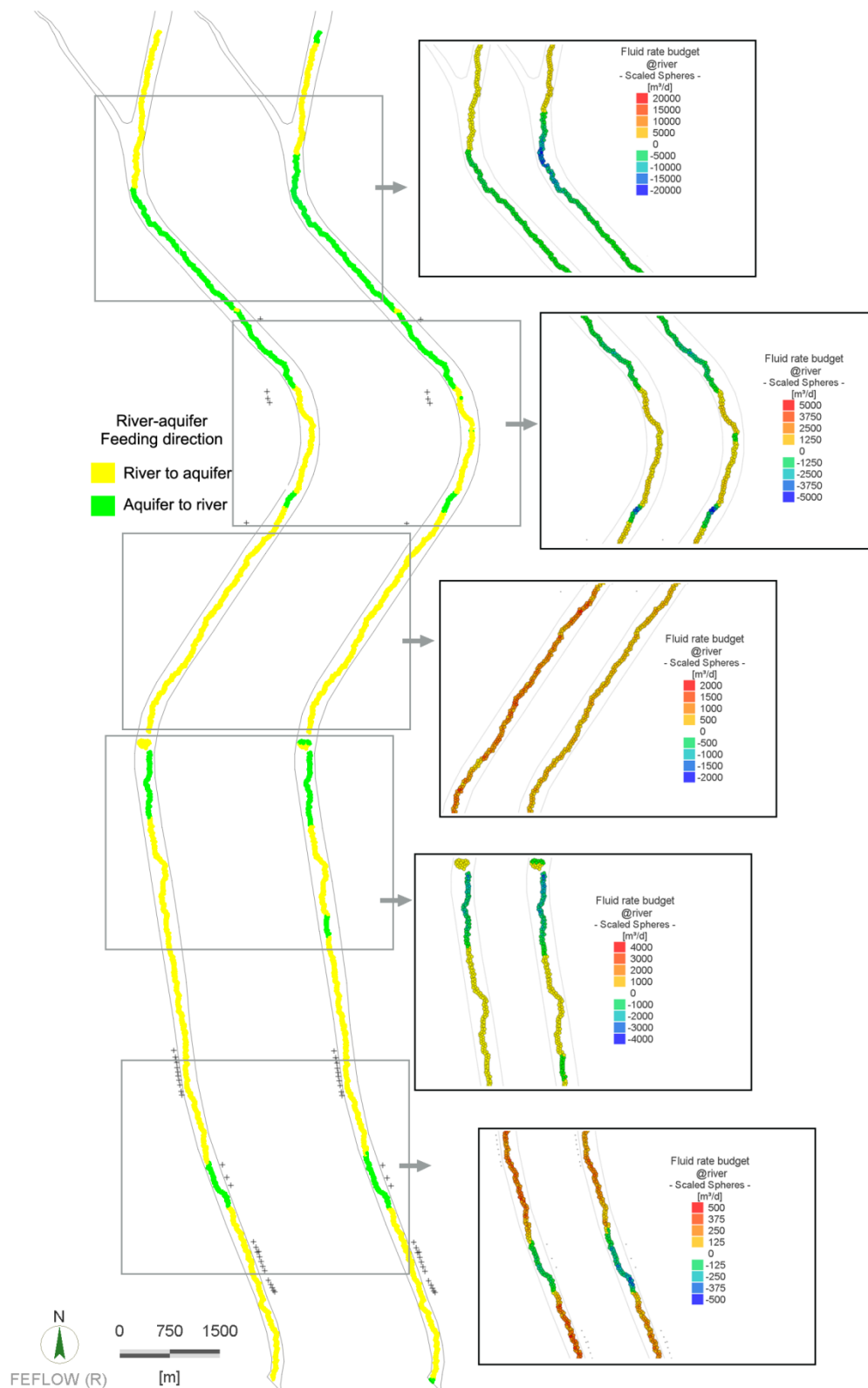


Figure III.45. River-aquifer exchanges during the dry period (left) and rainy period (right).

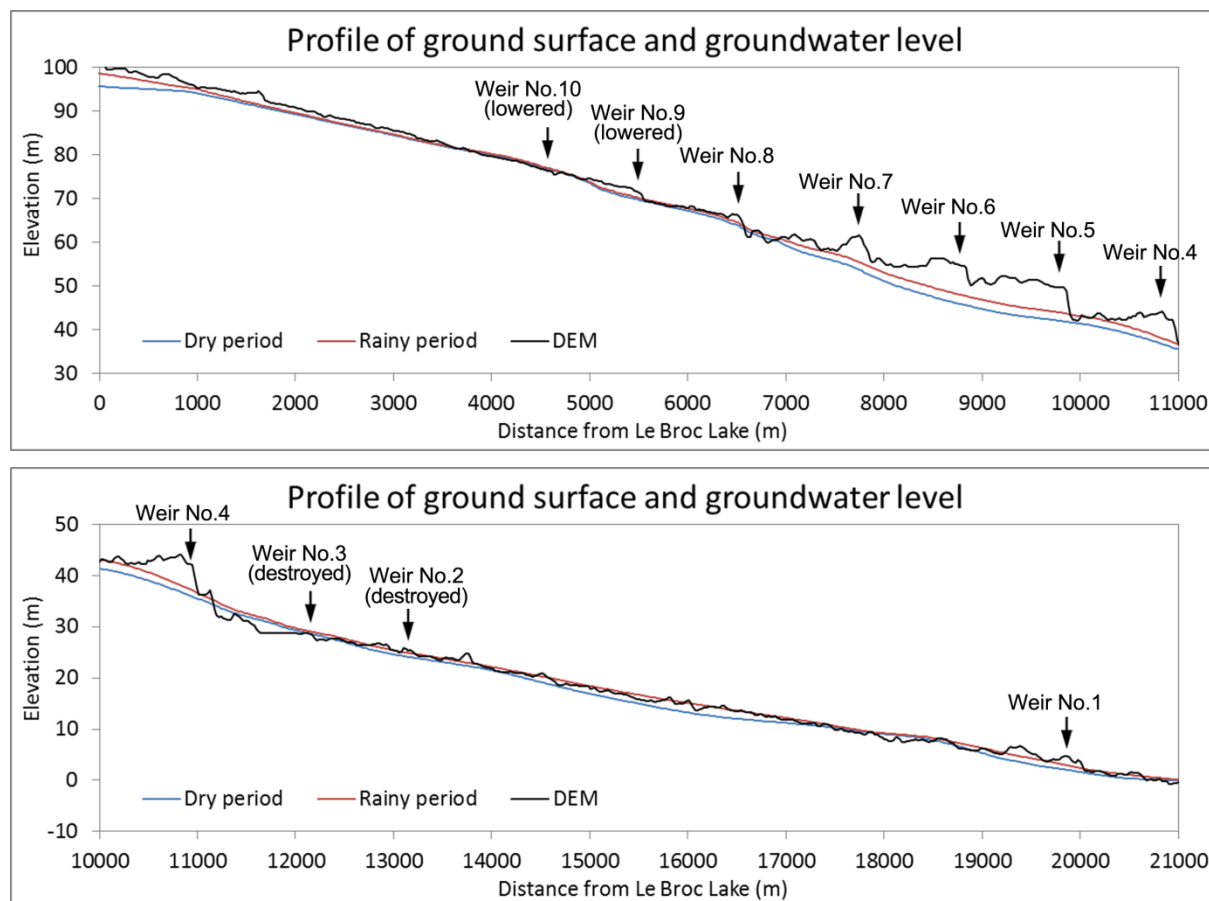


Figure III.46. Profile of ground surface and groundwater level along the streamline of Var river.

III.8 Conclusion

Through the application case in the lower Var river valley, the methodology of groundwater modeling has been validated and the understanding of the unconfined groundwater flow in saturated layer in Mediterranean coastal area is enhanced. First, a maximum of data has been collected and analyzed in order to understand hydrological background and the characteristic of the groundwater flow in the studied area. Secondly, a conceptual model has been set up with necessary assumptions based on the conclusion of data analysis. Thirdly, together with the data, a numerical model has been set up to simulate the groundwater flow in the lower Var river valley. A few parameters are studied with a sensitivity analysis then a calibration of these parameters has been carried out. Finally, the model has been validated by performing a simulation of 1266 days, the results have shown that the model is able to represent the hydrogeology at the scale of a sub-catchment of 146 km², and the hydrodynamics of the unconfined groundwater flow in the saturated layer of the lower Var river valley.

III.8.1 Model setup

Except for the upstream and downstream boundary conditions, three main source/sink terms are identified and considered in the groundwater modeling of unconfined aquifer in Mediterranean coastal area (Figure III.47). These three source/sink terms cover almost the main factors that determine the groundwater flow. The input files are made based on the measured data, but a lot of hypotheses are made in the preparation phase.

The direct water recharge/loss is calculated with precipitation and the actual evapotranspiration (AET). The monthly AET is calculated by using the Thornthwaite algorithm then equally distributed to a daily scale. The empirical parameter, easily usable reserve of water in the soil (EUR_{max}) is calibrated after having studied the hydrological condition from 2000 to 2013. The calibration gives an $EUR_{max} = 153$ mm in the lower Var river valley.

The river-aquifer exchanges are modeled by a transfer boundary. The water level in the river is simulated by a 1D river hydraulic model built with MIKE11, then used as an input in the groundwater flow model. The transfer rate ϕ is calibrated after a sensitivity analysis. In the numerical model, the disconnection between the river and the aquifer is modeled by introducing a virtual groundwater level. The groundwater extraction for domestic and industrial use is recorded by the municipality and the local water agency. The recorded values are highly reliable thus they are directly used as a model input. The groundwater extraction on the farmland is estimated to be equivalent to a flux of 0.015 m/s. This value is assigned only for the summer season in the model.

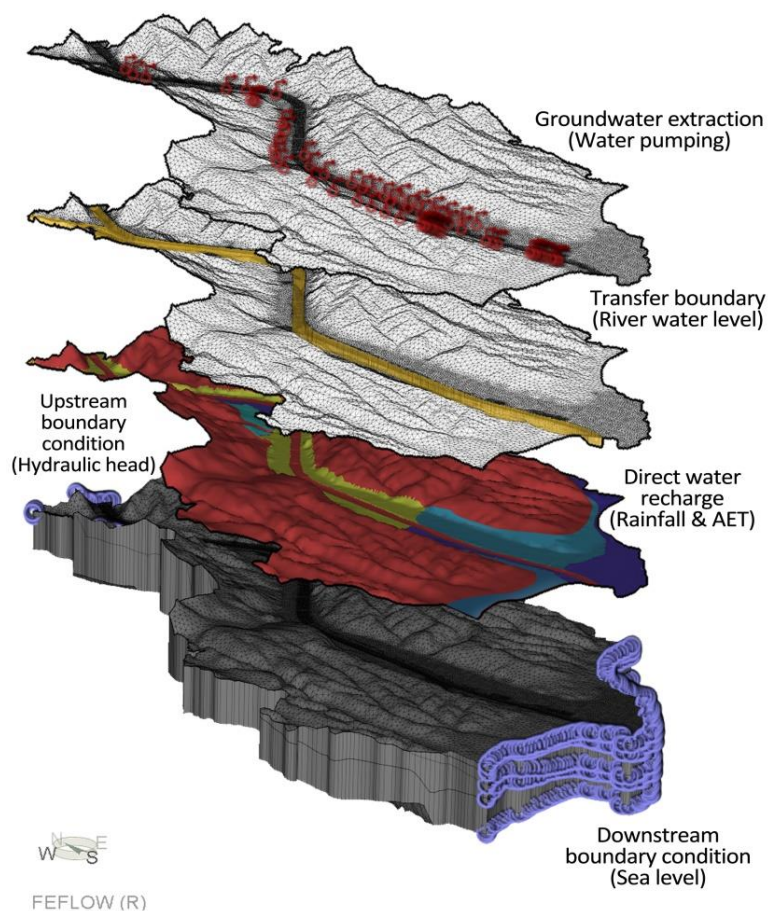


Figure III.47. Main boundary conditions and source/sink terms used in the numerical model.

A sensitivity analysis is performed by a series of simulations that last for 293 days from 2012 to 2013. Through the conclusion of the analysis, the specific yield influences the fluctuation of the peak values and the speed of the withdrawal after a peak. After the calibration of its value, a range between 0.05 to 0.2 is assigned for the valley with spatial distribution. Compared to the specific yield, the transfer rates have a more significant influence on the groundwater flow. The order of magnitude of calibrated in-transfer rate is 10^{-5} s^{-1} , while the out-transfer rate is around 10^{-4} s^{-1} . Similarly, they are assigned with spatial distribution on the riverbed.

The main conclusion of this application case study is that the conceptual model must be set up on the basis of a good knowledge of the study area. Then a huge quantity of data is the prerequisite to build a numerical model. Some data may be missing due to a difficult acquisition, but the sensitivity analysis gives useful information which can help to enhance the understanding of the numerical model as well as the impact of target variable. The conclusion of the analysis may also help to save time for model calibration.

III.8.2 Model results and analysis

Nash coefficient (NSE) and mean absolute error (MAE) are used as indexes to evaluate dynamic results that are evaluated on 6 points distributed along the valley. The results are satisfying at 5 points where the NSE is between 0.66 and 0.94, while the MAE varies between 13 and 24 cm. The model gives less accurate results at piezometer P16, where the simulated groundwater level during dry periods is underestimated. Besides, the model underestimates peak values of the groundwater level during extreme flood event. The error is more notable for the piezometers which are near the river banks than those which are far from the river banks.

Several discussions have been carried out based on the simulated results. Since the unsaturated layer is not considered, the loss due to the evapotranspiration is directly removed from the aquifer. Therefore the simulated groundwater level is underestimated, especially in low groundwater level area for a dry spring after a rainy winter.

Two methods that enable to model the disconnection between the river and aquifer are compared. The application of the “maximum flux” q_{max} is not recommended because it may underestimate the peak value and overestimate the trough value. The “virtual level” method, however, can give better result for both high level and low level conditions.

As it has been previously stated, like any other hydraulic models, the results of groundwater model is very sensitive to the quality of input data. A valid input data with high accuracy leads to a good result with good consistency. In contrast, a roughly estimated input data can hardly result in satisfying output. The inaccuracy of the result at P16 is probably due to the wrong estimation of the groundwater extraction, knowing that the land use in this area is quite complex. Therefore the quality of the result at P16 can be improved by assigning more precise groundwater extraction data. The underestimation of the peak values of groundwater level during flood events can be improved by applying the instantaneous discharge instead of the daily average discharge, which is used to build the numerical model.

Chapter IV. Model application in groundwater management

After having completed the modeling validation, the groundwater model could be accepted for supporting the decision-making process in groundwater management. One of the most concerned uses of the numerical modeling is to perform the scenario simulations in order to predict the possible conditions under certain circumstances, and also anticipate reaction plans based on the simulation results.

One of the biggest challenges in groundwater management in the lower Var river valley is to estimate the groundwater level during extreme hydrological events, such as flood and drought hazards. Based on the simulated results, the local water management services may carry out groundwater extraction plans in municipal pumping stations to maintain the groundwater level during drought events, and to ensure the drinking water quality during the flood hazards. The designed scenarios should show different levels of severity (*e.g.* different return periods) and their boundary conditions should be concluded from statistical analysis of recorded data.

In addition, as explained in Chapter I, the alluvial aquifer in the Var valley faces the threat of the groundwater pollution. Therefore the water management services have to anticipate the pessimistic case of the groundwater pollution. Even though the performed model validation focused on the hydrodynamics of the groundwater flow, the model is able to simulate the pollutant transport if certain parameters are correctly chosen.

Since the unconfined aquifer is connected to the Mediterranean Sea, the estuarine area of Var river has an intense interaction with the seawater. As the pumping stations located in the downstream part (Figure I.20) have a considerable pumped volume in both unconfined and confined aquifer, this area has a high possibility to be polluted by the salt water intrusion when the salt water wedge moves towards the land side under certain conditions (*e.g.* low groundwater level in unconfined aquifer, low hydraulic head in confined aquifer or high pumped volume). However, knowing that the salt water intrusion can only happen in the estuary, the current model area is too large to give a precise result for this study. Furthermore, in the current model, the alluvium is modeled by a single layer. This is not reasonable when the confined aquifer will be included in the study. Considering these factors explained above, a new, smaller but complex model has to be developed to study the saltwater

intrusion. Some basic input data of the current model can be also applied in this new model. Comparing with the current model, the new model kept the same material properties such as hydraulic conductivity of unconfined aquifer, in/out transfer rate and specific yield *etc.* The new model can also apply the outputs of the current model as its boundary conditions such as hydraulic head and Darcy flux (Section III.7.4). However, more detailed soil information like clay and silt lenses in the estuary were taken into account in the new model in order to model the hydrodynamics in confined aquifer. The initial goal of the AquaVar project is to develop a modeling system to study the hydrology, river hydraulics and groundwater hydraulics in the lower Var river valley. After the development of individual numerical models, a management tool which unites the three models needs to be developed. A preliminary conception of the management tool will be introduced in this chapter.

IV.1 Scenario simulations of extreme hydrological events

According to the characteristics of Mediterranean climate, the lower Var river valley suffers from a shortage of precipitation in the summer to the risk of flood due to the intense rainfall during winter. Consequently the scenario simulation should focus on these two types of events.

In this study, different return periods of the river discharge were calculated in order to quantify the severity of the events. The calculation is based on the recorded discharge instead of measured rainfall because, compared with the rainfall records which collected only cover the low Var valley, the discharge measured at the outlet of the Var catchment which could present the general hydrological condition of whole catchment. One of the main reasons of this data selection is that the groundwater condition in the lower Var valley is not only affected by the local precipitation. When there is no rainfall recorded at the lower Var valley, the groundwater could be still adequate as the big channel flow generated by the upstream rainfall event could continue feeding the aquifer in the downstream valley. Even during the flood event, compared with the impacts of river-aquifer exchanges (Figure III.45), the infiltration caused by rainfall (Figure III.32) on the groundwater table changes is relatively low.

To make sure the designed scenarios are able to represent the regional hydrological characteristics more reliable, the recorded discharge data were applied in scenarios design. Thanks for the long-time period discharge measurement at the outlet of Var catchment, the return periods of flood and drought

events can be calculated by statistical methods, then several special events that are corresponding to certain return periods are directly selected as the scenarios simulated by the numerical model.

IV.1.1 Methodology for scenario designing

In the lower Var river valley, a storm can lead to a flood during winter when the soil saturation reaches its maximum value. A single rainfall event during summer can hardly provoke a flood event because the soil is able to absorb a huge quantity of water thanks to the low saturation. Through the measured precipitation from 1944 to 2015 by Météo France, there are years for which the highest daily accumulative precipitation of the year happens during summer (June, July, August and September), but it is rare that the highest daily average discharge happens during these four months (Table IV.1 and Table IV.2). Therefore the flood scenarios should be the events that happen during the rainy season (October, November and December). Similarly, the drought scenarios should be events that happen during the dry season (July, August and September).

Table IV.1. Occurrence of the highest daily cumulative precipitation of the year through a measurement of 72 years from 1944 to 2015, at the airport station (Figure I.10, Source: Météo France).

Month	Jan.	Feb.	Mar.	Apr.	May	Jun.
Number of highest rainfall events occurred in the month	4	5	5	3	1	3
Month	July.	Aug.	Sep.	Oct.	Nov.	Dec.
Number of highest rainfall events occurred in the month	2	2	8	12	17	10

Table IV.2. Occurrence of the highest daily average discharge of the year through a measurement of 28 years from 1974 to 1976, from 1985 to 2000, the year of 2006, from 2008 to 2015, at the Napoléon III station (Figure I.15, Source: Eaufrance).

Month	Jan.	Feb.	Mar.	Apr.	May	Jun.
Number of highest discharge events occurred in the month	2	2	0	4	2	1
Month	July.	Aug.	Sep.	Oct.	Nov.	Dec.
Number of highest discharge events occurred in the month	0	1	0	7	7	2

IV.1.1.1 Statistical analysis of flood scenarios

For flood events, the Gumbel law [Gumbel, 1935; Gumbel, 1941; Laborde, 2010] is applied to calculate the return period of the discharge of the Var river. This method is a double exponential law which describes the distribution of the maximal values chosen from samples, which, in this case, are maximal daily average discharges through a measurement of 28 years.

According to Laborde [2010], a statistical law that involves more impact factors have a relatively higher uncertainty. Hence, the law with more than 3 factors could not be the prior choice when the amount of the samples is not big enough. For the study of maximal daily average discharge of the lower Var river, only 28 values are available, hence Gumbel law is preferable because it involves only two parameters: the gradex g which is the scale parameter, and the mode x_0 which is the position parameter. The cumulative distribution function of Gumbel distribution is:

$$F(u) = e^{-e^{-u}}, \quad \text{Eq. 36}$$

where u is defined by:

$$u = \frac{x - x_0}{g}. \quad \text{Eq. 37}$$

By combining the Eq. 36 and Eq. 37, the expression of the probability of a variable x is:

$$F(x) = e^{-e^{-\frac{x-x_0}{g}}}. \quad \text{Eq. 38}$$

In this case, the variable x is therefore the maximal value of the daily average discharge. The gradex g and the mode x_0 is defined by:

$$g = 0.78\sigma \text{ and } x_0 = \bar{x} - 0.577g, \quad \text{Eq. 39}$$

with \bar{x} the mean of the discharge and σ the standard deviation:

$$\bar{x} = \frac{\sum_{i=1}^n x_i}{n} \text{ and } \sigma = \sqrt{\frac{\sum_{i=1}^n (x_i - \bar{x})^2}{n-1}}, \quad \text{Eq. 40}$$

where n is the size of the sample, in this case study, it is the number of the measurements, x_i is the measured value. From Eq. 36 and Eq. 37, the relation between the variable and the probability is given below:

$$u = \frac{x - x_0}{g} = -\ln[-\ln(F(x))]. \quad \text{Eq. 41}$$

In risk analysis, return period is often used to describe the probability of an event. It is the inverse of the probability that the event will occur in any one year. For example, a 10-year flood has a $1/10=0.1$ (or 10%) chance of I in any one year and a 50-year flood has a 0.02 (or 2%) chance of I in any one year. The expression of the return period T of an event is defined as follow :

$$T = \frac{1}{1 - F(x)}. \quad \text{Eq. 42}$$

In order to calculate the discharge corresponding to a certain return period, the target variable in terms of the return period is given by combining the Eq. 41 and Eq. 42:

$$x = -g \cdot \ln \left[-\ln \left(1 - \frac{1}{T} \right) \right] + x_0. \quad \text{Eq. 43}$$

The confidence interval is an observed range that the probability of the observed value is contained within the interval limited by two boundaries p_1 and p_2 . For a confidence interval that equals to $\alpha\%$ on an estimation of a variable, there is a probability of $0.5\alpha\%$ that the variable is smaller than the upper boundary p_1 or bigger than the lower boundary p_2 . The confidence interval at $\alpha\%$ on quantile x_F is given by the standard division σ and the estimation of the quantile \hat{x}_F :

$$\hat{x}_F - h_1 \sigma \leq x_F \leq \hat{x}_F + h_2 \sigma, \quad \text{Eq. 44}$$

where the two parameters h_1 and h_2 depend on the sample size n , the probability F and the value of α :

$$h_1 = \frac{\frac{u_\alpha}{\sqrt{n}} \sqrt{1 + 1.13t_F + 1.1t_F^2} - \frac{u_\alpha^2}{n} (1.1t_F + 0.57)}{1 - 1.1 \frac{u_\alpha^2}{n}} \quad \text{Eq. 45}$$

$$h_2 = \frac{\frac{u_\alpha}{\sqrt{n}} \sqrt{1 + 1.13t_F + 1.1t_F^2} + \frac{u_\alpha^2}{n} (1.1t_F + 0.57)}{1 - 1.1 \frac{u_\alpha^2}{n}},$$

where, u_α is the probability of not exceeding $1 - \frac{1-\alpha}{2}$ of a variable that follows a standard normal distribution. For $\alpha=90\%$, $u_\alpha=1.6449$ and for $\alpha=95\%$, $u_\alpha=1.96$. t_F is the probability of not exceeding F of a variable that follows Gumbel distribution, given by the mean and standard deviation of the variable:

$$t_F = \frac{-\ln[-\ln(F)] - 0.577}{1.28}. \quad \text{Eq. 46}$$

There are 28 maximal values of daily average discharges recorded at Napoléon III bridge (Appendix 7). The gradex and the mode can be thus calculated by using Eq. 39.

$$g = 248.9 \text{ and } x_0 = 324.3 .$$

The distribution of the maximal value of daily average discharge can thus be calculated with the two parameters (Figure IV.1). A confidence interval of 90% is also shown on the same figure. The theoretical daily average discharge corresponding to events of different return periods are calculated by Gumbel law. The historical events with similar daily average discharge are chosen as scenarios to be simulated (Table IV.3). The discharge and precipitation data of flood events are illustrated in Figure IV.2. The figures show a strong correlation between the rainfall and the discharge. For the flood events, the lag time is normally less than 24 hours. It indicates that the lower Var river valley is characterized by a quick-response runoff.

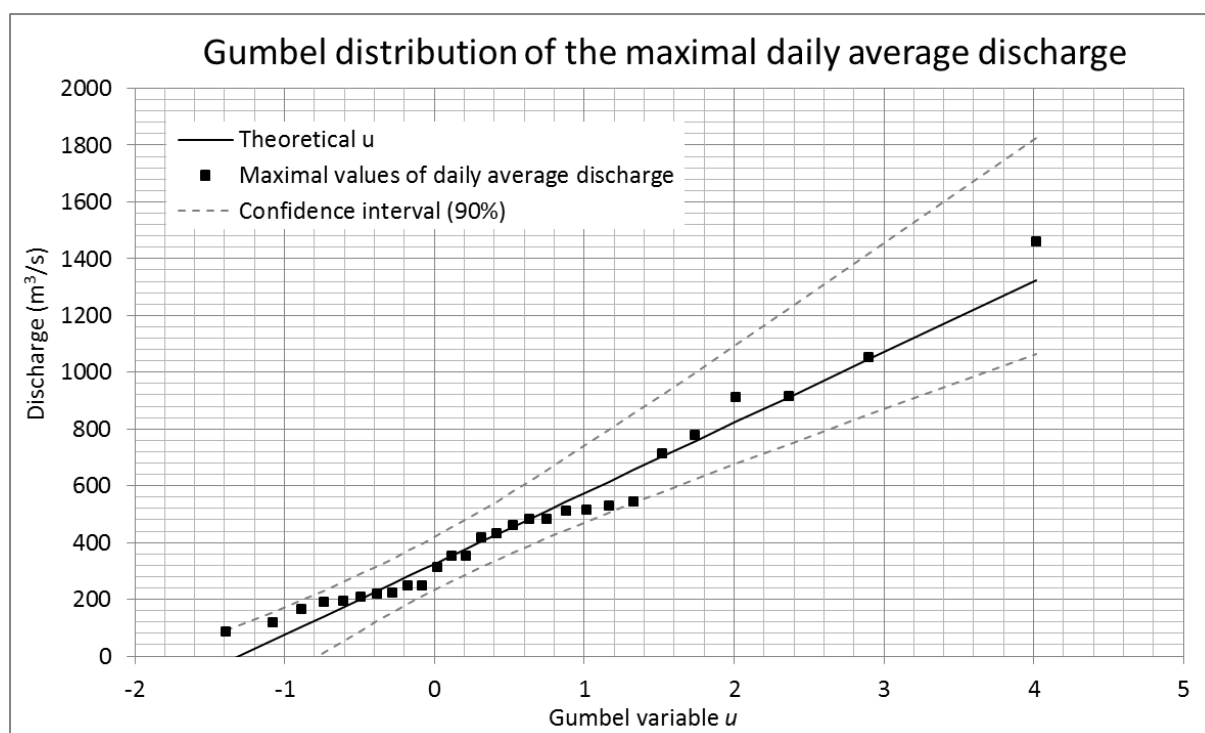


Figure IV.1. Gumbel distribution of the maximal values of daily average discharge measured at Napoléon III bridge.

Table IV.3. Flood events of scenario simulations

Return periods T (years)	Theoretical daily average discharges (m^3/s)	Recorded events	Recorded daily average discharges (m^3/s)
2	415.47	November 2014	482
5	697.55	October 1988	714
10	884.30	November 2011	910
20	1063.45	October 1993	1050
100	1469.09	November 1994	1460

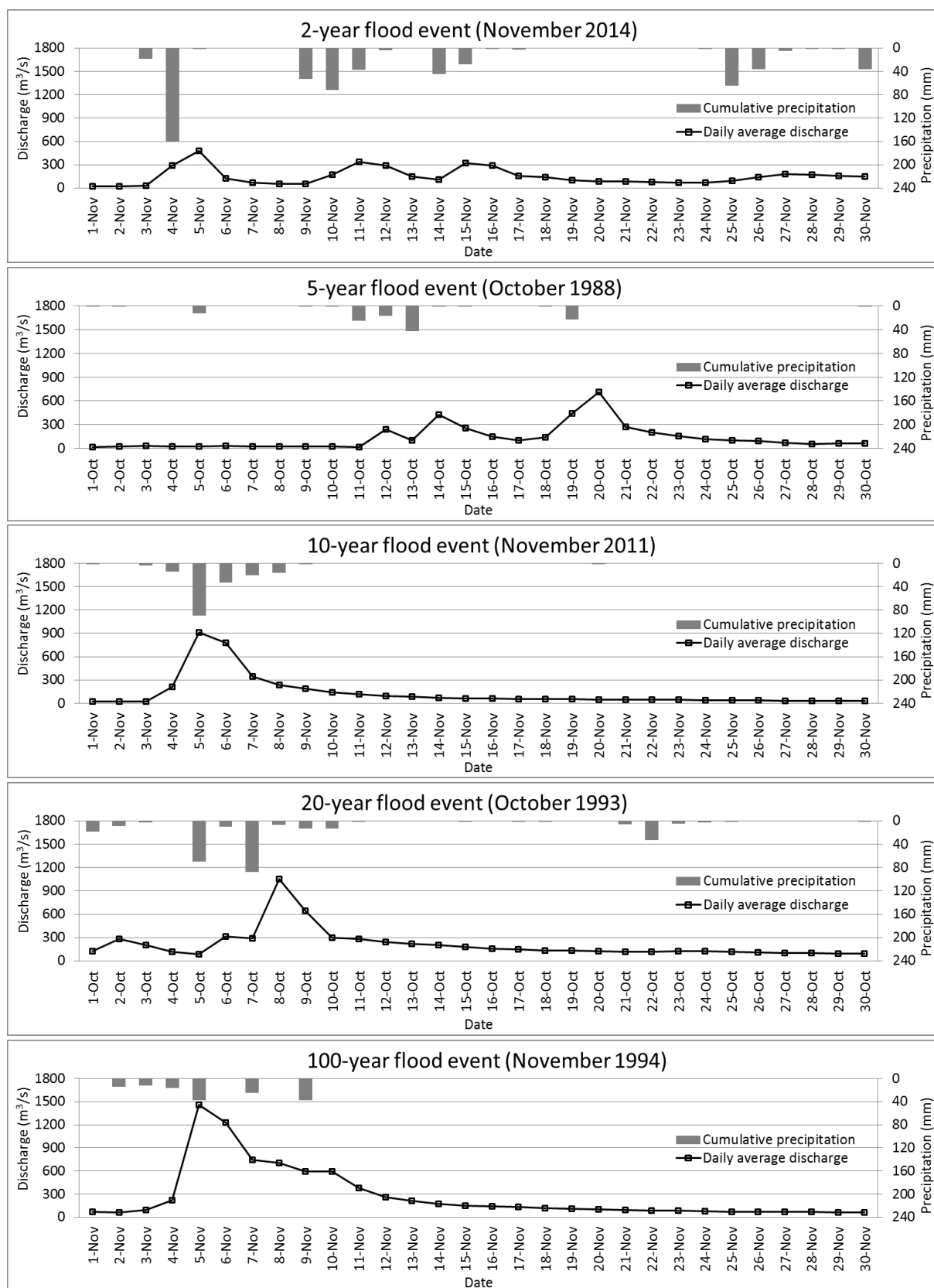


Figure IV.2. Rainfall and river discharge of flood events of scenario simulations, measured respectively at airport meteorological station and Napoléon III bridge gauging station (Figure I.10, Figure I.15).

These scenarios represent several types of flood happened in lower Var river valley. The 2-year flood represents a flood following a continuous rainfall. The biggest flood peak, which is also the first one, is generated by a heavy rainfall event (160 mm/day) after a long period without rainfall. Since the soil is not saturated, the discharge of flood peak is not extremely high (482 m³/s). The following peaks, however, are generated by less heavy rainfall.

The 5-year flood represents a major flood peak that occurs after a previous rainfall event. Since the soil is saturated, the precipitation that generates this peak is not very heavy. With the discharge contributed by the upstream sub-catchments, the measured discharge at the Napoléon III bridge is as high as 714 m³/s.

The 10-year flood is a single peak which is induced by a heavy rainfall event that lasts for 7 days. This flood peak is generated on a low base flow. Then the discharge recovered to its previous state progressively. The recorded daily average discharge of the peak is 910 m³/s, which arrives on the same day as the precipitation reaches its highest intensity, which equals to 92 mm/day.

The 20-year flood occurs on a high base flow due to previous rainfall events. The daily average discharge of the peak is 1040 m³/s, but the flow after peak maintains a high value more than 100 m³/s for a longtime because of the continuous light rainfall.

The 100-year flood is represented by the flood event of 1994 [Guinot and Gourbesville, 2003; Ma et al., 2016]. The flood peak occurs after a series of rainfall events. The flood lasts for 6 days due to a series of follow-up rainfall events. It takes also a long time for the river to recover its normal discharge after the flood peak.

IV.1.1.2 Statistical analysis of drought scenarios

In Mediterranean area, the drought period always happens during the summer season. The lack of rainfall leads to a low water recharge into the aquifer, meanwhile, it also provokes low water level in the river, thus the river cannot feed enough its aquifer. On the other hand, the demand of agricultural and domestic water use increases significantly during summer season, the increased groundwater extraction makes it even worse.

The Galton law, also called log-normal distribution [Johnson Norman et al., 1994], is used to calculate the return period of the river discharge of drought period [Kunatip and Supasit, 2012] in the lower Var river valley. As for the scenario design, the monthly average discharges of July, August and September are used to calculate the return period of the drought events.

In the theory of statistics, a random variable X follows a log-normal distribution if the variable $Y = \ln(X)$ follows a normal distribution. The log-normal distribution is given by the expression:

$$F(x) = \frac{1}{x\sqrt{2\pi}\sigma_Y} e^{-\frac{1}{2}\left(\frac{\ln x - \mu_Y}{\sigma_Y}\right)^2}. \quad \text{Eq. 47}$$

The log-normal distribution depends on two parameters: the scale parameter μ_Y and the form parameter σ_Y , their estimations with the method of moments are:

$$\sigma_Y = \sqrt{\ln\left(1 + \frac{\sigma_x^2}{\bar{x}^2}\right)} \quad \text{and} \quad \mu_Y = \ln \bar{x} - \frac{\sigma_Y^2}{2}, \quad \text{Eq. 48}$$

where \bar{x} is the mathematical expectation of the variable X and σ_x is the unbiased standard deviation of the variable X , which is defined as:

$$\sigma_x = \sqrt{\frac{1}{n} \left(\sum_{i=1}^n (x_i - \bar{x})^2 \right)}. \quad \text{Eq. 49}$$

More practically, the variable of Gauss distribution is used to calculate the quantile x_u :

$$x_u = e^{\mu_Y + u\sigma_Y}, \quad \text{Eq. 50}$$

where u is the variable of Gauss:

$$u = \frac{x - \bar{x}}{\sigma_x}. \quad \text{Eq. 51}$$

Its probability density function is

$$f(u) = \frac{1}{\sqrt{2\pi}} e^{-\frac{1}{2}u^2}. \quad \text{Eq. 52}$$

The confidence interval of α (in percentage) on the quantile x_u is a function of standard deviation σ_Y and expectation μ_Y :

$$x_{u1,2} = x_u \exp\left(\pm u_\alpha \frac{\sigma_Y}{\sqrt{n}} \sqrt{1 + \frac{x_u^2}{2}}\right), \quad \text{Eq. 53}$$

where u_α is the variable of Gauss corresponding to the probability not exceeding $1 - \frac{1-\alpha}{2}$ of a variable that follows a standard normal distribution. For $\alpha=90\%$, u_α equals to 1.6449 and for $\alpha=95\%$, u_α equals to 1.96.

There are 84 monthly average discharge values recorded during the summer season (July, August and September) at Napoléon III bridge (Appendix 8). The parameters can be thus calculated:

$$\bar{x} = 43.24 \text{ and } \sigma_x = 45.38 ; \sigma_Y = 0.716 \text{ and } \mu_Y = 3.511 . \quad \text{Eq. 54}$$

The distribution of the monthly average discharge is calculated with the four parameters (Figure IV.1). A confidence interval of 90% is also shown on the same figure. The theoretical monthly average discharge corresponding to events of different return periods are calculated by log-normal law. The historical events with similar monthly average discharge are chosen as scenarios to be simulated (Table IV.4).

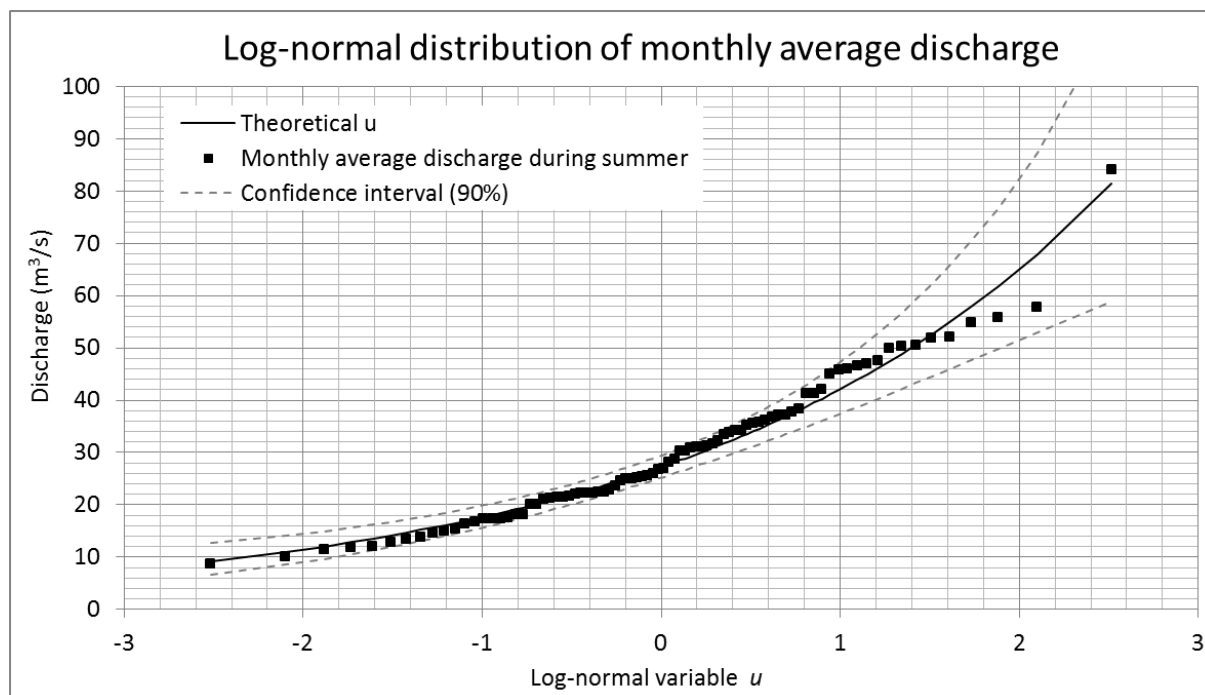


Figure IV.3. Log-normal distribution of the monthly average discharge measured at Napoléon III bridge.

Table IV.4. Drought events of scenario simulations.

Return period T (years)	Theoretical monthly average discharge (m^3/s)	Recorded events	Recorded monthly average discharge (m^3/s)
2	27.26	August 2008	28.07
5	18.91	July 2000	18.16
10	15.61	September 2011	15.35
20	13.33	August 1991	13.72
100	9.91	August 1990	10.10

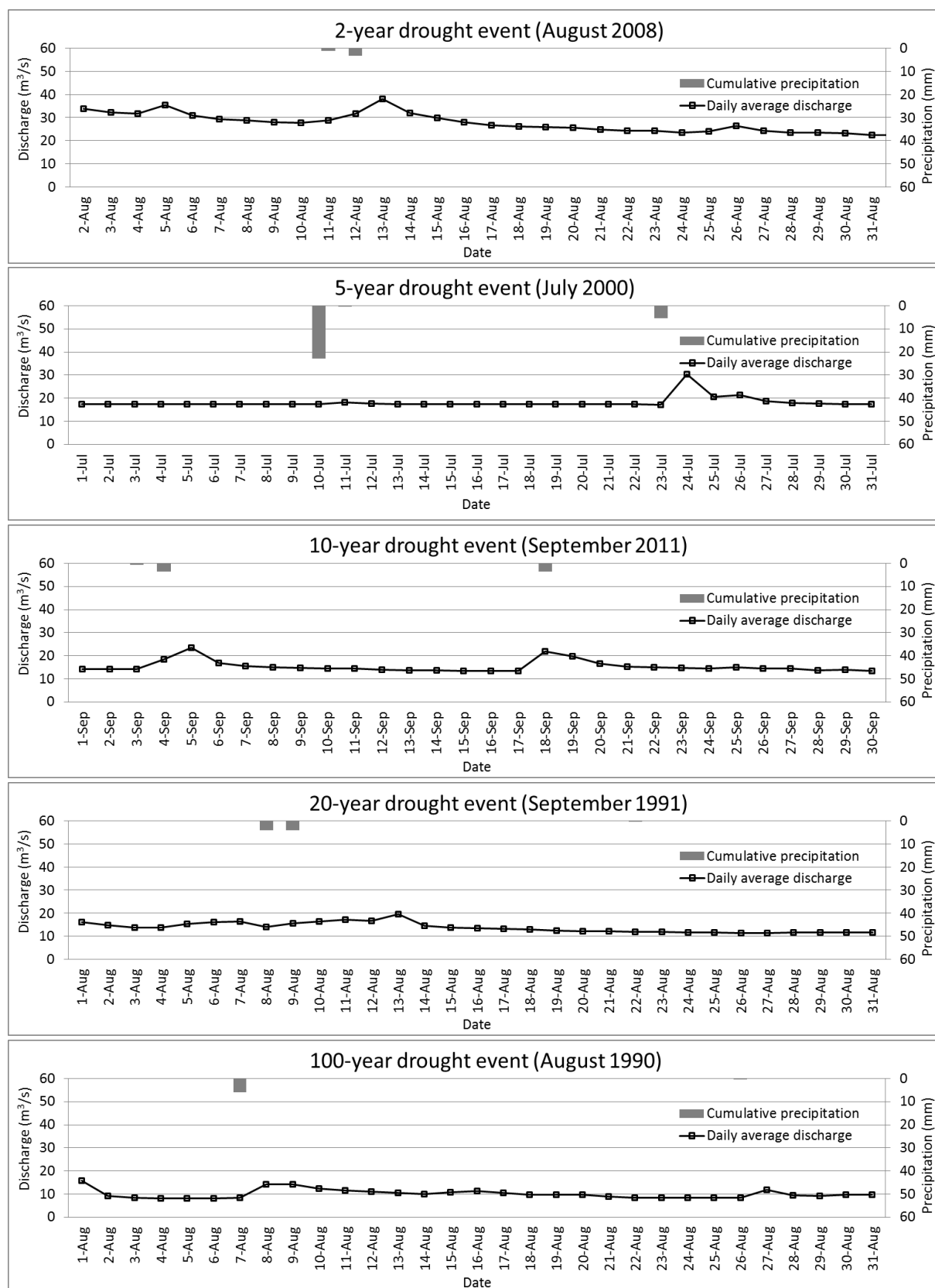


Figure IV.4. Rainfall and river discharge of drought events of scenario simulations, measured respectively at airport meteorological station and Napoléon III bridge gauging station (Figure I.10, Figure I.15).

IV.1.2 Inputs data for scenario simulations

The input data for the scenario simulation is obtained through statistical calculations on the input data used for validation case from 2009 to 2013. The model is built with the topographical data of 2009, therefore the model would be less coherent if the input data of this model is before 2009 or after 2013. The upstream boundary is the groundwater level at Charles Albert bridge. For the scenario simulations of flood events, the maximal values of the monthly average of groundwater level of each year are calculated, then the mean of the five values are used as the constant upstream boundary condition. As for the drought event, the upstream condition is calculated with the same equation but the H_{max}^n is replaced by the minimal values of the monthly average of groundwater level H_{min}^n recorded at the same place. It can be summarized as below:

$$\begin{aligned} H_{scf} &= \frac{1}{5} \sum_{n=2009}^{2013} H_{max}^n \\ H_{scd} &= \frac{1}{5} \sum_{n=2009}^{2013} H_{min}^n, \end{aligned} \quad \text{Eq. 55}$$

where, H_{scf} and H_{scd} are respectively the groundwater levels used as upstream boundary condition for flood and drought scenario simulations (m), H_{max} and H_{min} are respectively the maximal and minimal values of monthly average of groundwater level (m) and n denotes the year. With this method, the value of the H_{scf} for flood period is 107.51 m and H_{scd} for drought period is 103.77 m. The downstream boundary condition is the mean sea level, which always equals to 0.3 m.

The pumping rate of the municipal pumping stations is simulated with a constant value calculated from the monthly average of pumped volume which has been recorded during the target seasons (July August and September for drought event; October, November and December for flood season). The mean values of pumping rate are therefore used as the pumping rate for the scenario simulations. Table IV.5 shows the pumping rates assigned in the model for flood and drought events simulations. The industrial water use of the scenarios is assumed to be the same as the one used for the validation case, because the production of industrial companies is less sensitive to the hydrological conditions. The agricultural water use may increase when a severe drought strikes. But this increment of the water consumption for agricultural lands is not considered in the model due to the lack of arguments. Like the validation case, the pumping rates on agricultural lands are only assigned for the drought scenarios, because the irrigation in winter is considered as negligible.

Table IV.5. Pumping rates in the municipal pumping stations for scenario simulations.

Pumping station	Flood events		Drought events	
	Monthly pumped volume (m ³)	Equivalent pumping rate (l/s)	Monthly pumped volume (m ³)	Equivalent pumping rate (l/s)
Carros	34 048	13	42 288	16
Pugets	133 602	50	350 343	131
Saint-Laurent-du-Var	598 504	223	1 217 449	455
Prairies	100 481	38	86 417	32
Sagnes	281 782	105	416 713	156

The *AET* for the scenario is calculated in the same way as the pumping rate. The mean values of the whole season are used as the *AET* of the scenarios: 1.3 mm/day for flood scenarios and 0.85 mm/day for drought events. According to the Thornthwaite algorithm, the estimated *AET* is smaller in the drought season due to the lack of water storage in the soil and the low precipitation. With the method explained in Eq. 31, the water recharge of each event is thus estimated. The water level in the Var river for each event is simulated by the river hydraulic model mentioned in Section III.4.

IV.1.3 Scenario simulation results

As explained in Section IV.1.1, the scenario simulations are 1 month-long. This period is long enough to produce the model outputs that distinguish the influence of different events. The minimum time step is 0.01 day, which equals to 14 minutes, in order to avoid the computation instability.

In order to show the influence along the valley, 5 points are chosen to visualize the time series results of the simulated groundwater level (Figure IV.5). The point P38 represents the upstream part of the lower Var river, where the variation of the groundwater level between the dry season and flood season is enormous. The previous simulation results have proved that the feeding direction changes according to the hydrology condition (Figure III.45). PZS9AV is used to show the results near the Carros pumping station. The P57 is located in an agricultural area where the groundwater level drops more than 10 m under the ground surface. Therefore the simulation results of drought period are useful for the farmers to have anticipations for the worse case. P35 and PZ_PT are the important locations to be monitored because of the presence of two municipal pumping stations which provide drinking water for Saint-Laurent-du-Var and Nice.

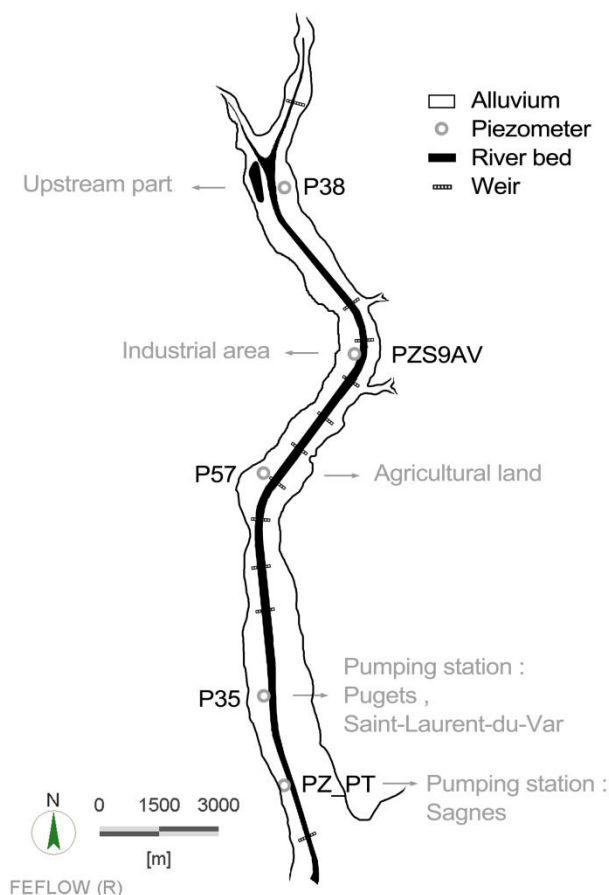


Figure IV.5. Location of the points used to compare the simulation results.

The comparison of the groundwater level of flood event focuses on the peak value. Therefore the peak values have been shifted from their measured dates to a same date in order to be presented more clearly. The groundwater level of drought period should be presented without peaks. Therefore the time series of drought period have also been shifted to in order to make a clear comparison. The simulated groundwater level of all the points are shown in Figure IV.6.

To understand the influence of the flood, there is no need to look at the groundwater level before the peak, which is determined by the base flow. The peak values of different return periods show that the reaction of the aquifer to a flood event varies according to the place. Within the five flood frequencies, the flood of 100-year return period leads to the highest groundwater level, and the 2-year flood induces the smallest peak values. For the drought period, it is normally the latter one has the highest level than the former one.

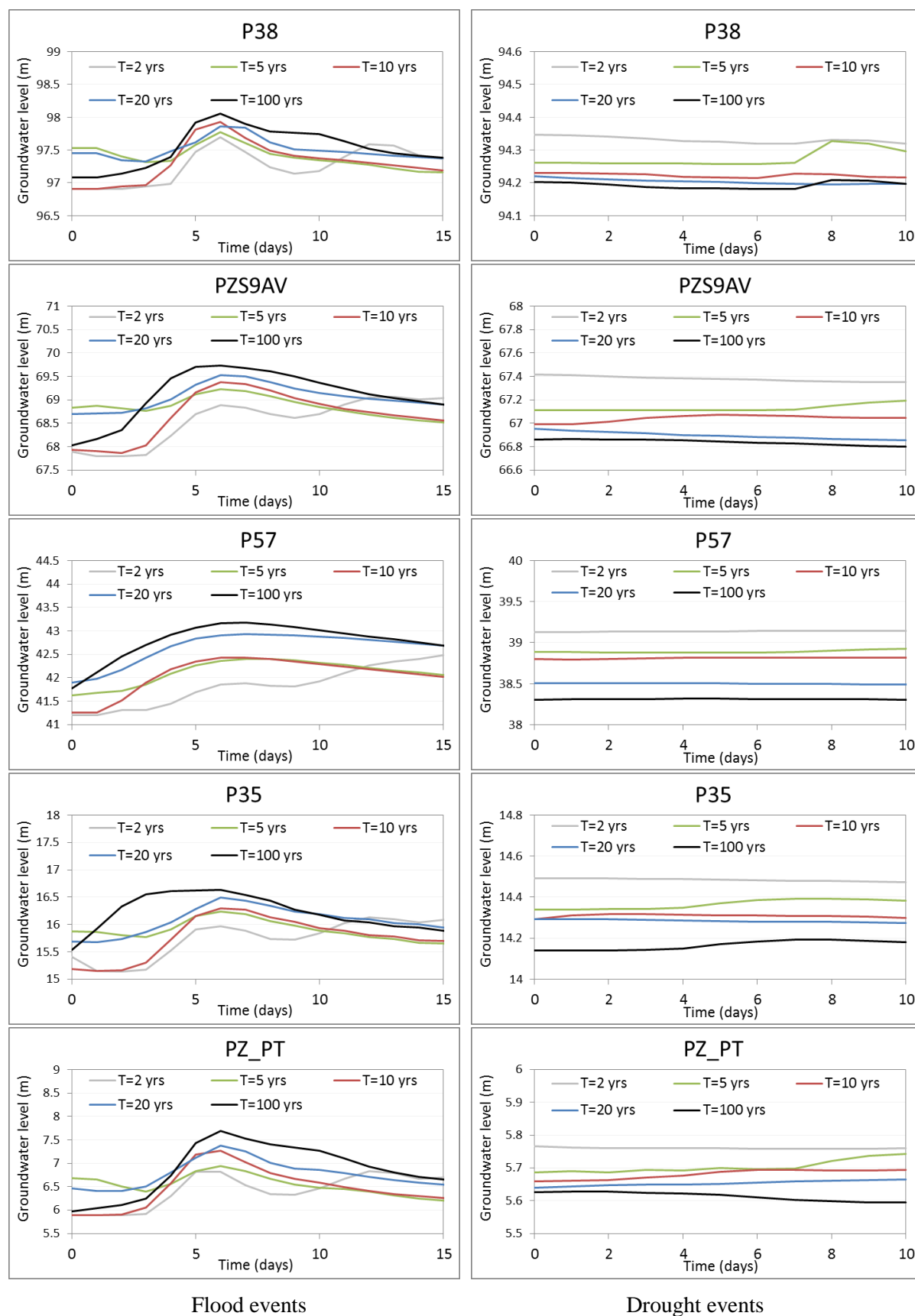


Figure IV.6. Scenario simulations of flood and drought events.

In the upstream part represented by P38, the aquifer is less sensitive to the extreme hydrological events. The difference of the peak values between the groundwater level of 2-year flood and that of 100-year flood is less than 0.5 m. And the difference between the groundwater level of 2-year drought and that of 100-year drought is less than 0.2 m. This result does not agree with observed data from 2009 to 2013 at P38 (Figure IV.6), where a difference of 1 m is shown on the dry period of 2011 and 2012. An under estimation made by the scenario simulations occurs because the observed data reflects the impact of hydrological conditions on certain years, when the pumping volume and upstream boundary conditions are different. While in the scenario simulations, these two input data are totally the same for all the scenarios. Furthermore, since the point P38 is close to the northern boundary of the model, it is more impacted by the upstream boundary conditions. Thus the decrease of the groundwater level at P38 during dry period is underestimated by the scenario simulations.

In the weir section which is represented by PZS9AV, the difference of the peak values of groundwater level between the 2-year flood and the 100-year flood is 1 m. While the difference between the groundwater level of 2-year drought and the 100-year drought is 0.6 m. This result indicates that the aquifer has a good resilience to the drought event. When an extreme drought event occurs, the river can regulate the groundwater level by feeding the aquifer. As for the flood event, the result of the 2-year flood event shows a cumulative effect of continuous small peaks. The magnitude of the second peak is smaller than the first one, but when it occurs only five days after the first one, the groundwater level still rises up to a higher level which is at the same level of a 5-year flood event.

The unconfined aquifer is disconnected to the river in the sections represented by P57. Due to the weak river-aquifer exchanges, the groundwater level has a slow reaction to the peak on the river flow. Once recharged by the river, the aquifer at P57 benefits from a groundwater level rise, but then the water propagates slowly to the downstream parts. The difference of the peak values between the groundwater level of 2-year flood and that of 100-year flood is the highest (1.5 m) compared to other points. However, the poor river-aquifer exchanges on this river section make this river section very vulnerable regarding the drought events. Knowing that this area is mainly occupied by the agricultural land, the groundwater depletion may become even serious because of the high groundwater demand during the dry period.

P35 and PZ_PT are the two points near to the river mouth, where the municipal pumping stations are built. The difference of the groundwater level between the 2-year drought and 100-year drought is less than 0.4 m. It means that the strong river-aquifer exchanges in the downstream part of the river can guarantee a high volume of groundwater extraction even during the dry period.

IV.2 Scenario simulation of pollutant transport

Groundwater pollution is a big concern in the lower Var river valley because the unconfined aquifer is the main fresh water resource of many municipalites. Therefore a pollutant transport module should be added into the validated model in order to provide useful information to anticipate the groundwater pollution events.

The pollutant transport is modeled by the mass transport equation [Diersch, 2014], which is written as below:

$$\frac{\partial(B\varepsilon C)}{\partial t} + \nabla(B\varepsilon C\mathbf{v}) + \nabla(B\varepsilon \mathbf{j}_c) = B\varepsilon \bar{r}_c, \quad \text{Eq. 56}$$

where, B is the thickness of the unconfined aquifer (m), ε is the porosity of the porous media (see also Eq. 10), C is the concentration of the pollutant (g/L), \mathbf{v} is the flow velocity (m/s), \bar{r}_c is the reaction term, which is not considered in this case study, \mathbf{j}_c is the mass flux which depends on the dispersion tensor \mathbf{D} :

$$\begin{aligned} \mathbf{j}_c &= -\mathbf{D} \cdot \nabla C \\ \mathbf{D} &= D_d \mathbf{I} + \mathbf{D}_m, \end{aligned} \quad \text{Eq. 57}$$

where, D_d is molecular diffusion (m^2/s), \mathbf{I} is the unit tensor in three dimensions, \mathbf{D}_m is the tensor of mechanical dispersion (m^2/s), which is commonly described by:

$$\mathbf{D}_m = (\beta_T \|\mathbf{v}\|) \mathbf{I} + (\beta_L + \beta_T) \frac{\mathbf{v} \otimes \mathbf{v}}{\|\mathbf{v}\|}, \quad \text{Eq. 58}$$

where β_L and β_T are the longitudinal and transverse dispersivity, respectively (m). Hence, 3 new parameters are needed to establish the pollutant transport module: molecular diffusion coefficient D_d , longitudinal and transverse dispersivity β_L and β_T . D_d is related to the property of the material (water), its value can be measured by experimental approach in laboratory. β_L and β_T are related to the property of the sediment, their values are often obtained by field measurement. Holz et al. [2000] has measured the molecular diffusion coefficient of water at 25 °C is $2.3 \times 10^{-9} \text{ m}^2/\text{s}$. This value is used to setup the pollutant transport model. Gelhar et al. [1992] has reviewed the values of β_L and β_T obtained

by field measurement in the aquifers of various locations. Among the measurements carried out in the quaternary alluvial aquifers, several studied cases are listed in Table IV.6. According to the similarity of the studied cases, the value 61/18 is used to setup the model for lower Var river valley.

Table IV.6. β_L and β_T values obtained by field measurement

References, year Location,	Site description	Scale of test (m)	Tracer and input	Dispersivity β_L/β_T (m)
Fried, 1975 Rhine aquifer, France	Alluvial deposit, mixture of sand, gravel with clay lenses	800	Cl- (contamination)	15/1
Gupta et al., 1975 Sutter basin, U.S.	Sandstone, shale, sand, alluvial sediments	50000	Cl- (environmental)	80-200/8-20
Konikow and Bredehoeft, 1976 Arkansas river valley, U.S.	Alluvium, inhomogeneous clay, silt, sand and gravel	18000	TDS (contamination)	30.5/9.1
New Zealand Ministry of work and development, 1977 Heretaunga aquifer, New Zealand	Alluvium, gravels	290	Cl- (contamination)	41/10
Robson, 1978 Barstow, U.S.	Alluvial sediments	3200	TDS (contamination)	61/18

Since no recorded pollution event has ever happened in the studied area, no data can be used to validate this module. The accuracy of the results of scenario simulations cannot be assured. However, since the hydrodynamic module is validated, the simulated result of groundwater flow is reliable. The pollutant transport in unconfined aquifer depends also on the groundwater flow. Thus the simulated results of pollution scenarios are still acceptable for qualitative study if reasonable explanations are provided.

The boundary conditions of pollutant transport module are the average values calculated with the validation case from 2009 to 2013. The precipitation and evapotranspiration are calculated with the observed meteorological data from 2000 to 2014, from which an annual precipitation of 878 mm and

annual *AET* of 583 mm are found. Assuming that the land is constant, the direct recharge/loss can thus be given with the run-off coefficient defined in the previous chapter (Table III.5 and Figure III.15). According to the recorded discharge on www.vigicrues.gouv.fr, the Var river has an annual average discharge of 50.2 m³/s at Napoléon III station. This value is used to calculate the transfer boundary condition for the pollutant transport simulation. The volume of water pumped by the municipal pumping stations is also an annual average value of the recorded data. The pumped volumes of water for industrial and agricultural use are the same values used in the simulation of model validation (Section III.5).

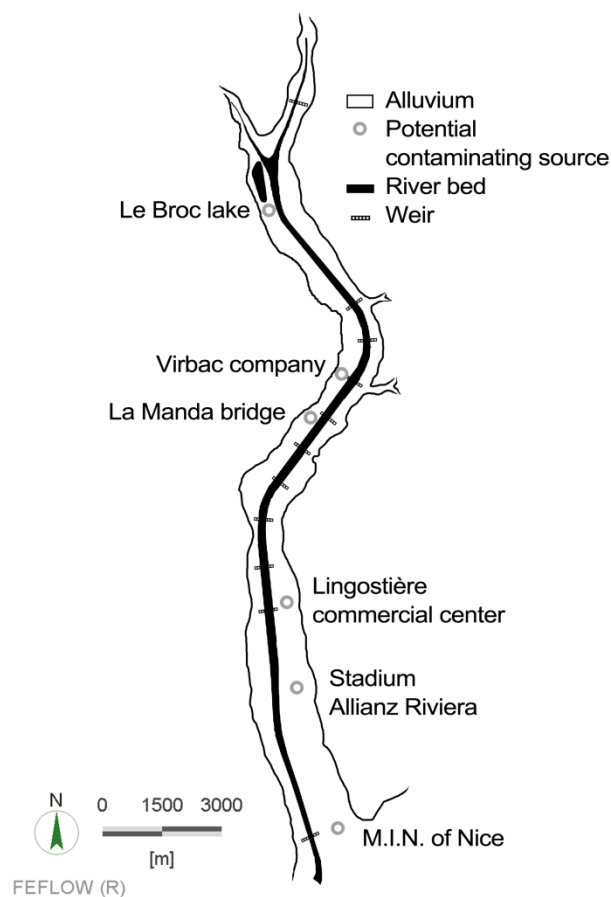


Figure IV.7. Location of the potential contaminating sources in the lower Var river valley.

Two types of pollution are considered in this analysis: accidental pollutions and long-term pollutant leakage. 6 potential pollutant sources are identified along the lower valley for the accidental pollutions simulation (Figure IV.7), in order to study the pollutant transport in porous media of different characteristics. For each simulation, a discharge of 300 m³/day of pollutant with a COD (chemical oxygen demand) concentration of 12500g/m³ (or 12500 mg/L) is injected directly in the aquifer during

1 hour at one pollutant source. The pollutant is assumed to be conservative without decay so as to know the pessimistic result of the scenario. The simulation period is 20 years because it is important for the decision maker to know the residual pollutant in the aquifer without intervention after a long time. The maximal time step is 0.1 day in order to optimize the computation time. The simulation results are shown in Figure IV.8 to Figure IV.13.

For the second type of pollution scenario, the long-term pollution event is carried out to study the pollutant transport with a constant source term in the porous media. A constant leakage discharge of $0.001 \text{ m}^3/\text{day}$ (1L/day) is injected in the southern boundary of Le Broc lake, which is the upstream part of the valley. The concentration and type of pollutant are the same as the accidental pollution event simulation. The simulation period is 3 years and the maximal time step is 0.1 day. The simulation period is shorter than that of accidental pollution scenario simulations, because in reality, it is impossible that a constant leakage continues for more than 3 years without being detected in the valley. The simulation results are shown in Figure IV.14.

These results can qualitatively show the pollutant transport at different locations in the valley. Nevertheless, the limitations of the simulations are also obvious. Since the hydrodynamic module does not consider the unsaturated flow, the pollutant is assumed to be injected directly into the unconfined aquifer, which could only happen when there is leakage into the pumping well. Otherwise a part of the pollutant would be kept in the unsaturated layer. The second limitation of this simulation is that the river-aquifer exchanges are modeled only in the hydrodynamic module but not in the pollutant transport module, thus this module cannot reproduce the process that the pollutant enters into the river through exfiltration, then conveyed by the surface water flow and re-enters into the aquifer by infiltration. Therefore, the results of the simulations are qualitatively correct but there must be an overestimation of the concentration at the section where the aquifer feeds the river, and an underestimation of the concentration at the section where the river feeds the aquifer.

Figure IV.8 shows an instantaneous seepage of pollutant at the southern boundary of Le Broc lake, where the groundwater flow has a high velocity (Figure III.44) so that the concentration of the pollutant is dispersed by the flow within one month. The pollutant moves towards the downstream part of the valley due to the high flow velocity. It reaches La Manda bridge by the end of the 6th month

after injected into the aquifer. By the end of the 2nd year, the residual concentration of the pollutant is less than 0.01 mg/L.

Figure IV.9 shows the consequences of an accidental pollution event at the Virbac company, which is a pharmaceutical industry. The simulation results show that, if there is waste water treatment failure, the pollutant will move slowly to the downstream area for the first 3 months. Then the concentration would be diluted by the freshwater coming from the rivers through the river-aquifer exchanges (Figure III.45). By the end of the 2nd year after the injection of the pollutant, its residual concentration is no more than 0.005 mg/L due to the effect of dispersion and dilution.

Figure IV.10 shows the results of an accidental pollution event at La Manda bridge, where several gas stations are located next to the bridge. The simulation results reveal that the concentration of the pollutant would be quickly diluted by the river-aquifer exchanges. For the rest of the pollutant transport process, a similar distribution of the concentration as Figure IV.9 is found.

Figure IV.11 is the simulation result of an accidental pollution event at Lingostière commercial center, which is a mixture of industrial and urban area. Once polluted, the pollutant stays in the same area for a long period and its concentration remains at a high level because of the slow groundwater flow (Figure III.44). By the end of the 2nd year after the injection, a residual concentration of 0.05 mg/L could still be found at the same area and the pollutant travels no more than 4 km towards the downstream part. However, the pollutant would be brought to the right bank side by the groundwater flow.

Figure IV.12 shows the results of an accidental pollution happening at the stadium Allianz Riviera. The same characteristics of pollutant transport as the Figure IV.11 can be found. The slow groundwater flow in this area has limited the propagation of the concentration of the pollutant. Progressively, the pollutant would be brought to the right bank side.

Figure IV.13 shows the results of an accidental pollution event in the aquifer near to the river mouth. The dispersion process is very slow due to the low groundwater flow velocity (Figure III.44) and weak river-aquifer exchanges (Figure III.45). Moreover, the pumping station of Sagnes and the pumping stations at the airport induce a flow direction towards the upstream side. This is the reason why the concentration of the pollutant remains at a high level at the same location for a long period. These results indicate that the aquifer near the river mouth has a lowest self-clean ability.

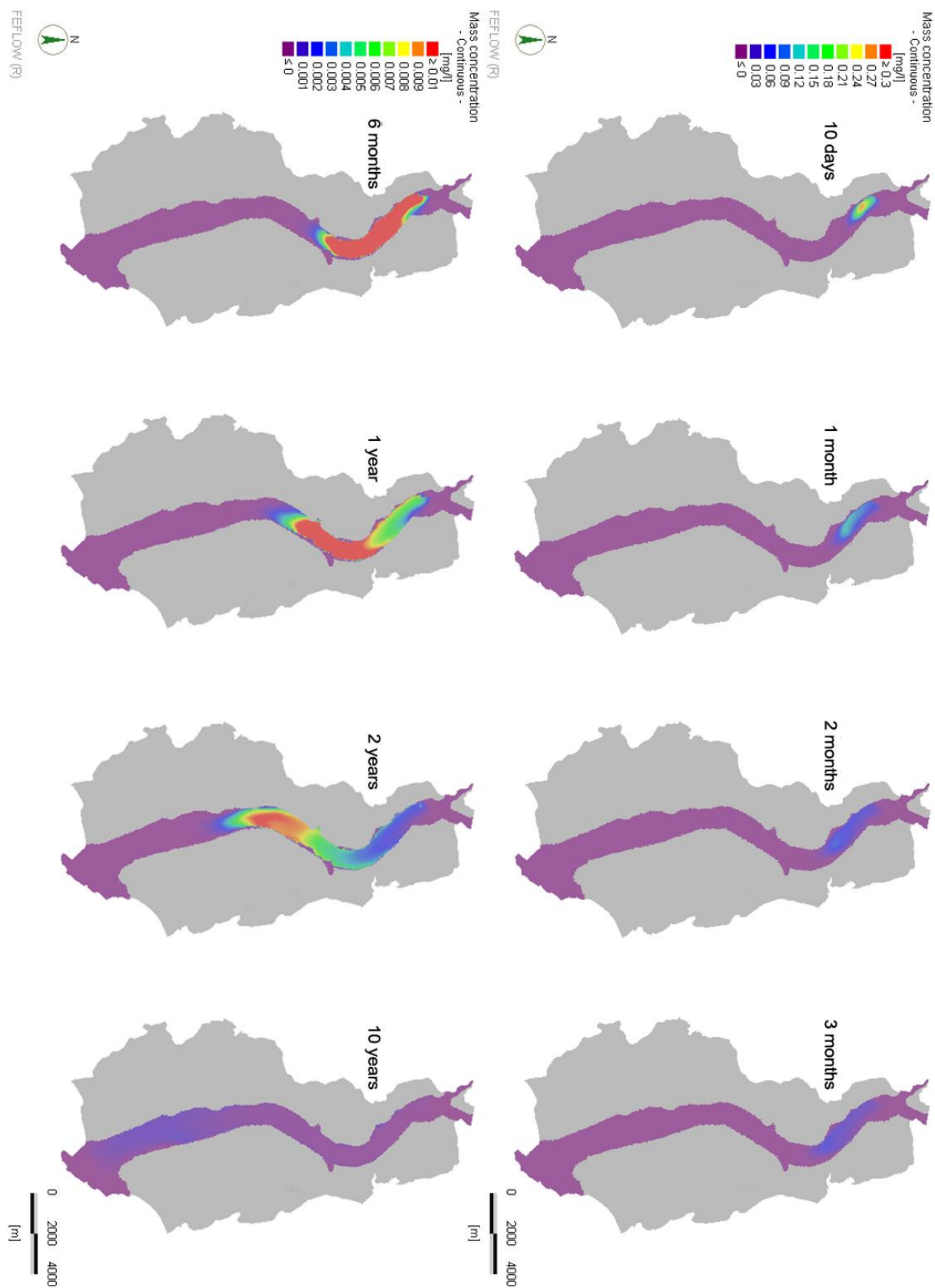


Figure IV.8. Simulated results of accidental pollution scenario: source at Le Broc lake.

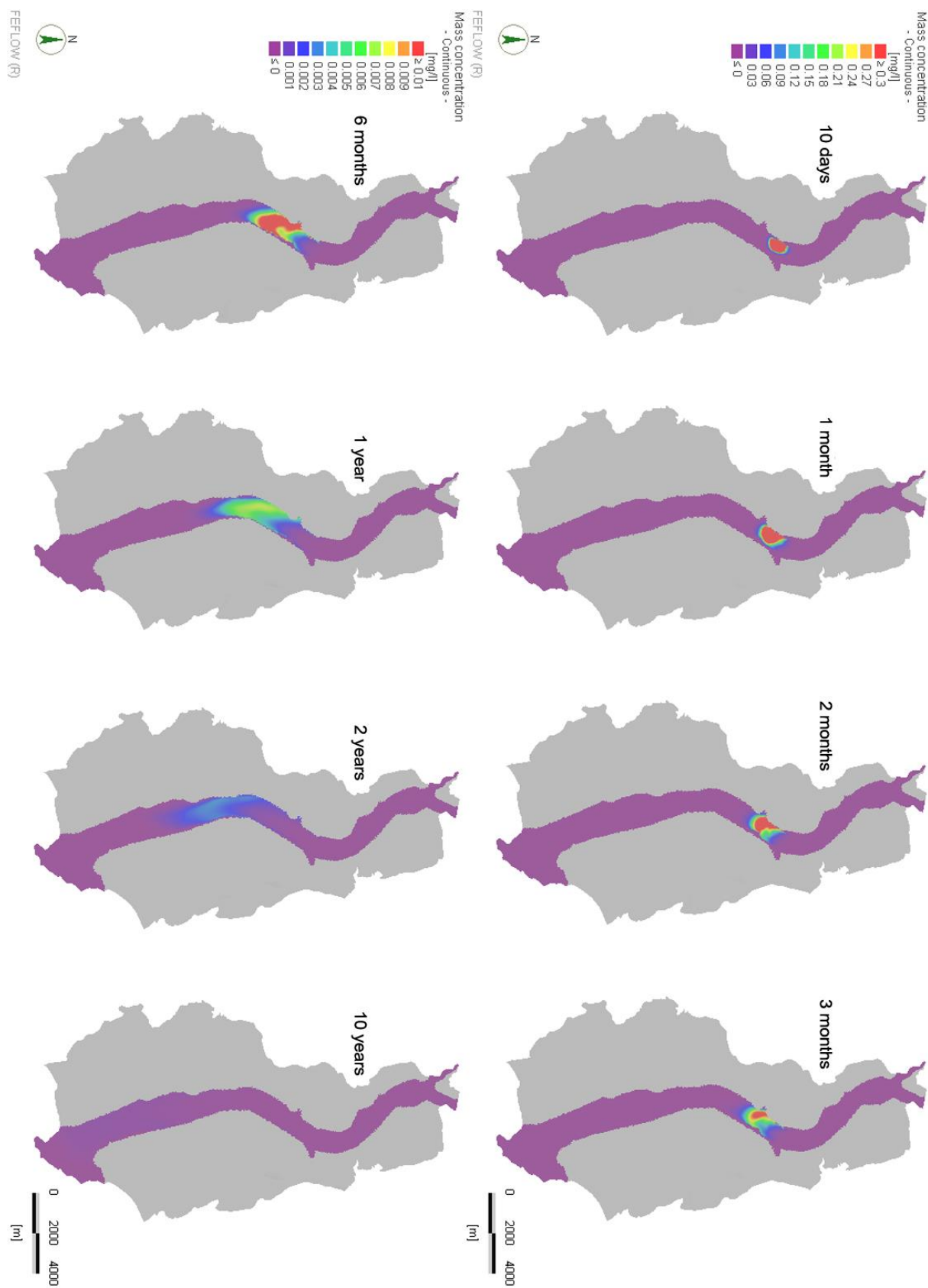


Figure IV.9. Simulated results of accidental pollution scenario: source at Virbac company.

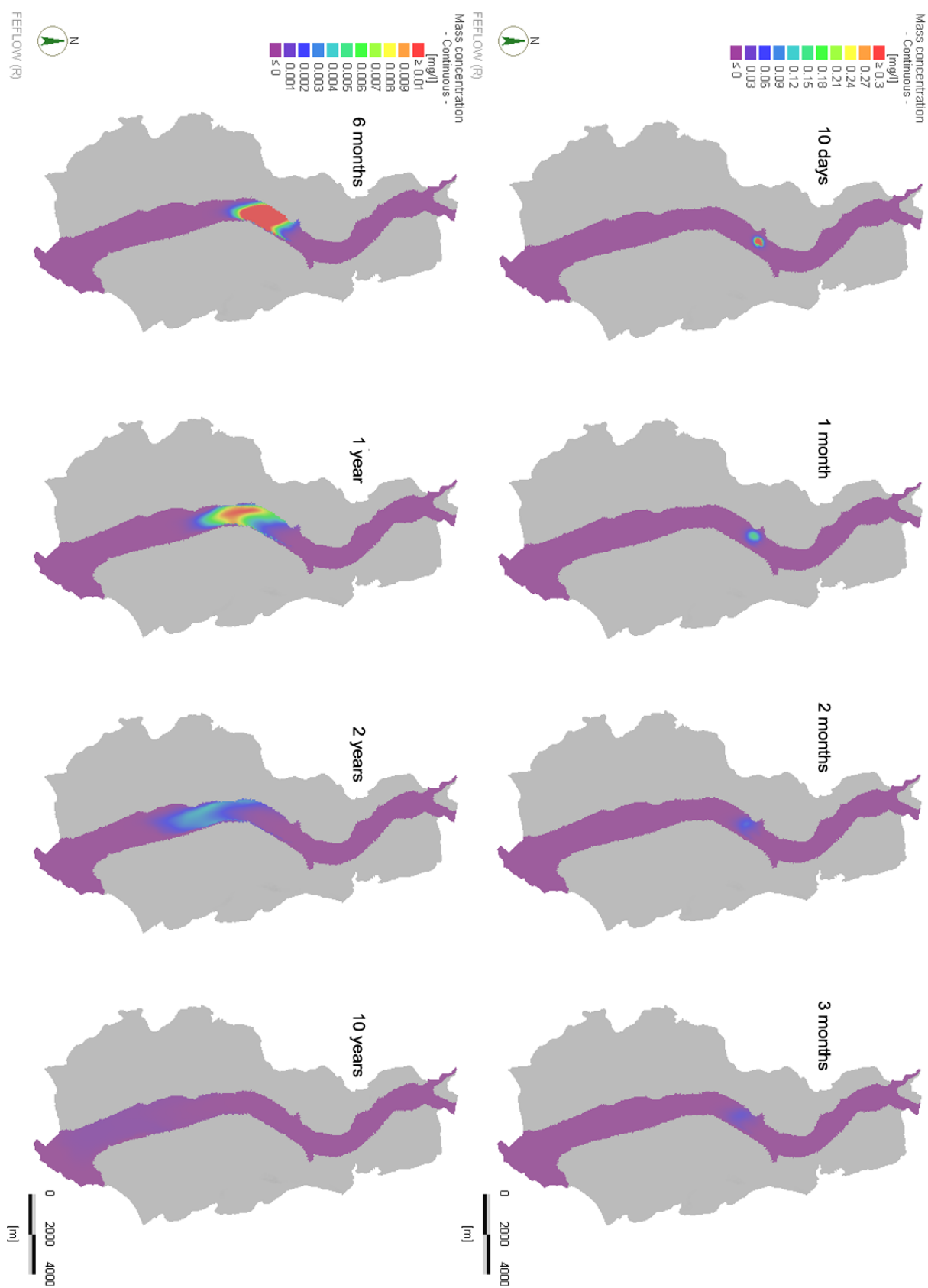


Figure IV.10. Simulated results of accidental pollution scenario: source at La Manda bridge.

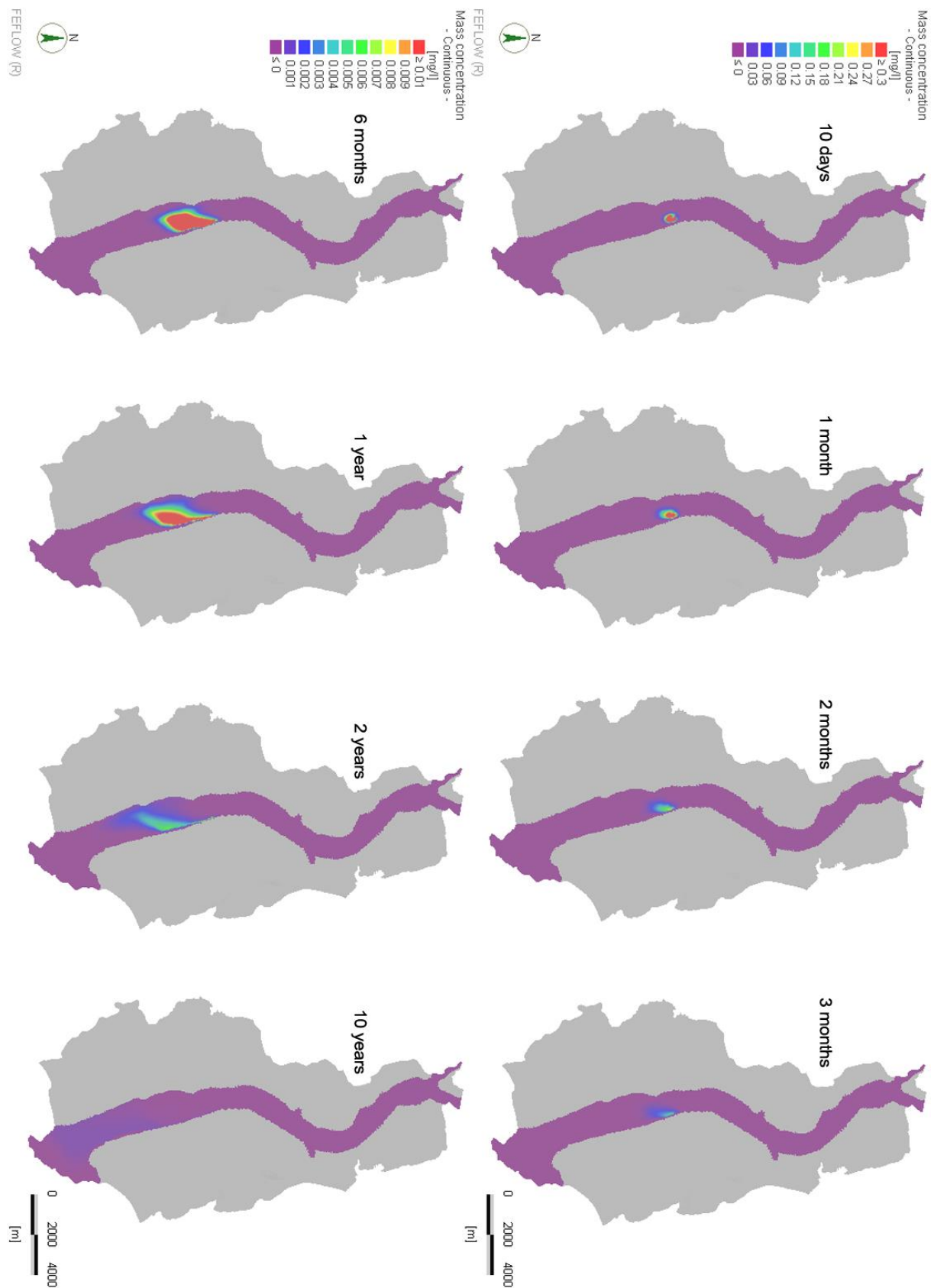


Figure IV.11. Simulated results of accidental pollution scenario: source at Lingosti ère commercial center.

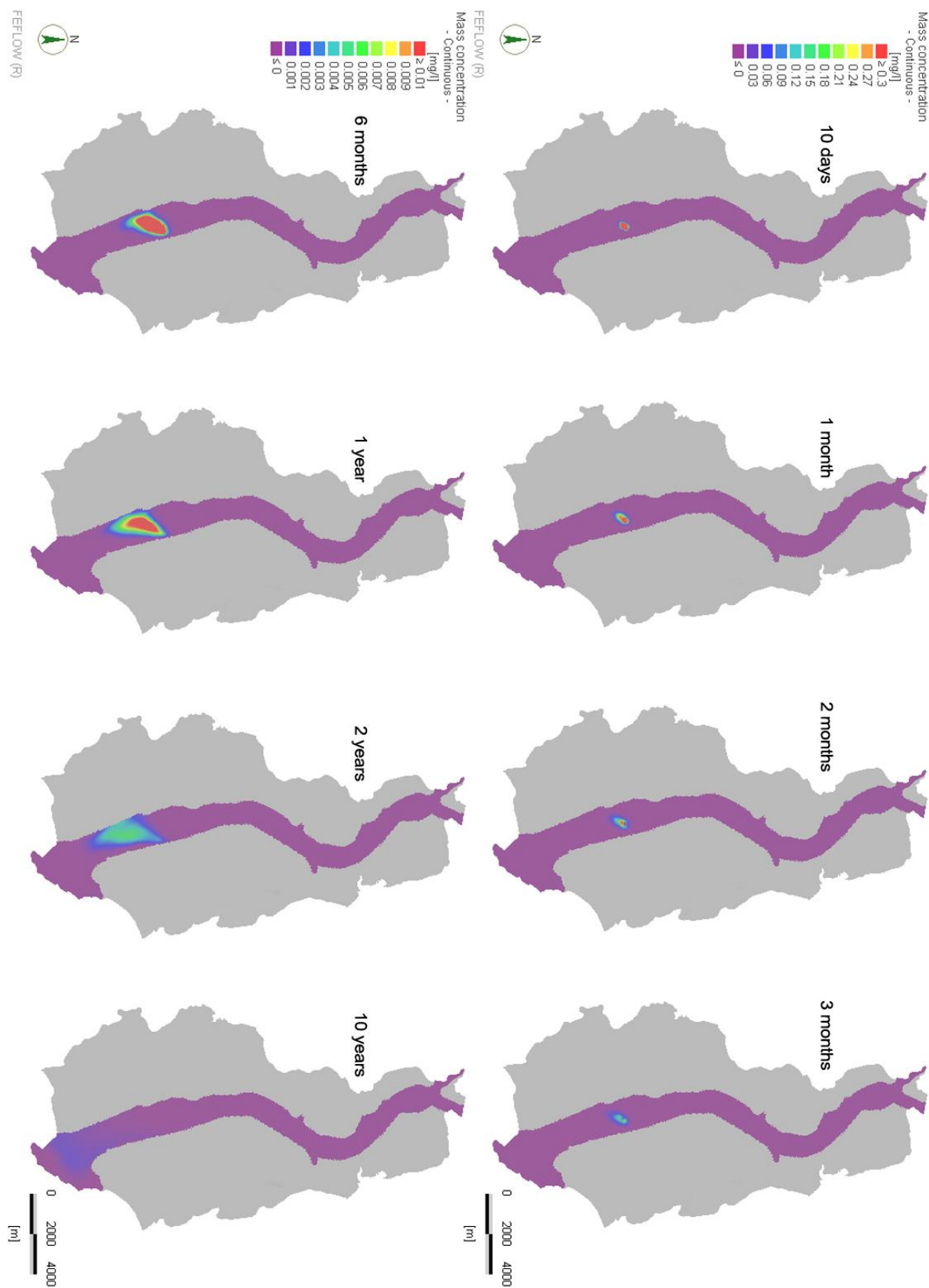


Figure IV.12. Simulated results of accidental pollution scenario: source at Stadium Allianz Riviera.

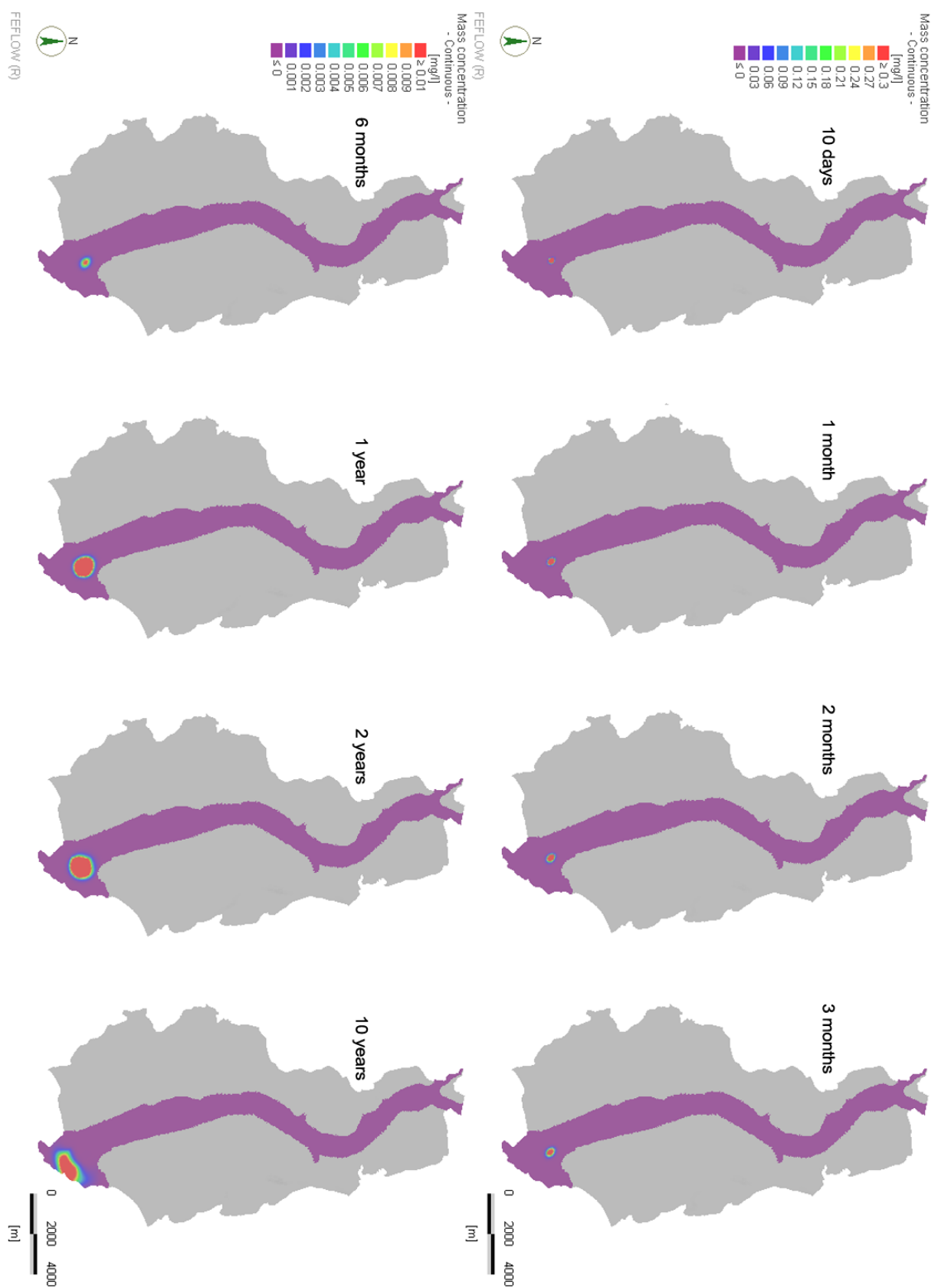


Figure IV.13. Simulated results of accidental pollution scenario: source at M.I.N. of Nice.

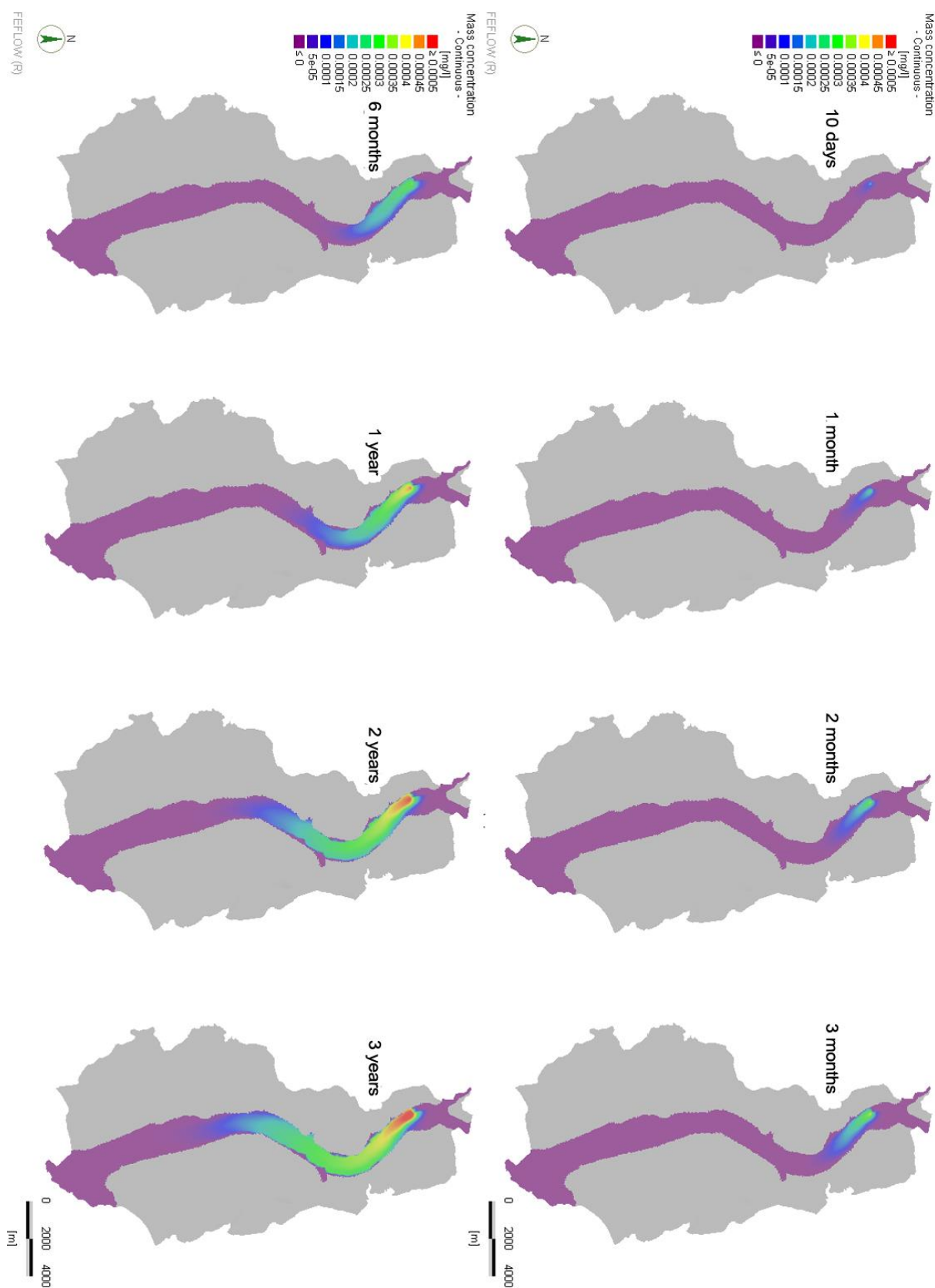


Figure IV.14. Simulated results of long-term pollution scenario: source at Le Broc lake.

Figure IV.14 shows a constant pollutant leakage into the aquifer at the upstream part of the valley. As the injection of the pollutant, the concentration at the source point keeps increasing and reaches 0.005 mg/L by the end of the 1st year after injection. Since the source point is located on the right bank side of the valley, the concentration of the pollutant on the right bank side is higher than that on the other bank side until the first meandering of the river, after which the concentration is equally distributed on both bank sides. Like the accidental pollution event, the pollutant moves faster in the upstream part due to the high velocity of the groundwater flow. It can be seen that, during the first year, the pollutant travels over 8 km with the groundwater flow and also by the effects of advection-dispersion. While during the next year, the pollutant only travels less than 4 km towards the downstream side.

IV.3 Scenario simulation of salt water intrusion

IV.3.1 Context of the seawater intrusion study in the lower Var river valley

The groundwater in aquifer is usually used as one of the main freshwater resources of the water supply system in urban zone. Seawater intrusion in coastal area is a common issue that threatens the sustainability of the water supply of coastal communities [Felisa et al., 2013; Cassardo and Jones, 2011]. Since the urbanization has increased significantly the water demand, the water storage in coastal aquifer has become more vulnerable [Werner et al. 2013]. Through decades, the seawater intrusion problem has occurred in many coastal areas in many countries. Therefore, a huge amount of freshwater pumping wells along the coastline have been shut down due to the contamination of the freshwater [Bolster, 2007; Felisa et al., 2013; Barlow and Reichard 2010]. Therefore the concern of the seawater intrusion has become a problematic subject for local water management services.

Henry [1964] proposed a classical analytical solution for seawater intrusion (Figure IV.15-1). It has been turned into a benchmark of such density dependent groundwater flow in steady state. Besides, Henry problem has also become a test case for diverse numerical models [Croucher and O'Sullivan 1995]. A brief history of the discussion of Henry problem and various analytical and numerical solutions are reviewed by Kalakan [2014]. Some of them have been successfully implemented in the water resource management procedure.

In estuarine area, the problem becomes more complicated because of the river-aquifer exchanges. The two exchange directions can rise or lower the groundwater table level (Figure II.11-1,2), as the hydraulic head changes, the seawater wedge can also be pushed backward to the sea side or pulled

forward to the inland side. In a real case, for a given moment, both directions may occur in different river sections. For a given location, the feeding direction can also vary according to the discharge [Winter et al., 1988]. Sometimes a disconnection between the river and aquifer is observed due to the presence of a clogging layer [Brunner et al., 2009; Brownbill et al., 2011]. Hence these hydraulic influences are inevitable in the study of seawater intrusion in estuarine area.

Another factor that can influence the seawater intrusion is the groundwater extraction (Figure IV.15-2,3,4). As the pumped volume in a well increases, the hydraulic head of the coastal aquifer decreases, the salt water wedge moves toward the inland side, vice versa. The water in aquifer is usually a predominant resource for domestic, industrial and agricultural use. As the development of urban area, the demand of the water increases. Once the safe yield capacity of the aquifer is reached, serious contamination problem will become unavoidable [Ergil, 2000]. It is wise and necessary to establish a groundwater abstraction plan by using hydraulic modeling approach, in order to preserve groundwater aquifers at sustainable levels.

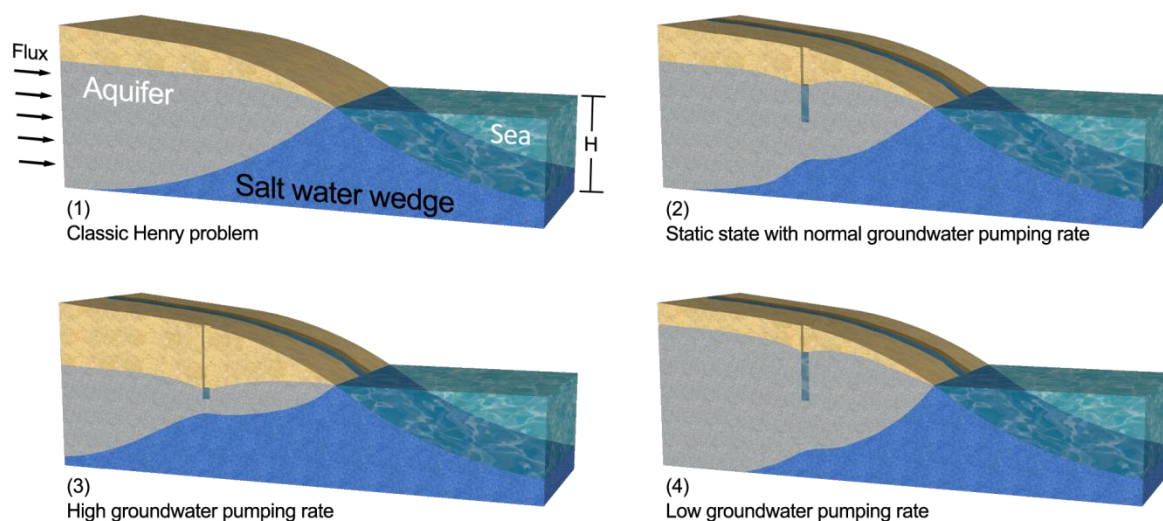


Figure IV.15. Illustration of seawater intrusion: Classic Henry problem (1) and case of urban estuarine area (2) (3) (4) (Author's design).

In the lower valley (Figure I.8), the unconfined aquifer exists in the Holocene alluvium and Pliocene conglomerate [Guglielmi, 1993]. Most pumping wells extract water from the alluvium aquifer, whose maximum thickness can reach 150 m at some river sections. Lenses of clay are observed beneath the airport near the downstream boundary, where a confined aquifer is formed (Figure I.19). The average gradient of groundwater table of the whole valley is 0.005, while at the estuarine area a milder value of

0.003 is observed (Figure III.46). At the downstream boundary, the aquifer is in direct contact with the sea.

Under the influence of a Mediterranean climate, the Var river is characterized by a low discharge in summer and a high discharge at the beginning of winter. The average annual discharge is $50.2 \text{ m}^3/\text{s}$. During dry season, the discharge is as low as $20 \text{ m}^3/\text{s}$ and it can last for one month (*e.g.* August 2015), while the maximum instantaneous peak discharge measured during a flood event was $3760 \text{ m}^3/\text{s}$ (*e.g.* November 1994) [Guinot and Gourbesville, 2003; Ma et al. 2016].

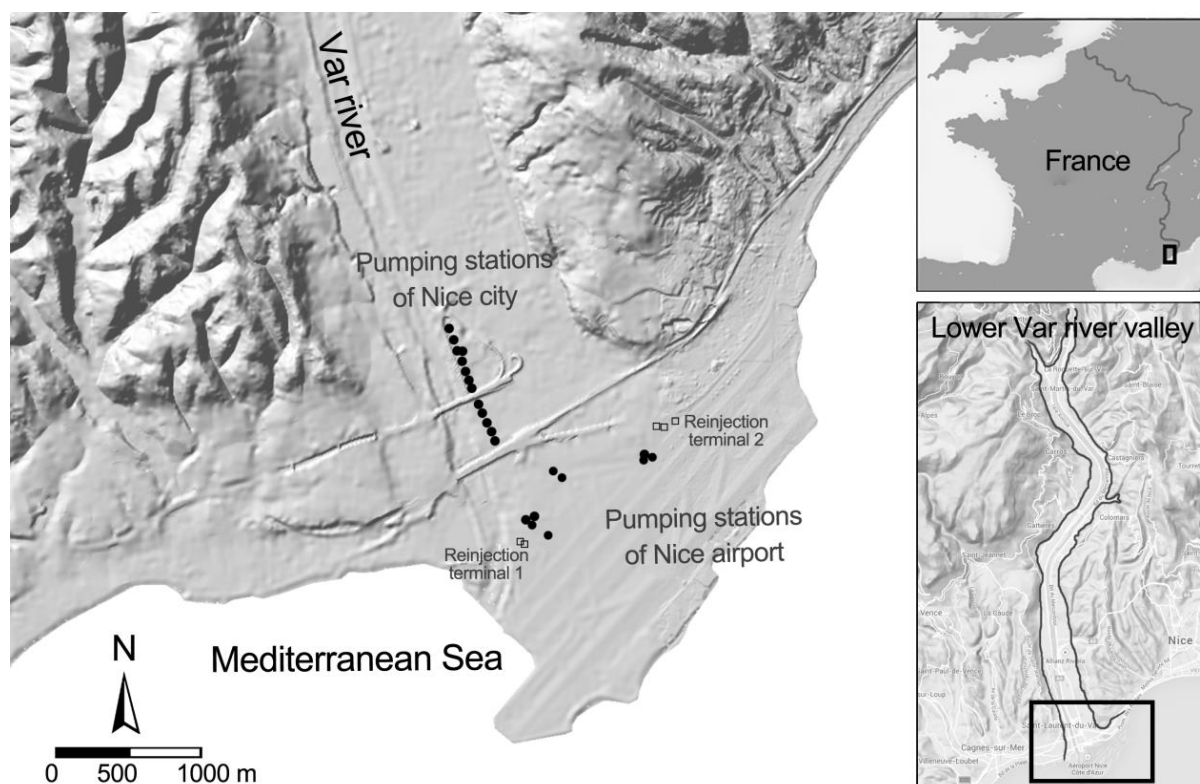


Figure IV.16. Studied area of the seawater intrusion model of the Var river mouth.

As shown in Figure IV.16, the study of the seawater intrusion focuses only on the zone where a possible exchange between the freshwater and seawater could happen. Two groups of pumping stations have been created to meet the demand for domestic and industrial water-use. The pumping station of Nice city contains 13 boreholes, which abstract $14.338 \text{ million m}^3$ water each year for drinking water production. The airport possesses four pumping stations. Three of them extract water from the deep, confined aquifer, which meet the demand of the air conditioning water consumption in two terminals. This quantity of water is then reinjected into the shallow unconfined aquifer in order to restore the equilibrium of hydraulic head between the aquifer and the sea. The amount which is really

consumed is the drinking water and plant watering. The net water consumption of the airport is thus around 0.6 million m³ (calculated from the data 2002-2009). Boreholes are also authorized for individuals and collectives, but such type of pumping in the estuarine area is too little to be considered compared to these pumping stations.

Considering all these conditions including a dynamic exchange between the aquifer and the sea, a huge volume of groundwater extraction and the low water level that may happen during dry period, the estuary of the valley faces the threat of seawater intrusion, which may contaminate the boreholes of the airport or even the municipal pumping station of Nice city. The water quality standard has been drawn up in Article L1321-1 to L1321-12 in French Public Health Code, according to which, the maximum concentration of Sodium and Chloride in produced drinking water in France must be less than the threshold value $C_{Na^+} = 200$ mg/L and $C_{Cl^-} = 250$ mg/L. These values provide criteria to water quality study regarding the seawater intrusion in France. Considering the complex hydraulic condition in estuarine area, a hydraulic model can be set up to carry out a series of simulations to figure out the impacts of groundwater abstraction plan on the groundwater table. Based on the simulation results, practical plans or quantitative conclusions will be given in order to ensure the water quality in pumping stations.

IV.3.2 Setup of the seawater intrusion model of Var estuary

IV.3.2.1 Modeled domain and mesh

The hydraulic model that has been built for hydrodynamic and pollutant transport simulation considers the whole 22 km valley. In this model, the alluvium is represented by a single geological layer with an anisotropy factor of 0.1 of hydraulic conductivity. This hypothesis helps to simplify the model and reduces largely the simulation time, but it gives less accurate results at the downstream area, where, in reality, lenses of clay and silt are observed so there should be more than one geological layer. Apparently, the study of the seawater intrusion focuses only on the estuarine area and the confined aquifer formed under the aquitard must be considered. Therefore a smaller model domain and more accurate geological representation are needed for the study of seawater intrusion. The alluvium is represented by 10 layers in the seawater intrusion model.

The new model takes its northern boundary at the beginning of the Sagnes pumping station. It is extended 2 km to the west and 3 km to the east in order to include all the bay area formed by the beach of Saint-Laurent-du-Var and the airport of Nice. Its downstream boundary is located 500 m away from

the shoreline (Figure IV.17). Vertically, the new sea water intrusion model has a geological layer with a thickness of 150 m, which means that the bottom of the model is the conglomerate layer. The lenses are reproduced according to the map shown in Figure I.19.

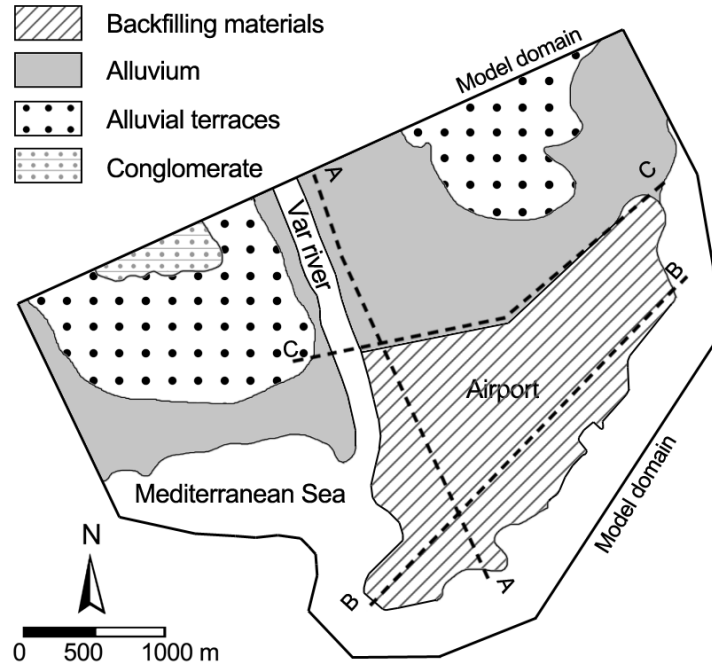


Figure IV.17. Modeled domain of the seawater intrusion model of the Var estuary. The profiles A, B and C are shown in Figure I.19.

The degree to which advection dominates the transport is reflected by Peclet number [Huysmans and Dassargues, 2004]:

$$P_e = \frac{vL}{D}, \quad \text{Eq. 59}$$

where, P_e is the Peclet number, L is the characteristic length for the scale of the problem (m), v is the average velocity in the direction of flow in porous media (m/s) and D is the dispersion coefficient (m^2/s). If molecular diffusion is trivial, which is probably the case in a situation where the advection is a dominant effect, then a simplified Peclet number can be used:

$$P_e = \frac{\Delta L}{\beta}, \quad \text{Eq. 60}$$

where, ΔL is the dimension of $x/y/z$ grid cell at the critical location (m), β is the dispersivity in that direction at the location (m). When advection dominates the dispersion, a numerical model with small Peclet number (less than 2 or even smaller) will decrease oscillations and improve accuracy of the simulation. The Peclet number can be thus used to estimate the grid cell of the numerical model.

Considering the β_L used in the pollutant transport module, for a Peclet number P_e smaller than 2, the ΔL must be less than 120 m. Therefore the maximum cell size of numerical model is set to be 100 m in the inland area. Smaller cell size that ranges from 20 to 30 m is applied in the transition area where the interchange between seawater and freshwater is active, and in the pumping area where the hydraulic gradient is strong. With this cell size configuration, 8521 nodes and 16736 2D elements are generated (Figure IV.18) on each slice and 15 layers (16 slices) are created.

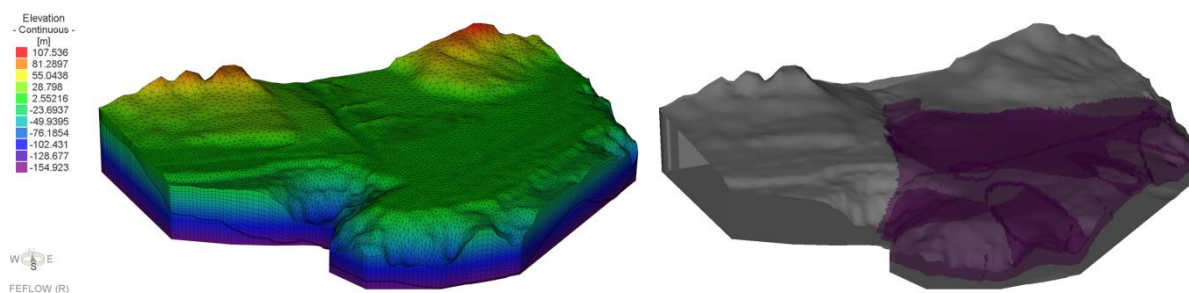


Figure IV.18. Illustration of the computational mesh (left) and lenses in alluvium (right) of the seawater intrusion model.

IV.3.2.2 Boundary conditions

All the flow boundary data comes from the simulation results of the hydrodynamic groundwater flow model in lower Var river valley, which has been built and validated (Chapter III). The validation result reveals that the input flux in alluvium at the upstream boundary of the seawater intrusion model varies from 0.16 to 0.38 m/day, and the input flux in conglomerate equals to 0.001 m/day. The layer of alluvial terraces is neglected to simplify the upstream boundary condition because it does not contain any aquifer. The static of sea level is used as the downstream boundary condition, which equals to 0.3 m. Pumping stations are represented by the well boundary conditions in both unconfined and confined aquifer according to their real depth. Measured pumping volume is assigned to the well boundary condition. In the airport, reinjections of fresh water are modeled by flux boundaries on the top slice (Figure IV.19).

The data for the transport boundary are obtained from previous study on the hydrochemistry of the water source in lower Var river valley [Potot, 2011]. A measurement campaign from 2007 to 2009 has revealed the concentration of chloride in the downstream part of Var river, alluvial aquifer and conglomerate aquifer along the valley. It is concluded that, despite the seasonal effect, the concentration of chloride in these water resources, especially groundwater, varies little over time in the downstream area. The average value is therefore used as the transfer boundary condition of freshwater.

Guglielmi [1993] has studied the nearshore salinity of the seawater by a series of measurement surrounding the airport. The vertical distribution of the salinity has shown that the mixture of freshwater and seawater stays at the surface layer between 0 to -4 m. From -6 m to the sea floor which is deeper than -80 m, the salinity of the seawater varies from 37.8 g/L to 38.1 g/L. Thus the downstream chloride concentration is set to be 23.11 g/L, which is equivalent to 38.1 g/L of sodium chloride (Figure IV.19).

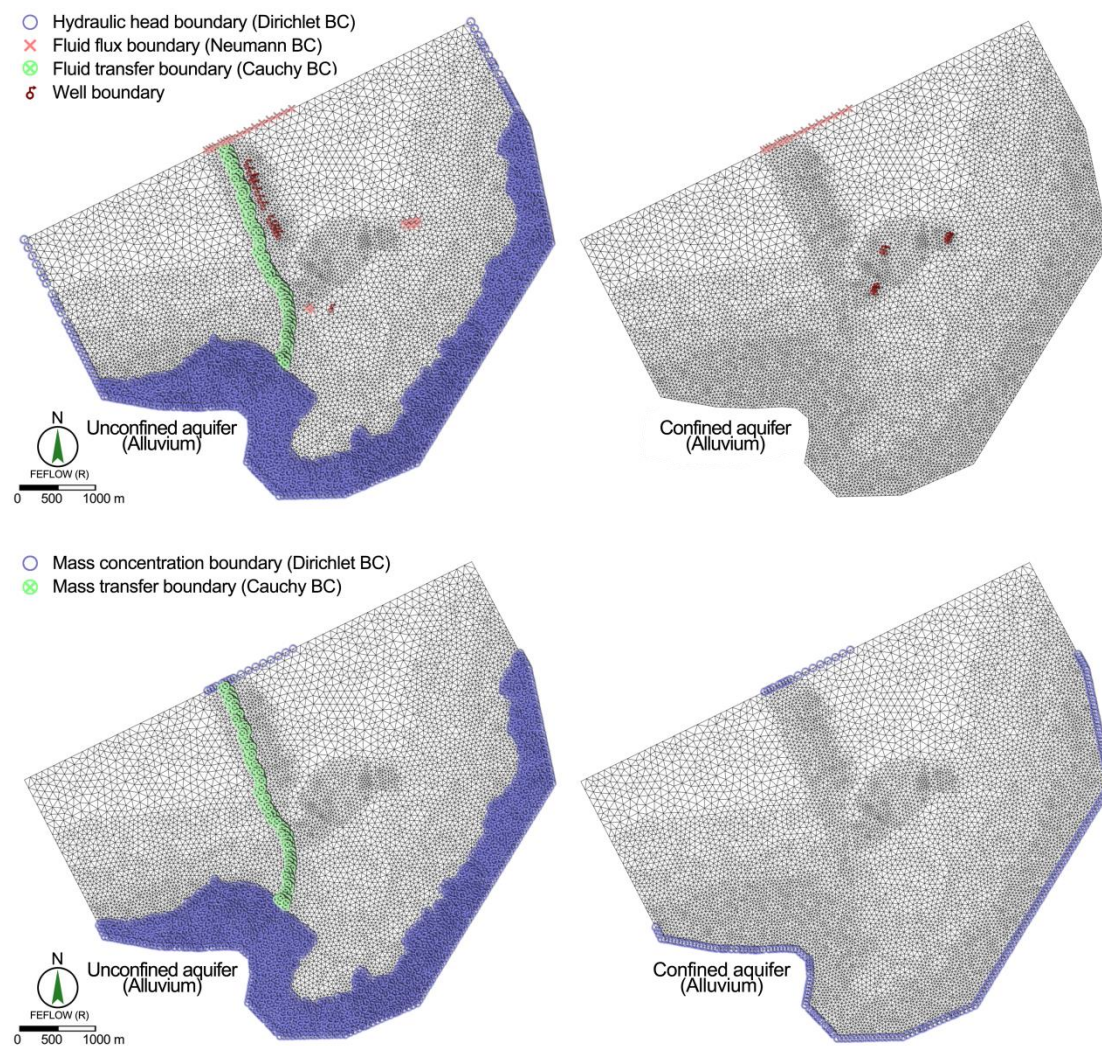


Figure IV.19. Boundary conditions of hydrodynamic module (upper part) and pollutant transport module (lower part) in the seawater intrusion model of the Var estuary.

IV.3.2.3 Material property

The material property parameters used in the hydrodynamic module have been presented and validated in previous section (Section III.2.4 Hydraulic parameters). For the parameters used in the pollutant transport module such as molecular diffusion coefficient and dispersivity, the values of references are

used (Section IV.2): the molecular diffusion coefficient of seawater at 25 °C is $2.30 \times 10^{-9} \text{ m}^2/\text{s}$ [Holz et al., 2000], and the β_L/β_T are respectively 61/18 [Gelhar et al., 1992].

The only difference between the global model and the seawater intrusion model is the representation of the lenses. The hydraulic conductivity of the lenses that consist of clay and silt is $1 \times 10^{-9} \text{ m/s}$. The specific yield S_y is 0.02 (Table III.3) and the specific storage S_s is 0.001 m^{-1} (Table III.2).

The seawater intrusion is driven by the difference of the density between the freshwater and the seawater. This difference is quantified by the density ratio r , which is defined as:

$$r = \frac{\rho_s - \rho_f}{\rho_f}, \quad \text{Eq. 61}$$

where, r is the density ratio of the seawater (dimensionless), ρ_s is the density of the seawater (kg/m^3) and ρ_f is the density of the fresh water (kg/m^3). In FEFLOW, the default value of the r is 0.024. This value is used in the seawater intrusion simulations of Var estuary.

IV.3.3 Scenario design

This study focuses on the short term evolution (within 20 years) in the estuary area, thus the effect of the sea level rise caused by climate change can be neglected. In fact, there are numerous factors that are able to impact the seawater intrusion. In this study, only the pumping plan is studied as a factor that influences the seawater intrusion.

The pumping volume of Nice city is determined by the municipal water services. In consequence of lower drinking water demand, the pumping volume in these stations has been significantly decreased (Figure IV.20). It can be seen that the pumping volume has once reached 12.24 million m^3 on 2006, but it has remained less than 4 million m^3 from 2011 to 2013. For fear that the high pumping level plan would be implemented again, two scenarios, including a low pumping rate (named as Scenario A) and a high pumping rate (named as Scenario B) are simulated to indicate the influence of the pumping plan. As for the airport, the water consumption depends only on the passenger and cargo throughput. Since this economic level remains almost stable, the annual water consumption of the airport can also be assumed as a constant.

The average monthly discharge (1975-2015) measured at the estuary of Var river is $50.2 \text{ m}^3/\text{s}$. This value is used as the input data in a surface hydraulic model in the lower Var river valley. The calculated water level is assigned as transfer boundary to carry out the simulation with the density flow model.

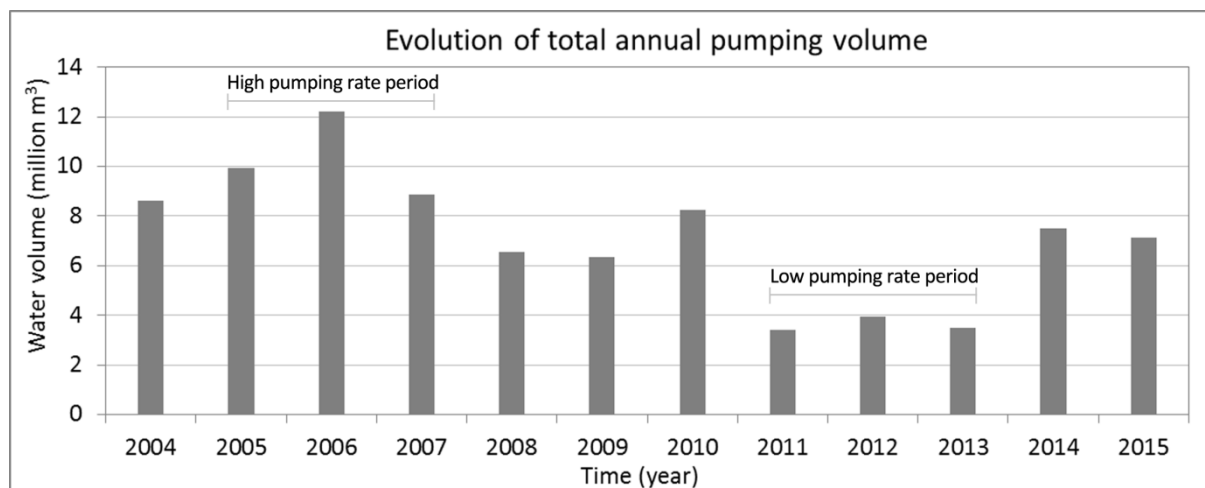


Figure IV.20. Evolution of total annual pumping volume in Nice city pumping station from 2004 to 2015.

A high pumping rate scenario whose reference year is 2012 and a low pumping rate scenario whose reference period is from 2011 to 2013 are simulated in this study. The pumping rates of the two scenarios are 764.4 and 2576.1 m³/d, respectively. Table IV.7 shows the detailed information of the 2 designed scenarios. Unlike the previous simulations, the seawater intrusion is simulated with steady state instead of transient state, because the computation on steady state is less time consuming. In FEFLOW, the governing equations are the same for both steady state and transient state simulation, thus the model output generated by the two modes of calculation should be very close or even the same. In this case study, in order to simulate a long-term effect, the boundary conditions are the average values that can describe the average state of the concerned variables, therefore, it would be better to perform the simulation with steady state.

Table IV.7. Summary of boundary conditions and material properties of seawater intrusion simulations (C_{Cl^-} is the concentration of chloride).

Boundary conditions	Value	Material properties	Value
Input flux in alluvium	0.28 m/d	Hydraulic conductivity of alluvium	Distributed
Input flux in conglomerate	0.001 m/d	Density ratio	0.024
Downstream hydraulic head	0.3 m	Porosity of alluvium	0.1
C_{Cl^-} in alluvium (initial)	32.5 mg/L	Porosity of conglomerate	0.05
C_{Cl^-} in conglomerate	10.9 mg/L	Effective rainfall	232 mm/yr
C_{Cl^-} in Var river	20.3 mg/L	Molecular diffusion coefficient	2.3×10^{-9} m ² /s
C_{Cl^-} in seawater	23.1 g/L	Longitudinal/Transversal dispersivity	61/18 m

IV.3.4 Seawater intrusion simulation results

Figure IV.21 and Figure IV.22 show respectively the top view of the concentration of chloride and Darcy flux in unconfined and confined aquifer. Figure IV.23 shows the vertical distribution of the chloride concentration on the profile which connects the shoreline and the boreholes of the airport.

An obvious difference between the two iso-contours can be seen on the top view of the unconfined aquifer (Figure IV.21). The iso-contour of 250 mg/L, which is the threshold value of the concentration of chloride in drinkable water, is 300 m away from the nearest borehole in scenario A, while in scenario B, the iso-contours of 250 mg/L have already passed the shallow boreholes of the airport. As the pumping volume in the upstream stations is increased by more than 3 times, the mixing zone (C_{Cl} varies from 1000 mg/L to 23111 mg/L) at the west and east borders of the airport is seriously influenced. However, the middle part of the airport is not in the mixing zone. It indicates that there is an unconfined groundwater outlet in the submarine sediment. The Darcy flux on the top slice of the unconfined aquifer proves the existence of the outlet. On the top slice, the groundwater flows into the sea through the shore line. On the bottom slice of the unconfined aquifer, the seawater wedge goes into the aquifer and meets the fresh water flowing along the opposite direction. The encounter between the fresh water flow and the seawater wedge has generated an area with small velocities of groundwater flow. In the southwest part of the airport, where the foundation is surrounded by the seawater, the encounter is located much more inland than other parts of the airport. The comparison between the two scenarios shows a great difference on the groundwater flow velocities at the pumping station, but the flow velocities near to the downstream boundary are not significantly influenced.

The simulation results of the top view of the confined layers (Figure IV.22) shows that, the high pumping volume has pulled seawater wedge by 300 m towards the inland direction. Therefore the iso-contour of 250 mg/L almost reaches the deep boreholes at the airport. It can be seen that the mixing zone is larger in the confined layer than in the unconfined layer. The simulated Darcy flux of the top slice of the confined aquifer is more complicated than that in the unconfined aquifer. It shows that there is also an outlet of the freshwater under the southeast boundary of the airport, where the groundwater flows towards the sea. While in the southwest part and east part of the airport, groundwater flows towards the inland direction due to the pumping activity in the deep boreholes. On

the bottom slice of the confined aquifer, the groundwater flows towards the inland direction because of the huge pumping rate in the deep boreholes.

The profile view (Figure IV.23) has revealed the influence of aquitard on the vertical distribution of concentration. In the numerical simulation, the aquitard is modeled with a layer whose hydraulic conductivity is extremely low (1×10^{-9} m/s) in order to ensure the continuity of the computation in porous media. This is the reason why the isolines are always connected in the profile results even though they pass through an aquitard. These results confirm the existence of separated density flow in unconfined and confined aquifer. The seawater wedge is pushed towards the sea by the groundwater flow in both unconfined and confined aquifer. However, the mixing zone travels further into the inland in confined aquifer than in unconfined aquifer. Compared to scenario A, the isoline of 250 mg/L in scenario B is pulled towards the inland much longer in unconfined area due to the increment of the pumping volume in the pumping station of Nice city, which only extracts water in unconfined aquifer. Nevertheless, this increment can also induce an obvious change of the flow direction in the confined aquifer. In the mixing zone where the concentration varies from 1000 to 4000 mg/L, such an increase in the pumping rate would almost double the concentration of chloride in both unconfined and confined aquifer.

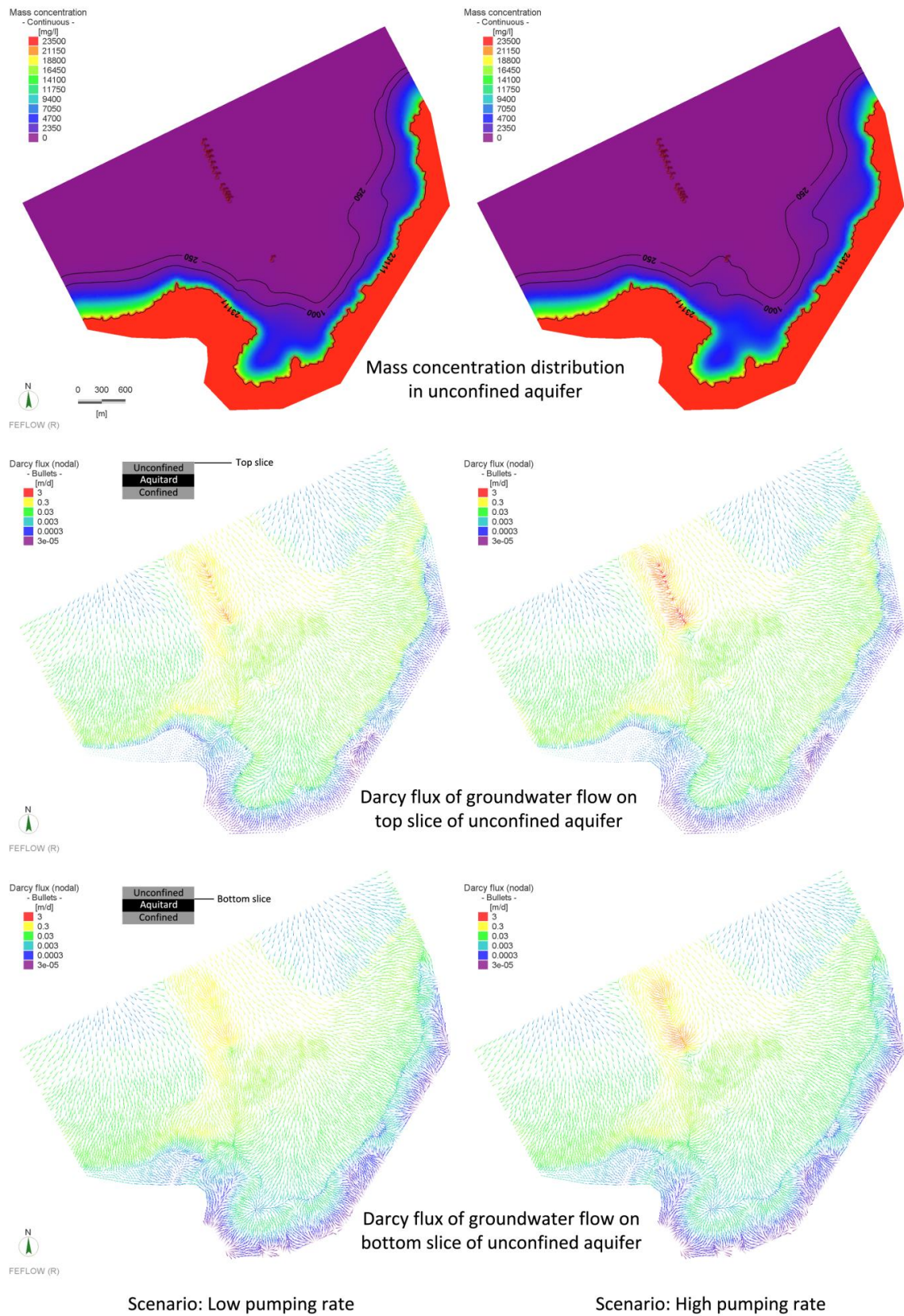


Figure IV.21. Top view of the simulation results in the unconfined aquifer.

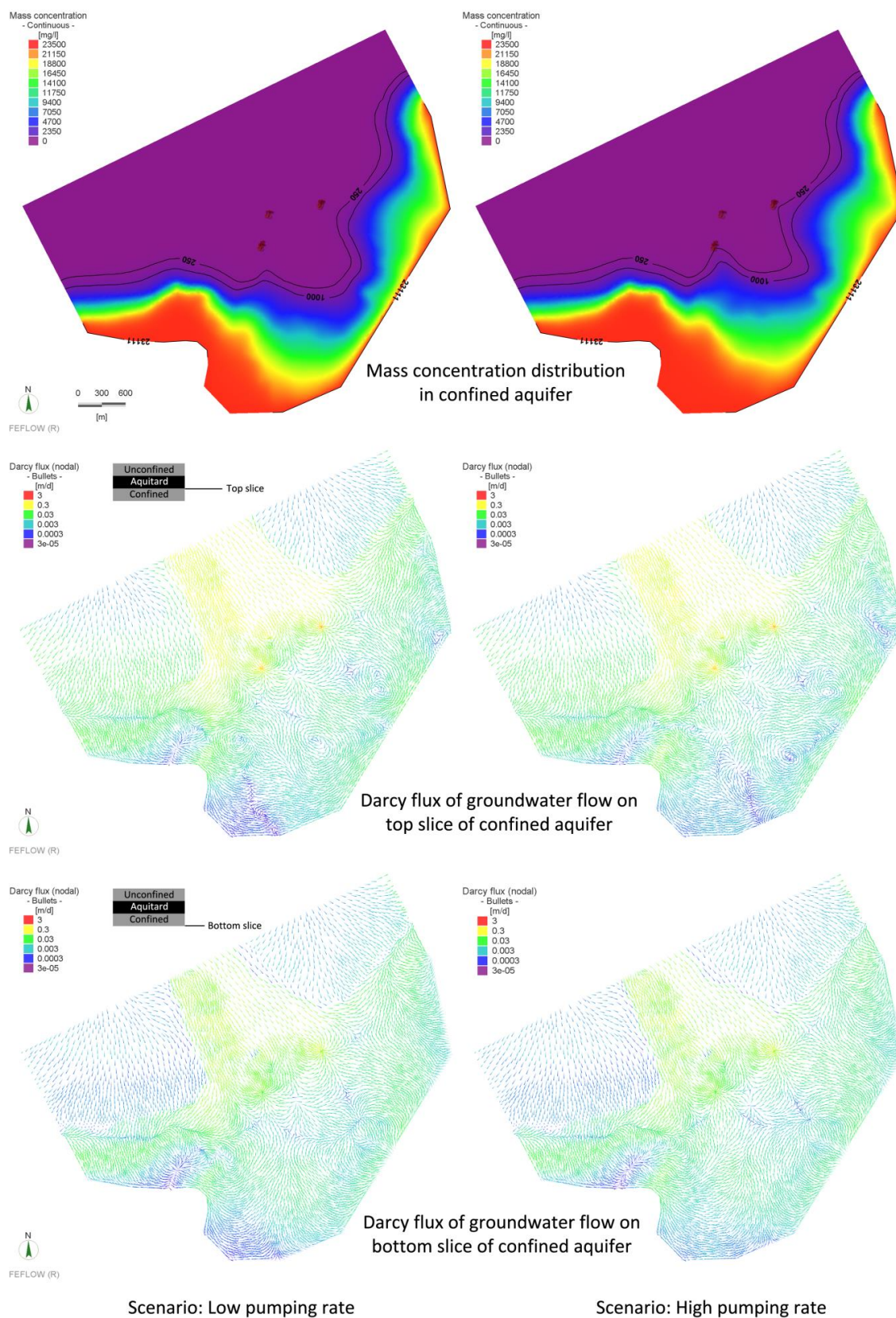


Figure IV.22. Top view of the simulation results in the confined aquifer.

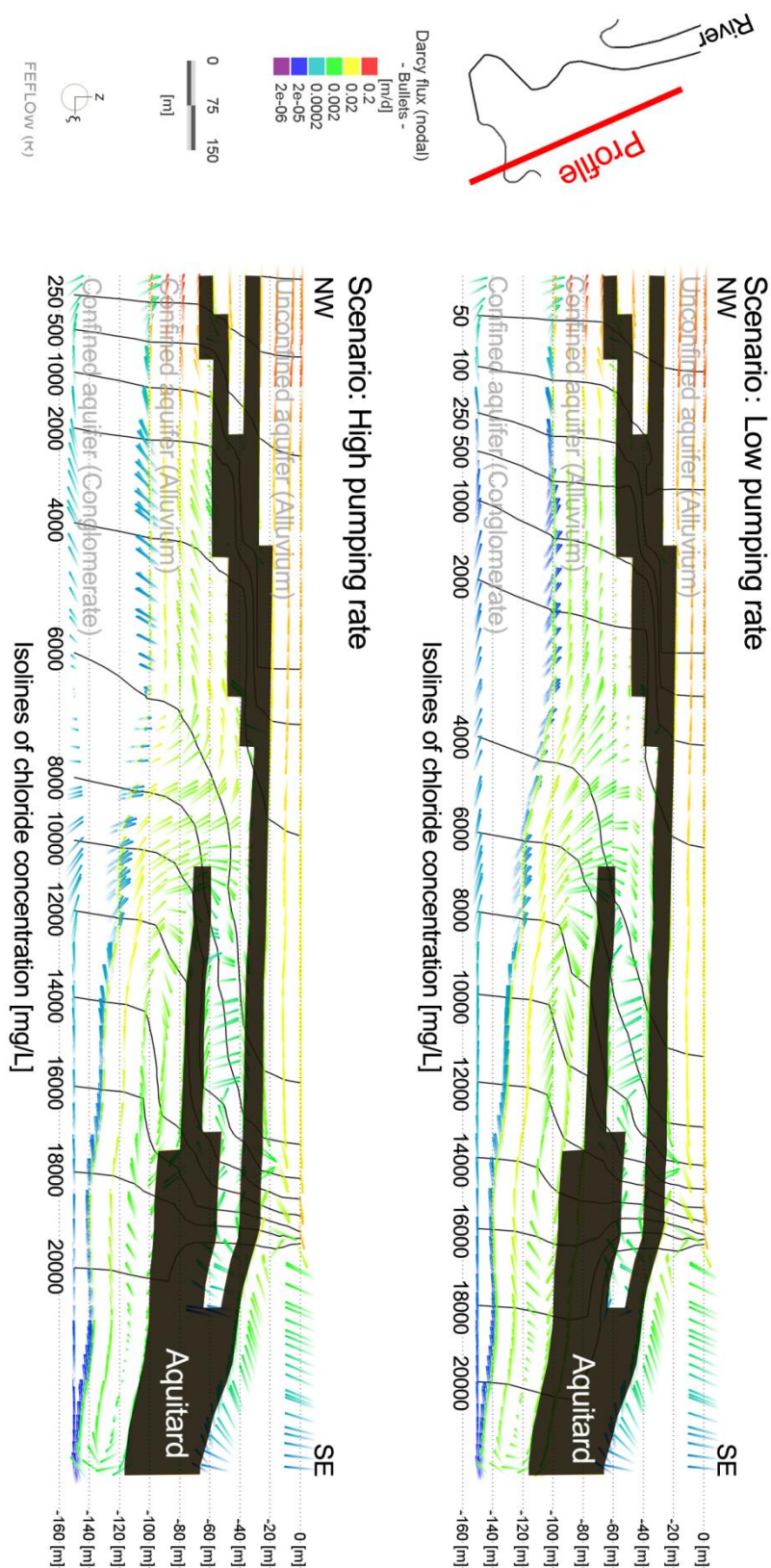


Figure IV.23. Profile view of the simulation results.

IV.4 Conception of a management tool based on the numerical models

IV.4.1 Integrated monitoring system

As explained in the preface, the aim of the AquaVar project is to develop a decision support system (DSS) in Var catchment [Gourbesville et al., 2016], which is dedicated to provide information by a holistic approach that integrates various situations such as flood and lack of drinking water. The core of this system is a monitoring system that consists of a field data measurement network and a numerical modeling system. The field data measurement network collects various types of data such as precipitation, temperature, water level, flow velocity *etc.*, by numerous sensors installed all along the catchment and especially in the lower Var valley. The modeling system is an implementation of the hydrological model, surface hydraulic model and the groundwater flow model. The hydrological model calculates the runoff of the Var catchment from the precipitation by considering several physical processes including evapotranspiration, infiltration and snow melting. The surface hydraulic model takes the discharge of the Var river calculated by the hydrological model as an input and calculates the water level in the lower Var river, by considering the effect brought by the weirs and the mini-hydropower plant on the riverbed. It also contains a sediment transport module that simulates the short term morphological evolution induced by floods. The groundwater flow model uses the water level as an input to calculate the groundwater level and flow velocity in the unconfined aquifer of the lower Var river valley.

Figure IV.24 shows the data flow of the monitoring system of the DSS. The time series data is recorded by the sensors and then stored in the ASCII format. The stored data can be visualized by users on an application web. This process forms the function of the module No.1, which is a real-time monitoring module. The disadvantage of the module is that the monitored data is only the time series measured at the points. For the place where no sensor has been installed, no data can be provided to the decision maker.

The second module of the monitoring system involves the three numerical models (hydrological model, hydraulic model of the river and hydraulic model of the groundwater flow). The measured time series data are used as inputs for the three models. For example, the measured discharge of the Var river can be used in the surface hydraulic model to produce the water level, which is an input of the groundwater flow model that calculates the groundwater level in the valley. The output of this module

can provide a spatially distributed simulated result, which will be more direct and easy to be read by the decision makers. Since this module reflects also the actual state of the studied area, only small simulation period can be used in order to decrease the computation time. Thus the key technical point is to update the inputs of the models automatically and run the models in a loop. The results of the simulation are stored and visualized on the application web.

The third module is the scenario simulation with customized input data from users. The simulation period is longer and the input data that needs to be changed is more than boundary conditions which are times series data. For example, user can update the topographical data of the model to perform a simulation with lowered weir or newly built infrastructures. In this module, the simulation results are also stored and visualized on the application web, but they are also archived as a reference for the water management service.

Even though the software used to build the numerical models is not open source, it is possible, however, to create codes that send commands lines to the software to achieve many functions such as converting input data and performing simulations. MIKE SDK is a development toolkit that enables the programmers to design external tools that use MIKE software components. IFM (interface manager) can be used to add plug-ins into FEFLOW to achieve added functions and exchange input/output data. Moreover, all the three software can be used under command line mode, which makes it possible to operate the data flow without modifying the source code of the software.

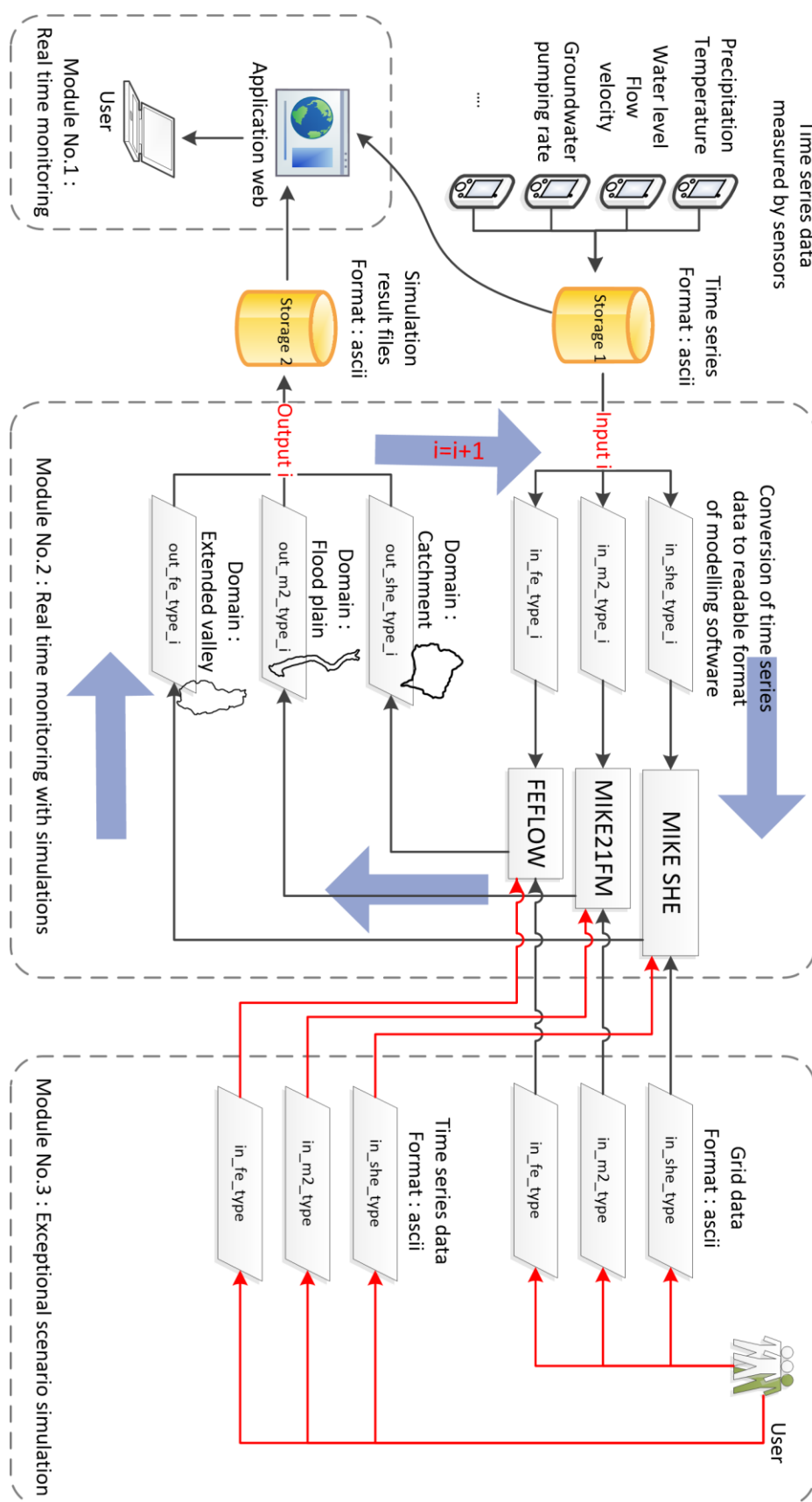


Figure IV.24. Data flow chart of the integrated monitoring system in Var catchment (Author's design).

Computational power is the biggest challenge of the setup of this monitoring system. In module No.2, simulations need to be performed in a loop with updated data. Therefore the computation time must be as short as possible. With the current computational power (2 processors of Intel i7-4790, 3.6Ghz, Ram of 16 Gb), the computation of a 6-hours-simulation of a flood event takes 2 hours in total for the three models (50 min for MIKE SHE, 50 min for MIKE21FM, 5 min for FEFLOW and 15 min for data conversion or other operations). For the drought event simulation, 2 hours of computation time (20 min for MIKE SHE, 80 min for MIKE21FM, 5 min for FEFLOW and 15 min for data conversion or other operations) can cover a simulation period of 20 hours. According to these examples, the computational power of the current computer can be summarized as: for a computation time of T hours, the monitoring system is able to simulate (or predict, if the predicted precipitation data from MétéoFrance is applied) a flood event that lasts for $3T$ hours, or a drought event that lasts for $10T$ hours.

In AquaVar project, the DSS can be applied by various users for different purpose. Figure IV.25 shows the data flow of the DSS of the AquaVar project. The users are classified into three types according to their profiles and their potential needs:

- Expert users: the expert refers to the administrator of the models. After having built the model and the DSS for Var catchment, they are also supposed to validate the new acquired data, update the existing model and validate the updated model. Therefore they have the full access to the system and to the models.
- Professional users: the professionals are the project partners who are the decision makers of water related issues. They have the access to web application and they can also prepare the inputs of scenarios to perform simulations. Simultaneously, the professional users need to provide new data to update the model and enrich the database of the project.
- Public users: the public users are the researchers, students who need hydrology and hydraulic data, and even citizens who are concerned about the water related crisis. They have the access to the web application and they can only read and download the measured data and simulation results that are opened to them.

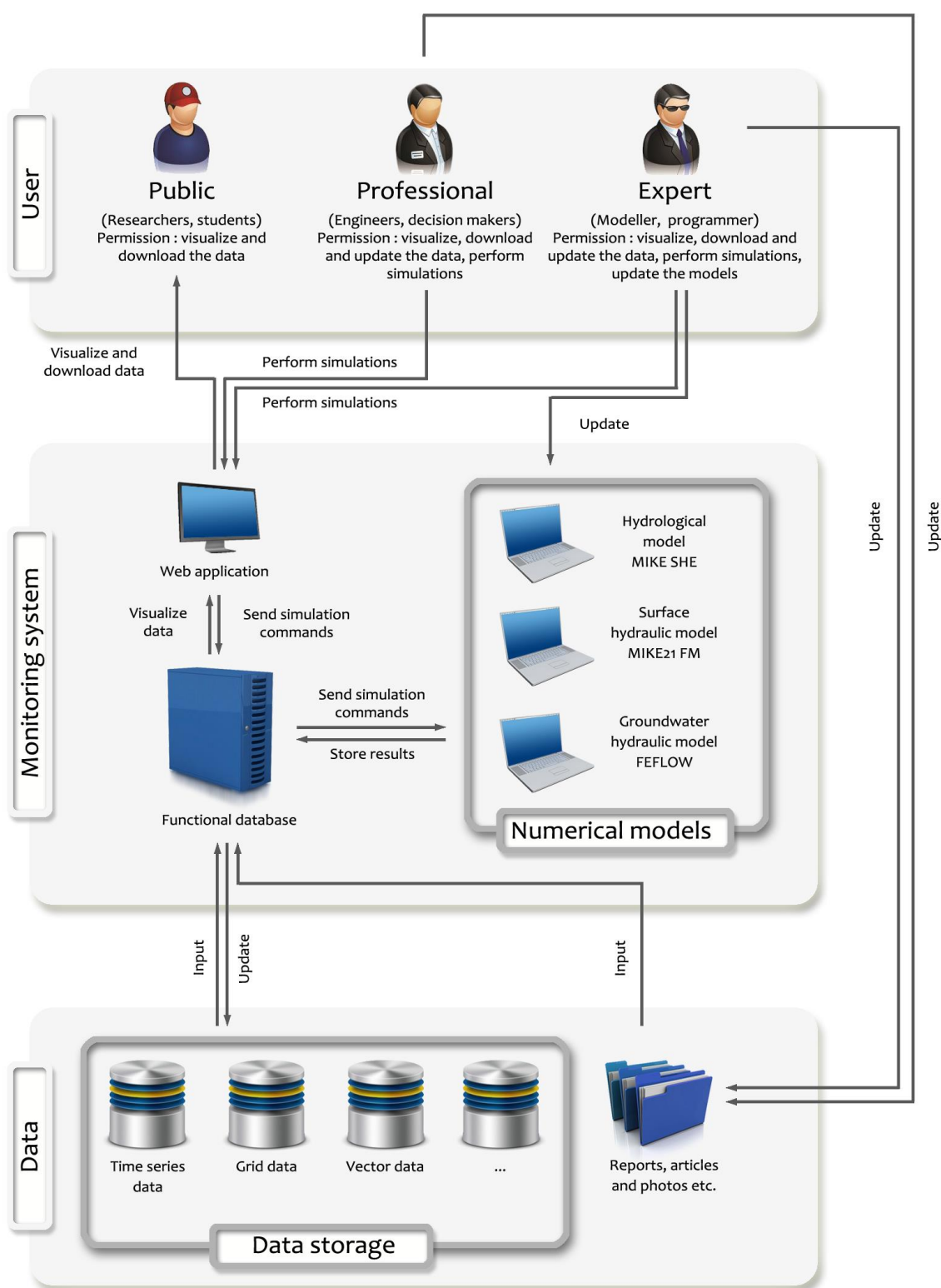


Figure IV.25. Conceptual framework of the utilization process of the DSS of the Var catchment (Author's design).

IV.4.2 Data update in groundwater flow model

The data used to setup the model presented in Chapter III has a lot of uncertainties. The study of the surface water flow and the groundwater flow is still ongoing and will continue as the development of the valley goes on. Thus new data can be acquired to update the current groundwater flow model, in order to increase the knowledge of the behavior of the aquifer, and to produce more reliable simulated results. The following data can be updated if the new data satisfy certain conditions.

The topographical data used to build the current model is the DEM of 5 m resolution measured in 2009 measured by the municipality of Nice Côte d'Azur. Since the river morphology can be strongly influenced by the flood event or the demolition of the weirs, the topographical data should be updated in both surface hydraulic model and groundwater model. Otherwise the river-aquifer exchanges would not be modeled correctly with wrong streamlines. On the other hand, the DEM only records the surface elevation, thus the water surface is recorded as the ground surface and used in the numerical model. A bathymetric survey would be the best solution to improve the topographical data.

In the current numerical model, the geological layers are reproduced based on the map made by Guglielmi [1993] and Emily et al. [2010]. The accuracy of such a map is acceptable for geological analysis, but it is too inaccurate to build a numerical model. Therefore the more accurate geological data are always needed for the model improvement.

As an important input that may influence a lot the result, hydraulic conductivity of the alluvium is obtained by geological drilling tests. But so far the number of the tests is not enough for a numerical model (Figure III.11). Besides, the alluvium is represented by one layer in the groundwater flow model, while sometimes the hydraulic conductivity value obtained from the test is not representative due to the existence of the lenses. Once new data have been collected, the values need to be validated before using them in the numerical model.

The transfer rate ϕ is an empirical parameter that quantifies the ability of exchanging water between the river and the aquifer. It depends on the thickness and composition of the clogging layer on the riverbed. If the weirs are lowered or removed, even a small flood event is able to change the morphology of the riverbed. In this case, the clogging layer would not keep the same characteristics any longer, hence the transfer rate should also be recalibrated.

After the model validation (Chapter III), it has been concluded that the daily average discharge is the main reason for the underestimation of the simulated peak value of groundwater value. If new sensors can be installed to measure the discharge with a smaller time step (*e.g.* hourly data), the accuracy of the model output, especially for the peak values, would be significantly increased.

For other inputs such as upstream boundary condition, precipitation, actual evapotranspiration, and groundwater extraction, it is only a matter of data replacement according to the aim and duration of the scenarios.

IV.5 Conclusion

In this chapter, the validated numerical model is applied to perform simulation of scenarios. The aim of these simulations is not only to study the behavior of the aquifer under certain circumstances, but also to test the feasibility of reusing the model as a DSS for further studies. Several types of scenario are considered, including extreme hydrological events, pollutant transport in the unconfined aquifer and the seawater intrusion in Var catchment.

The scenarios of extreme hydrological events consist of a series of flood events and a series of drought events. For each type of event, five occurrences corresponding to return periods of 2, 5, 10, 20 and 100 years are simulated. The results show that the unconfined aquifer is more sensitive to the flood events than to the drought events. The difference between the groundwater level of a 2-year flood and 100-year flood is about 0.5 to 1.5 m, according to the locations. But the difference for the drought events is usually less than 0.5 m. This means that the Var river regulates the groundwater level by river-aquifer exchanges when the aquifer faces a drought event. In conclusion, the water level in the river plays an important role in the hydrodynamic simulation. Therefore, to simulate the flood and drought events, the most important boundary conditions to be modified is the water level in the river. By this example of model application, the hydrodynamic module of the model is proved to be reusable and functional for scenarios studies. However, the model validation gives the conclusion that the simulated peak of the groundwater level may be underestimated due to the coarse input data (daily average discharge), therefore the scenario simulations of the flood events may also be underestimated. According to the model validation results (Figure III.33 and Figure III.34), the expected level of the peak value could be 0.1 to 1 m higher than the simulated value.

A pollutant transport module has been added to the model. Then this module was applied to simulate a series of pollution events in the aquifer of the lower Var river valley. The results of the accidental events indicate that the pollution transport in the unconfined aquifer has different characteristics along the valley. For an accidental event, the concentration of the pollutant dispersed more quickly in the upstream part than in the downstream part. In the area near to the Broc lake, a pollution event with an initial concentration of 12500 mg/L can decrease to 0.3 mg/L within 3 months. But in the downstream area near to the estuary, the simulation results claim that the pollution stays for a longer time in the downstream aquifer than in the upstream part. A constant pollution event is then simulated, the results show that for the first three years, the pollutant is dispersed and conveyed through a distance of 10 km toward the downstream direction. Hence, based on the modeling results, in both accidental and constant pollution event, the first 10 days after the injection of the pollutant is the most important period for the local managers to take reaction before the pollutant gets diffused, especially for the upstream area, where the polluted area gets diffused very fast.

The pollutant transport module is setup with the values of longitudinal and transverse dispersivities that have been estimated based on similar case studies. Neither calibration of the parameters nor a validation has been done due to the lack of the case study. More studies are needed if more reliable simulation results are needed for the further application. Besides, the pollutant transport module is setup based on the hydrodynamic module without unsaturated flow, which means the scenarios are assumed to be a direct injection or leakage of the pollutant in the unconfined aquifer. But in reality it is highly possible that the injection or leakage start from the ground surface. In this case, the infiltration process would lead to a portion retained in the unsaturated layer. Moreover, the pollutant simulated in these scenarios is assumed to be conservative without any decay. Hence, the simulation results with the current numerical models are likely to provide an overestimated concentration of the pollutant in the aquifer. In other words, the simulation of pollution events with the current model always offers pessimistic output.

Seawater intrusion is simulated with a new model, which is more localized and more accurate than the original model. The modeled domain is reduced to the estuary of Var river and the alluvium is divided into 10 layers in order to represent the aquitard that consists of clay and silt lenses. Two scenarios are simulated to show the seawater intrusion with different pumping rates in Sagnes pumping station. The

results reveal that the seawater intrusion in both unconfined and confined aquifer is influenced by the pumping rate in Sagnes station. A low pumping rate like the period from 2011 to 2013 would not cause any threat of the water quality in the existing boreholes. However, a high pumping rate as for the year of 2006 would threat the quality of water pumped by the borehole at the airport. The water pumped from the confined aquifer would not meet the drinkable condition unless the water consumption of the airport changes.

This new model is an example of a secondary development based on the existing model. For further application, it is probable that the current model is too coarse to be used for certain studies, therefore a new model can be developed with more detailed data and more specific aims. In this case study, the aquitard layers are added as a new data while the hydrodynamic parameters and the boundary conditions are obtained from the existing model. The model is not validated due to the lack of measured data. Therefore this model can be improved if there are further studies that can provide the measured data for model validation.

A first conception of the DSS of water resource management in Var river has been presented in this chapter. The main component of this system is an integrated monitoring system that contains three numerical models (hydrological model, hydraulic model of the river and hydraulic model of the groundwater flow). Technically, this system is feasible, but the computational power would be a great challenge for the realization of the system. There are three types of user profile (expert, professional and public), each user profile corresponds to a specific access of data and it is compulsory to provide certain data to update the numerical models. This conception is merely a preliminary attempt to discuss the monitoring system in the point of view of modelers. More details need to be discussed regarding the informatics and hardware aspects such as the parallel computation, the software coupling, the GPU accelerated modeling software and the compute clusters.

Chapter V. Coupled groundwater and surface water model

V.1 A brief review of groundwater and surface water coupling

In the case study of Var, the water level in the river is considered as a transfer boundary that is calculated separately by a river hydrodynamic model (Section III.4). The river-aquifer exchange is modeled by Eq. 3. This method, which avoids to use Richards equation for disconnected area, helps to simplify the model and to reduce the computation time. This performance is an advantage for the Decision support system (DSS). However, this method considers the river and the aquifer as two separated systems, because the water level in the river is pre-calculated. When there is an exchange between the river and the aquifer, the river cannot gain or lose water since the river-aquifer exchange is only simulated by the groundwater flow model. In reality, the exchanges between the surface water and groundwater obey the conservation of the mass, which means that the water lost by the river is gained by the aquifer, vice versa. For the Var river case, the interaction between the river and the aquifer is especially intense due to the geomorphological conditions. Therefore the river and the aquifer should be modeled as a single system.

Without coupling, the water level in the Var river is only a boundary condition of the groundwater flow model. It is calculated before the groundwater flow simulation. The quantity of the water in the river does not reduce or increase due to the infiltration or exfiltration. A better way to model the interaction is to couple the surface water model and the groundwater model. Furman [2008] and Spanoudaki et al. [2009] have summarized the widely used coupling protocol for surface water and groundwater. Numerous coupled models have been developed. Some of them combine 1D or 2D shallow water equations with a groundwater model [Swain and Wexler, 1996; Sparks, 2004; Liang et al., 2007; Li et al. 2008]. For some of them, the fully dynamic shallow water equations are replaced by the diffusion and kinematic wave approximations [Jobson and Harbaugh, 1999; Vanderkwaak, 1999; Hussein and Schwartz, 2003; Panday and Huyakorn, 2004; Morita and Yen, 2002; Gunduz and Aral, 2005; Sochala, 2008, Sochala and Piperno, 2009; Sudicky et al., 2003; Weill, 2007; Weill et al. 2009]. Regarding the groundwater flow model, there are 2D or 3D saturated or variably saturated models that solve either Darcy or Richards equations [Furman, 2008] with the continuity equation for the groundwater flow. Liu et al. [2007] have studied the groundwater response to overland flow with a

1D/2D/3D coupled model. The overland flow was modeled by coupling MIKE SHE and MIKE11 codes, while the overland flow and groundwater flow were coupled by using MIKE SHE codes.

Generally, the basic concept for coupling is to calculate and exchange a common variable between coupled equations. In this case, the flux of exchange caused by infiltration and exfiltration between the river and the aquifer is the common variable. It is considered as the source term in the continuity equations of both shallow water system and groundwater flow system. The coupling methods that are widely used to couple surface water model and groundwater model are either in an iterative or non-iterative manner [Swain and Wexler, 1996; Jobson and Harbaugh, 1999]. The iterative manner requires that the solutions of the common variable given by the surface water and groundwater flow equations are included within a specified tolerance interval at each time step. The non-iterative method involves the solution of the surface water and groundwater flow equations in succession. The iterative method gives a more accurate result, but the computation time is much longer than the non-iterative method [Gunduz and Aral, 2005].

As commercial software, FEFLOW provides the possibility to add plug-ins by using IFM (Interface Manager) to accomplish data transfer, but the modification of the code is not possible. Therefore all the extensions developed to couple FEFLOW and other codes should be non-iterative. So far, four coupled models have been developed for FEFLOW:

- IFMMIKE11 [Monnikhoff, 2004] has been developed for the coupling between FEFLOW and MIKE11 (unidimensional modeling software);
- IFMHYDRO_AS-2D [Schäzl and Nujic, 2004] has been developed for the coupling between FEFLOW and HYDRO_AS-2D (bidimensional modeling software);
- MIKE SHE_FEFLOW [Yamagata, 2012] has been developed by using Open MI to couple FEFLOW and MIKE SHE (tridimensional modeling software)
- MIKE GWSW [Cornaton, 2016] has been developed for the coupling between FEFLOW and MIKE21FM (bidimensional modeling software).

In MIKE GWSW, the groundwater flow model has to be a variably saturated model in order to consider the unsaturated layer in case there is a disconnection between the water body and the aquifer. This configuration potentially provides an accurate result because it is realistic, but, on the other hand, increases the computation time for the simulation. Since the model will be implemented in the DSS,

the computation time is a critical factor to evaluate for the functionality of the DSS. Therefore a balance between the computation time and the accuracy of the results has to be found.

Knowing that the model developed for AquaVar project ignores the unsaturated layer and the results of model validation show that the associated errors are within a tolerable range (Section III.7), an interface that couples the saturated flow model in FEFLOW and the river model in MIKE21FM seems to be a good option to keep the accuracy, but reduce the computation time. Compared to MIKE GWSW, this coupled model needs less computation time, thus it is more convenient to be implemented in the DSS.

Brandmeyer and Karimi [2000] have analyzed various coupling methodologies according to their characteristics from a modeler's perspective. They have divided the coupling into five types regarding the level of model control:

- one way data transfer: modeler interfaces with each model, manually transfers data;
- loose coupling: modeler interfaces with each model, uses automated data transfer;
- shared coupling: single graphical user interface (GUI) and separate data storage, or multiple GUI and common data storage;
- jointed coupling: one model embedded in other or two in parallel, single GUI, common data storage;
- tool coupling: framework provides tools to support embedded and integrated models, single GUI, common data storage.

The first two coupling levels are less complicated than the last three. In the current groundwater flow model, the water level is calculated by an independent surface water flow model and then assigned manually in the GUI of FEFLOW. This one-way data transfer is exactly the first level mentioned above. This kind of data transfer can be hardly called as coupling because the link between the two models is not in dynamic mode.

FEFLOW and MIKE21FM are two commercial closed codes thus code modification is not possible. The GUI and the storage of the data cannot be shared. Thus the “shared coupling”, “jointed coupling” and “tool coupling” cannot be achieved by the modeler. The only way to couple these two modeling tools is to establish a “loose coupling” by creating an automatic data transfer interface with plug-ins such as MIKE SDK or IFM (Section IV.4.1 Integrated monitoring system).

V.2 Conception of the coupling interface

In the continuity equation for groundwater flow in porous media implemented in FEFLOW (Eq. 19), the variable P is the mass accretion due to the external sources. When the value is positive, it refers to a gain of water from precipitation or infiltration. When the value is negative, it refers to a loss of water due to the evapotranspiration or exfiltration. Putting precipitation and evapotranspiration aside, P is the variable that should be exchanged between the surface water model and the groundwater model:

$$(S_s B + S_y) \cdot \frac{\partial h}{\partial t} + \nabla(B\mathbf{q}) = B\varepsilon Q + P. \quad \text{Eq. 19}$$

The 2D shallow water equations [Delestre, 2010, DHI, 2011] solved by MIKE21FM is written as below:

$$\begin{aligned} \frac{\partial h}{\partial t} + \frac{\partial hu}{\partial x} + \frac{\partial hv}{\partial y} &= P - I \\ \frac{\partial hu}{\partial t} + \frac{\partial(hu^2 + \frac{gh^2}{2})}{\partial x} + \frac{\partial huv}{\partial y} &= gh(S_{0x} - S_{fx}) , \\ \frac{\partial hv}{\partial t} + \frac{\partial huv}{\partial x} + \frac{\partial(hv^2 + \frac{gh^2}{2})}{\partial y} &= gh(S_{0y} - S_{fy}) \end{aligned} \quad \text{Eq. 62}$$

where, g is the gravitational constant (m/s^2), h is the water depth (m), u (respectively v) is the orthogonal projection of water velocity aligned with x -axis (respectively y -axis) (m/s), $P(t, x, y)$ is the gain of water per unit area (m/s), $I(t, x, y)$ is the loss of water per unit area (m/s), S_{fx} , S_{fy} are the friction terms depending on the friction law considered (Manning, Chézy, etc.), S_{0x} , S_{0y} are the terms of slope on x -axis and y -axis, $z(x, y)$ is the topography (m).

The variable P and I are the external source terms. P represents precipitation from the atmosphere and exfiltration from the aquifer, while I represents the evapotranspiration to the atmosphere and infiltration to the aquifer. Putting aside the influence of the precipitation and evapotranspiration, the external sources P and I are thus the variable exchanged between the surface water model and the groundwater model.

To unify the different notions of the same variable, q_{ex} is defined as the exchange flux between river and aquifer. In the model without coupling, q_{ex} is calculated as a transfer boundary (Eq. 3). For the coupling of the two models, q_{ex} replaces all the terms of external sources. The coupling interface to be

developed is a Java script programmed to achieve the exchange of data with a specific time step Δt (Figure V.1).

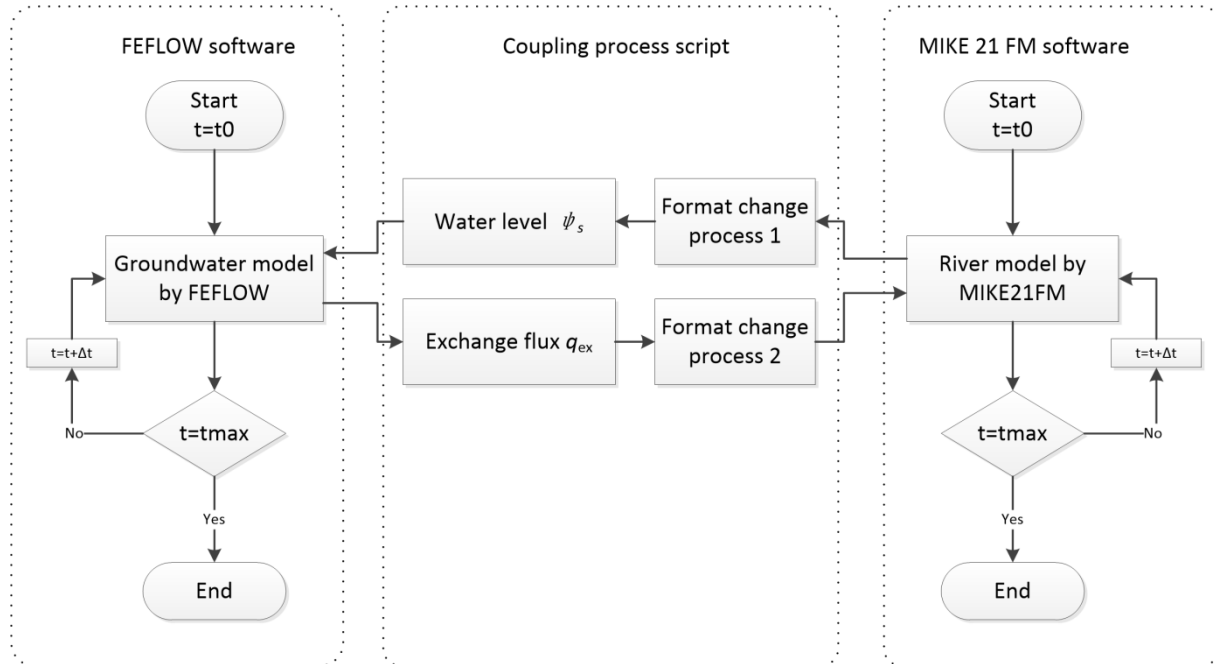


Figure V.1. Data flow of coupling process between the 3D saturated groundwater flow model (FEFLOW) and the 2D surface water flow model (MIKE21FM).

When the coupling begins, MIKE21FM runs for the first time step. At the end of this time step, the first data exchange starts. The surface water model provides the water level in the river ψ_s as an output. This value is delivered to FEFLOW after a process of format adaptation and assigned as a transfer boundary in order to calculate the exchange flux with Eq. 3. FEFLOW performs then the simulation for the first time step and gives as output the exchange flux. The format of the output is adapted to MIKE21FM before the following cycle begins. The coupling time step Δt is usually bigger than both computation time step of FEFLOW δt_f (from 15 min to 1 day) and the computation time step of MIKE21FM δt_m (from 1 to 10 s). Therefore Δt must be an integer multiples of both δt_m and δt_f in order to not producing residual error of the simulation time, as shown in Figure V.2.

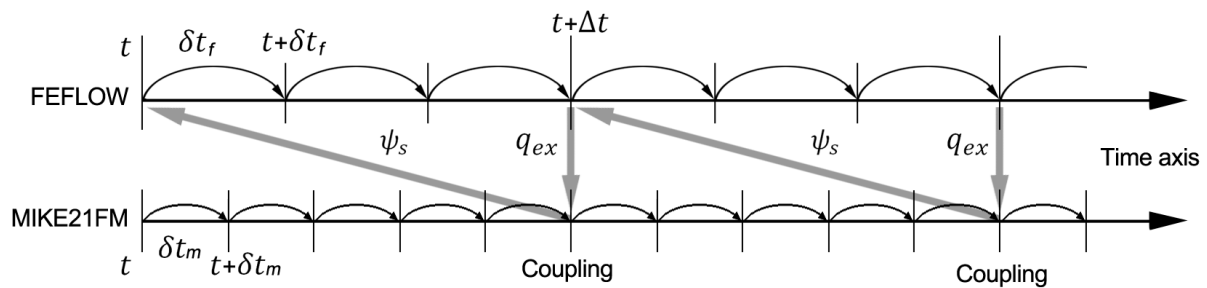


Figure V.2. Time step adaptation between the coupling time step and the computation time step.

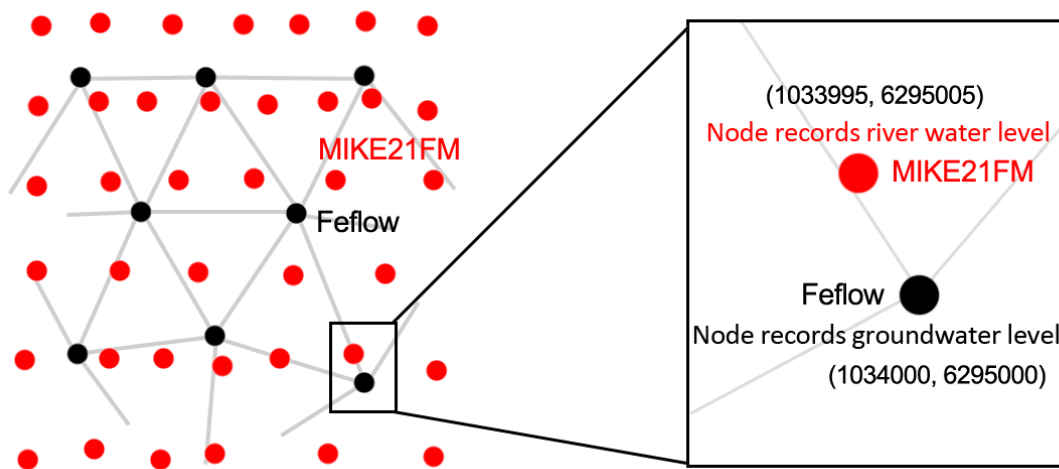


Figure V.3. Mesh adaptation of the coupling interface.

For the same river, FEFLOW and MIKE21FM do not use the same mesh. Since the velocity of the river flow is much faster than in the groundwater flow, the mesh used in MIKE21FM must be smaller to satisfy the stability criteria, the Courant–Friedrichs–Lewy (CFL) convergence condition. For the models built for the lower Var river valley, the cell size of the groundwater model is defined to 25 m on the riverbed and the cell size of the surface water model is fixed to 5 m. When the two meshes overlay, a node in FEFLOW needs to find its nearest node in MIKE21FM (Figure V.3). A calculation is performed before the coupling in order to establish the links for each node in FEFLOW. The links are then stored as a constant input for the whole coupling process because, once the models are built, the mesh and the number of the nodes in both FEFLOW and MIKE21FM are constant. The exchange of data is always performed through these links.

After having defined coupling process, time step adaptation and mesh adaptation, the last problem to solve is the conversion of the exchanged data format. MIKE21FM is based on the MIKE Zero

platform for which all the input and output data are converted into a binary format with specific extensions. While the input and output data in FEFLOW are in ASCII format that can be handled by the Java script. The involved files are listed in Table V.1 and the data flow for the conversion process is shown in Figure V.4.

Table V.1. Data format of the input and output files involved in the coupling process.

Extension	Format	Involved software(s)	Data type
*.fem	ASCII	FEFLOW	Simulation file which contains all the configurations of the model
*.dar	ASCII	FEFLOW	Result file that records groundwater level, flow velocity on x, y and z directions
*.xyz	ASCII	FEFLOW & MIKE21FM	Common format used for recording spatially distributed data
*.ASCII	ASCII	MIKE21FM	Common format used as a intermediary format for data conversion
*.dfs0	binary	MIKE21FM	Time series data file
*.dfs2	binary	MIKE21FM	Spatially distributed data file that records values in structured grid
*.dfsu	binary	MIKE21FM	Spatially distributed data file that records values in unstructured mesh
*.mzt	binary	MIKE Toolbox	Operational file of MIKE Toolbox which can achieve the conversions

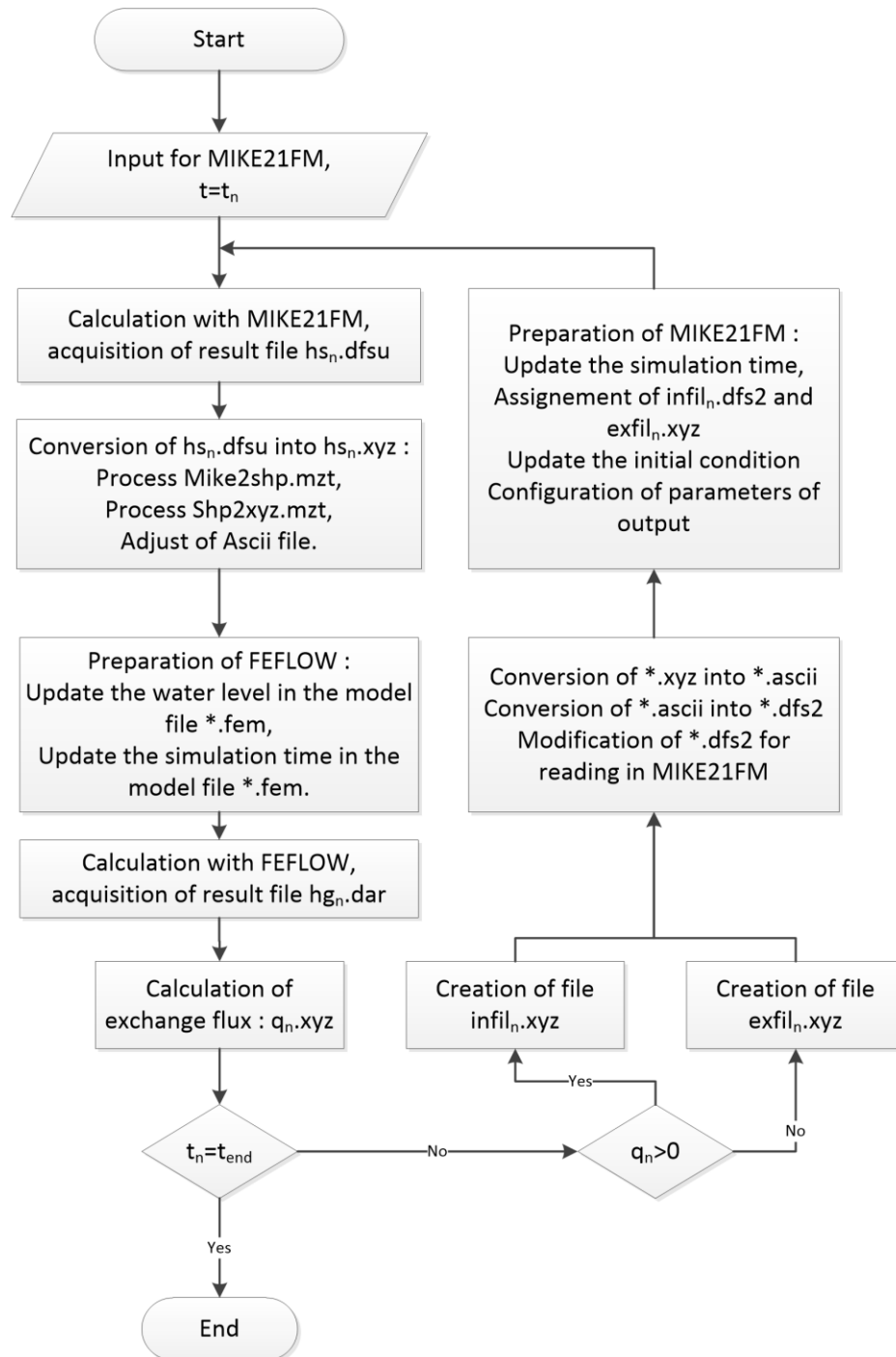


Figure V.4. Flow chart of the data conversion process.

V.3 Simulation test with the developed coupling interface

A simple test case has been designed in order to test the coupling interface between FEFLOW, the saturated groundwater model, and MIKE21FM, the surface water model. The defined test case is a straight channel with an uniform slope of 0.5%, which is the average slope of the lower Var river. The canal is located on a two-layer soil with a dimension of $9 \times 9 \times 8$ m (Figure V.5). In the groundwater model, no upstream or downstream boundaries are defined because the test area is too small, thus the boundary conditions would constrain too much the groundwater level. The initial groundwater level, however, must be given in order to set a groundwater table connected with the river. This protocol corresponds with the coupling hypothesis between a saturated groundwater flow and a surface flow. In this test case, the initial groundwater level is 9 m, which is equivalent to a depth of 1 m at the downstream side. The material properties of this soil block are the values that are similar to the porous media of the unconfined aquifer in the lower Var river valley: hydraulic conductivity $K=0.001$ m/s, specific yield $S_y=0.1$, in/out transfer rate $\phi_{in} = \phi_{out} = 2 \times 10^{-5} \text{ s}^{-1}$. In the surface water flow model, the discharge enters in the canal from the upstream boundary is $2.5 \times 10^{-6} \text{ m}^3/\text{s}$ and the downstream water level is 9.7 m. The value of Manning roughness coefficient for the riverbed of the canal is $0.033 \text{ s/m}^{1/3}$. The simulation test is assumed to be a period of drought, when the discharge is stable in the canal and no precipitation is considered in the calculation. The total duration of the simulation is 7 days, which contains 7 coupling calculations. The computation time step of the groundwater flow model is 0.01 day, and the time step in the surface water flow model is 10 seconds.

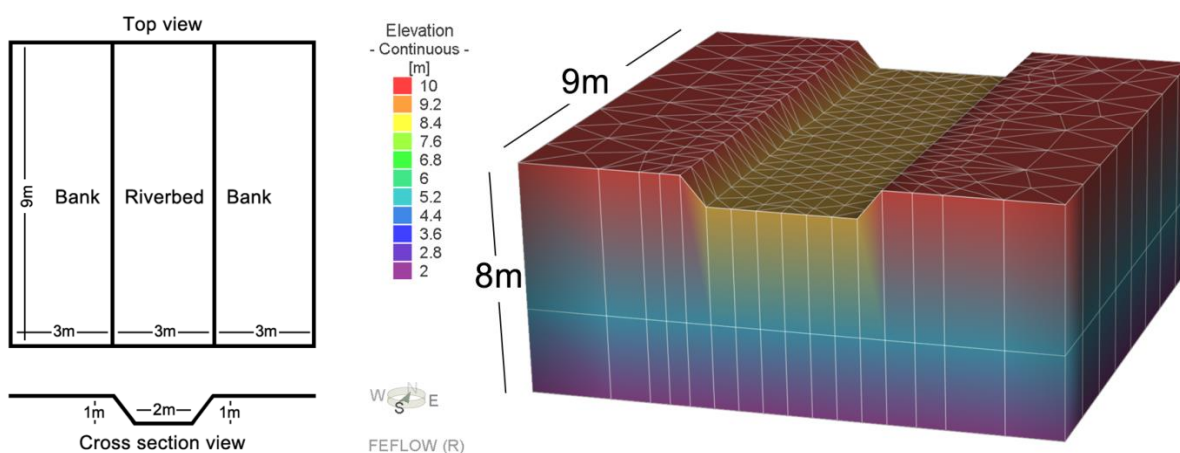


Figure V.5. Geometry of the test case for coupling interface between saturated groundwater and surface water models.

The intermediary exchanged data, water level in the river ψ_s and the exchanged flux q_{ex} are calculated for each coupling time step. Figure V.6 shows the exchanged data of the 1st coupling time step. The water depth at this moment (on the right) is delivered to FEFLOW and assigned as the transfer boundary. The exchanged flux q_{ex} (on the left) is calculated by FEFLOW and then passed to MIKE21FM as an “infiltration” input in the model. It means that at this moment, the river has a higher hydraulic head and it is feeding the aquifer.

This simple simulation is performed to test the functionality of the coupling interface. The results indicate the algorithm works correctly but there is still a lot of work to do to make a complete test of the coupling interface, and also to validate the coupled groundwater and surface water model in the lower Var river valley.

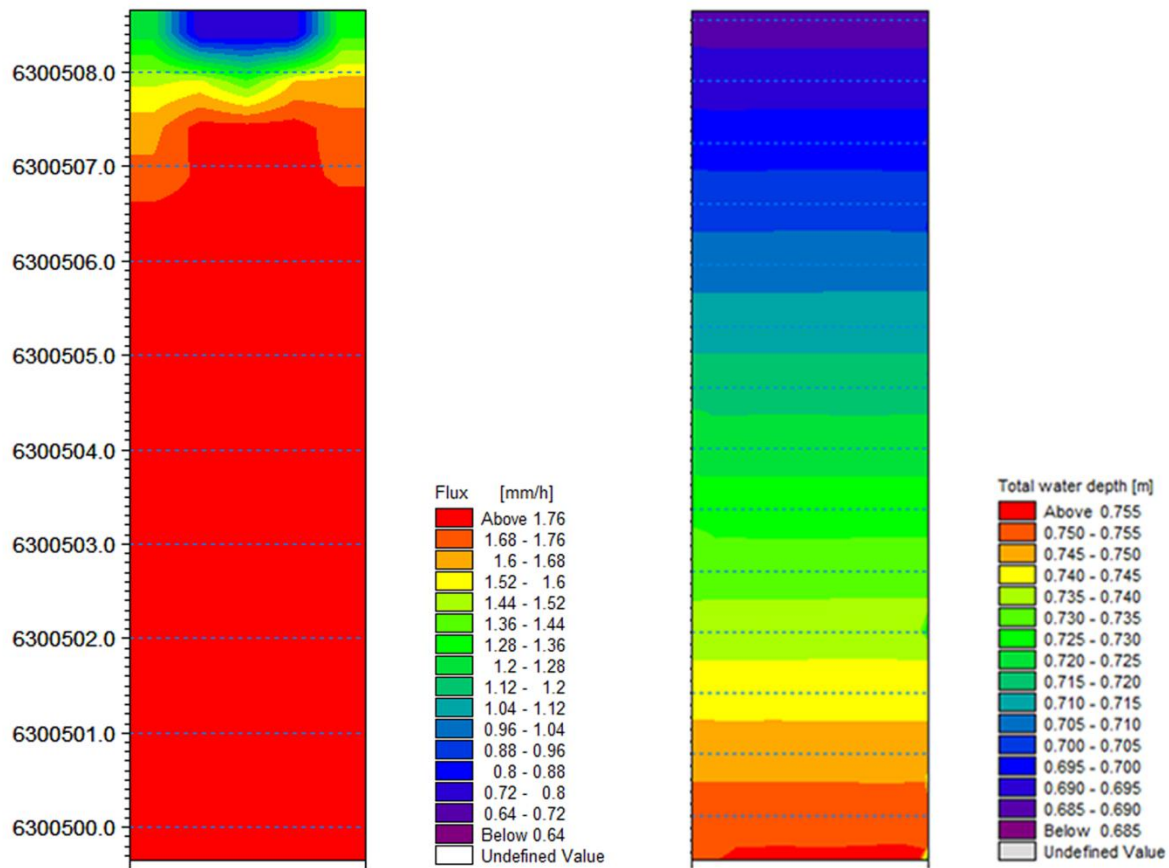


Figure V.6. Examples of exchanged data for coupling calculation of the test: water level in the river ψ_s (left) the exchanged flux q_{ex} (right).

V.4 Conclusion

The present chapter provides a theoretical background of the surface water and groundwater coupled model, and a first attempt to couple MIKE21FM and FEFLOW codes. The algorithm of the coupling interface is developed by using a Java script, which enables the transfer of data and the conversion of the input/output data format.

The test of the coupling interface on a simple, straight channel indicates the feasibility of the method. However, the coupled model has not been validated. A series of benchmark simulations need to be performed in the following studies. After all, this algorithm only couples the surface water flow and the saturated groundwater flow in order to reduce the simulation time. Thus the accuracy of this method needs to be studied.

Regarding the application of the coupled model, since the data transfer and file conversion is automated, the coupled model is more suitable for the DSS. After having validated the accuracy of the coupling algorithm, further developments can be carried out in order to complete the model functions. For example, the coupling interface can be extended to couple the transport equations, so that the exchange of the pollutant can be modeled with coupled approach.

General conclusions and perspectives

The aim of the AquaVar project is to develop a deterministic modeling system that is able to simulate the water cycle at the catchment scale and to simulate the river-aquifer exchanges in sub-catchment scale in order to implement an efficient and operational management of water resources. The modeling system will be integrated into a Decision Support System (DSS) and used as a water management tool. In this framework, this study focuses on the development of a hydraulic model of the lower Var river valley that simulates the unconfined aquifer as well as the river-aquifer exchanges.

The main challenge of this work has been the lack of measured data. As a physically based model has been selected, this type of model needs various data sets for the development, calibration and validation phases. The quality of the model outputs depends largely on the quality of the input data. Therefore, reasonable hypotheses are the key points to build a model that can correctly represent the hydraulic and hydrological features of the groundwater flow in the studied area. These hypotheses have been given based on the knowledge of the studied area and hydraulic/hydrological modeling.

The contribution of this study to the local water management service is quite obvious. The unconfined aquifer of the lower Var river valley is a typical case of the Mediterranean alluvial aquifers. It is characterized by the complex geological structure, steep hydraulic gradient, intense river-aquifer exchanges and the strong influence of the urbanization. Despite many previous studies that have been carried out with various methods, including geological drilling tests and trace elements, the hydrodynamic feature of the unconfined aquifer is still partially unknown and none of the previous studies can provide a predictive analysis of specific scenarios. This work has successfully developed a deterministic numerical hydraulic model that considers the major factors that may influence the groundwater flows, such as precipitation, evapotranspiration, river-aquifer exchanges and groundwater extraction. This model has been validated and the high quality of the simulation results demonstrates that the model is able to be used as a reliable water management tool and can be implemented into the DSS.

At the same time, on a theoretical point of view, this work has produced new developments that can be summarized in two aspects. The simulation results have demonstrated that, even with limited data sets, a reliable deterministic numerical model can be built on physically meaningful hypothesis. The

methodology of the development can be repeated and implemented for similar case studies. Besides, since this case study is very representative for the Mediterranean aquifers, the conclusions that have been drawn from the numerical simulations can be also extended for other hydrodynamic characteristics of coastal aquifers with steep hydraulic gradients. The results of the numerical simulations that revealed the influence of the weirs on the groundwater flow are also useful as a reference for similar cases.

M. Setup of the groundwater hydrodynamic model

A model is a conceptual tool to help to enhance the understanding of the real world. The real hydrologic cycle is too complicated to be modeled with all the component processes. Normally, only the key processes are considered according to the aim of the modeling. Even so, a hydraulic model may involve various disciplines such as hydrology, hydraulics, meteorology, geophysics, hydrogeology, applied mathematics and computing science. In the lower Var river valley, most of the groundwater extracted by people is from the unconfined aquifer. Therefore the groundwater flow in the unconfined aquifer is the primary target to be modeled.

In this context, the modeled domain is the hydrogeological catchment delimited by the edge of the permeable layer and the geological faults (Section III.2). The variably saturated layer has been ignored in order to simplify the model, thus only saturated flow is modeled. The geological layers have been represented by several geophysical parameters that may significantly influence the groundwater such as hydraulic conductivity K , specific yield S_y and transfer rate ϕ , *etc.* The direct water recharge/loss, river-aquifer exchanges and groundwater extraction have been considered as the main factors that could impact the groundwater hydraulics in the studied area.

Precipitation and the actual evapotranspiration form a direct water recharge/loss from the top slice of the model (Section III.3). The Thornthwaite algorithm has been employed to estimate the actual evapotranspiration. The advantage and the disadvantage have been unfolded with a comparison of the results simulated with different EUR_{max} values. Since the unsaturated layer is not considered in the model, the water loss due to the evapotranspiration is directly removed from the saturated aquifer. Therefore the simulated groundwater level is underestimated, especially in low groundwater level area for a dry spring after a rainy winter. However, this error is not significant and, for the aquifer where

the groundwater level has a variation of more than 2 meters, the error caused by this model assumption is totally acceptable.

The river-aquifer exchanges are modeled by a transfer boundary in the groundwater model (Section III.4). The exchanged flux is a simple function of the difference between the groundwater level and the surface water level, which is the output of another surface water flow model. The only parameter to calculate the exchange flux is the transfer rate that needs to be calibrated because there is no field measurement regarding this value. In the river section with the weirs, the groundwater level is disconnected from the bottom of the riverbed. Two methods, including the use of a virtual “minimum groundwater level” and a virtual “maximum exchanged flux”, have been compared in order to find the best way to model this phenomenon. The application of the “maximum exchanged flux” is not recommended because it may underestimate the peak value and overestimate the trough value.

The groundwater extraction influences significantly the groundwater level (Section III.5). Municipal pumping stations, industrial pumping wells and individual boreholes (mainly for agricultural use) are the three types of groundwater extraction considered in the model. The water volume pumped by individual boreholes is neither recorded by the local water management service, nor by the owner of the boreholes. The possible volume pumped by the individual boreholes on the farmland has been thus estimated with inverse simulation approach. The agricultural water consumption is $q_{ag}=0.015$ m/s during the dry season in summer.

The model has been validated with a simulation of 1266 days (Section III.7). 6 piezometers have been chosen to compare the observed data and the simulated results. Nash coefficient and mean absolute error have been used as indexes to evaluate dynamic results on 6 points distributed along the valley. The Nash coefficient is between 0.66 and 0.94, and the mean absolute error varies between 13 and 24 cm. Knowing that some model input does not have a good quality, the validation result is quite satisfying, at least it proves that the assumptions are correct for most of the studied area. The simulation result for the dry period at piezometer P16 is underestimated. A discussion has been made regarding this poor simulation result. Two possible reasons are found to explain the problem. Since only the result of dry period has a big error while the peak value at P16 is well simulated, it could be the groundwater extraction which is not correctly estimated because the real land use of this area is much more complicated than what is assigned in the numerical model. Another possible explanation is

that, the low quality of the input data, especially the thickness of the alluvium in this area, should be responsible for this error because the alluvium layer is created from a handmade map with merely 21 cross sections for a valley of 22 km, which is too coarse as an input for a numerical model. In summary, the two kinds of uncertainty of the numerical model can be described as (1) the wrong assumptions due to the lack of input data and (2) the low quality of the input data.

2. Model application and DSS

Several examples of model application have been presented, including extreme hydrological events, pollutant transport in the unconfined aquifer and the seawater intrusion in Var catchment. These examples have been made to show the efficiency of model and as a key component of the DSS.

The extreme flood and drought events have been properly simulated with the model (Section IV.1). River discharges associated to five different return periods have been simulated with the groundwater model in order to reveal potential consequences. The results have demonstrated that the groundwater water level is strongly connected to the river discharges through the river-aquifer exchanges. The flood in the river would cause a sudden rise of the groundwater level and the river can also regulate the groundwater level from dropping too much by feeding the aquifer. The comparison among the events shows that the aquifer is more sensitive to the flood events than to the droughts.

A pollutant transport module has been added into the hydrodynamic module in order to simulate the accidental pollution events and long term pollutant leakages/contamination in the aquifer (Section IV.2). Since no pollution event has ever happened in the valley, the longitudinal and transverse dispersivity have to be estimated according to previous analysis carried out in similar aquifers and without validation. This simulation makes the simulated results less reliable than the ones given by the hydrodynamic module. For accidental pollution events with a high initial concentration, the pollutant may disperse very quickly, especially in the upstream area. However, most of the municipal pumping stations are located in the downstream part. Therefore the upstream part of the valley is more vulnerable than the downstream area, but the downstream part could suffer more severe consequences if it really happens. Nevertheless, these simulations are performed for the pollution in the aquifer. In reality, it is more likely to have a contamination on the surface of the ground then the pollution goes into the aquifer by infiltration. Since the model does not consider the variably saturated layer, it cannot

consider residual pollutant captured in the soil. Therefore the model is likely to give overestimated results of the pollutant concentration.

A seawater intrusion model of the Var estuary has been developed by using more detailed inputs (Section IV.3). The boundary conditions of the new model came from the outputs of the previous general model. The modeled domain has been reduced to the estuary. The clay or silt lenses have been represented by a low hydraulic conductivity value. The density driven flow has been added into the model to simulate the dynamic of the seawater wedge. The simulation results of two pumping scenarios indicate that the pumping plan in the Sagnes pumping station can significantly influence the seawater intrusion in both unconfined and confined aquifer, even though the wells of Sagnes pumping station only pump water from unconfined aquifer. If the pumped volume remains as high as the year of 2006, when the pumping rate is around 12 million m³/year, the water that pumped by the airport boreholes would be no longer “drinkable” as the salt concentration will be too high.

This work provides the first component of the DSS based on three models and operates in three modes (Section IV.4). The real time monitoring module visualizes the data measured by sensors installed in the field. The real time monitoring with simulations can take the measured data as boundary conditions of the model and visualize the 2D simulation results. The third module takes the user defined input and performs simulations of designed scenarios. Since the software can be operated under command line mode, the realization of the tool is technically feasible. The biggest challenge for the DSS creation of this DSS is the computational power because the second module needs to run the model very frequently.

3. Coupled model for groundwater and surface water flows

DHI has developed a coupled model MIKE GWSW, which coupled the variably saturated model built with FEFLOW and the surface water flow built with MIKE21FM. For the DSS tool, the groundwater model is built for the saturated flow, thus a coupling interface is developed using a Java script in order to achieve an automatic exchange of data. The coupling interface considers the time step adaptation, mesh overlaying and the conversion of the data format. The simulation results of the test case indicate that the interface functions as expected.

The interface is a script that enables the automatic data exchange and data conversion without the modification of the code. Therefore the two models cannot run simultaneously. This leads to an

inaccuracy if the time step of coupling is too long. For a simulation of a drought period when there is no significant variation of the water level in the river, a larger time step of coupling can be applied. As for a flood event of a heavy rainfall event, the water level in the river or in the aquifer may vary rapidly, so a small time step is needed for the coupling. This test case is only a first test of the functionality of the interface. More aspects of the coupling interface should be tested progressively before the validation of the coupling interface with a real event.

4. Improvements and perspectives

Hydraulic modeling of groundwater is today a widely used method for groundwater resource management. It completes the aquifer knowledge in the studied area and provides holistic information for decision makers with a relatively low cost. However, the quality of the model output depends on the quality of the input data. In this study, a physically based model is built to simulate the groundwater flow in the lower Var valley. In general, the model gives good results in most of the studied areas, but there are still places where the simulation results are less satisfying. Hence, several input data need to be updated to improve the quality of the model.

The geological layers in the model are reproduced by digitalizing handmade maps, which are obtained based on geological drilling tests. Nevertheless, the number of the tests is not adequate to build an accurate numerical model over the 22 km valley. The elevation of the bottom of alluvium needs to be described with more measured data. Secondly, hydraulic conductivity is also a parameter to be updated. As a predominant input that can influence significantly the groundwater flow, hydraulic conductivity varies horizontally and vertically. The key point is to collect large quantities of measured data and then filter the ones that can represent an area. The volumes of groundwater extraction in the boreholes used by individuals, especially for agricultural use, are still unknown. These three types of data should have the priority to be updated, particularly in the area where the model gives less satisfying result.

Another improvement to be considered is the model structure. For the reason of computation time, the Richards equation that simulates the variably saturated layer, especially in the case of disconnection between the river and the aquifer, is not applied in this model, because the disconnection happens only in a small river section of 4 km from the weir No.4 to No.8. Thus the variably saturated layer is ignored for the whole valley. This approximation does not influence too much in the current model

because the disconnection is modeled by using the “minimum level approach” (Eq. 3). But it would be more accurate and more reasonable to use Richards equation. In that case, the layer of alluvium in the numerical model should be divided into several sub-layers to ensure the stability of the computation. Moreover, it is now possible to use GPU (graphical processing units) and parallel computation to speed up the computation with MIKE21. The time cost of a simulation with MIKE21FM can be reduced by more than 100 times. A parallel computation version or GPU accelerated version of FEFLOW may also be developed in the future. Therefore the computation time could be largely reduced and the simulation with Richards equation could be implemented in the DSS.

Model validation is a necessary step in the whole procedure of the development of the model. In this study, only one simulation is performed to validate the model. Actually, more representative events should be found to validate the model, because the simulation of validation presented in this work is from 2009 to 2013, which is only valid for scenarios that have similar hydrological conditions. As the construction in the valley is still going on, both land use and river morphology will change. New validation will be needed once a major change happens in the valley (*eg.* Lowered weirs or newly built industrial areas). In a similar way, the pollutant transport module also needs to be validated with measured data. Even though the real pollution event never happened in the valley, tracer experiments with non-harmful materials could be a proper way to collect measured data in order to validate the pollutant transport module.

The perspectives of the application of the model are promising, because the water resources managers in the lower Var valley are facing a series of challenges (Section II.2). This deterministic model presented in this work has provided an approach to analyze the water-related issues with low cost. In fact, the model has recently been applied to analyze the impact of the creation of a new pumping station within the riverbed in the lower Var valley. The outcome of this analysis has provided useful information for the decision makers. This is a good example of the model application and it has demonstrated a strong need for the DSS as well.

As the groundwater is a common drinking water resource in the Mediterranean area, the methodology that has been used to set up the model for the lower Var valley can be repeated for other similar aquifers. For most of the smaller aquifers, the main obstacle that makes it difficult to develop a numerical model is the constraint of the data set. The methodology presented in the current work,

however, is based on the very situation that the data set is incomplete. With reasonable hypothesis, the model can still provide good results for a long period simulation. Therefore, this work has proposed a new work flow of groundwater management based on deterministic model, that is, a numerical model can be first developed with available data set, then the model could be improved by acquiring data from field measurement. This mode would also lead to a smaller investment because the measurement is narrowed down to certain areas and aspects.

Bibliography

- Abily M., Bertrand N., Delestre O., Gourbesville P., Duluc C.-M., 2016. Spatial Global Sensitivity Analysis of High Resolution classified topographic data use in 2D urban flood modeling. *Environmental Modeling & Software*, 77: 183-195.
- Alley W. M., 2006. Tracking US Groundwater: Reserves for the Future? *Environment: Science and Policy for Sustainable Development*, 48(3): 10-25.
- Anderson, M. P., Woessner, W. W., 1992. *Applied Groundwater Modeling. Simulation of flow and advective transport*. Academic Press, San Diego. 381 pages.
- Anthony E.J., Cohen O., Sabatier F., 2011. Chronic offshore loss of nourishment on Nice beach, French Riviera: A case of over-nourishment of a steep beach? *Coastal Engineering* 58: 374– 383.
- Ashraf A., Ahmad Z., 2008. Regional groundwater flow modeling of Upper Chaj Doab of Indus Basin, Pakistan using finite element model (FEFLOW) and geoinformatics. *Geophys. J. Int.* 173: 17–24.
- Bahreman A., De Smedt F., 2008. Distributed hydrological modeling and sensitivity analysis in Torysa watershed, Slovakia. *Water Resources Management*, 22(3): 293–408.
- Barlow, P. M., and Reichard E.G., 2010. Saltwater intrusion in coastal regions of North America. *Hydrogeology Journal*, 18(1): 247-260.
- Barry, D.A. 2013. Seawater intrusion processes, investigation and management: Recent advances and future challenges. *Adv. Water Resour.* 51: 3–26.
- Bear, J., 1979. *Hydraulics of groundwater*, McGraw-Hill (Ed.), New York, 569 pages.
- Bern M., Eppstein D., 1992. Mesh generation and optimal triangulation. *Computing in Euclidean geometry*, Du D. Z. and Hwang F., (Ed.), World scientific: 23-90.
- Bittelli M., Tomei F., Pistocchi A., Flury M., Boll J., Brooks E. S., Antolini G., 2010. Development and testing of a physically based, three-dimensional model of surface and subsurface hydrology. *Advances in Water Resources*, 33(1): 106-122.
- Black P. E., 2007. Revisiting the Thornthwaite and Mather Water Balance, *Journal of the American Water Resources Association*, 43(6): 1604-1605.
- Bloschl G, Sivapalan M., 2006. Scale issues in hydrological modeling – A review. *Hydrol Proc.* 9: 251-290.
- Bolster, D.T.; Tartakovsky, D.M.; Dentz, M. 2007. Analytical models of contaminant transport in coastal aquifers. *Adv. Water Resour.* 30: 1962–1972.

- Brandmeyer J. E., Karimi H. A., 2000. Coupling methodologies for environmental models. *Environmental Modeling & Software*, 15: 479–488.
- Bredehoeft, J., 2005. The conceptualization model problem—surprise. *Hydrogeology journal*, 13:37–46.
- Brownbill R.J., Lamontagne S., Williams R.M., Cook P.G., Simmons C.T., Merrick N., 2011, Interconnection of surface and groundwater systems – river losses from losing-disconnected streams. Technical report , NSW Office of Water, Sydney, 48 pages.
- Brunner P., Cook P. G., Simmons C. T., 2009a. Hydrogeologic controls on disconnection between surface water and groundwater. *Water Resources Research* 45 (1).
- Brunner P., Simmons C. T., Cook P. G., 2009b. Spatial and temporal aspects of the transition from connection to disconnection between rivers, lakes and groundwater. *Journal of Hydrology*. 376 : 159–169.
- Carrega P., 1988. L' évapotranspiration potentielle et réelle dans le Midi méditerranéen. Son originalité par rapport au reste de la France. *Méditerranée*, 66(4), *Recherches climatiques en régions méditerranéennes II* : 3-8.
- Cassardo, C., Jones, J.A.J., 2011, Managing water in a changing world. *Water*. 3, 618–628.
- Chahine, M.T., 1992. The hydrological cycle and its influence on climate. *Nature*, 359 : 373-380.
- Chaouche K., Neppel L., Dieulin C., Pujol N., Ladouche B., Martin E., Salas D., Caballero Y., 2010. Analyse des variables précipitation, température et évapotranspiration en région méditerranéenne française dans un contexte de changement climatique. *Comptes Rendus Geoscience*, 342(3) : 234–243.
- Chery L., Cattani A., 2003. ADES : la banque de données nationale sur les eaux souterraines. *La houille blanche*, 2 : 1-5.
- Chery L., Martin A., Legrand H., 2008. Les systèmes de diffusion nationaux de données : exemple du portail ADES. *Techniques sciences méthodes*, 2 : 85-92.
- Chow, V.T., 1959, *Open-channel hydraulics*. New York, McGraw-Hill, (Ed.) Blackburn Press: 680 pages.
- Clauzon, G., 1978. The Messinian Var canyon (Provence, southern France) – Paleogeographic implications. *Marine Geology*, 27(3-4): 231-246.
- Cornaton F. J., 2016. MIKE GWSW: Coupling of FEFLOW and MIKE 21 Flow Model FM, User manual, version 0.3. MIKE Powered by DHI, 32 pages.

- Croucher A. E. and O'Sullivan M. J., 1995. The Henry problem for saltwater intrusion. *Water resources research*, 31(7) : 1809-1814.
- Cunge J. A., 1995. *Modèles mathématiques en hydraulique et en hydrologie*. (Ed.) Techniques Ingénieur, 18 pages.
- Cunge, J. A., 2003. Of data and models. *Journal of Hydroinformatics*, 5(2) : 75-98.
- Das A., Datta B., 2001. Application of optimization techniques in groundwater quantity and quality management, *Sadhana*, 26(4): 293-316.
- Delaroziere-Bouillin O., 1971. Evaluation des ressources hydrauliques, utilisation comparée des formules de Thornthwaite, Turc mensuelle, Turc annuelle et Penman, pour le calcul de l'évapotranspiration potentielle et de l'évapotranspiration réelle moyenne, application au territoire français (69 SGL 294 HYD). Technical report, Bureau de recherches géologique et minières, Ministère du développement industriel et scientifique, Orléans, France, 22 pages.
- Delestre O., 2010. Simulation du ruissellement d'eau de pluie sur des surfaces agricoles. Université d'Orléans, France, 293 pages.
- Delestre, O., Cordier S., Darboux F., Du M., James F., Laguerre C., Lucas C., Planchon O., 2014. FullSWOF: A Software for Overland Flow Simulation, *Advances in Hydroinformatics*, Gourbesville P., Cunge J., Caignaert G. (Ed.), Springer Hydrogeology: 221-231.
- DHI, 2009. MIKE 11: A modeling system for Rivers and Channels, Reference Manual, Danish Hydraulic Institute, Horsholm, Denmark. 524 pages.
- DHI, 2011. MIKE21 & MIKE3 flow model FM, hydrodynamic and transport module scientific documentation, Danish Hydraulic Institute, Horsholm, Denmark. 56 pages.
- Diersch H. J., 2005. FEFLOW: Finite element subsurface flow & Transport simulation system. Reference manual. WASY GmbH, Berlin, 292 pages.
- Diersch H. J., 2014. FEFLOW: Finite element modeling of flow, mass and heat transport in porous and fractured media. Springer, Heidelberg, 671 pages.
- Diersch H. J., Kolditz O., 1998. Coupled groundwater flow and transport: 2. Thermohaline and 3D convection systems. *Advances in water resources*, 21(5): 401-425.
- Domenico P. A., Mifflin M. D., 1965. Water from low permeability sediments and land subsidence. *Water Resources Research*, 1(4): 563-576.
- Domenico, P.A., Schwartz F.W., 1990. *Physical and Chemical Hydrogeology*, John Wiley & Sons, New York, 824 pages.

- Du M., Zavattero E., Ma Q., Delestre O., Gourbesville P., Fouché O., 2016a. 3d modeling of a complex alluvial aquifer for efficient management – application to the lower valley of Var river, France. Submitted to La Houille blanche.
- Du M., Zavattero E., Ma Q., Delestre O., Gourbesville P., Fouché O., 2016b. 3d hydraulic modeling of a complex alluvial aquifer for groundwater resource management, *Procedia engineering*, special issue of the 12th international conference on hydroinformatics, 154: 340-347.
- Dubar, M., 2003. The Holocene deltas of Eastern Provence and the French Riviera: geomorphological inheritance, genesis and vulnerability. *Geomorphologie : relief, processus, environnement* : 263-270.
- Dubar, M., Guglielmi, Y. et Falguères, C., 1992. Néotectonique et sédimentation côtière quaternaires en bordure de l'arc subalpin de Nice (A.M., France). *Quaternaire*: 105-110.
- Dumasdelage R., Delestre O., Clamond D., Gourbesville P., 2016. Storm Events of Nice Bay: A Numerical Modeling of the Interactions Between Wave, Current, and Solid Transport. *Advances in Hydroinformatics SIMHYDRO 2014*, Gourbesville et al. (Ed.) : 17-29.
- Emily A. Tennevin G., Mangan C., 2010. Etude hydrogéologique des nappes profondes de la basse-vallée du Var (Alpes-Maritimes), Technical report, H2EA Consulting firm and Mangan Consulting firm, Nice, France, 101 pages.
- Ergil M.E., 2000. The salination problem of the Guzelyurt aquifer, Cyprus. *Wat. Res.* 34(4): 1201-1214.
- Felisa G., Ciriello V., Di Federico V., 2013, Saltwater Intrusion in Coastal Aquifers: A Primary Case Study along the Adriatic Coast Investigated within a Probabilistic Framework, *Water*. 5: 1830-1847.
- Fine Rana A., Millero F. J., 1973. Compressibility of water as a function of temperature and pressure. *Journal of Chemical Physics*, 59(10): 5529–5536.
- Fitts, C. R., 2002. *Groundwater science*: Academic Press, San Diego, California, 450 pages.
- Fouché O., Hirschauer A., 2013. Hydrologie et niveaux d'eau dans le sol. Chapter 2 of *Théorie et pratique de la géotechnique*, Claude Plumelle (Ed.), 999 pages.
- Furman A., 2008. Modeling coupled surface–subsurface flow processes: a review. *Vadose Zone Journal*, 7(2) : 741-756.
- Gargani J. 2004. Modeling of the erosion in the Rhone valley during the Messinian crisis (France). *Quaternary International*, 121 : 13–22.
- Garnier J.L., 1987. Synthèse des connaissances géologiques et hydrogéologiques acquises sur le site de l'aéroport de Nice (06) (RP- 87 SGN 581 PAC). Technical report, Bureau de recherches

- géologique et minières, Ministère du développement industriel et scientifique, Marseilles, France, 26 pages.
- Garnier J. L., Goudon A., Syssau A., 1981. Champ de captage des Pugets à Saint-Laurent-du-Var (06) – Réalisation d'un puits de captage pour complément d'adduction d'eau potable – Contrôle des opérations de développement et de pompages d'essai (RP-81 SGN 261 PAC). Technical report, Bureau de recherches géologique et minières, Ministère du développement industriel et scientifique, Marseilles, France, 19 pages.
- Garrigues S., Oliso A., Calvet J.C., Martin E., Lafont S., Moulin S., Chanzy A., Marloie O., Buis S., Desfonds V., Bertrand N., Renard D., 2015. Evaluation of land surface model simulations of evapotranspiration over a 12-year crop succession: impact of soil hydraulic and vegetation properties. *Hydrol. Earth Syst. Sci.*, 19: 3109-3131.
- Garrote L., Molina M., Mediero L., 2007. Probabilistic forecasts using Bayesian networks calibrated with deterministic rainfall-runoff models. Vasiliev, O.F., Gelder, P.H.A.J.M. van, Plate, E.J., Bolgov, M.V. (Eds.), Springer Netherlands: 173-183.
- Gaultier G., Boisson M., Canaletta B., 2012. Geothermal modeling at city district level for optimized groundwater management. 3rd International FEFLOW user conference, Berlin.
- Gelhar L.W., Welty C., Rehfeldt K.R., 1992. A critical review of data on field-scale dispersion in aquifers. *Water resources research*, 28(7): 1955-1974.
- Geoffrion A.M., 1989. Integrated Modeling Systems, *Computer Science in Economics and Management*, 2: 3-15.
- Gourbesville P., 2008. Integrated river basin management, ICT and DSS: Challenges and needs. *Physics and chemistry of the earth*, 33(5): 312-321.
- Gourbesville P., Du M., Zavatiero E., Ma Q., 2016. DSS Architecture for water uses management, *Procedia engineering*, special issue of the 12th international conference on hydroinformatics, 154: 928–935.
- Guglielmi Y., 1993. Hydrogéologie des aquifères Plio-Quaternaires de la basse vallée du Var, PhD thesis, Université d'Avignon et des Pays du Vaucluse, France, 200 pages.
- Guglielmi Y., Reynaud A., 1997. Etude de la variation piézométrique de la nappe du Bec de l'Estéron en vue de la réalisation d'une zone d'activité Technical report, Laboratoire de Géologie Appliquée, Besançon, 9 pages.
- Guinot, V., Gourbesville, P., 2003. Calibration of physically based models: back to basics? *Journal of Hydroinformatics*, 5, 233–244.

- Gumbel E. J., 1935. Les valeurs extrêmes des distributions statistiques, The yearbooks of Henri Poincaré Institute, 5(2) : 115–158.
- Gumbel E. J., 1941. The return period of flood flows. The yearbooks of Mathematical Statistics, 12: 163–190.
- Gunduz O., Aral M. M., 2005. River networks and groundwater flow: a simultaneous solution of a coupled system. Journal of Hydrology 301(1–4): 216–234.
- Havnø K., Madsen M., Dørge J., Singh V., 1995. MIKE 11-a generalized river modeling package, Computer models of watershed hydrology, 733–782.
- Heath, R.C., 1983. Basic ground-water hydrology, U.S. Geological Survey Water-Supply Paper 2220, 86 pages.
- Henry, H. R. 1964. Effects of dispersion on salt encroachment in coastal aquifers. Seawater in Coastal Aquifers, J. Hilton H. Cooper, F. A. Kohout, H. R. Henry, and R. E. Glover, eds., U.S. Geological Survey Water-Supply Paper 1613-C, C70-C82.
- Holz M., Heil S. R., Sacco A., 2000. Temperature-dependent self-diffusion coefficients of water and six selected molecular liquids for calibration in accurate ¹H NMR PFG measurements. Physical chemistry chemical physics, 2: 4740-4742.
- Hussein M., Schwartz F.W., 2003. Modeling of flow and contaminant transport in coupled stream–aquifer systems. Journal of Contaminant Hydrology 65 (1–2): 41–64.
- Huysmans M. and Dassargues A., 2004. Review of the use of Peclet numbers to determine the relative importance of advection and diffusion in low permeability environments. Hydrogeology Journal, 13 :895–904.
- Irr F., 1984. Paléoenvironnements et évolution géodynamique néogène et quaternaire de la bordure nord du bassin méditerranéen occidental, Nice, 464 pp.
- Jobson H.E., Harbaugh A.W., 1999. Modifications to the diffusion analogy surface water flow model (Daflow) for coupling to the modular finite-difference groundwater flow model (Modflow). United States Geological Survey, Open file report 99-217.
- Johnson, L. E., 1986. Water resource management decision support systems. Journal of water resources planning and management, 112(3), 308-325.
- Johnson Norman L, Kotz S., Balakrishnan N., 1994. Lognormal Distributions, Continuous univariate distributions. Vol. 1, Wiley Series in Probability and Mathematical Statistics: Applied Probability and Statistics (2nd Ed.), John Wiley & Sons (Ed.), New York.
- Kalakan C., 2014. Investigation of saltwater intrusion based on the Henry problem and a field-scale problem. University of Florida, U.S. 2014.

- Kassem P., Peirol J., Fournier I., 1997. Forage de reconnaissance et pompage d'essai sur le champ de captage des Plans – Simulation du débit d'exploitation. RP-A09480. Technical report, ANTEA, Marseille, 28 pages.
- Kunatip R., Supasit K., 2012. Low Flow Analysis and Possible Impact of the Mekong River. International Conference on Environmental Science and Development. APCBEE Procedia 1:309 – 317.
- Kundzewicz Z. W., Döl P., 2009. Will groundwater ease freshwater stress under climate change? Hydrol. Sci. J. 54(4): Special Issue: Groundwater and Climate in Africa, 665-675.
- Kundzewicz Z. W., Matczak, P., 2015. Extreme hydrological events and security. Proceedings of the International Association of Hydrological Sciences, 369, 181-187.
- Kundzewicz Z. W., Rosbjerg D., Simonovic S. P., Takeuchi K., 1993. Extreme hydrological events in perspective. IAHS Conference Proceeding, 213: 1-7
- Laborde J. P., 2010. Eléments d'hydrologie de surface. Université de Nice-Sophia Antipolis, France, 194 pages.
- Li Q., Unger A. J. A., Sudicky E. A., Kassenaar D., Wexler E. J., Shikaze S., 2008. Simulating the multi-seasonal response of a large-scale watershed with a 3D physically-based hydrologic model. Journal of Hydrology, 357(3): 317-336.
- Li Y.-H., Gregory S., 1974, Diffusion of ions in seawater and in deep-sea sediments. Geochimica et cosmochimica acta, 38: 703-714.
- Liang D., Falconer R.A., Lin B., 2007. Coupling surface and subsurface flows in a depth averaged flood wave model. Journal of Hydrology 337: 147–158.
- Lin K.-P., Chou P.-C., Shih D.-S., 2016. To study hydrological variabilities by using surface and groundwater coupled model – A case study of PingTung plain, Taiwan. Procedia engineering, special issue of the 12th international conference on hydroinformatics, 154: 1034–1042.
- Liu H. L., Chen X., Bao A. M., Wang L., 2007. Investigation of groundwater response to overland flow and topography using a coupled MIKE SHE/MIKE 11 modeling system for an arid watershed. Journal of Hydrology, 347(3) : 448-459.
- Ma Q., Zattero E., Du M., Vo N. D., Gourbesville P. 2016. Assessment of high resolution topography impacts on deterministic distributed hydrological model in extreme rainfall-runoff simulation. Procedia Engineering, 154 : 601-608.
- Mangan C., 2000. Forage du M.I.N. (06 – Nice) – Projet de mise en service pour alimenter le réseau spécialisé de distribution d'eau brute d'arrosage et de protection incendie de Nice. Technical report, Cabinet Mangan, Nice, 20 pages.

- Mangan C., 2005. Z.A.C. de l'Arénas (06 – Nice) – Gestion des débits exhaures. Technical report, Cabinet Mangan, Nice, 23 pages.
- Mangan C., 2011. Rabattement de nappe par pompages dans le cadre de chantiers simultanés. Technical report, Cabinet Mangan, Nice, 34 pages.
- Mangan C., 2012. Nappe alluviale de la Basse Vallée du Var – Recherche par forages au Bec de l'Estéron (06 – Gilette). Technical report, Cabinet Mangan, Nice, 7 pages
- Marti, P., 2005. Assessment of Surface Water and Groundwater Interchange in the Walla Walla River Watershed. Washington State Department of Ecology, 67 pages.
- Martin-Carrasco, F. J., Garrote, L., 2007. Drought-induced water scarcity in water resources systems. In Extreme hydrological events: new concepts for security. Vasiliev, O.F., Gelder, P.H.A.J.M. van, Plate, E.J., Bolgov, M.V. (Eds.), Springer Netherlands: 301-311.
- McDonald M. G., Harbaugh A. W., 1984. A modular three-dimensional finite-difference ground-water flow model. R83-875. Technical report, U.S. Geological Survey. 528 pages.
- McNamara, J. P., Kane, D. L., Hinzman, L. D., 1997. Hydrograph separations in an Arctic watershed using mixing model and graphical techniques. *Water Resour. Res.* 33(7): 1707–1719.
- Milnes E., Renard P., 2004. The problem of salt recycling and seawater intrusion in coastal irrigated plains: an example from the Kiti aquifer (Southern Cyprus). *Journal of Hydrology* 288: 327–343.
- Monninkhoff B., 2004. Coupling of the groundwater model FEFLOW with the hydrodynamic model MIKE 11, German-Chinese Conference “Modern methods and instruments for water management and flood protection”, IWU-Tagungsberichte, Germany, 161-173.
- Morita M., Yen B. C., 2002. Modeling of conjunctive two-dimensional surface-three-dimensional subsurface flows. *Journal of Hydraulic Engineering*, 128(2):184–200.
- Murray-Smith, D. J., 2000. The inverse simulation approach: a focused review of methods and applications. *Mathematics and computers in simulation*, 53(4), 239-247.
- Nash J. E., Sutcliffe J. V., 1970. River flow forecasting through conceptual models part I — A discussion of principles, *Journal of Hydrology*, 10 (3): 282–290.
- Nicod J. Péguy Ch.-P., 1974. Carte climatique de Nice : CNRS, Carte climatique détaillée de la France au 1/250 000. *Annales de Géographie*, Nice. 83(455) : 112-113.
- Ormella Mancha A., Okwir G., Kafi M. A. H., Azim Beg M. N., Du M., Anza Gomez L., Rambert S., Bah A., Agafon Danila C., Sainz Garcia A., 2013. Hydroeurope – Hydraulic and hydrological modeling of the Var river catchment – Final report. University of Nice, 64 Pages.

- Panday S., Huyakorn P. S., 2004. A fully-coupled physically-based spatially-distributed model for evaluating surface/subsurface flow. *Advances in Water Resources* 27(4) : 361–382.
- Potot C., 2011. Etude hydrochimique du système aquifère de la basse vallée du Var, apport des éléments traces et des isotopes (Sr, Pb, $\delta^{18}\text{O}$, ^{226}Ra , ^{228}Ra). PhD thesis. Université Nice Sophia Antipolis, France, 240 pages.
- Potot C., Féraud G., Schäfer U., Barats A., Durrieu G., Le Poupon C., Travi Y., Simler R., 2012. Groundwater and river baseline quality using major, trace elements, organic carbon and Sr–Pb–O isotopes in a Mediterranean catchment: The case of the Lower Var Valley (south-eastern France), *Journal of Hydrology*, 472: 126–147.
- Richards, L.A., 1931. Capillary conduction of liquids through porous mediums. *Physics*, 1 (5): 318–333.
- Righetti C., Gigliuto A., Chini A., Rossetto R., 2009. Saltwater intrusion in a coastal contaminated aquifer density-dependent finite element model of flow and transport to assess remediation strategies and saltwater intrusion at a coastal gas plant site. 2nd international FEFLOW® user conference, Berlin, Germany.
- Roads, J.O., S.C. Chen, A. Guetter, and K. Georgakakos., 1994. Large-scale aspects of the United States hydrologic cycle, *Bull. Amer. Met. Soc.*, 75: 1589-1610.
- Rodda, J.C., 1995. Guessing or assessing the world's water resources. *J. Char. Inst. Water and Env. Mgmt.*, 9: 360-368.
- Roelvink J. A., 2005. Integrated hydraulic-environmental modeling. *Environmentally Friendly Coastal Protection*, Zimmermann et al. (Ed.): 93-105.
- Saltelli A., 2002. Sensitivity analysis for importance assessment. *Risk Analysis*, 22 (3): 1–12.
- Savenije, H. H. G., 1996. The runoff coefficient as the key to moisture recycling. *J. Hydrol.* 176: 219–225.
- Schäzl P., Nujic M., 2004. Kopplung des Grundwassermodells FEFLOW mit dem 2D-hydrodynamischen Modell HYDRO_AS-2D, German-Chinese Conference “Modern Methods and Instruments for Water Management and Flood Protection”, IWU-Tagungsberichte, 183-188.
- Shepard D., 1968. A two-dimensional interpolation function for irregularly-spaced data. *Proceedings of the 1968 ACM National Conference*: 517–524.
- Sherif M., Sefelnasr A., Javadi A., 2012. Incorporating the concept of equivalent freshwater head in successive horizontal simulations of seawater intrusion in the Nile Delta aquifer, Egypt. *Journal of Hydrology* 464–465: 186–198.

- Shewchuk, J. R., 1996. Triangle: Engineering a 2D quality mesh generator and Delaunay triangulator. *Applied computational geometry towards geometric engineering*. Springer Berlin Heidelberg: 203-222.
- Short, D., Dawes W.R., White I., 1995. The practicability of using Richards equation for general purpose soil-water dynamics models. *Environment International*, 21(5) : 723-730.
- Sochala P., 2008. Méthodes numériques pour les écoulements souterrains et couplage avec le ruissellement. PhD thesis. Ecole Nationale des Ponts et Chaussées, France, 114 pages.
- Sochala P., Ern A., Piperno S., 2009. Mass conservative BDF-discontinuous Galerkin/explicit finite volume schemes for coupling subsurface and overland flows. *Computer Methods in Applied Mechanics and Engineering*, 198(27): 2122-2136.
- Souriguère K., 2003. Etat des lieux-diagnostic, SAGE nappe et basse vallée du var. Syndicat mixte d'études de la basse vallée du Var. Carros, France.
- Souriguère K., 2006. Atlas cartographique du SAGE nappe et basse vallée du Var. Syndicat mixte d'études de la basse vallée du Var. Carros, France.
- Spanoudaki K., Stamou A. I., Nanou-Giannarou A., 2009. Development and verification of a 3-D integrated surface water-groundwater model. *Journal of Hydrology* 375(3):410-427.
- Sparks T., 2004. Integrated modeling of 2-D surface water and groundwater flow with contaminant transport. *Proceedings of XXXI IAHR Congress*, Seoul, Korea.
- Sudicky E. A., Vanderkwaak J. E., Jones J. P., Keizer J. P., McLaren R. G., Matanga G. B., 2003. Fully-integrated modeling of surface and subsurface water flow and solute transport: Model overview and application. *Developments in Water Science*, 50: 313-318.
- Swain E.D., Wexler E.J., 1996. A coupled surface-water and groundwater flow model (Modbranch) for simulation of stream-aquifer interaction. United States Geological Survey, *Techniques of Water Resources Investigations (Book 6, Chapter A6)*.
- Tavakoli S., Mousavi A., Poslad S., 2013. Input variable selection in time-critical knowledge integration applications: A review, analysis, and recommendation paper. *Advanced Engineering Informatics*, 27(4): 519-536.
- Teresita Betancur V., Carlos Alberto Palacio T. and John Fernando Escobar M., 2012. Conceptual Models in Hydrogeology, Methodology and Results, *Hydrogeology – A Global Perspective*, Dr. Gholam A. Kazemi (Ed.).
- Thornthwaite C. W., Mather J. R., 1957. Instructions and tables for computing the potential evapotranspiration and the water balance. *Laboratory of Climatology*, Elmer, NJ (Ed.), 10(3): 185-311.

- Tocci, M. D., Kelley C. T., Miller C. T., 1997. Accurate and economical solution of the pressure-head form of Richards' equation by the method of lines, *Adv. Wat. Resour.*, 20(1), 1–14.
- Todd, D.K., 1980. *Groundwater Hydrology*, 2nd ed., John Wiley & Sons, New York, 535 pages.
- Vanderkwaak J.E., 1999. Numerical simulation of flow and chemical transport in integrated surface–subsurface hydrologic systems. Ph.D. Thesis, University of Waterloo, Waterloo, Ontario.
- Verruijt, A., 1970. *Theory of groundwater flow*. Macmillan Education UK (Ed.), 182 pages.
- Voss, C. I., 2005. The future of hydrogeology. *Hydrogeology journal*, 13:1–6.
- Wagener, T., Sivapalan, M., Troch, P., Woods, R., 2007. Catchment Classification and Hydrologic Similarity. *En : Geography Compas.* 1(4), 901-931.
- Weill S., 2007. Modélisation des échanges surface subsurface à l'échelle de la parcelle par une approche darc éenne multidomaine, PhD thesis. Ecole des Mines de Paris, France, 160 pages.
- Weill S., Mouche E., Patin J. 2009. A generalized Richards equation for surface/subsurface flow modeling. *Journal of Hydrology*, 366(1): 9-20.
- Werner,A.D., Bakker ,M., Post ,V.E. A., Vandenbohede ., Lu,C., Ataie-Ashtiani,B., Simmons,C.T., Barry,D.A., 2013. Seawater intrusion processes, investigation and management: Recent advances and future challenges. *Advances in water resources* 51, 3-26.,
- Winter, T.C., LaBaugh J.W., and Rosenberry D.O., 1988. The design and use of a hydraulic potentiometer for direct measurement of differences in hydraulic head between groundwater and surface water. *Limnology and Oceanography*, 33(5), 1209-1214.
- Yamagata K., Butts M. B., Grooss J., Clausen T. H., Graham D. N., Clausnitzer V., Monninkhoff B. 2012. OpenMI coupling of FEFLOW and MIKE SHE. 3rd International FEFLOW user conference, Berlin.
- Zektser, I.S., Loaiciga H.A., 1993. Groundwater fluxes in the global hydrologic cycle; past, present and future, *J. Hydrol*, 144: 405-427.
- Zhao C., Wang Y., Chen X., Li B., 2005. Simulation of the effects of groundwater level on vegetation change by combining FEFLOW software. *Ecological Modeling*, 187: 341–351.

List of tables

Table I.1. Summary table of geographical information of the 5 sub-cathments. (Source: 75 m DEM provided by NCA)	20
Table I.2. Summary table of land use information of the 5 sub-cathments. (Source: 75 m DEM provided by NCA)	20
Table I.3. Surface water quality evaluation in the lower Var river (Source: Water agency of RMC)	38
Table I.4. Annual groundwater pumping volume for industrial water use in the lower Var river valley (Source: Water agency RMC, Nice Airport).	44
Table I.5. Altitude and borehole depth of the piezometers in the lower Var river valley (Source: Eaufrance).	45
Table III.1. Representative values of vertical drained compressibility of various geologic materials (Source: Domenico and Mifflin [1965]).	84
Table III.2. Representative values of specific storage S_s of various geologic materials (Source: Domenico and Mifflin [1965]).	85
Table III.3. Representative values of porosity ε , specific yield S_y and specific retention S_r of various geologic materials (Source: Heath [1983]).	85
Table III.4. Hydraulic conductivity values used in the numerical model.	86
Table III.5. Land use description and estimated runoff coefficient in the lower Var river valley.	94
Table III.6. Summary of the parameters included in the sensitivity analysis.	103
Table III.7. Result of sensitivity analysis of specific yield S_y	111
Table III.8. Result of sensitivity analysis of the in-transfer rate ϕ_{in}	111
Table III.9. Result of sensitivity analysis of the out-transfer rate ϕ_{out}	111
Table IV.1. Occurrence of the highest daily cumulative precipitation of the year through a measurement of 72 years from 1944 to 2015, at the airport station (Figure I.10, Source: Météo France).	141
Table IV.2. Occurrence of the highest daily average discharge of the year through a measurement of 28 years from 1974 to 1976, from 1985 to 2000, the year of 2006, from 2008 to 2015, at the Napoléon III station (Figure I.15, Source: Eaufrance).	141
Table IV.3. Flood events of scenario simulations	145
Table IV.4. Drought events of scenario simulations.	150

Table IV.5. Pumping rates in the municipal pumping stations for scenario simulations.	153
Table IV.6. β_L and β_T values obtained by field measurement	158
Table IV.7. Summary of boundary conditions and material properties of seawater intrusion simulations (C_{Cl-} is the concentration of chloride).....	177
Table V.1. Data format of the input and output files involved in the coupling process.	198

List of figures

Figure I.1. Illustration of physiography of Var catchment and cross sections (Author's design. Source: 5 m DEM from Métropole Nice Côte d'Azur, noted as NCA in the text below).....	19
Figure I.2. Elevation (left) and map (right) of the lower valley of Var river (Author's design. Source: 75 m DEM from NCA, bathymetry contour from National Institution of Geography and Forestry, noted as IGN in the text below, Guglielmi [1993], ESRI world map).	22
Figure I.3. The demographic evolution of Nice city since the 19 th century (Source: Data base of the National Institute of Statistics and Economic Studies of France - INSEE).	23
Figure I.4. Embankments built with rubbles and concrete blocks along the lower Var river (photo taken by author on July 2014).	23
Figure I.5. Evolution of the Est éron-Var confluence and the formation of Le Broc lake (Source: IGN and www.valleeduvar.fr).	24
Figure I.6. Highly urbanized zone in the estuarine area of Var river (Author's design. Source: www.geoportail.gouv.fr).	25
Figure I.7. Land use map of the lower valley of Var river (Source: Data base of European Environment Agency, data of 2006, resolution of 100 m).....	26
Figure I.8. Geological map of lower valley of Var river (Source: Emily et al. [2010]). .	28
Figure I.9. Cross sections of the profiles displayed in Figure I.8, the legend is the same as the one used in geological map (Source: Emily et al. [2010])	29
Figure I.10. Location of the precipitation monitoring points in the Var catchment and the lower Var river valley (Source: M é éo-France).	30
Figure I.11. Comparison of the monthly precipitation in 2014 among Levens, Carros and Airport stations (Source: M é éo-France).....	30
Figure I.12. Precipitations in different time scale (daily, monthly and annual scale) recorded in the meteorological station of Nice airport (Source: M é éo-France).	31
Figure I.13. Average monthly precipitation recorded at Nice airport station from 1943 to 2015 (Source: M é éo-France).....	33
Figure I.14. Average potential and actual evapotranspiration at Nice from 1980 to 1984 (Source: Carrega [1988], M é éo-France).	33

Figure I.15. Average monthly discharge of lower Var river and Est éron river, measured at three stations (Source: Eaufrance).....	35
Figure I.16. Monthly discharge measured at Napol éon III station from 1985 to 2015 (Source: Eaufrance).....	36
Figure I.17. Flood in Var, recorded in 1994 (Source: Eaufrance, M é éo-France).	37
Figure I.18. Freshet in Var, recorded in 2009 (Source: Eaufrance, M é éo-France).....	37
Figure I.19. Geological profiles at the estuarine area of the lower Var river valley (Author's design. Source: Emily et al. [2010]).	40
Figure I.20. Location of the water pumping stations and main groundwater consuming companies in the lower Var river valley (Source: Veolia company, municipality of Nice Côte d'Azur, Nice Airport).	41
Figure I.21. Monthly pumping volumes of the municipal drinking water stations in the lower Var river valley (Source: Veolia company and municipality of Nice Côte d'Azur).	42
Figure I.22. Location of the piezometers in the lower Var river valley (Source: Eaufrance).	45
Figure I.23. Representative groundwater level recorded by piezometers along the Var river (Source: Eaufrance).	46
Figure I.24. Groundwater level contour map in the lower Var river valley. The map of 1994 and 1999 are made by Guglielmi Y. and Hocahrt M. [Potot 2011], the map of 2015 is made by Du M. and Zavattero E.....	49
Figure II.1. Illustration of a general example of the water cycle in estuarine area (Author's design).....	51
Figure II.2. Illustration of a typical profile of an unconfined aquifer (Author's design).	52
Figure II.3. The weir No.1 (left, photo taken by author on July 2014) and the weir No.16 (right, photo taken by Mossot on October 2011).	54
Figure II.4. Evolution of the riverbed of the lower Var river from 1969 to 2009 (Source: IGN).	55
Figure II.5. Evolution of the groundwater level from 1970 to 2010 at weir No.2, recorded by the piezometer P16 (Source: Eaufrance).	56
Figure II.6. Sediments distribution on the riverbed of lower Var river, measured by author on July 2014.	58
Figure II.7. Comparison of the groundwater level pattern during summer between agricultural land (P16) and urban area (P35) (Source: Eaufrance, Veolia).....	59

Figure II.8. Flood of 1994 in the lower valley of Var river and the levees located on the left bank in the downstream part (Source: Nice-Matin, Google Street).....	61
Figure II.9. Work flow of groundwater modeling. This diagram also explains the general hydraulic modeling approach, in this case, the equations and computer code should be replaced by their related substitutions.	63
Figure II.10. Conceptual model developed for unconfined aquifer in the lower Var river valley.	64
Figure II.11. Illustration of all possible feeding relations between river and its unconfined aquifer: (1), (2) and (3). The overestimated exchange flux for disconnection situation calculated with general equation (4). The exchange flux calculation with modified equation for disconnection situation (5) (Author's design).	66
Figure II.12. Illustration of the direct water recharge/loss in the unconfined aquifer (Author's design).....	68
Figure III.1. Illustration of the derivation of the fluid continuity equation of the transient, saturated groundwater flow (Author's design).....	71
Figure III.2. Illustration of Darcy equation of the saturated groundwater flow (Author's design.).	73
Figure III.3. Illustration of the definition of hydrological catchment and hydrogeological catchment (Author's design).	76
Figure III.4. Model domain delimitation: hydrogeological catchment boundary on the cross sections (left) and the model domain (right) (Source: Emily et al. [2010])....	77
Figure III.5. Improvement of the mesh of the model, the cells on the right side are the improved ones.	79
Figure III.6. Different grid sizes of the mesh of the model and the interior angle of the grids.....	80
Figure III.7. Representation of discontinuity of geological layers in reality (on the left) and in the numerical model (on the right).	81
Figure III.8. Creation of the geological layer information on each cross section (Source: Emily et al., [2010] and Guglielmi [1993]).....	82
Figure III.9. Interpolation of the cross sections so as to set up the 3D model that consists of 6 layers.	83
Figure III.10. Stratified sediments of the porous media in the alluvium of lower Var river valley (Photo taken by author on July 2014).....	87

Figure III.11. Representation of hydraulic conductivity anisotropy in the numerical model.....	88
Figure III.12. Data flow diagram for AET calculation. The variables with subscripts “M” denote the monthly value and “A” means the annual value.....	89
Figure III.13. Sensitivity analysis of the EUR_{max}	92
Figure III.14. Results of the calibrated EUR_{max} and comparison of the AET_A calculated by the two methods.	93
Figure III.15. Land use map in the lower Var river valley.....	94
Figure III.16. Illustration of 1D shallow water equation.....	95
Figure III.17. River hydraulic model built by MIKE11 (left) and the transfer boundary condition assigned in groundwater flow model (right).	98
Figure III.18. Groundwater level measured by the piezometer in the farmland in lower Var river valley from September 6 th to 22 nd for different piezometers (Source: Eaufrance).	100
Figure III.19. Illustration of the groundwater pumping wells and water reinjection points in the lower Var river valley.	100
Figure III.20. Location of the area for grid convergence study and the 4 different cell sizes.	101
Figure III.21. Comparison of the simulation results for grid convergence study at two points of interest.	102
Figure III.22. Location of the piezometers used in the calibration.	104
Figure III.23. Daily discharge in the river (left) and upstream boundary condition (right) for the simulations of sensitivity analysis (Source: Eaufrance).	105
Figure III.24. Direct water recharge/loss in the model for the simulations of sensitivity analysis.	105
Figure III.25. Sensitivity analysis of the specific yield S_y at different locations.....	108
Figure III.26. Sensitivity analysis of the in-transfer rate ϕ_{in} at different locations.....	109
Figure III.27. Sensitivity analysis of the out-transfer rate ϕ_{out} at different locations...	110
Figure III.28. Calibrated values of specific yield S_y and in/out-transfer rate ϕ_{in} , ϕ_{out}	112
Figure III.29. Grading curves of the sediments in boreholes LMPZ4 and LMPZ5.....	113
Figure III.30. Location of the piezometers used in the validation of the model and the represented characteristics of the domain.	114

Figure III.31. Daily discharge in the river and upstream boundary condition for the simulations of model validation (Source: Eaufrance).	114
Figure III.32. Direct water recharge/loss for the model validation for different land use.	115
Figure III.33. Simulation results of the model validation at the upstream piezometers of the study area.	116
Figure III.34. Simulation results of the model validation at the downstream piezometers of the study area.	117
Figure III.35. Linear regression of measured and simulated groundwater level at different piezometers.	120
Figure III.36. NSE coefficient of the simulation results of model validation at different piezometers.	122
Figure III.37. Mean absolute error (MAE) of the simulation results of model validation.	123
Figure III.38. Difference between the real process of evapotranspiration and the conceptual process applied in the numerical model (Author's design).	124
Figure III.39. Comparison of the simulation results with different EUR_{max} value.	125
Figure III.40. Principle of two methods to model the disconnection between the river and the aquifer (Author's design).	126
Figure III.41. Comparison of the results simulated with two methods that model the disconnection.	126
Figure III.42. Complicated land use in the area of piezometer P16 (Author's design. Source: www.geoportail.gouv.fr).	129
Figure III.43. Contour map of groundwater level during the dry period (left) and rainy period (right).	131
Figure III.44. Nodal Darcy flux of groundwater flow during the dry period (left) and rainy period (right).	132
Figure III.45. River-aquifer exchanges during the dry period (left) and rainy period (right).	134
Figure III.46. Profile of ground surface and groundwater level along the streamline of Var river.	135
Figure III.47. Main boundary conditions and source/sink terms used in the numerical model.	137

Figure IV.1. Gumbel distribution of the maximal values of daily average discharge measured at Napoléon III bridge.	145
Figure IV.2. Rainfall and river discharge of flood events of scenario simulations, measured respectively at airport meteorological station and Napoléon III bridge gauging station (Figure I.10, Figure I.15).	146
Figure IV.3. Log-normal distribution of the monthly average discharge measured at Napoléon III bridge.	150
Figure IV.4. Rainfall and river discharge of drought events of scenario simulations, measured respectively at airport meteorological station and Napoléon III bridge gauging station (Figure I.10, Figure I.15).	151
Figure IV.5. Location of the points used to compare the simulation results.....	154
Figure IV.6. Scenario simulations of flood and drought events.....	155
Figure IV.7. Location of the potential contaminating sources in the lower Var river valley.	159
Figure IV.8. Simulated results of accidental pollution scenario: source at Le Broc lake.	162
Figure IV.9. Simulated results of accidental pollution scenario: source at Virbac company.	163
Figure IV.10. Simulated results of accidental pollution scenario: source at La Manda bridge.....	164
Figure IV.11. Simulated results of accidental pollution scenario: source at Lingosti ère commercial center.	165
Figure IV.12. Simulated results of accidental pollution scenario: source at Stadium Allianz Riviera.	166
Figure IV.13. Simulated results of accidental pollution scenario: source at M.I.N. of Nice.	167
Figure IV.14. Simulated results of long-term pollution scenario: source at Le Broc lake.	168
Figure IV.15. Illustration of seawater intrusion: Classic Henry problem (1) and case of urban estuarine area (2) (3) (4) (Author's design).	170
Figure IV.16. Studied area of the seawater intrusion model of the Var river mouth.	171
Figure IV.17. Modeled domain of the seawater intrusion model of the Var estuary. The profiles A, B and C are shown in Figure I.19.	173

Figure IV.18. Illustration of the computational mesh (left) and lenses in alluvium (right) of the seawater intrusion model.	174
Figure IV.19. Boundary conditions of hydrodynamic module (upper part) and pollutant transport module (lower part) in the seawater intrusion model of the Var estuary.	175
Figure IV.20. Evolution of total annual pumping volume in Nice city pumping station from 2004 to 2015.	177
Figure IV.21. Top view of the simulation results in the unconfined aquifer.	180
Figure IV.22. Top view of the simulation results in the confined aquifer.	181
Figure IV.23. Profile view of the simulation results.	182
Figure IV.24. Data flow chart of the integrated monitoring system in Var catchment (Author's design).	185
Figure IV.25. Conceptual framework of the utilization process of the DSS of the Var catchment (Author's design).	187
Figure V.1. Data flow of coupling process between the 3D saturated groundwater flow model (FEFLOW) and the 2D surface water flow model (MIKE21FM).	196
Figure V.2. Time step adaptation between the coupling time step and the computation time step.	197
Figure V.3. Mesh adaptation of the coupling interface.	197
Figure V.4. Flow chart of the data conversion process.	199
Figure V.5. Geometry of the test case for coupling interface between saturated groundwater and surface water models.	200
Figure V.6. Examples of exchanged data for coupling calculation of the test: water level in the river ψ_s (left) the exchanged flux q_{ex} (right).	201

List of appendix

Appendix 1. International chronostratigraphic chart

Appendix 2. Geological layers in the lower valley

Appendix 3. Geological drilling test of confined aquifer in the estuarine area of Var river

Appendix 4. Measurement of groundwater level in the lower Var river valley

Appendix 5. Computational mesh types and characteristics

Appendix 6. Geological survey methods

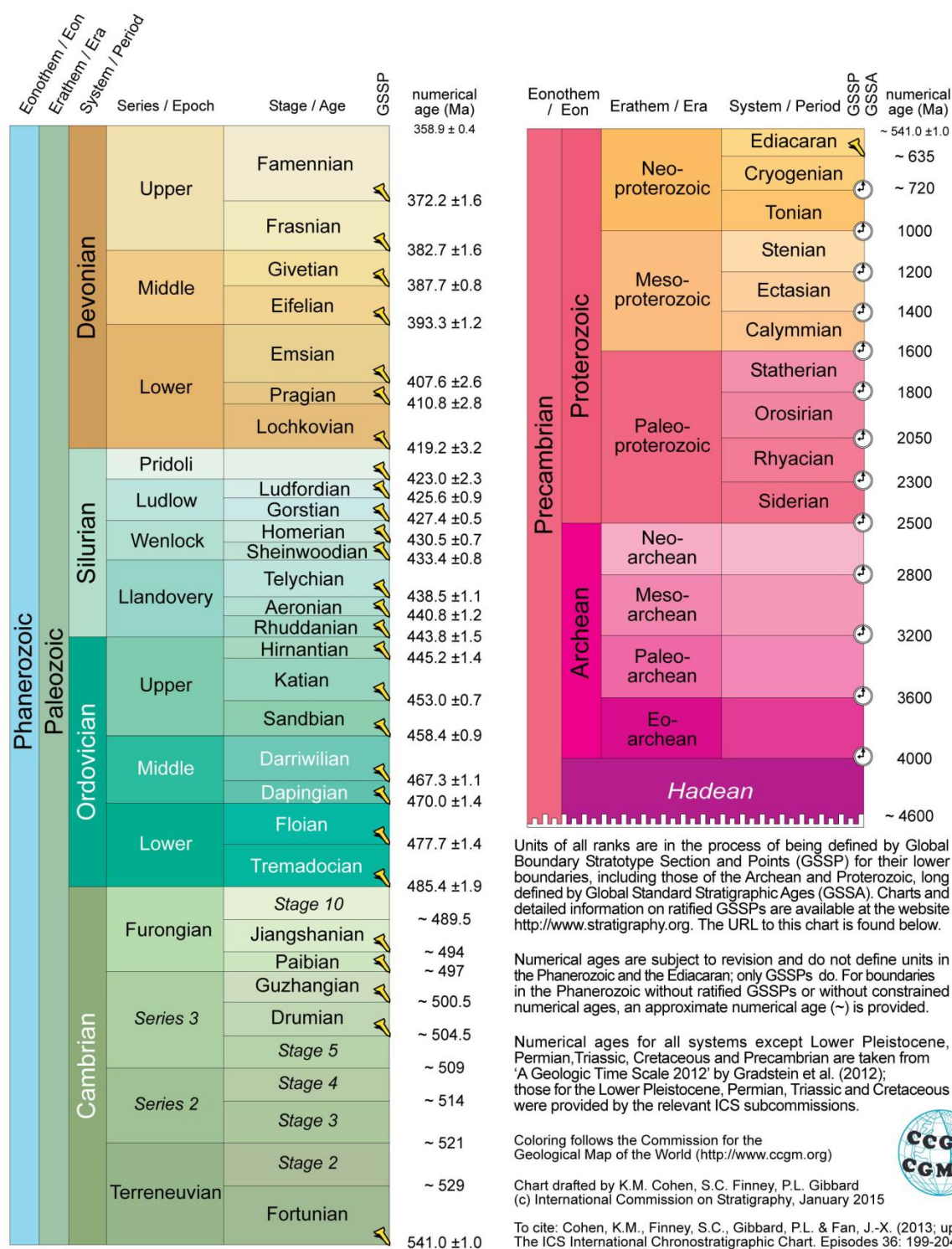
Appendix 7. Maximal values of daily average discharge measured at Napoléon III bridge used for Gumbel law calculation

Appendix 8. Monthly average discharge measured at Napoléon III bridge used for log-normal law calculation

Appendix 1. International chronostratigraphic chart

	Eonothem / Eon	Erathem / Era	System / Period	Series / Epoch	Stage / Age	GSSP	numerical age (Ma)		
Phanerozoic	Cenozoic	Quaternary	Holocene		present	↙	0.0117		
					Upper		0.126		
			Pleistocene		Middle		0.781		
					Calabrian	↙	1.80		
					Gelasian	↙	2.58		
					Piacenzian	↙	3.600		
		Neogene	Pliocene		Zanclean	↙	5.333		
					Messinian	↙	7.246		
			Miocene		Tortonian	↙	11.63		
					Serravallian	↙	13.82		
					Langhian		15.97		
					Burdigalian		20.44		
					Aquitanian	↙	23.03		
			Oligocene		Chattian		28.1		
					Rupelian	↙	33.9		
		Paleogene	Eocene		Priabonian		37.8		
					Bartonian		41.2		
					Lutetian	↙	47.8		
					Ypresian	↙	56.0		
			Paleocene		Thanetian	↙	59.2		
					Selandian	↙	61.6		
					Danian	↙	66.0		
		Mesozoic	Cretaceous	Upper	Maastrichtian	↙	72.1 ±0.2		
					Campanian		83.6 ±0.2		
					Santonian	↙	86.3 ±0.5		
					Coniacian		89.8 ±0.3		
					Turonian	↙	93.9		
					Cenomanian	↙	100.5		
					Albian		~ 113.0		
					Aptian		~ 125.0		
					Barremian		~ 129.4		
					Hauterivian		~ 132.9		
					Valanginian		~ 139.8		
					Berriasian		~ 145.0		
Phanerozoic	Mesozoic	Jurassic	Upper		Tithonian		~ 145.0		
					Kimmeridgian		152.1 ±0.9		
			Middle		Oxfordian		157.3 ±1.0		
					Callovian		163.5 ±1.0		
					Bathonian	↙	166.1 ±1.2		
					Bajocian	↙	168.3 ±1.3		
					Aalenian	↙	170.3 ±1.4		
					Toarcian	↙	174.1 ±1.0		
			Lower		Pliensbachian	↙	182.7 ±0.7		
					Sinemurian	↙	190.8 ±1.0		
					Hettangian	↙	199.3 ±0.3		
							201.3 ±0.2		
		Triassic	Upper		Rhaetian		~ 208.5		
					Norian		~ 227		
			Middle		Carnian	↙	~ 237		
					Ladinian	↙	~ 242		
					Anisian		247.2		
					Olenekian		251.2		
			Lower		Induan	↙	252.17 ±0.06		
					Changhsingian	↙	254.14 ±0.07		
		Permian	Lopingian		Wuchiapingian		259.8 ±0.4		
					Capitanian	↙	265.1 ±0.4		
			Guadalupian		Wordian	↙	268.8 ±0.5		
					Roadian	↙	272.3 ±0.5		
			Cisuralian		Kungurian		283.5 ±0.6		
					Artinskian		290.1 ±0.26		
					Sakmarian		295.0 ±0.18		
					Asselian	↙	298.9 ±0.15		
	Paleozoic	Carboniferous	Pennsylvanian	Upper	Gzhelian		303.7 ±0.1		
					Kasimovian		307.0 ±0.1		
			Middle		Moscovian		315.2 ±0.2		
					Bashkirian	↙	323.2 ±0.4		
			Lower		Serpukhovian		330.9 ±0.2		
					Visean	↙	346.7 ±0.4		
		Mississippian	Middle		Tournaisian	↙	358.9 ±0.4		

International chronostratigraphic chart published by International Commission on Stratigraphy, version 2015 (www.stratigraphy.org), part 1



International chronostratigraphic chart published by international commission on stratigraphy, version 2015 (www.stratigraphy.org), part 2

Appendix 2. Geological layers in the lower valley

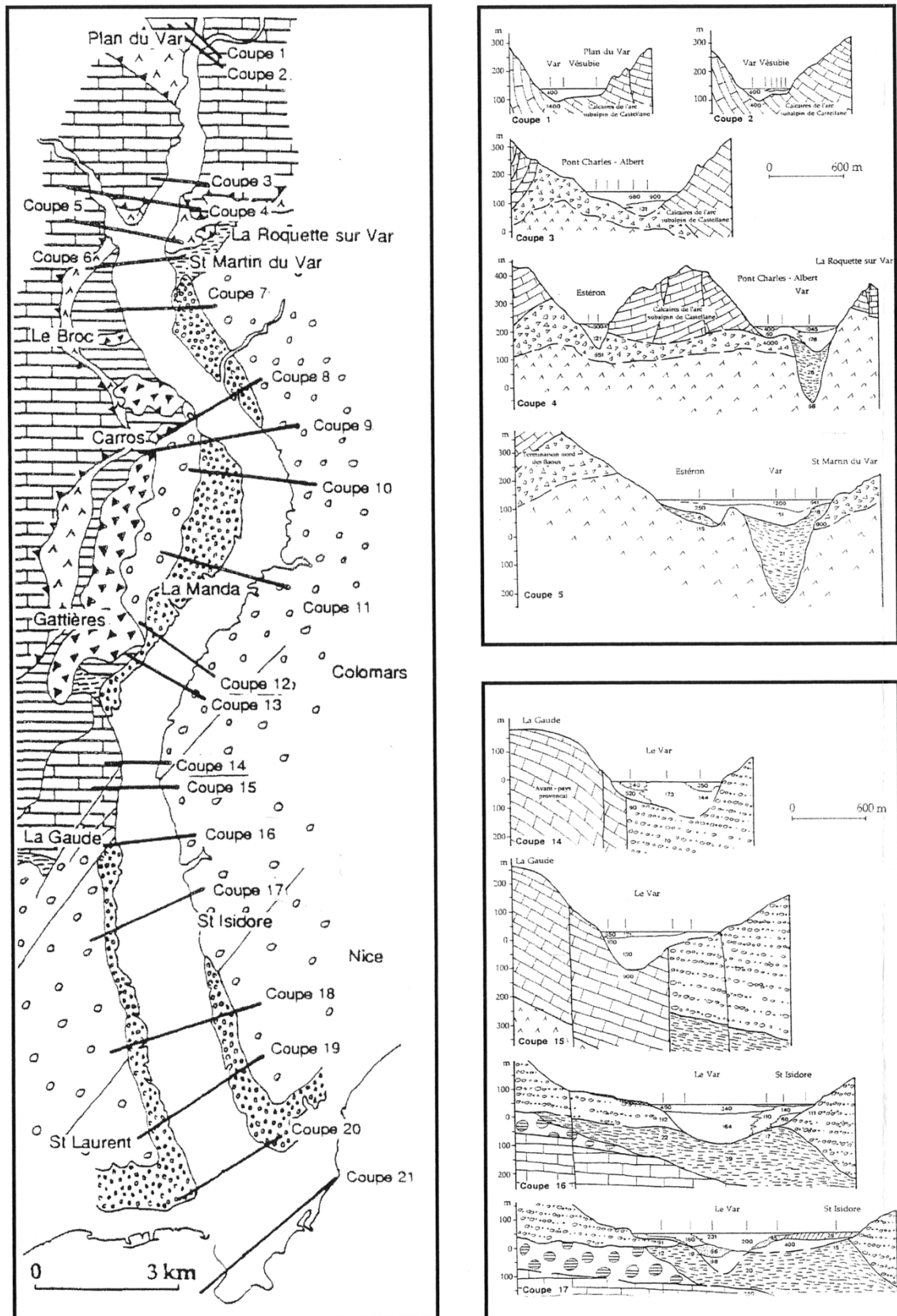


Figure. Geological layers in the lower Var river valley provided by Guglielmi [1993], part 1

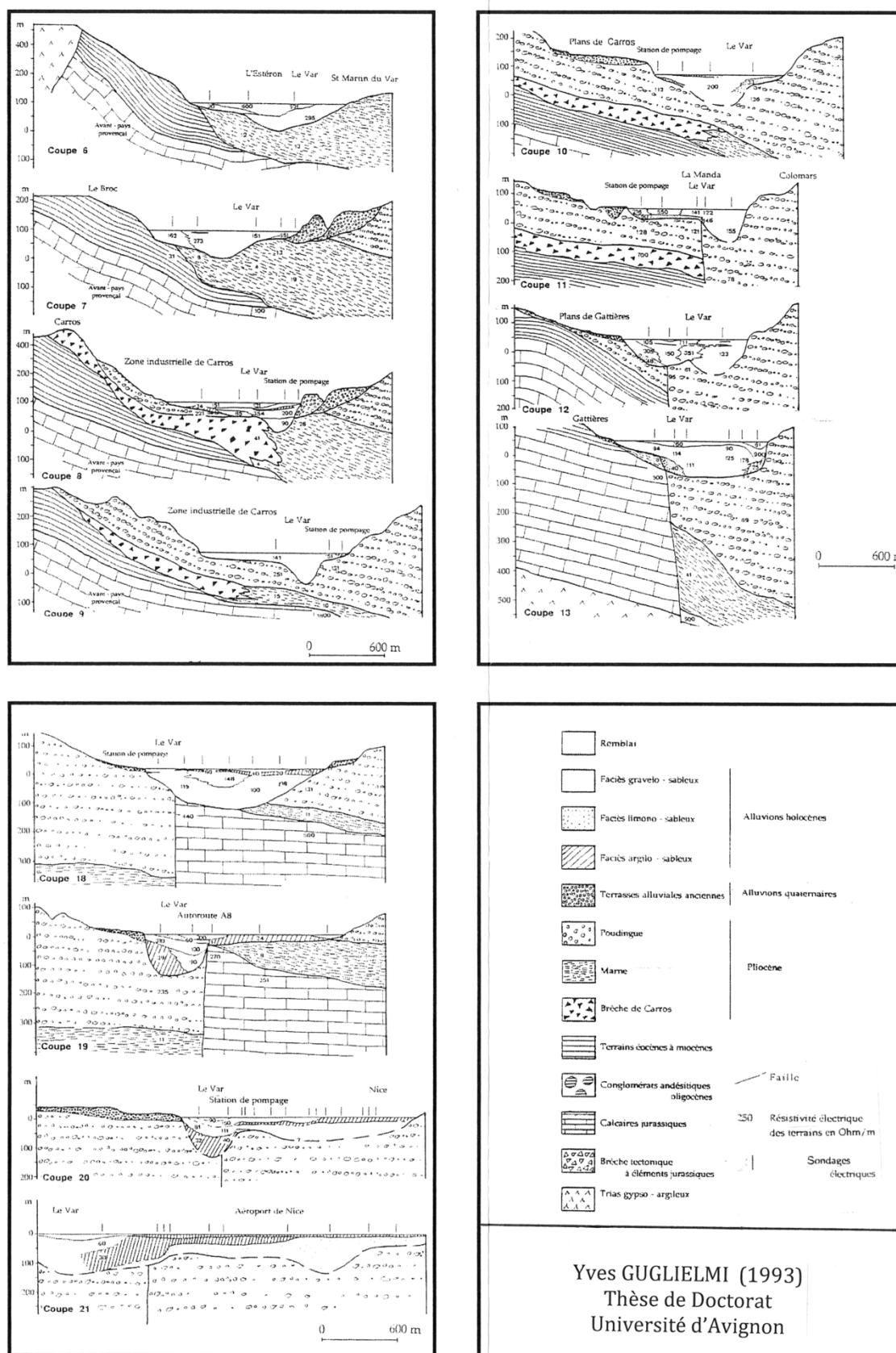


Figure. Geological layers in the lower Var river valley provided by Guglielmi [1993], part 2

Appendix 3. Geological drilling test of confined aquifer in the estuarine area of Var river

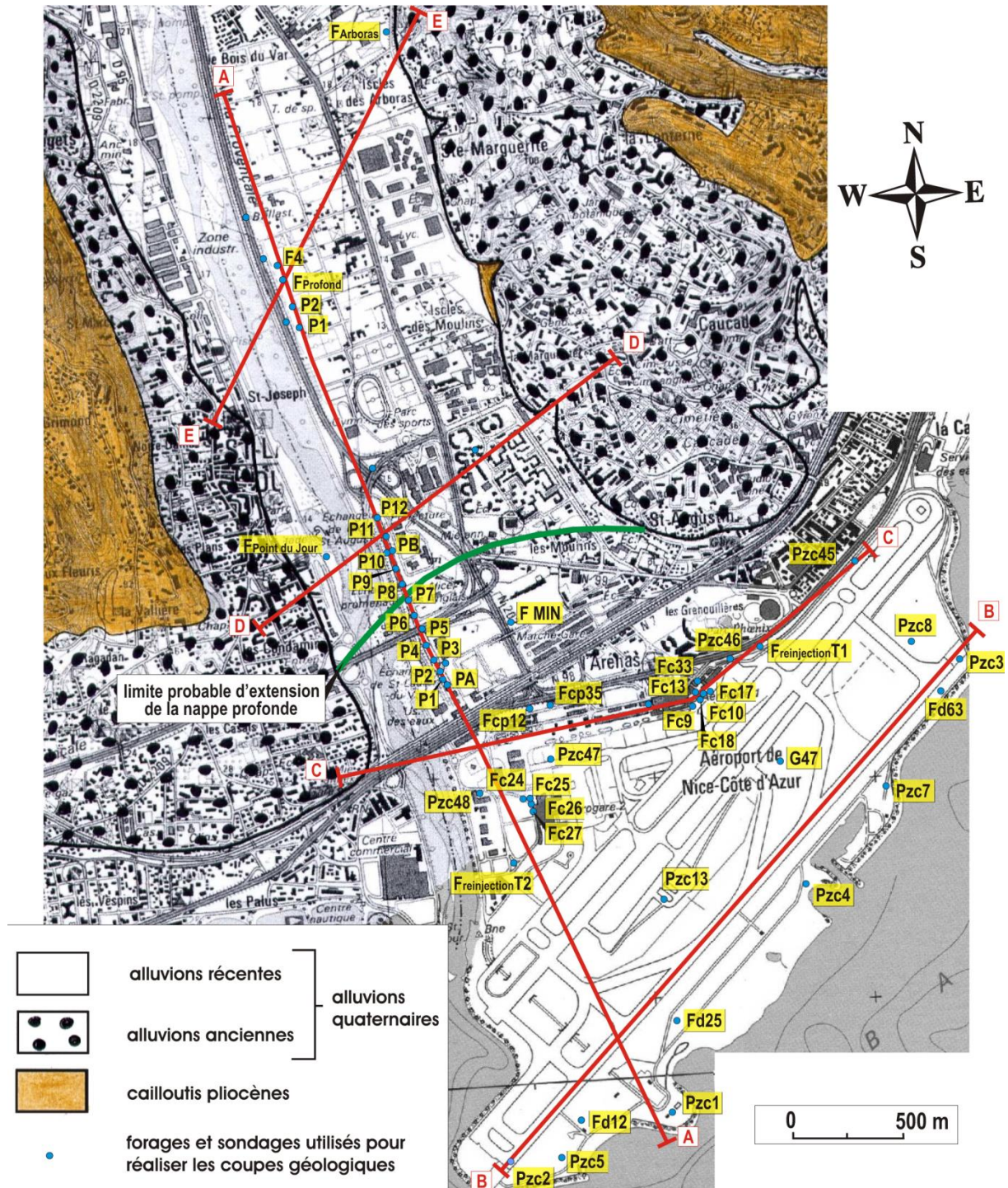


Figure. Location of the geological drilling tests used by Emily et al. [2010] to generate the geological profiles

Appendix 4. Measurement of groundwater level in the lower Var river valley

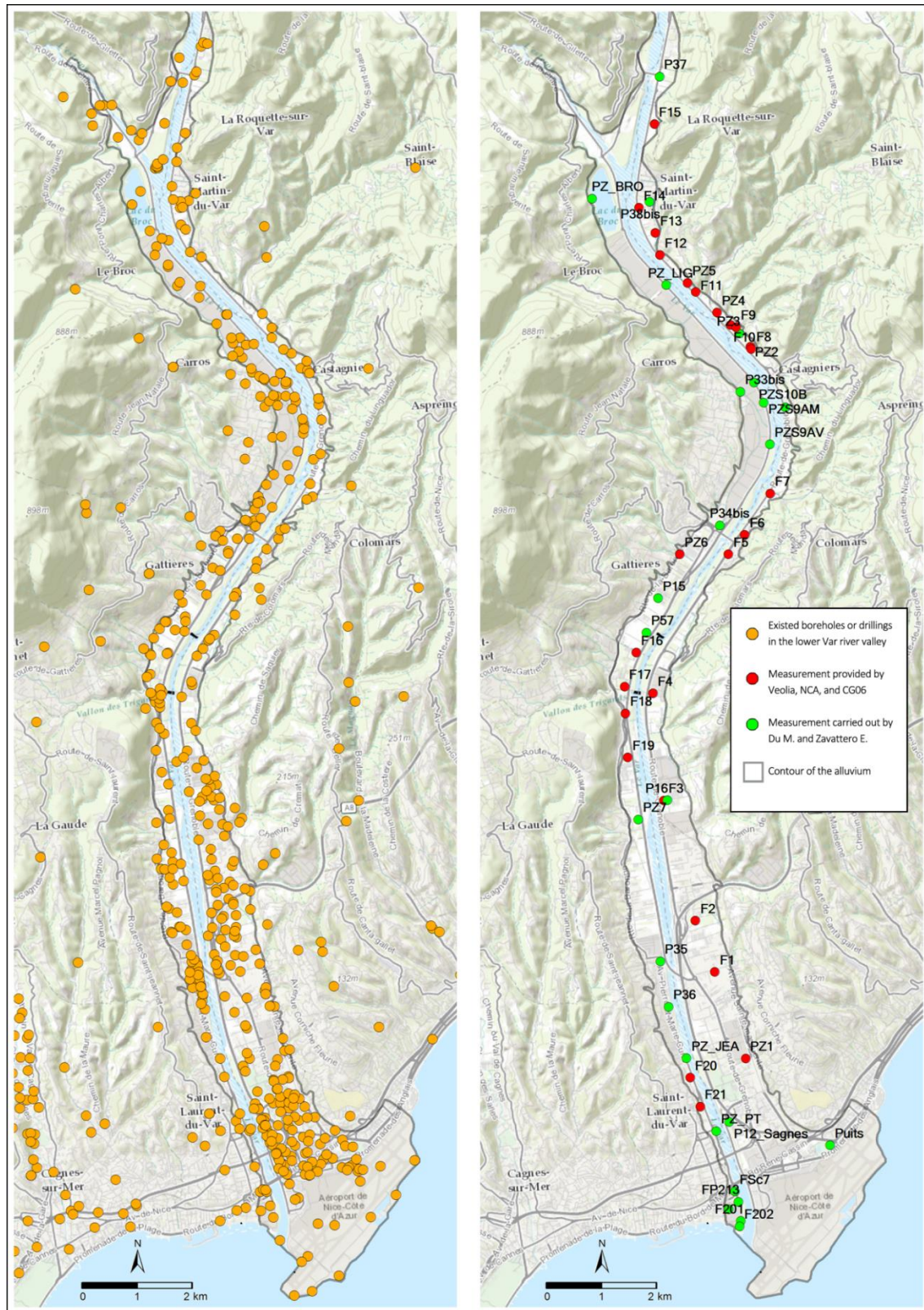


Figure. The existed boreholes (left) and the chosen boreholes to produce the groundwater level contour map (right)

Table. Measurement of the groundwater level from July 27th to 31st, 2015

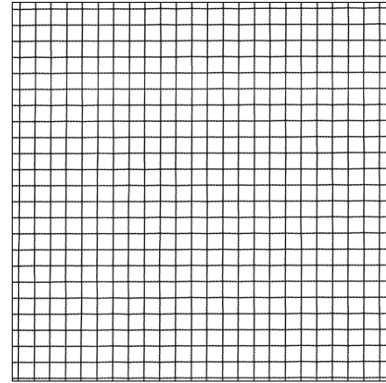
Point	X (m NGF)	Y (m NGF)	Z (m NGF)	Groundwater surface depth (m)	Groundwater level (m NGF)
PZ1	1038702.44	6296141.58	13.597	5.35	8.247
F3	1037288.18	6300629.09	35.729	13.57	22.159
F5	1038413.3	6304917.6	60.676	5.98	54.696
PZ2	1038759.35	6308569.07	82.61	4	78.610
PZ3	1038598.13	6308776.63	83.74	4.03	79.710
F10	1038457.05	6308914.4	84.56	3.81	80.750
PZ6	1037574.75	6304916.2	58.472	6.7	51.772
F9	1038543.98	6308876.32	83.895	3.56	80.335
F11	1037844.47	6309494.72	89.985	4.21	85.775
PZ4	1038219.41	6309138.07	86.739	3.85	82.889
F12	1037221.92	6310132.1	95.69	5.24	90.450
F13	1037141.89	6310517.48	99.465	6.88	92.585
F14	1036854.94	6310957.87	102.96	8.8	94.160
F15	1037124.59	6312412.9	114.681	15.6	99.081
PZ5	1037701.59	6309647.78	91.739	4.61	87.129
Puits	1040187.78	6294617.89	5.477	3.75	1.727
F4	1037097.62	6302493.62	47.134	13.6	33.534
F1	1038176.7	6297638.99	19.548	6.05	13.498
F16	1036807.91	6303208.51	48.97	10.87	38.100
F17	1036602.89	6302613.66	46.131	12.18	33.951
F18	1036621.89	6302148.55	44.999	15.07	29.929
F19	1036660.02	6301378.04	40.888	16.3	24.588
PZ7	1036847.4	6300299.53	35.022	13.54	21.482
F7	1039144.12	6305974	66.089	3.02	63.069
F6	1038701.82	6305261.26	62.576	4.95	57.626
F21	1037922.38	6295294.07	12.275	6.06	6.215

F20	1037749.79	6295797.52	14.492	6.23	8.262
FP213	1038590.14	6293634.26	2.9	1.44	1.460
F201	1038632.44	6293298	7.5	6.81	0.690
F202	1038610.18	6293208.34	5.3	4.47	0.830
FP211	1038416.22	6293503.6	2.05	1.2	0.850
FSc7	1038529.19	6293814.05	8.5	7	1.500
F2	1037839.16	6298534.16	24.454	8.42	16.034
P40BIS	1039410.2	6307481.5	75.37	3.55	71.82
P57	1036985.1	6303555.5	52.37	12.3	40.07
PZS9AM	1039028.72	6307565.75	77.52	4.51	73.01
PZS9AV	1039139.35	6306834.28	73.02	4.7	68.32
PZ_BRO	1036036.01	6311117.55	105.17	10.15	95.02
PZS10B	1038861.27	6307915.75	80.23	5.12	75.11
P38BIS	1037037.59	6311062.67	104.63	10.67	93.96
PZ_LIG	1037330.38	6309610.52	94.56	6.25	88.31
PZ_PT	1038200.9	6294865.05	13.44	8.54	4.90
PZ_JEA	1037684.26	6296136.22	16.26	6.91	9.35
P33BIS	1038623.5	6307750.6	79.25	3.99	75.26
P34BIS	1038265	6305424	65.09	7.91	57.18
P15	1037189.9	6304152.6	54.64	9.85	44.79
P16	1037352	6300632	35.97	13.79	22.18
P35	1037224.8	6297825.5	24.28	10.91	13.37
P36	1037370	6297034.8	20.43	8.65	11.78
P37	1037212.3	6313242.1	121.03	17.41	103.62
P12_Sagnes	1038428.57	6295029.88	9.92	4.07	5.85
PZS10A	1038733.62	6308071.27	61.628	5.07	76.54
PZ1BEC	1036567.06	6311676.82	109.29	13.99	95.3

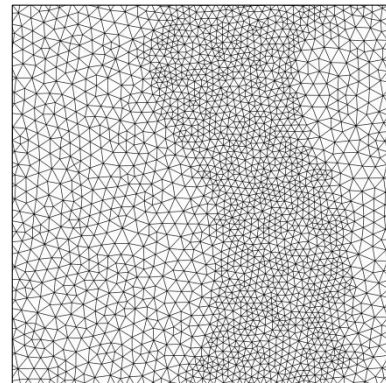
Appendix 5. Computational mesh types and characteristics

Computational mesh is used to discrete the geometry of the modeled domain, in order to approximate the governing equations of the numerical models. It partitions the space into different types of cell. The common cell shapes used in computational fluid dynamics are triangle and quadrilateral. The triangular cell is most commonly used in unstructured mesh, while the quadrilateral cell is usually used in structured mesh.

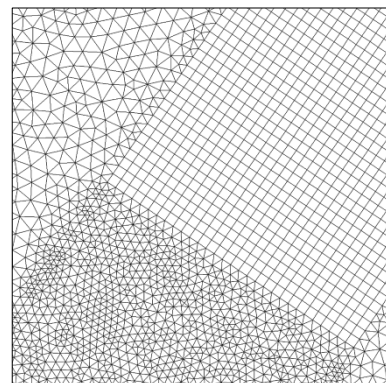
A structured mesh has regular connectivity among the cells. On a 2D surface, a structured mesh is usually presented with quadrilateral cells. This type of mesh is highly space efficient since the neighborhood relationships are defined by storage arrangement (ASCII or matrix etc.). The structured mesh has a better convergence and higher resolution over the whole domain than the unstructured mesh.



An unstructured mesh has irregular connectivity among the cells. It allows a better representation of the geometry of the targeted domain while the other area can be represented by coarse cells. This enables to save computation time of the simulation. However, compared to structured mesh, this type of mesh can be highly storage inefficient since it calls for explicit storage of neighborhood relationships.



A hybrid mesh contains a mixture of structured portions and unstructured portions. It integrates the structured mesh and the unstructured mesh in an efficient manner. The areas with regular geometry can have structured mesh and those with complex geometry can have unstructured mesh.



Appendix 6. Geographical survey methods

All the geological information that has been used in this study is from previous studies in the lower Var river valley. Two geological survey methods are concerned in these studies: Electrical resistivity survey, which is used by Gulglielmi [1993] to analyze the profiles of the alluvium in the valley, and the geological drilling test, which is commonly used by most of the studies to obtain the sediment samples of the alluvium in the valley.

Electrical resistivity survey (www.geopotential.biz)

Electrical resistivity is a geophysical method in which an electrical current is injected into the ground through steel electrodes in an attempt to measure the electrical properties of the subsurface. Most soils and non-ore bearing rocks are electrically resistive, (*i.e.*, insulators). Soil moisture and groundwater are often electrically conductive due to contained dissolved minerals. Therefore the resistivity measured in the ground is predominantly controlled by the amount of moisture and water within the soil and rock (a function of the porosity and permeability), and the concentration of dissolved solids (salts) in that water. The basic method requires at least 4 steel electrodes be driven into the ground. An electrical current is then applied to the outer electrodes by a battery or generator. A voltage is measured between the 2 inner electrodes using a simple voltmeter. Through Ohm's Law ($V = IR$, where V is the voltage, I the electric current and R the resistance) and by knowing the input current, the measured voltage and the geometry of the electrode array, a value known as resistance can be calculated. Resistivity, measured in Ohm-meters, is resistance multiplied by area divided by distance. Because the actual current flow is highly influenced by conductive layers, the value measured is known as the "apparent resistivity". In its simplest terms, it represents an average value encompassing all of the different materials within the volume (half-space) of materials being measured. Most modern resistivity meters calculate apparent resistivity once the geometric parameters are input.

Geological drilling test (en.wikipedia.org)

Drilling test is a geophysical method in which boreholes are created in the ground by drilling rigs, in order to sample the subsurface deposits such as test rock, soil and groundwater physical properties. It can be also used to install subsurface fabrications, such as underground utilities, instrumentation, tunnels or wells. Drilling rigs can be mobile equipment mounted on trucks, tracks or trailers, or more permanent land or marine-based structure (such as oil platforms, commonly called 'offshore oil rigs' even if they don't contain a drilling rig). The term "rig" therefore generally refers to the complex of equipment that is used to penetrate the surface of the Earth's crust.

All holes must maintain outer diameter; the diameter of the hole must remain wider than the diameter of the rods or the rods cannot turn in the hole and progress cannot continue. Friction caused by the drilling operation will tend to reduce the outside diameter of the drill bit. This applies to all drilling

methods, except that in diamond core drilling the use of thinner rods and casing may permit the hole to continue. Casing is simply a hollow sheath which protects the hole against collapse during drilling, and is made of metal or PVC. Often diamond holes will start off at a large diameter and when outside diameter is lost, thinner rods put down inside casing to continue, until finally the hole becomes too narrow.

Appendix 7. Maximal values of daily average discharge measured at Napoléon III bridge used for Gumbel law calculation

Year	Month	Date	Daily average discharge (m ³ /s)
1974	February	2	164
1975	February	12	223
1976	October	13	530
1985	May	14	481
1986	April	26	351
1987	October	12	352
1988	October	20	714
1989	April	13	207
1990	October	84	84
1991	November	30	778
1992	June	25	190
1993	October	8	1050
1994	November	5	1460
1995	April	24	193
1996	January	12	916
1997	December	20	459
1998	May	29	219
1999	October	21	248
2000	November	6	430
2006	August	19	247
2008	January	12	312
2009	December	25	418
2010	November	1	511
2011	November	5	910
2012	November	11	542
2013	April	30	513
2014	November	5	482
2015	October	4	116

Appendix 8. Monthly average discharge measured at Napoléon III bridge used for log-normal law calculation

Year	Monthly average discharge (m ³ /s)		
	July	August	September
1974	42.1	22.4	27.0
1975	46.1	36.7	46.6
1976	36.2	33.5	54.8
1985	30.9	16.8	13.5
1986	52.0	26.8	17.3
1987	35.6	25.1	20.2
1988	47.0	30.3	25.1
1989	22.3	15.1	12.8
1990	14.6	10.1	8.6
1991	25.0	13.7	49.9
1992	50.4	38.3	41.2
1993	24.6	18.0	50.5
1994	34.2	23.6	84.1
1995	31.0	35.7	35.2
1996	45.9	37.1	37.2
1997	33.8	31.3	22.7
1998	28.6	21.4	22.2
1999	22.5	21.0	31.7
2000	18.2	17.3	20.1
2006	30.3	34.2	45.0
2008	52.0	28.1	22.0
2009	47.5	25.4	25.6
2010	41.3	22.2	11.8
2011	26.0	17.5	15.4
2012	21.6	16.4	21.5
2013	57.8	32.2	21.3
2014	55.7	37.7	31.2
2015	17.3	11.4	12.1